University of Pretoria

Evaluation of a strategy based on multi-drug targeting of cancer proteins in breast cancer cell lines

by
Evangeline Nortje
(10474588)

Submitted in partial fulfilment of the requirements for the degree
Philosophiae Doctor (Ph.D) degree in Human Physiology

Department of Physiology
School of Medicine
Faculty of Health Sciences
University of Pretoria

Supervisor: Dr BA Stander
Co-supervisors: Prof PJ du Toit, Prof AD Cromarty

2020

Declaration

University of Pretoria
Faculty of Health Sciences
Department of Physiology

Title of Project:

Evaluation of a strategy based on multi-drug targeting of cancer proteins in breast cancer cell lines.

I, Evangeline Nortje (Student number: 10474588), declare that:

I understand what plagiarism is and am aware of the University's policy in this regard.
I declare that this project is my own original work. Where other people's work has been used, this has been properly acknowledged and referenced in accordance with departmental requirements.
I have not used work previously produced by another student or any other person to submit as my own.
I have not allowed, and will not allow, anyone to copy my work with the intention of presenting it as their own.

Signature

.....

Acknowledgements

Completion of this project would not have been possible without the necessary guidance, support and contribution from many people, whom I would like to sincerely acknowledge:

My supervisor, Dr André Stander, and co-supervisors, Prof Peet du Toit and Prof Duncan Cromarty, for accepting me as their student, sharing their knowledge, influential advice and constructive criticisms. For providing guidance and direction, and for their unceasing patience to make this work a reality.

Prof Annie Joubert, head of the Department of Physiology, for allowing me the time and the use of the facilities; and also for her words of wisdom, encouragement and support throughout.

Lab mates, previous and present, Trophimus Tembo, Desiree Fraser, Ting-Hua Chang, Daniel Joubert for their assistance and support.

Dr Iman van Den Bout for the confocal microscopy training and affording the time and space for use of the CNE facilities.

My fellow support staff colleagues, Dalene, Sumari, Sandra, Abe, Michelle and Michael for lifting the load of departmental responsibilities during the tough times and for creating a pleasant environment at the work place.

Professor Piet J Becker from the unit for Biostatistics, Faculty of Health Sciences, University of Pretoria, for the infinite confidence in his field, his recommendations and assistance with statistical analysis.

My friends, long withstanding and anew, for their friendship, upliftment and support throughout this endeavour.

Lastly, my family, for all of their encouragement, understanding, support and sacrifice.

Dedicated with thanks to:

My husband for his unwavering love, encouragement, moral support and patience as well as strengthening my resolve to complete this endeavour;

My daughter who has inspired me in ways she can never imagine;

My parents for instilling in me the ambition to thrive and persevere, both academically and in life;

'Now to Him who is able to do immeasurably more than all we ask or imagine, according to His power that is at work within us'

(Ephesians 3:20)

Executive summary

Therapeutic inefficacy of conventional cancer treatment is a particular dilemma associated with metastatic triple negative breast cancer (TNBC), with patients still facing poor prognosis. The design and development of novel anticancer agents specifically targeted to cancer-associated pathways is of therapeutic interest. The rationale is twofold: firstly, targeted therapy overcomes widespread toxicity and adverse effects of conventional chemotherapy due to the selectivity of the treatment modality. Secondly, synergistic combinations of different classes of highly targeted therapies could hold therapeutic promise to overcome resistance by simultaneously circumventing multiple cancer hallmarks. This study evaluates the *in vitro* antiproliferative activity of six compounds using breast cancer cell lines as experimental model. Five of these compounds are novel, agents designed *in silico* to selectively target cancer hallmarks *via* inhibition of specific cancer-associated proteins. The compounds include an antimitotic (STX1972), three variants of bromodomain 4 (BRD4) inhibitors (Bzt-W41, Bzt-W49 and Bzt-W52), an inhibitor of both sirtuin (SIRT) 1 and 2 (W137) and an inhibitor of janus kinases 1 and 2 (Ruxolitinib). The synergism between paired combinations was also explored.

Two breast cancer cell lines, MDA-MB-231 and MCF-7 were used as experimental models. The MDA-MB-231 cell line is oestrogen receptor (ER), progesterone receptor (PR) and human epidermal growth factor receptor 2 (HER2) negative and is therefore commonly used to model triple negative breast cancer with invasive and metastatic properties. MCF-7 cells are ER and PR positive and represent the hormone-dependent breast cancer model. The endothelial EA.hy926 cell line was used to represent non-cancerous cells. A crystal violet assay was used to determine the half maximal inhibitory concentration (IC_{50}) of the six compounds on the tested cell lines after 48 h exposure. Drug combination studies based on the Chou-Talalay method of paired drug combinations were performed. Effects of treatment on cell morphology was assessed by means of confocal-microscopy. Flow cytometry was used to study the effects on cell cycle progression, apoptosis, autophagy/lysosomal activity, reactive oxygen species (ROS) production, changes in mitochondrial membrane potential ($\Delta\Psi m$) and the serine 70 phosphorylation status of Bcl-2. Real-time quantitative PCR was used to analyse the effects of the compounds on the mRNA expression levels of

p53, *c-myc* and *bcl-2*. Quantitative protein expression of c-MYC was analysed by means of enzyme-linked immunosorbent assay.

In vitro screening for antiproliferative activity revealed that the compounds showed cancer-selective cytotoxic effects when compared to the EA.hy926 control cell line. The initial screening identified three compounds for further investigative inclusion, namely the antimitotic (STX1972), the BRD4i (Bzt-W41) and the SIRTi (W137). STX1972 was found to inhibit cell growth in the nanomolar concentration range, whilst the rest of the compounds showed growth inhibition in micromolar concentration ranges. Bzt-W41 showed significant preferential selectivity for the TNBC MDA-MB-231 cell line versus the hormone-dependent MCF-7 cell line, while STX1972 and W137 exhibited only slight differential selectivity. Two combinations (STX + Bzt-W41 and Bzt-W41 + W137) exhibited synergism, whilst the STX + W137 combination exhibited antagonistic interaction. Cell cycle and apoptosis analysis revealed that STX1972 and Bzt-W41, alone and in combination, selectively induced cell cycle arrest and apoptosis in cancer cells. However, the W137 +Bzt-W137 combination did not show preferential targeting of breast cancer cell lines, with apoptosis induced equally or even more so in the control EA.hy926 cell line. STX1972 and Bzt-W41, as well as their paired combination, was further probed in aim of deciphering their individual and combined mode of action.

STX1972, Bzt-W41 as well as the paired combination proved to selectively inhibit cancer targets resulting in several molecular changes, leading to downstream pathway activation which culminates in both apoptotic and autophagy-related cellular demise. The study contributed towards deducing possible hypotheses regarding the mechanistic behaviours of the individual compounds and elucidated their combined effect during dual treatment. Results warrant future studies to further probe the intricate interaction of pathways involved in the synergistic combination of antimitotics and epigenetic regulators as a novel anticancer therapeutic modality.

Keywords: breast cancer, antimitotic, bromodomain inhibitors, sirtuin inhibitors, combination index, apoptosis, autophagy, *c-myc, bcl-2*

Research outputs

Participation in conferences

53rd Annual Conference of the South African Society for Basic and Clinical Pharmacology (SASBCP), Pretoria, Gauteng (October 2019)

Poster: Synergistic *in vitro* effects of combining a polypharmacological antimitotic, STX1972, and a bromodomain 4 inhibitor, Bzt-W41, on breast cancer cells. Nortje, E.; Stander, B.A.; du Toit, P.J.; Potter B.; Cromarty, A.D.

University of Pretoria, Faculty of Health Sciences, Faculty Day (August 2019)

Poster: Synergistic *in vitro* effects of combining a polypharmacological antimitotic, STX1972, and a bromodomain 4 inhibitor, Bzt-W41, on breast cancer cells. Nortje, E.; Stander, B.A.; du Toit, P.J.; Potter B.; Cromarty, A.D.

University of Pretoria, Faculty of Health Sciences, Faculty Day (August 2018)

Poster: Synergistic anticancer effects of a potent antimitotic and an *in silico* designed bromodomain inhibitor on breast cancer cells. Nortje, E.; Stander, B.A.; du Toit, P.J.; Potter B.; Cromarty, A.D.

43rd Annual Congress of the Physiology Society of Southern Africa (PSSA), Parys, Free State (September 2015)

Speaker: *In vitro* evaluation of selectively targeting in silico designed anticancer compounds on breast cancer cells. Nortje, E.; Stander, X.X.; du Toit, P.J.; Stander, B.A.; Potter B., Cromarty, A.D.

University of Pretoria, Faculty of Health Sciences, Faculty Day (August 2015)

Speaker: *In vitro* evaluation of selectively targeting in silico designed anticancer compounds on breast cancer cells. Nortje, E.; Stander, X.X.; du Toit, P.J.; Stander, B.A.; Potter B., Cromarty, A.D.

Table of Contents

List of Figures

List of Tables

List of abbreviations

%	Percentage
Δψm	Mitochondrial membrane potential
2ME2	2-Methoxyestradiol
Abs	Absorbance
ACD	Accidental cell death
AIF	Apoptosis inducing factor
AMPK	AMP activated protein kinase
ANOVA	Analysis of variance
AO	Acridine orange
Apaf-1	Apoptotic peptidase activating factor
ATCC	American type culture collection
Bax	Bcl-2-associated X protein
BET	bromodomain and extraterminal
Bid	BH3 interacting-domain
Bcl-2	B-cell lymphoma 2 protein
BRD4	Bromodomain containing protein 4
BRD4i	BRD4 inhibitor
BSA	Bovine serum albumin
°C	Degrees Celsius
CDKs	Cyclin Dependent Kinases
Caspase	Cysteinyl aspartate specific protease family
CI	Combination Index
CADD	Computer aided drug design
CF	Combination fraction
CO_2	Carbon dioxide
DCFH-DA	2’,7’-dichlorodihydrofluorescein diacetate
DEPC	Diethylpyrocarbonate
DFO	Deferoxamine mesylate salt
dH2O	Distilled water
$DiOC_6(3)$	3,3'-dihexyloxacarbocyanine Iodide
DMEM	Dulbecco’s Modified Eagle’s Medium

DMSO	Dimethylsulfoxide
DNA	Deoxyribonucleic acid
EDTA	Ethylenediamine tetraacetic acid
ELISA	Enzyme-linked immunosorbent assay
EMT	Epithelial-mesenchymal transition
ER	Oestrogen receptor
FITC	Fluorescein isothiocyanate
FoxoH1	Forkhead box protein H1
g	Gravity
G_1 phase	Gap 1 phase
G_2/M phase	Gap-2/mitosis
GAPDH	Glyceraldehyde-3-phosphate dehydrogenase
GSH	Glutathione
GSSG	Glutathione disulfide
GST	Glutathione S-transferases
H	Hour
HAT	Histone acetyltransferase
HCO3-	Bicarbonate ion
HDAC	Histone deacetylase
HEPES	4-(2-hydroxyethyl)-1-piperazine ethanesulfonic acid
Her2	Human epidermal growth factor receptor 2
HIV	Human immunodeficiency virus
IC_{50}	Concentration of compound which results in 50% inhibition
IL-6	Interleukin-6
Ki	Inhibitor constant
LBDD	Ligand based drug design
MDM2	Murine Double Minute 2
mg	Milligram
min	Minute
MiT/TFE	Microphthalmia family of bHLH-LZ transcription factors
mM	Millimolar
MRP2	Multidrug resistance-associated protein 2
mTOR	Mammalian target of rapamycin

NAC	N-acetyl-L-cysteine
NADPH+	Reduced nicotinamide adenine dinucleotide phosphate
NAD	Nicotinamide adenine dinucleotide
NaHCO3	Sodium bicarbonate
NF- κB	Nuclear factor kappa B
nM	Nanomolar
O2-	Superoxide radical
OD	Optical density
p53	Tumour suppressor protein 53
p53	Gene encoding for tumour suppressor protein 53
P	Probability
PR	Progesterone receptor
PS	Phosphatidylserine
PBS	Phosphate buffered saline
PCD	Programmed cell death
PCR	Polymerase Chain Reaction
pH	Negative logarithm of the hydrogen ion concentration
PI	Propidium iodide
PI3K	Phosphoinositide 3-Kinase
PKC	Protein kinase C
PlasDIC	Polarisation-optical differential interference contrast
PP2A	Protein phosphatase 2A
P-TEFb	Positive transcription elongation factor b
Rb	Retinoblastoma protein
RCD	Regulated cell death
R/GFIR	Red-to-green fluorescence intensity ratio
R/GFIR-T	Red-to-green fluorescence intensity ratio threshold
RT-qPCR	Quantitative Real Time Polymerase Chain Reaction
RMSD	Root mean square deviation
ROS	Reactive oxygen species
RTF	Random Tree Forest
siRNA	Small interfering RNA
SIRT	Sirtuins

SIRTi	Sirtuin inhibitor
SBDD	Structure based drug design
SP	Standard precision
STS	Steroid sulphatase
TNBC	Triple negative breast cancer
TPSA	Topological polar surface area
µg	Microgram
µg/mL	Micrograms per millilitre
µL	Microlitre
ULK	UNC-51-like kinase
µM	Micromolar
w/v	Weight per volume

Chapter 1: Introduction

1.1 Background

Cancer remains one of the most devastating global epidemics to face humankind and is accountable for 15% of the annual worldwide mortality rate [1]. This number is on the rise with cancer incidence estimations projecting a 70% increase in the number of newly diagnosed cases by the year 2030 [1-2]. Breast cancer ranks as the second most common cancer world-wide and the fifth cancer-caused death globally [1,3]. Among female populations in less developed regions breast cancer is the primary cause of cancer death and statistics forecast the cancer burden to rise disproportionately in the developing world [1]. According to the World Health Organization's cancer country profiles, breast cancer has the highest incidence rate and is the second highest cause of cancer-related mortality among South African women [4].

Unfortunately, the existing and projected data on cancer incidence and mortality underpin the gloomy reality that a solution to overcome this prodigious disease is not yet imminent. Therefore, an attempt to mitigate the growing cancer endemic calls for novel research to pioneer innovative cancer treatment strategies.

Knowledge gained from decades of cancer research steered the discovery of the various cancer treatment approaches available today, which include: chemotherapy [5], radiation therapy [6], surgery [7], hyperthermia [8], immunotherapy [9], stem cell transplants [10], photodynamic therapy [11], laser therapy [12], hormone therapy and targeted therapy [13]. In some cases these oncology treatments are prescribed in isolation but often combinations are used as adjunctive therapy, depending on the patient's cancer type and stage [13]. Each treatment option presents valid arguments for its practise but not without accompanying pitfalls, among which are resistance, specificity, recurrence and a plethora of side effects. Common side effects of cancer therapeutics include anaemia, thrombocytopenia, alopecia, infection and neutropenia, lymphedema and peripheral neuropathy [13].

Conventional cancer treatments have not proven effective in the eradication of cancer, in fact, evidence suggests that many of the cancer therapies augment cancerous cell

adaptation and insensitivity to drugs and could play a causal role in cancer recurrence and reduced patient survival [14-15]. Treatment induced drug resistance causes therapeutic inefficacy in more than 90% of metastatic cancer cases [16]. Numerous molecular mechanisms contribute to the evolution of chemoresistant subclones, these include: decreased drug influx through altered expression or mutation of membrane transporters causing reduced cellular uptake of drugs [17-19]; increased drug efflux via overexpression of active transporters [20]; drug inactivation or degradation [21]; transformed anticancer drug targets through oncogenic mutation and/or altered expression levels [16]; and increased DNA repair capacity subsequent to drug-induced damage [22].

The current breast cancer treatment selection process relies largely on the type of breast cancer diagnosed. This is because breast cancer is not simply a single disease, but rather a complex heterogeneous malignancy which is divisible into numerous subtypes. Breast cancer subtypes are based on several clinical and histological features including the site of tumour origin (ductal, lobular or other), nodal involvement, the extent of spread (*in situ*, invasive or metastatic), as well as tumour type (inflammatory or distinct), grade, stage and size [23-26]. However, inter-tumour phenotypic variation is paralleled by pervasive differences in gene expression patterns [27]. Systematic investigation of the genetic diversity amongst tumours, or gene expression profiling techniques, has provided a means to distinguish breast cancer subsets based on their distinct molecular portraits [23,28-30]. Molecular taxonomy is based on biological characteristics such as oestrogen receptor status (ER^-/ER^+), progesterone receptor status (PR^+/PR^-) and human epidermal growth factor receptor-2 expression ($HER2^+/HER2^-$) [23,31-33]. The prognostic value gained from inter-tumour molecular profiling dwarfs that of histopathalogical parameters and provides more relevant insight to the most beneficial subtype-based neoadjuvant or adjuvant treatment selection [13,28,30].

Despite advances in molecular characterization and successively improved guidelines for therapeutic recommendations, prognosis of several breast cancer subtypes remains poor. In South Africa the death rate for HER2-enriched tumours is 2.5 fold higher compared to oestrogen receptor (ER) and progesterone (PR) positive, and HER2 negative (ER+/PR+/HER-) tumours [34]. Death rates are 3-fold higher for breast

cancers with the triple negative phenotype ($ER^-/PR^-/HER2^-$) compared to ER+/PR+/HER- tumours [34]. Triple negative breast cancers (TNBC) are considered to have a particularly pessimistic prognosis due to insensitivity to hormonal therapy, increased recurrence probability and decreased survival rates [23,35-36]. Chemotherapy remains the primary systematic treatment for TNBCs but the lack of targeted therapies contributes to the poor outcome of this disease and new therapeutic options for this disease continues to be developed [37].

To the opposite end, there are occurrences where breast cancer subsets with more favourable prognoses have been found to respond unpredictably, or not at all, despite appropriate therapeutic modality [38]. Variation in the clinical outcome of breast cancer patients treated with trastuzumab [39], tamoxifen [40] and taxane-based therapies [41] epitomizes the predicament. Manifestations such as these can be explained by the intercellular genetic and phenotypic diversity found within a tumour [42]. Intratumour heterogeneity is triggered by genomic instability which fosters an increased mutation rate and the differential evolution of tumour subpopulations [42-43]. Subclonal morphing varies during the progressively malignant stages of cancer and is thought to be augmented by cancer therapy, thereby facilitating therapeutic resistance, propagating tumour progression and debilitating patient outcome [42,44-45].

Intertumour and intratumour architectural complexities contextualize the therapeutic challenge posed by this vexatious disease and provide reasoning behind paradoxical tumour behaviour in response to customary treatments. Therefore, cancer heterogeneity embodies the onslaught of impending anticancer drug research. Currently, much of the research focusses on the development of precision medicines which are designed to selectively target the molecular defects of tumour cells [13].

The concept of synthesising molecular compounds with precise targets was introduced more than a century ago by German scientist and Nobel laureate Paul Ehrlich [14,46-47]. His ‘magic bullet’ theory pioneered the evolution of therapeutic pharmacology and revolutionized contemporary drug design approaches [46-47]. The cornerstone of this theory is the deliberate engineering of chemical structures based on their pharmacological selectivity towards the altered physiology of cancer cells, thus leaving normal cells unaffected. Hence, the intention to develop rationally

designed molecularly targeted drugs with promising outcomes first requires critical understanding of the differences between malignant cells and normal cells.

1.2 Normal cell biology: division and death

Normal cell biology depends largely on the homeostatic regulation of cell growth, division and death, and disruptions in the control mechanisms of these pathways have been implicated in neoplastic progression. Therefore, exploring the molecular basis of these cellular processes validates the rationale behind many targeted cancer therapies.

1.2.1 Cell cycle

The cell cycle is a ubiquitous physiological process which entails a highly regulated series of events culminating in the production of two daughter cells, each containing genetic material identical to that of the parent cell. The cyclic pattern of DNA duplication and cell division can be categorized into four distinct phases: S phase (synthesis phase), M phase (mitosis) and two Gap phases (G_1 and G_2) as illustrated in Figure 1.1 [48]. The G_1, S and G_2 phase are collectively referred to as interphase and describe the non-dividing stage of the cell cycle. Upon mitogenic signalling cells enter the first gap phase (G_1) which marks the onset of cell growth, chromosomal preparation for replication and duplication of cellular components [49]. As cells transition into the S phase chromosomal DNA is duplicated from a normal diploid (2N) to a tetraploid (4N) state. Tetraploid cells enter the second gap phase (G_2) where DNA integrity is checked and cells prepare for division and entry into mitosis [49]. Mitosis is divided into four subphases that take place in the following order: prophase, metaphase, anaphase, and telophase. Finally, at completion of the M phase, following cytokinesis, two identical diploid daughter cells are born. Daughter cells may be signalled to re-enter the cell cycle for repeated division or may exit the cell cycle. Metabolically active cells which are not in the process of replicating exit the cell cycle and enter a non-dividing state of quiescence (G_0) [50]. Precise and successive progression through each of the phases is pragmatically orchestrated by multiple regulatory proteins and is central to normal growth and development.

1.2.1.1 Cell cycle regulation and checkpoints

Cell cycle regulation

The cell cycle is regulated by an elaborate, multi-layered homeostatic control mechanism. Chronologic progression to the next phase is irreversible and dependent on successful completion of the previous [51]. Central to cell cycle control are the cyclins and cyclin-dependent kinases (CDKs) [52]. As implied by their name, CDKs are dependent on association with their cognate regulatory cyclin proteins for activation [52]. The four classes of cyclins (cyclin D, E, A, and B) are expressed in oscillations throughout the cell cycle and are defined by the phase of the cell cycle in which they bind to their CDK (Figure 1.1) [53]. During G_1 the D-type cyclins associate with CDK4 and CDK6, preparing the cell for S-phase and aiding in the progression through the G_1-S checkpoint [53]. Cyclin E binds to CDK2 at the end of G_1 and commits the cell to DNA replication while cyclin A-CDK2 mediates S phase progression [53]. G_2 transition is facilitated by cyclin A-CDK1 and M phase entry and mitotic events require cyclin B-CDK1 interaction [53].

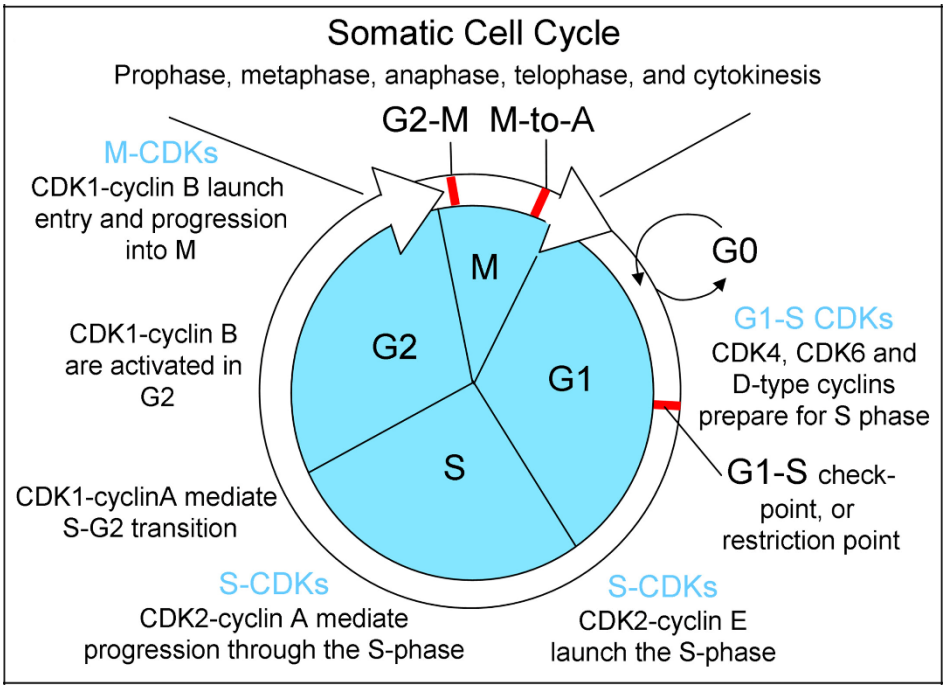

Figure 1.1: Overview of the cell cycle phases and phase specific CDK-cyclin interaction required for progression [53].

Phase-specific expression, degradation, activation and inhibition of the cyclin-CDK complexes is controlled by various up- and downstream regulators. In terms of quantitative control, the number of circulating cyclins and CDKs depends on an interplay between transcriptional activation and/or repression and proteolysis via ubiquitylation. Protein synthesis is regulated by E2F transcription factors (E2Fs 1-8) and the retinoblastoma (RB) pocket protein family (pRB, p107, and p130) [54]. Transcriptional activation occurs when pRB is phosphorylated and inactivated allowing dissociation from E2F1-3a; and transcription is actively repressed when p107 and p130 associate with E2F4-5 [54]. Ordered cell cycle transition is also subject to timely ubiquitin-dependent degradation of cell cycle regulators by two multicomponent E3 ubiquitin ligases [55]. The SKP1-CUL1-F-box-protein (SCF) is a cullin-based ligase which is active during late G_1 to early M phase and the anaphase-promoting complex/cyclosome (APC/C) is active during mid M phase to the end of G_1, warranting phase-specific cyclin fluctuation [55-56]. Additional positive and negative mediators add to the intricacy of the regulatory biology of cell cycle progression. CDK activity is modulated by CDK-activating kinases (CAKs) and phosphatases (Cdc25A,B,C) through a series of phosphate transfer actions ultimately ensuring the required phosphorylation status for cyclin-CDK complex stabilization [57]. To the opposite end, CDK activity is antagonized by two main classes of endogenous CDK inhibitors: INK4 and CIP/KIP [53,57]. Both groups of inhibitory peptides retard cell cycle transition when deleterious to the cell [53].

Cell cycle checkpoints

Checkpoints are, as the name implies, points of surveillance in the cell division cycle. At a checkpoint cellular conditions are examined and transition of a cell to the next phase is either granted or halted dependent on the successful completion of critical events [58]. Regulation at internal checkpoints prevents proliferation of compromised cells and ensures high genomic fidelity [59]. Checkpoint loss or disruption is implicated in tumorigenesis and malignancy [58]. The three main checkpoints which regulate cell cycle progression are located near the end of G_1 (G_1/S checkpoint), at the G_2/M transition (G_2/M checkpoint), and at the transition from metaphase to anaphase (spindle assembly checkpoint) as illustrated in Figure 1.1 [60]. Each checkpoint monitors whether a specific set of prerequisites have been met before granting clearance for

transition to the successive phase. The G_1/S checkpoint assesses external molecular signals, cell size, available nutrient reserves and DNA integrity, and prevents the cell from entering the S phase unless all conditions for cell division are favourable [60]. The G_2/M checkpoint assesses chromosome replication completeness and checks that the replicated DNA is not damaged [60]. If the prerequisites are not met, the cell is paused to allow for completion of DNA duplication or DNA repairs [60]. Irreparable damage may prompt cells to self-destruct by means of programmed cell death, ensuring that DNA with compromised integrity is not carried over to daughter cells during mitosis [59-60]. The spindle assembly checkpoint ensures equal separation of chromosomes during each cell division by delaying the segregation of sister chromatids until there is proper chromosome alignment and stable kinetochore to microtubule attachment [61].

1.2.2 Cell death

Cell death is an inevitable part of the cellular lifecycle but should not be mistaken as a spontaneous consequence thereof. Cells which are redundant, potentially harmful or suffer from unrecoverable perturbations are led to their demise via activation of a signal transduction pathway linked to a specific cell death modality [62]. The Nomenclature Committee on Cell Death (NCDD) have defined a broad range of regulated cell death (RCD) subroutines based on molecular mechanisms [62]. Since RCD relies on the activation of specific signalling pathways it infers that pharmacologic or genetic modulation of these molecular mechanisms is possible [63-64].

1.2.2.1 Apoptosis

Apoptosis is a highly regulated form of programmed cell death (PCD), which culminates in cellular self-destruction. Morphologically, apoptosis manifests with macroscopic alterations including cell shrinkage, nuclear condensation and fragmentation, membrane blebbing and the formation of apoptotic bodies [62]. Apoptosis is a structured and orderly mechanism which is vital for homeostatic maintenance and pathological protection. Intrinsic and extrinsic apoptosis are two PCD subroutines distinguished by the initiation event involved and the signal transduction modules executing the cell death. Extrinsic apoptotic pathways are regulated via death receptor ligand binding and intrinsic apoptosis culminates in cell death via mitochondrial and endoplasmic reticulum regulated caspase activation.

Extrinsic apoptosis

Extrinsic apoptosis is a death receptor-mediated RCD subroutine which is initiated by extracellular microenvironment insults [62,65]. Receptors belong to the tumour necrosis factor gene super family and include CD95 (also called Fas, Apo1), tumour necrosis factor receptor-1 (TNFR-1, also known as p55, CD120a), Death receptor-3 (DR3, also called Apo3, TRAMP, LARD), Death receptor-4 and 5 (DR4, DR5, known as TRAIL-r1, TRAIL-r2) [62,65]. Death receptor ligation results in the activation death domains, tumour necrosis factor receptor type 1-associated DEATH domain (TRADD) and Fas associated death domain (FADD) located on the intracellular tail of the receptor [62,65]. FADD drives assembly of the death-inducing signalling complex (DISC) via death effector domain (DED)- dependent recruitment of procaspase 8, ultimately resulting in the multistep maturation of caspase 8 [62,65]. Activated caspase 8 is released from DISC and extrinsic apoptosis is driven by caspase 8-induced activation of effector caspases 3 and 7 (Figure 1.2) [62,65].

Intrinsic apoptosis

The intrinsic apoptosis pathway is initiated by intracellular or extracellular factors including endoplasmic reticulum stress, DNA damage, and reactive oxygen species (ROS) overload [62]. Intrinsic apoptosis is demarcated by irreversible mitochondrial outer membrane depolarization, committing the cell to death [62]. The B-cell lymphoma-2 (Bcl-2) protein family plays a central role in modulating mitochondrial membrane integrity via pro-apoptotic (Bax, Bak, Bok) and anti-apoptotic (Bcl-2, Bcl-w, Bcl-xL, Mcl-2 and Bcl-A1) family members [65]. Upon apoptotic stimuli Bax, Bak and Bok form homodimers in the outer cell membrane of the mitochondria, forming pores and resulting in mitochondrial membrane permeabilisation [65]. Mitochondrial outer membrane permeabilisation is opposed by the pro-survival family members (Bcl-2, Bcl-w, Bcl-xL, Mcl-1 and Bcl-A1) by preventing oligomerization and inhibiting the formation of pores [62,65]. A third class of Bcl-2 proteins, Bcl-2 homology (BH)3-only (BH-3 proteins), include Bad, Bid, Bik/NBK, Bmf, Hrk/DP5, Noxa, Bim and PUMA/BBC3 as members [65]. The BH-3 proteins indirectly promote apoptosis by inhibiting activity of the anti-apoptotic Bcl-2 proteins [65].

Mitochondrial outer membrane permeabilisation results in the release of apoptogenic molecules usually contained within the intermembrane space [65-66]. Cytochrome *c*, mitochondrial EndoG nuclease and apoptosis inducing factor (AIF) are but three of the pro-apoptotic factors released, resulting in downstream activation of execution caspases [65]. Upon release cytochrome *c* promotes the formation of an apoptosome by combining with apoptotic peptidase activating factor (Apaf-1) and procaspase 9 [65]. Addition of cytochrome *c* to the complex matures procaspase 9 to initiator capase 9, ultimately catalysing the activation of effector caspase 3 (Figure 1.2) [65].

Activation of pro-apoptotic Bak and Bax proteins have also been implicated in endoplasmic reticulum (ER) stress signalling [62]. Bak and Bax oligomers perforate ER membranes resulting in the cytosolic leak of Ca^{2+} ions [62,65]. Increased extra-ER Ca^{2+} concentrations have been implicated in the activation of cell death pathways. Calcineurin activation by Ca^{2+} leads to subsequent Bid (BH-3 protein) activation [65]. Furthermore, increased cytoplasmic Ca^{2+} upregulates DNA-damage-inducible transcript 3 (DDIT/CHOP) activity resulting in Bcl-2 inhibition, with pro-apoptotic consequences via mitochondrial pathways [65]. Calcium ion (Ca^{2+} activated M-Calpain triggers Caspase 4 activity leading to endoplasmic reticulum stress-induced apoptosis via Caspase 7 execution (Figure 1.2) [65].

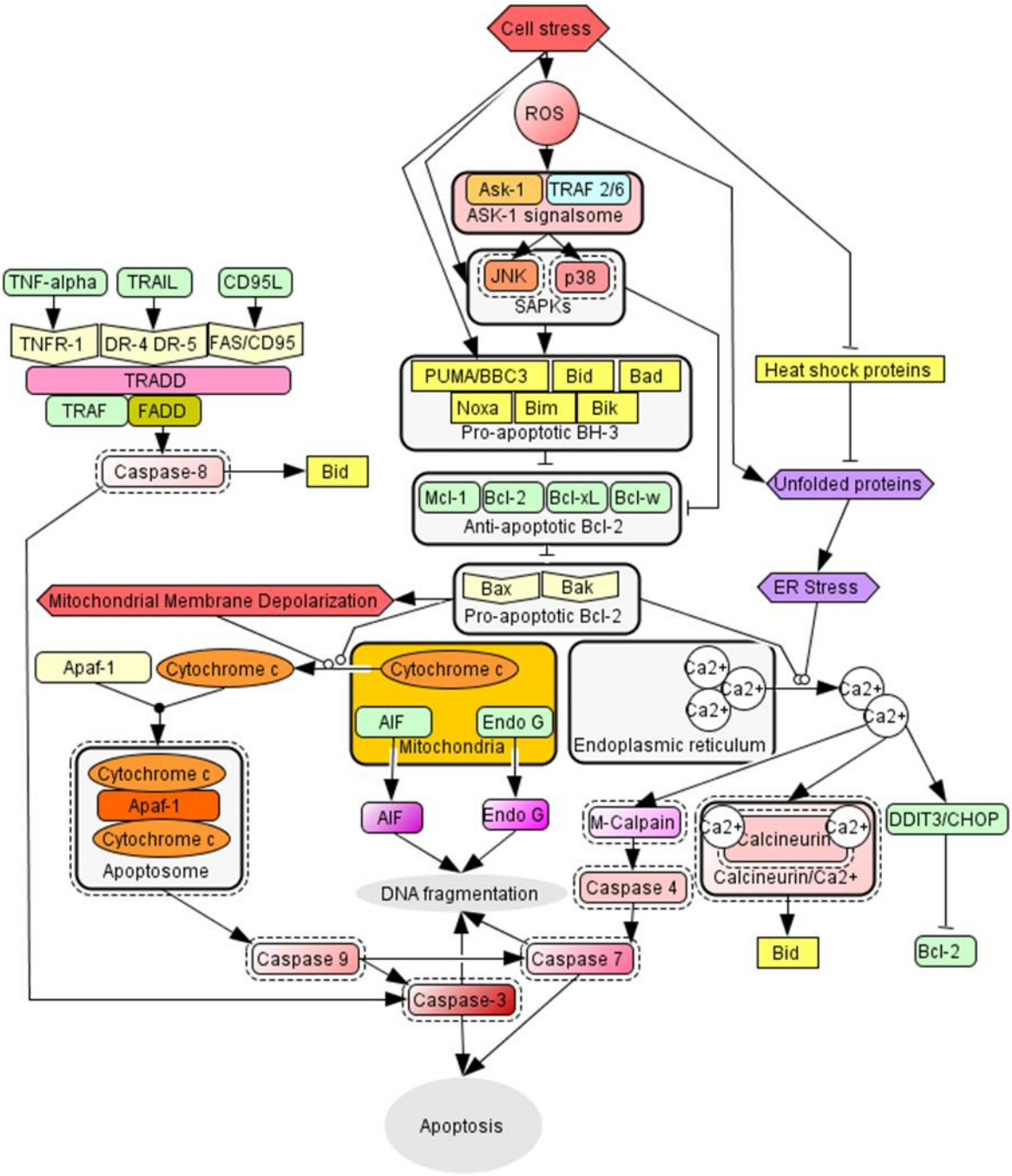

Figure 1.2: Cell stress-mediated signalling pathways culminating in activation of apoptosis via execution caspases. Extrinsic apoptosis is initiated via death receptor ligand binding, propagated by caspase 8 and precipitated by executioner caspase 3. Intrinsic apoptosis is propagated via mitochondrial and endoplasmic reticulum regulated pathways triggering caspase 3 and 7 activation [65].

1.2.2.2 Oxidative stress and cell death

Cellular perturbations caused by ROS overload lead to the programmed demise of the cell via mitochondrial and/or endoplasmic reticulum-regulated signalling modules as previously described. The stress-activated pathway is initiated by the oxidation of thioredoxin (Trx), allowing the binding of the apoptosis signal-regulating kinase 1-Trx (ASK1-Trx) complex to tumor necrosis factor receptor-associated factor 2 and 6 (TRAF2 and 6), thereby resulting in an activated ASK-1 signalsome [65]. The activated ASK-1 signalling complex initiates mitogen-activated protein kinase (MAPK) kinase pathways [65]. MAPK kinase 4 and 7 (MKK 4 and 7)-c-Jun-N-terminal kinase (JNK) and MAPK kinase 3 and 6 (MKK3 and 6)-p38 MAPK signalling cascades have been implicated as important role-players in redox signalling [65]. Downstream activation of stress-activated protein kinases (SAPKs) JNK and p38, induce the expression of pro-apoptotic genes *c-jun*, gene encoding for tumour suppressor protein 53 (*p53*), activating transcription factor 2 (ATF2) and transcription of BH-3 proteins, Bid and Bim (Figure 1.3); ultimately culminating in apoptotic cascade activation via mitochondrial and/or endoplasmic reticulum regulated pathways (Figure 1.2) [65]. Normally, JNK-related apoptotic signalling is inhibited by glutathione (GSH) and glutathione S-transferases (GST) [65]. However, increased pro-oxidant status and secondary glutathione disulfide (GSSG) formation leads to ROS-induced GSH inhibition and subsequent GST-JNK dissociation [65].

Of note, intracellular ROS and activation of JNK and p38 does not exclusively culminate in apoptosis induction since transient stimulation of the SAPKs are paradoxically associated with pro-survival signalling (Figure 1.3) [67]. Ultimately, cell fate is determined by the magnitude and duration of SAPK activation in response to the redox status perturbation [65,67]. Cancer cells commonly exhibit an increased pro-oxidant status, implying that they can be selectively targeted for ROS induced death by means of pharmacological intervention [68].

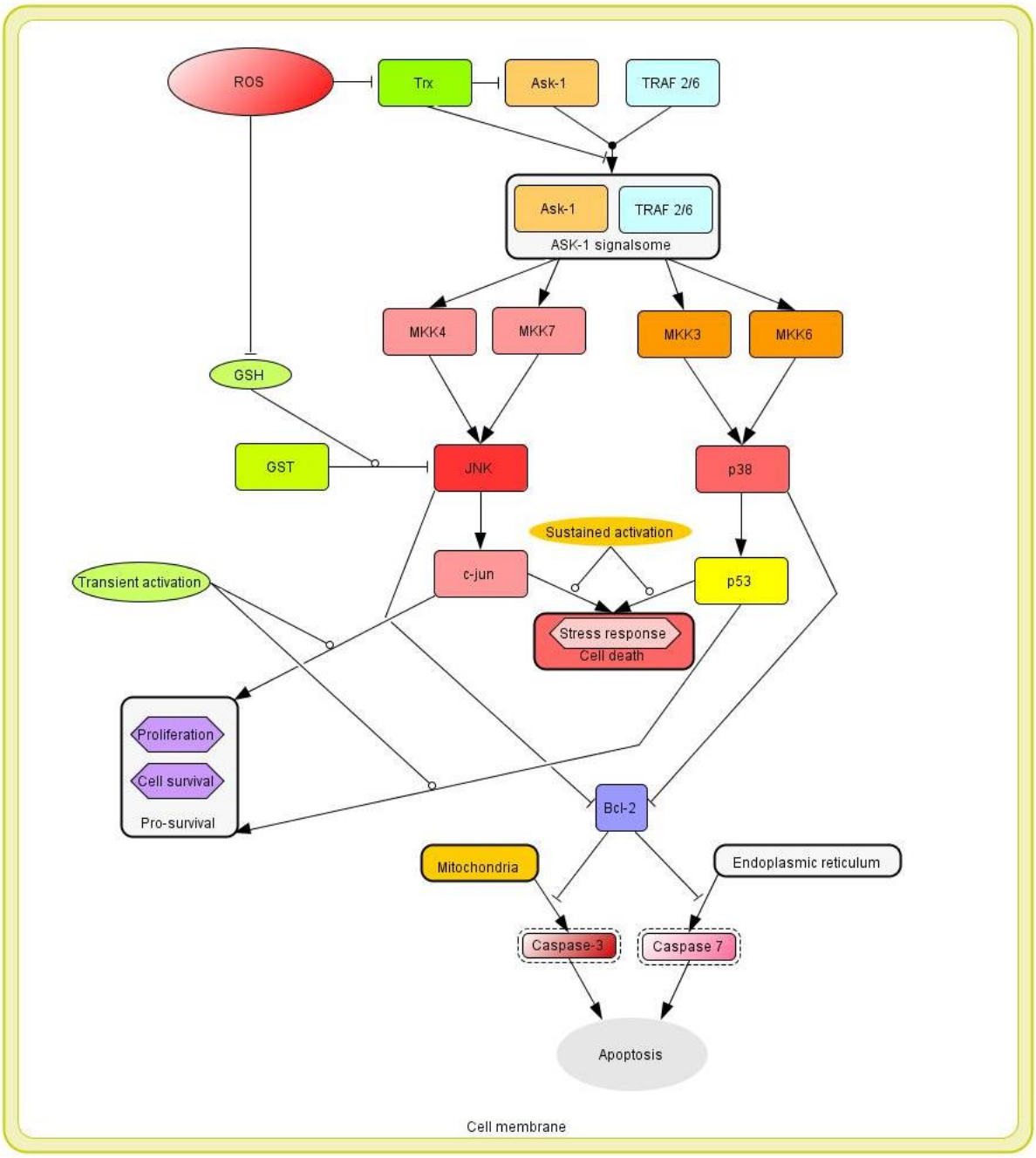

Figure 1.3: ROS signalling pathways. ROS results in activation of SAPKs implicated in both pro-apoptotic and pro-survival signalling. Cell fate is determined by the magnitude and duration of SAPK activation in response to the redox status perturbation [65]. Adapted with permission.

1.2.2.3 Other mechanisms of cell death

Autophagy

Autophagy refers to a RCD modality which involves the lysosomal degradation of cellular proteins and organelles [65]. The process of self-cannibalization plays a role in cytosolic component turnover, metabolic homeostasis, growth regulation and, in conditions of starvation, cell survival [65,69]. Upon initiation, a multi-step process leads to the formation of autophagic vacuoles which degrade cytosolic components by lysosomal hydrolases [65]. Products of the enzymatic degradation are recycled for cellular metabolism [65,69]. Late stage autophagy manifests with morphological alterations such as the presence of multiple, large autophagic vacuoli and mild pyknosis [65].

Mitotic catastrophe

Mitotic catastrophe is a mode of cell death which occurs due to mitotic failure coupled with defective G_2/M and spindle assembly checkpoints [70]. By default, these unfavourable intracellular events usually result in activation of apoptotic signalling pathways. However, cells capable of evading apoptotic death proceed through the cell cycle resulting in incomplete mitosis and consequent aneuploidization [70]. Mitotic catastrophe serves as the next line of defence in the control of aneuploid cells, thereby suppressing oncogenesis [70]. Mitotic death is a form of RCD which is driven by mitotic catastrophe, most often via intrinsic apoptosis [62].

Necrosis

Necrosis is an accidental cell death (ACD) modality. In striking contrast to PCD, ACD refers to the almost immediate and catastrophic demise of a cell as a direct result of the physical, chemical or mechanical insult they are exposed to [62]. Cell structures are severely degenerated, normal cell physiology collapses, cellular contents are leaked and inflammatory pathways are activated [71].

1.3 Cancer cell biology and hallmarks of cancer

Douglas Hanahan and Robert Weinberg have identified an underlying commonality in the complexity of cancer science [72-73]. Amidst the intricacy of the disease, they proposed a simplistic framework for understanding cancer cell biology based on ten features, or so called hallmarks, which are generic to most cancer cells [72-73]. In their initial review, Hanahan and Weinberg attempted to simplify the complex biology of cancer into six primary hallmarks: sustained proliferative signalling, insensitivity to growth suppressors, evading cell death, replicative immortality, sustained angiogenesis, and activation of invasion and metastasis (Figure 1.4) [73]. A decade later, they published an updated review adding two emerging hallmarks: altered bioenergetics and avoiding immune destruction, as well as two enabling characteristics: genome instability and mutation, and tumour-promoting inflammation (Figure 1.5) [72]. This enumeration of traits has been identified as the set of enabling and acquired biological capabilities which embody cancer cell physiology [72-73].

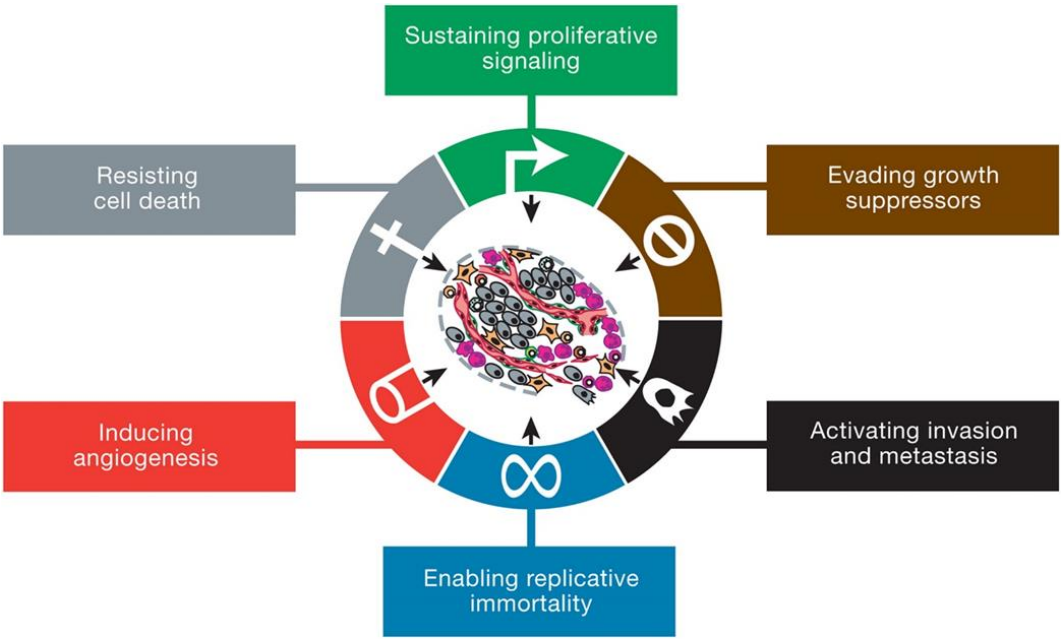

Figure 1.4: The Hallmarks of Cancer. Six acquired capabilities of cancer cells as described in Hanahan and Weinberg's initial review: the hallmarks of cancer [73].

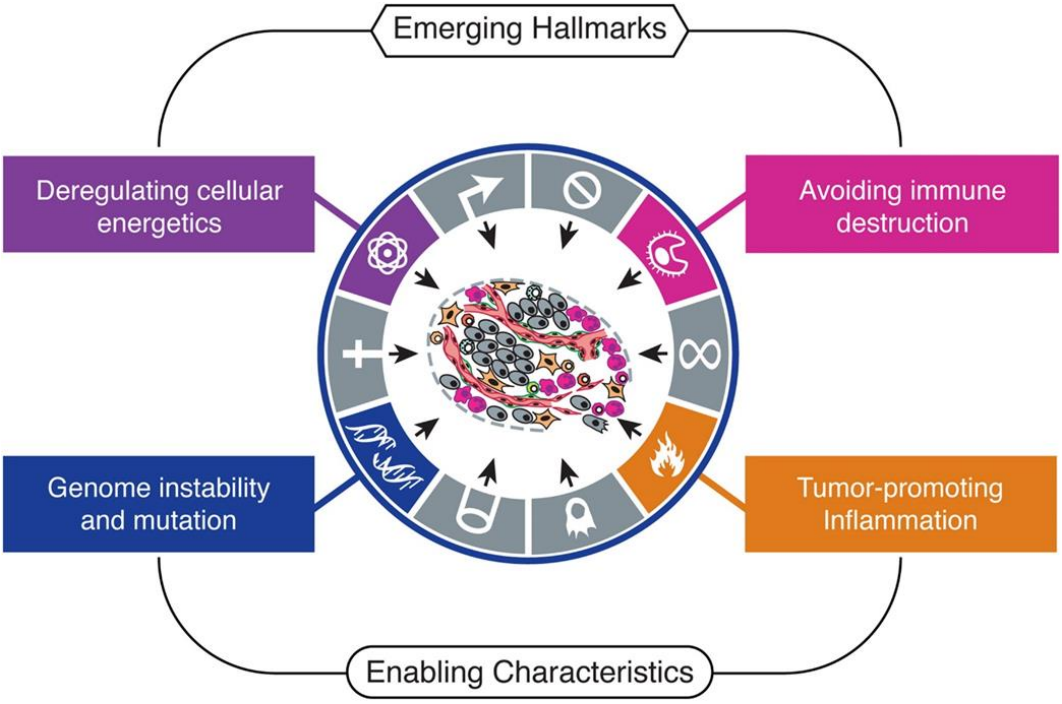

Figure 1.5: Emerging Hallmarks and Enabling Characteristics. Four additional cancer-specific traits as suggested in Hanahan and Weinberg's updating review [72].

The first few essential features are variations of the same theme, that is, cancer cell's independence from normal cellular controls. Since cancer is fundamentally a proliferative disease, the first and most obvious hallmark is the aberrant proliferation of cancer cells [73]. Normal cells are generally quiescent and cell division is only stimulated in response to mitogenic signals, whereas cancer cells display sustained proliferative signalling independent of normal growth commands [72-73]. The second distinguishing trait of tumour cells is their capacity to abrogate the multiple anti-growth signals which usually control normal cells in order to maintain tissue homeostasis [72-73]. The third hallmark is centred around the understanding that normal cells have adopted a strategy for programmed suicide so that if anomalous behaviour is apparent signals are evoked to induce cellular apoptosis [72-73]. Tumour cells, however, have acquired the capability to limit, if not eliminate, the propensity for cell suicide either through over expression of survival signals or increased expression of anti-apoptotic signals [72-73]. The fourth hallmark involves yet another checkpoint of continuous chronic proliferation which is the counting mechanism embedded in the telomeres of chromosomes [72-73]. These protective caps shorten with every cell division essentially regulating cellular mortality [72-73]. Cancer cells have the acquired ability to preserve telomere ends thereby gaining extensive replicative capacity and immortality [72-73].

The next two hallmarks go beyond the cancer cell to look at the tumour as an organ. Tumours, like normal organs, require vascularization and have consequently contrived mechanisms for sustained angiogenesis [72-73]. Tumours also display the capability to invade across tissue beds and migrate long distances (metastasis) [72-73]. Another common feature is the reprogramming of cellular energetics metabolism, which is necessary to support the rapid growth of cancer cells [72-73]. Successful cancer development also requires the ability to circumvent the challenges erected by the immune system by avoiding detection or limiting immunologic killing [72-73]. The final features, genomic instability and tumour-promoting inflammation, are considered enabling characteristics because they underpin and provoke many of the aforesaid hallmarks [72].

The discovery of cancer stem cells adds to the myriad of cancer complexities. The cancer stem cell model alleges that this subpopulation of cells which display perpetual self-renewal and multilineage differentiation play a pivotal role in tumorigenesis, chemotherapeutic resistance, recurrence and metastasis [74-76]. Although cancer stem cells and non-cancer stem cells are related by origin they exhibit consistently differential gene expression and molecular profiles and can be recognized by specific cell surface markers [77-78]. Intratumour dynamic equilibrium between these two subclones is regulated by stochastic transmutation of cancer cells into cancer stem cells, a process putatively mediated by the multifunctional cytokine interleukin-6 (IL-6) [78-80].

Inflammation drives the upregulation of IL-6 expression via activation of Nuclear factor kappa B (NF- κB), resulting in subsequent initiation of the janus activated kinase (JAK)/signal transducer and activator of transcription (STAT) pathway [78-79,81-82]. However, IL-6 reinforces NF- κB activation thereby generating a positive feedback loop between the tumour microenvironment and tumour cells [77,80-81]. Many conventional cancer therapeutics pronominally provoke inflammation, thereby inciting pro-inflammatory IL-6 signalling and subsequent expansion of the cancer stem cell population.

Furthermore, differentiated cancer cells cause the inducible transformation of cancer stem cells via IL-6 secretion through the JAK1/STAT3/Oct 4 signal transduction

pathway [79]. This proposes that a subpopulation of non-cancer stem cells are intrinsically converted to cancer stem cells through Oct-4 gene overexpression [79]. Oct-4 forms part of the POU (Pit-Oct-Unc) - domain transcription factor family which has been found to enhance cancer stem cell-like properties in various cancers [83].

1.4 Selectively targeting cancer-associated proteins

Targeted therapy forms the foundation of next generation anticancer drug design. This approach differs from conventional chemotherapeutics in several ways. Firstly, targeted therapies are deliberately designed to interfere with distinct molecular targets associated with the acquired capabilities of cancer, thereby significantly reducing nonspecific toxicity caused by empirical approaches [72,84]. Furthermore, most hallmark-targeting therapies are cytostatic agents which subvert tumour cell proliferation and progression, whereas standard chemotherapies are cytotoxic drugs inducing cell death [13,84]. The following section elaborates on some of the cancer-associated proteins involved in the targeted hallmarks.

1.4.1 Tubulin

Selective targeting of cancer cells during the cell division process is still considered a relevant and amenable chemotherapeutic strategy [85-86]. Mitosis marks the cell cycle phase during which chromosome separation and cell division takes place in order to produce genetically identical progeny [85]. It is considered the most vulnerable phase during cell cycle progression and therefore serves as a critical intervention point in aim of perturbed cancer cell proliferation and induced cell death [85,87]. Given the fundamental role of microtubules during mitosis it is no surprise that mitosis-selective anticancer strategies are centralized around disrupting normal microtubule dynamics [85,87-88]. The mechanism of action of antimitotic compounds involves interfering with microtubule dynamics resulting in cells blocked in metaphase followed by induction of apoptosis [89]. Microtubules consist of alpha and beta tubulin heterodimer subunits which assemble to form a linear protofilament structure [88]. Tubulin is therefore a suitable and strategic molecular target for anti-microtubular drugs. Microtubule-targeted agents are designed to suppress and/or disrupt microtubule function, thereby inducing mitotic arrest and eventually leading to cell death [86,88].

Three major classes of tubulin-binding agents have been identified a) colchicine analogues, b) vinca alkaloids, and c) taxanes [90]. These tubulin-targeted drugs are distinguished by their interaction with distinct binding sites in tubulin subunits [90]. Colchicine analogues competitively bind to the colchicine binding domain close to the alpha/beta interface on tubulin subunits [90]. These agents are largely based on phenstatin and combretastatin molecules [86]. Vinca alkaloids (vinblastine, vincristine, and vinorelbine) bind both at the end of the microtubule and along the length of the microtubule [88]. Vinca-related drugs are often used in combination with other chemotherapeutic agents in the treatment of breast cancer [85]. Both of these mitosis-targeted drug classes cause microtubule destabilization and inhibition of tubulin polymerization, resulting in catastrophe [86,88].

Taxanes such as paclitaxel, docetaxel, and nab-paclitaxel interact with hydrophobic binding pockets along the luminal side of beta tubulin subunits [88,90]. Binding of these agents cause microtubule stabilization and stimulates microtubule polymerization, resulting in metaphase block and cell death [85,88]. Although the taxane-related drug class has proven considerable anticancer therapeutic efficacy, there is evidence proposing evolved drug resistance linked to transformed beta tubulin subunits and/or mutated drug efflux transporters [85].

Besides the mainstay of tubulin-binding drugs mentioned, several other classes of drugs also target microtubule dynamics including: destabilizing agents such as halichondrins, and eribulin; and microtubule stabilizing epothilones such as ixabepilone [88]. Despite different mechanisms for microtubule disruption and different microtubule binding sites, all of the aforementioned drug classes are classified as antimitotic agents because of their ability to compromise mitotic activity in cells [88].

To date, several oestrogen analogues have also been identified to exhibit antimitotic activity [91-94]. Besides validated antiproliferative action the oestradiol derivatives also demonstrate antiangiogenic effects, culminating in multi-targeted anticancer activity [91-92]. One such compound is 2-methoxyestradiol (2ME2) [91]. This oestradiol analogue progressed to phase II of clinical trials for the treatment of various cancers, however the drug did not prove potent enough to induce the expected anticancer activity and

issues with toxicity and bioavailability stunted progression of the compound to further clinical testing stages [91-92]. Aryl O-sulfamate oestradiol antimitotics appear to have increased bioavailability and reduced toxicity whilst still eliciting dual anticancer activity against proliferation and angiogenesis [93-95].

1.4.2 Carbonic anhydrase II (CAII)

Carbonic anhydrase (CA) enzymes drive the reversible formation of bicarbonate from carbon dioxide and water [96]. This family of zinc-dependant enzymes has been implicated in the favourable alteration of the cellular microenvironment to support tumour growth, invasion and metastasis [96]. Given their role and over expression in human cancers, CAs have gained notable interest as potential therapeutic targets [96-97].

The CAII isoform is located in the cytosol of red blood cells and contains an active site which allows the reversible binding of many sulphonamide drugs [96]. The dual binding of steroid sulphatase (STS) targeted drugs to CAII has elucidated the possibility that the oncosuppressive success of these inhibitors could partly be attributed to properties related to CAII inhibition, such as improved bioavailability [96,98-99]. The discovery of CAII-binding sulfamate drugs has prompted further structure-based investigation and design of these dual inhibitors [100]. Evidence reveals that simultaneous inhibition of cytosolic CAII leads to stabilization and enhanced delivery of STS-targeted drugs [100-101].

1.4.3 Carbonic anhydrase IX (CAIX)

Carbonic anhydrase IX (CAIX) was the first CA isozyme to be prominently linked to cancer and was initially described as a tumour antigen [102]. This tumour-associated enzyme is only expressed in a few normal tissues but exhibits ectopic hyperexpression in several cancers [102]. Transcriptional activation and differential overexpression is directed by the hypoxia-inducible factor (HIF-1) which is associated with hypoxic tumour conditions [102]. Increased hypoxia also results in excessive lactic acid production via high glycolysis rates necessitated for energy generation via anaerobic respiration [102-103]. Therefore, the characteristic acidification of the tumour environment is attributed to bioenergetic alterations as well as CAIX-induced carbonic acid build up

(Figure 1.6) [102]. Acidotic conditions favour tumour cell growth, survival, metastasis and invasion [102-103]. Considering the obvious role of CAIX in the facilitation of tumorigenesis it is considered an attractive target for anticancer drugs [102]. To date, sulfamate and coumarin-based small molecules as well as CAIX-specific monoclonal antibodies have proven therapeutic efficacy as potential anticancer agents, with some reaching clinical trials [104].

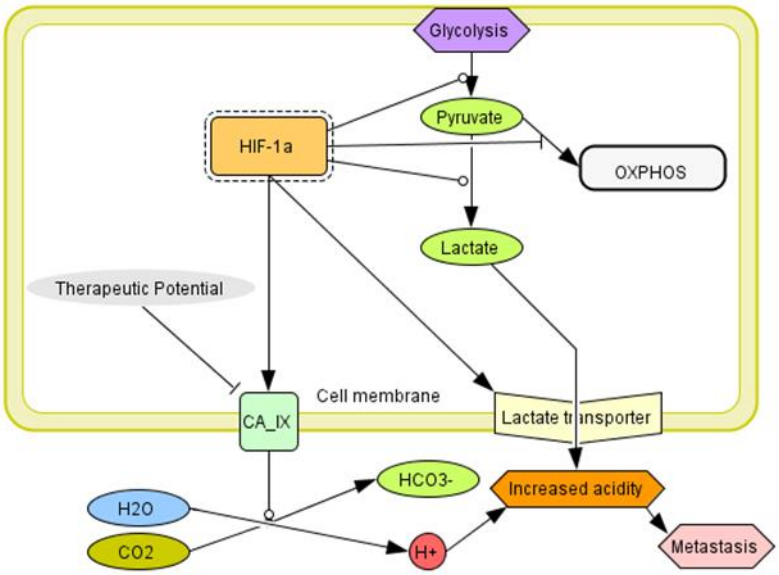

Figure 1.6: Acidification of the tumour environment via bioenergetic alterations and CAIX-induced carbonic acid build up. Therapeutic targeting of CAIX could reduce acidosis and thereby abrogate tumorigenic progression favoured by acidotic conditions [65].

1.4.4 Steroid sulphatase (STS)

Steroid sulphatases are involved in several physiological processes, however, their pivotal role in regulating oestrogen and dehydroepiandrosterone (DHEA) synthesis in endocrine-dependent cancer has been of specific interest [105]. In breast cancer, STS activity exceeds that of aromatase activity and upregulated STS mRNA expression is associated with a poor prognosis [106]. Identification of the active pharmacophore for the inhibition of STS (i.e. a sulphamate ester group linked to an aryl ring) has led to development of several potent STS-targeted agents offering promising therapeutic potential for the treatment of hormone-dependent breast cancer [106-108].

1.4.5 Bromodomain proteins

Advances in genomic research has revealed that the molecular aetiology of complex diseases does not merely rely on genetic make-up, but instead also depends on epigenetic processes that modulate genomic DNA transcription [109]. This implies that although genetic predispositions cannot be altered, epigenetics provides the opportunity to modify and reset genotype to phenotype translation [109]. Histone post-translational modifications is one of the epigenetic processes that plays a critical role in regulation beyond the DNA genome [109]. Chromosomal DNA is packaged in the nucleus as tightly coiled chromatin. Chromatin comprises of repeated histone-containing subunits called nucleosomes [110]. A nucleosome complex consists of DNA wrapped around a discrete protein octamer composed of H2A, H2B, H3, and H4 dimers [110]. Post-translational modification of histone tails through methylation, phosphorylation or acetylation creates a complex histone code which is recognized and deciphered by epigenetic reader domains [109].

The bromodomain and extra terminal (BET) family of bromodomain (BRD) proteins, which include BRD2, BRD3 and BRD4, are involved in the regulation of transcription [111]. Bromodomain-containing proteins are chromatin reader proteins that recognize and bind to acetylated lysine residues on histones, subsequently attracting transcription factors and rendering the acetylated site transcriptionally active [109,112]. Besides their role in transcriptional initiation and elongation, BRD proteins are also key regulators of cell cycle progression [111]. Bromodomains (BRDs) have been linked to various diseases and disease processes, among which include cancer, inflammation, viral replication, obesity, HIV/AIDS, neurological disorders and type 2 diabetes mellitus [109,112-114]. The cancer-promoting properties of BRD proteins include the activation of anti-apoptotic and growth-promoting pathways as well as driving mechanisms involved in metastasis and invasion [109,111-112,115].

Early reports showed that dysregulation of BRD4-associated promote cancer metastatic potential in breast cancer [116]. During mitosis BRD4 remains bound to M/G_1 growth-associated genes (e.g. JunB and *c-myc*) causing the prompt transcription of these genes in daughter cells [117-118]. Inhibiting this process with BRD4 inhibitors causes the suppression of key G_1 and growth-associated genes which in turn leads to

a G_1 cell cycle arrest and apoptosis in various cell types, including TNBC cells [117,119]. Selective inhibition of BRD4 is thus an attractive target against breast cancer in general as well as TNBC specifically.

Bromodomain proteins BRD2 and BRD3 are also attractive targets for breast cancer. Recent gene set enrichment analysis from public datasets implicates upregulation of BRD2 with detrimental outcome in HER2 positive tumors with BRD2 and 4 upregulated in basal-like breast cancers [120]. The mRNA levels of BRD3 is elevated in invasive lobular carcinoma of the breast and inhibition of this protein may provide therapeutic benefits for this subset of breast cancer [121]. The BRD3 protein plays a central role in estrogen-responsive gene expression in MCF-7 cells [122].

Given their unequivocal role in tumorigeneses, BRD proteins are considered amenable chemotherapeutic targets and have prompted pharmaceutical interest in the development of molecular compounds which abrogate these epigenetic regulator proteins. BRD inhibitors act by displacing the BET bromodomain proteins from chromatin by competitively binding to the acetyl-lysine recognition pocket [123-124]. To date, studies on BRD inhibiting compounds such as JQ1, I-BET151 and I-BET762 have demonstrated the ability of these agents to induce apoptosis, reduce proliferation and/or cause cancer cell differentiation in several cancers [124-131].

It is apparent from the pre-clinical data that targeted inhibition of BET bromodomain proteins is an attractive method to target various cancers including TNBC. However, a recent clinical trial of BET bromodomain protein inhibitors against TNBC was stopped due to lack of efficacy (https://clinicaltrials.gov/ct2/show/NCT02259114). Also, several side effects of BRD inhibitors have been observed in clinical trials including severe fatigue, thrombocytopenia, gastrointestinal bleeding, nausea, hyperglycemia etc. [132]. Nevertheless, the results from several clinical trials against various malignancies are eagerly awaited and various combinatorial therapeutic studies with BRD inhibitors show promise in preclinical studies. BRD4 inhibitors show synergistic activity with various classes of compounds including rapamycin [133] and CDK inhibitors [134] against osteosarcoma, ibrutinib against lymphoma [135], panobinostat against neuroblastoma cells [136], phosphoinositide-3-kinase inhibitors against haematological malignancies [137]. Our laboratory identified the glycolytic inhibitor, 3-

bromopyruvate, as a compound that acts synergistically with the BRD4 inhibitor Bzt-W41 (ITH-47) against U937 acute myeloid leukemia cells [138].

The pre-clinical data, current ongoing clinical trials and combination studies on BRD inhibitors fortifies the rationale behind the design and development of improved novel BRD inhibitors alone or in combination in search of antineoplastic agents with clinically translatable efficacy.

1.4.6 Sirtuins

The sirtuin family consists of 7 members (SIRT1-7) and these proteins are nicotinamide adenine dinucleotide $(NAD)^+$-dependent enzymes that modify proteins via deacetylation of lysine, ADP-ribosylation and deacylation [139]. Sirtuins play important roles in regulating metabolism, proliferation, gene expression, cell survival and apoptosis, genome integrity as well as cellular stress mechanisms [140]. Of the sirtuin family, sirtuin 1 (SIRT1) and sirtuin 2 (SIRT2) are of particular interest for their putative roles in conferring cancer cell abilities such as survival, proliferation, angiogenesis and drug resistance [139-141]. SIRT1 expression is amplified in several cancers and is associated with tumour initiation and development, whereas tumours overexpressing SIRT2 display chemotherapeutic immunity [142].

Interestingly SIRT1 can act as both a tumour promoter and a tumour suppressor in breast cancer and this appears to be dependent on the breast cancer subtype [143]. For example, reduced expression of SIRT1 in luminal A cancer is predictive of lymph node metastasis, suggesting that SIRT1 act as a tumour suppressor in this breast cancer subtype [144]. In contrast, elevated expression of SIRT1 in TNBC is associated with increased tumour invasion and lymph node metastases [145-146]. SIRT1 can act as a tumour promoter via several mechanisms including promoting tumour invasion and metastasis by modulating epithelial-mesenchymal transition (EMT) process [146] and p53 inactivation through deacetylation of p53 [141].

One of the cancer-related hallmarks is the acquired ability of tumour cells to evade apoptosis. Normal cells have surveillance systems which monitor intracellular operations and genomic integrity. Upon signalling from stress and abnormality sensors

the surveillance proteins, as part of regulatory circuits, govern decisions regarding the fate of the damaged cell [73]. Most notable of the supervisory proteins is the p53 tumour suppressor protein [73]. The p53 protein polices DNA damage and chromosomal abnormalities and, depending on the degree of impairment, forces cells into either senescence or apoptosis [147]. If the damage is reparable cell-cycle progression is suppressed allowing for genetic rectification and normalization, implicating p53 as a canonical regulator of cell proliferation [72-73]. Alternatively, if substantial DNA damage is detected p53 functions as a proapoptotic regulator triggering programmed cell suicide in aim of conserving genomic stability [72-73]. The apoptotic defence mechanism entails sequential upregulation of Bax, mitochondrial cytochrome *c* and ultimately a collection of intrinsic effector caspases resulting in cell death [73,148]. The evolution of cancer cells has harboured several strategies to limit or circumvent the propensity for cell suicide [72-73]. The most preeminent of these being the ability to mollify p53 functionality, thereby eliminating the key regulator from the apoptosis-inducing circuitry and deeming the entire network redundant [72-73]. Inactivation of the p53 tumour suppressor protein is seen in more than half of cancer cases, underpinning this as a central hallmark-conferring strategy [149]. SIRT1 deacetylates p53 at its C-terminal Lys382 residue, alleviating its transactivation activity and thereby inhibiting its tumour suppressor functions [141].

Sirtuin 2 (SIRT2), similar to SIRT1, can act as a tumour promoter and a tumour suppressor. SIRT2 can act as a tumour suppressor by suppressing peroxiredoxin-1 (Prdx-1) expression resulting in breast cancer cells becoming more sensitive to reactive oxygen species (ROS) damage [150]. However, prolonged activation of SIRT2 can cause oxidative damage and genome instability and this turn promote cancer progression and changing SIRT2 into a tumour promoter. SIRT2 can also act as a tumour promoter by promoting invasion in basal-like, including TNBC, breast cancer patients [151]. Several studies show that inhibition of SIRT2 is able to induce cell death via stabilization of p53. In HeLa cells it was shown that SIRT2 down-regulation induces p53 accumulation by decreasing p300 in a p38 activation-dependent manner [152]. Dual inhibition of SIRT1 and 2 results in stabilization of p53 followed by cell death induction [141]. The last study showed that both SIRT1 and 2 inhibition is needed for this effect on the MCF-7 cells [141].

In conclusion, selective dual inhibition of SIRT1 and SIRT2 provides a strategy to reactivate p53 activity in breast cancers where SIRT1 and 2 act as a tumour promoter and inhibitor of p53 activity.

1.4.7 JAK 1/2

One of the challenges in the development of breast cancer treatments is the existence of cancer stem cell subpopulations. These subsets of cancer cells are characterized by their distinct capacity for self-renewal, multilineage differentiation potential, and high level of chemotherapeutic resistance [74,153]. Stem cell-like abilities such as these are postulated to not only drive oncogenesis and cause disease recurrence but are also implicated in breast metastasis [74,112]. The latter is of particular clinical relevance given the poor prognosis of metastatic breast cancers.

As previously mentioned, the dynamic equilibrium between cancer stem cells and non-cancer stem cells is largely mediated by IL-6 secretion via several signalling pathways activated through intrinsic and/or extrinsic factors. Multiple conventional chemotherapeutic modalities have been implicated in the inducible formation of cancer stem cells, thereby conferring chemoresistance and provoking tumour re-emergence. Putative evidence of cancer stem cell subpopulation expansion implicates widely used platinum-based cancer drugs cisplatin [154] and carboplatin [155], as well as other recognized anticancer agents such as trastuzumab [80] and paclitaxel [156] as extrinsic mediators. Furthermore, it has been found that cancer stem cell side-populations of some cancers are resistant to radiotherapy [157-158]. The principle mechanisms that govern both chemoresistance and radioresistance involve inflammatory signalling [159].

Besides therapy-induced inflammation, clonal evolution of stem cells is also provoked by tumour-associated inflammatory signalling [159]. This implicates the involvement of intrinsic cytokine pathways in protumourigenic processes such as malignant conversion, survival and metastasis [159]. Collectively, the resounding deduction is that several types of inflammation directly impact and regulate various stages of tumorigenesis, thus highlighting its multifaceted role in cancer pathology.

Although contentious, the stem cell hypothesis highlights critical conceptual implications which need to be considered in the quest for developing a curative breast cancer treatment. This posits the necessity for novel strategies to selectively target the mechanisms which drive inflammatory responses in order to increase therapeutic sensitivity and reduce recurrence. Elucidation of the complex transduction pathways involved in inflammation has revealed decisive molecular role-players. In breast cancer models IL-6 signalling and activation of JAK1/STAT [79] and JAK2/STAT [78] pathways are robustly implicated in the clonal evolution of stem cells and concomitant tumorigenic behaviour. Thereby, in aim of preventing cancer stem cell expansion and chemotherapeutic immunity in breast cancer it is prudent to block IL-6/JAK/STAT signalling. Given their involvement, JAK1 and JAK2 kinases have been identified as rational molecular drug targets in breast cancer.

1.5 Test compounds for selective targeting of cancer proteins

1.5.1 STX1972: polypharmacological compound

Polypharmacology aims at identifying more effective drugs that are able to target multiple pathways. STX1972 is a polypharmacological compound which targets tubulin, STS and cancer-associated CAIX and CAII activity. This multi-targeted anticancer compound is a C-17-substituted estratriene-3-O-sulfamate derivative (Figure 1.7) and was developed by Professor Barry V. L. Potter *et al.* (Oxford University, UK) [95]. The chemical structure has been refined through a series of modifications based on structure-activity relationship (SAR) studies of its predecessor analogues. The estratriene backbone is functionally decorated with an H-bond receptor at the C-17 substituent for optimal antiproliferative activity and microtubule disruption [95]. The sulfamate group permits irreversible inhibition of STS and also allows for reversible interaction with CAII, which is associated with improved bioavailability (85, 86). SAR studies on oestradiol analogues from the same class have delivered promising results [95,160] and have proven notable advancement in efficacy and uptake since the first generation compounds [161]. ESE-15-ol exhibits dual antimitotic and cancer-associated CAIX activity (131) and STX140 has shown dual antimitotic and STS inhibitory effects (132). STX1972 has shown *in vivo* antiangiogenic activity and antimitotic effects in breast cancer cells, regardless of

hormone receptor status, at nanomolar concentrations - making this the most potent antimitotic compound to date [95]. Evidence suggests that the therapeutic potential of STX1972, and similar members from the next generation sulfamate series, could supersede those already in preclinical development [95].

Simultaneous polypharmacological inhibition of tubulin, STS, CAII and CAIX by STX1972 proposes to interfere with the tumorigenic ability to resist death, evade growth suppressors, sustain proliferative signalling, induce angiogenesis and activate invasion and metastasis. Thereby targeting five of the ten cancer hallmarks defined by Hanahan and Weinberg [72].

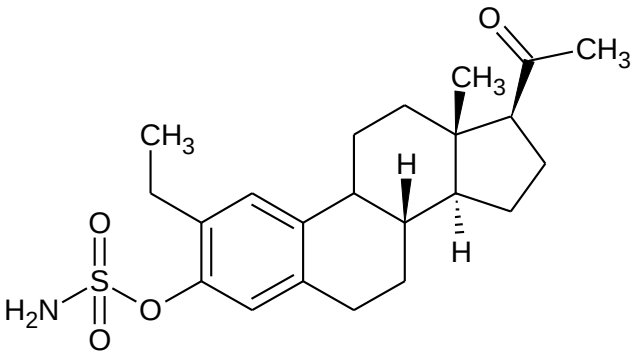

Figure 1.7: The chemical structure of STX1972.Structure was generated using ACD/ ChemSketch (Freeware) version: 12.01.

1.5.2 Bzt-W41, Bzt-W49 and Bzt-W52: Bromodomain inhibitors

The BRD inhibitors, Bzt-W41, Bzt-W49 and Bzt-W52, incorporated in this study are novel benzotriazepine analogues (Figure 1.8). *In silico* design of the compounds was done by Dr André Stander (University of Pretoria) and compound synthesis was done by WuXi AppTec (Pty) Ltd (Hong Kong). The benzotriazepine analogs were designed to avoid the need for a stereo selective synthesis route or separation of enantiomers of the 7-membered ring found in other benzodiazepine inhibitors of BRD4 [162-163]. Bzt-W41 is 2.28 times more selective at inhibiting BRD4 (IC_{50} = 0.49 µM) compared to BRD2 (IC_{50} = 1.12 µM) [138], Bzt-W49 is 10.42 times more selective at inhibiting BRD4 (IC_{50} = 1.27 µM) compared to BRD2 (IC_{50} = 13.23 µM) and Bzt-W52 is 3.43 times more selective at inhibiting BRD4 (IC_{50} = 5.67 µM) compared to BRD2 (IC_{50} = 19.47 µM) [164].

Selectivity towards BRD4 for this study was considered an important factor due to the fact that evidence alludes to the explicit involvement of BRD4 in several types of cancers, including breast cancer [163,165]. BRD4 forms part of the BET family of bromodomains and drives tumorigenesis by initiating anti-apoptotic and pro-growth pathways, and promoting metastatic and invasive behaviour [109,112]. BRD4 shows strong interactions with acetylated peptides derived from the histone 4 N-terminal tail [166], suggesting that BRD4 is an important mediator for reading Hbo1 mediated histone H4 acetylation. BRD4 amplification in breast carcinomas triggers the aberrant transcription of proto-oncogene *c-myc*, propagating the subsequent overexpression of oncoprotein c-MYC, which is implicated in over 40% of breast cancers and is associated with poor prognosis [163,167-169]. Recent studies have demonstrated that inhibitors of BRD4 have therapeutic potential for the treatment of various cancers [115,163,170].

Oestrogen is known to induce the expression of c-myc in hormone sensitive breast cancer cells [171]. This suggests that BRD4 inhibitors may have synergistic potential with STS inhibitors such as Irosustat. BRD4 inhibitors also shows synergistic activity with various other classes of compounds including rapamycin [133] and CDK inhibitors [134] against osteosarcoma, ibrutinib against lymphoma [135], panobinostat against neuroblastoma cells [136] and phosphoinositide-3-kinase (PI3K) inhibitors against haematological malignancies [137]. BRD4 also appears to play a crucial role in the completion of mitosis [117,172-175] and interestingly plays an important role the cellular response to mitotic stress that is induced by antimitotic compounds [176]. Therefore, combining antimitotic compounds with and BRD4-selective inhibitors may yield a synergistic combination by killing cells that escape antimitotic-induced cell death during mitosis. Furthermore, research from our laboratory demonstrated that Bzt-W41 (ITH-47) acts synergistically with the glycolytic inhibitor, 3-bromopyruvate, on U937 acute myeloid leukemia cells [138].

In conclusion, successful inhibition of BRD4 by Bzt-W41, Bzt-W49 and Bzt-W52 proposes to debilitate cancer cells' acquired ability to sustain proliferative signalling and evade growth suppressors and these compounds show promise to act synergistically with compounds with different mechanisms of action.

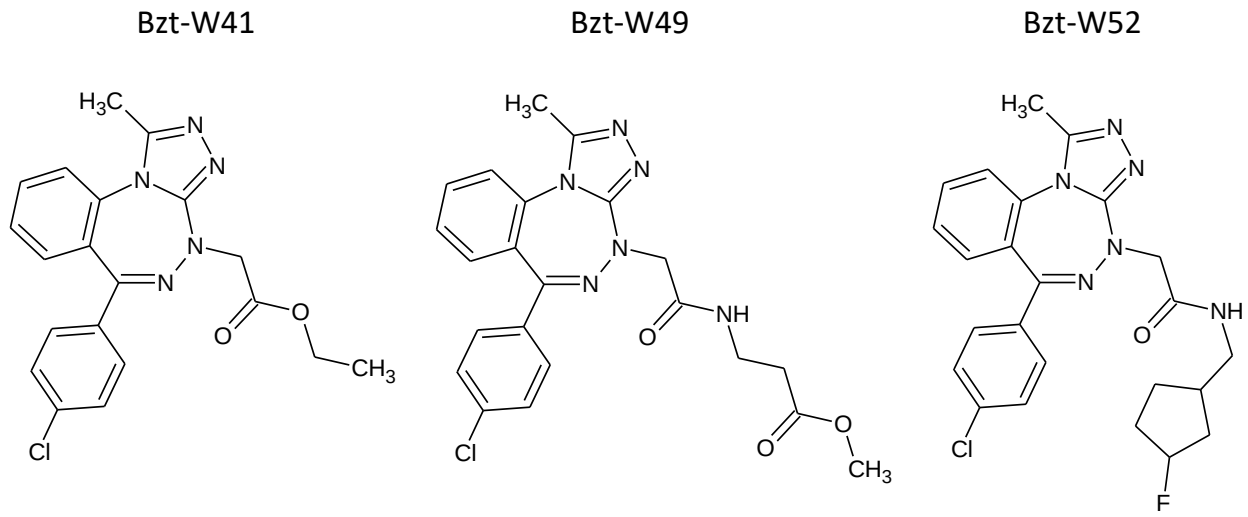

Figure 1.8: Chemical structures of Bzt-W41, Bzt-W49 and Bzt-W52. Structure was generated using ACD/ChemSketch (Freeware) version: 12.01.

Emerging evidence alludes to the explicit involvement of BRD4 in several types of cancer, including breast cancer [163,165]. BRD4 forms part of the BET (bromodomain and extra-terminal domain) family of bromodomains and drives tumorigenesis by initiating anti-apoptotic and pro-growth pathways, and promoting metastatic and invasive behaviour [109,112]. BRD4 shows strong interactions with acetylated peptides derived from the histone 4 N-terminal tail [166], suggesting that BRD4 is an important mediator for reading Hbo1 mediated histone H4 acetylation. BRD4 amplification in breast carcinomas triggers the aberrant transcription of proto-oncogene *c-myc*, propagating the subsequent overexpression of oncoprotein c-MYC, which is implicated in over 40% of breast cancers and is associated with poor prognosis [163,167-169]. Recent studies have demonstrated that inhibitors of BRD4 have therapeutic potential for the treatment of various cancers [115,163,170].

Oestrogen is known to induce the expression of c-myc in hormone sensitive breast cancer cells [171]. This suggests that BRD4 inhibitors may have synergistic potential with STS inhibitors such as Irosustat. BRD4 inhibitors also shows synergistic activity with various other classes of compounds including rapamycin [133] and CDK inhibitors [134] against osteosarcoma, ibrutinib against lymphoma [135], panobinostat against neuroblastoma cells [136] and phosphoinositide-3-kinase (PI3K) inhibitors against haematological malignancies [137]. BRD4 also appears to play a crucial role in the

completion of mitosis [117,172-175] and interestingly plays an important role the cellular response to mitotic stress that is induced by antimitotic compounds [176].

Successful inhibition of BRD4 by Bzt-W41, Bzt-W49 and Bzt-W52 proposes to debilitate cancer cells' acquired ability to sustain proliferative signalling and evade growth suppressors.

1.5.3 W137: Sirtuin inhibitor

The novel sirtuin analogue, compound W137, was designed *in silico* by Dr André Stander (University of Pretoria) and synthesized by WuXi AppTec (Pty) Ltd (Hong Kong). The chemical compound structure (Figure 1.9A) was functionally designed to target and inhibit both SIRT1 and 2, with the intention of inducing p53 acetylation and sensitizing tumour cells to programmed cell suicide. Compound W137 is based on the work by Disch *et al.* (2013) that synthesized potent pan SIRT1, 2 and 3 inhibitors with thieno carboximide moieties [177]. Disch *et al.* (2013) showed that selectivity towards SIRT1 and SIRT2 could be achieved by changing the Y atom to a carbon and the Z atom to a nitrogen [177]. Furthermore, optimal potency was achieved with a nitrogen at position 6 [177]. The compound was synthesized by Wuxi APPtec (>95% purity). The IC_{50} concentrations for W137 against SIRT1, SIRT2 and SIRT3 was determined to be 14.8 µM and 14.6 µM and >100 µM respectively [178]. W137 is >6x more selective against SIRT1 and SIRT2 activity compared to SIRT3. W137 is able to induce an increase in expression of K382 acetylated p53 protein when the SH-SY5Y neuroblastoma cell line was exposed to 25 µM of W137 [178]. The study by Otto *et al*. (2018) showed that W137 inhibited cell proliferation in both the U937 and SH-SY5Y cell lines in a dose-dependent manner through the inhibition of cell growth and the induction of cell death *in vitro* [178]. ROS levels were unaltered or reduced by W137 and *p53* and *C-MYC* gene expression was down-regulated by W137 in SH-SY5Y neuroblastoma and acute myeloid leukemia U937 cell lines. In the present study compound W137 was chosen as a SIRT1 and 2 inhibitor to annul cancer cells' capability to evade cell death and restore genomic stability in breast cancer cells.

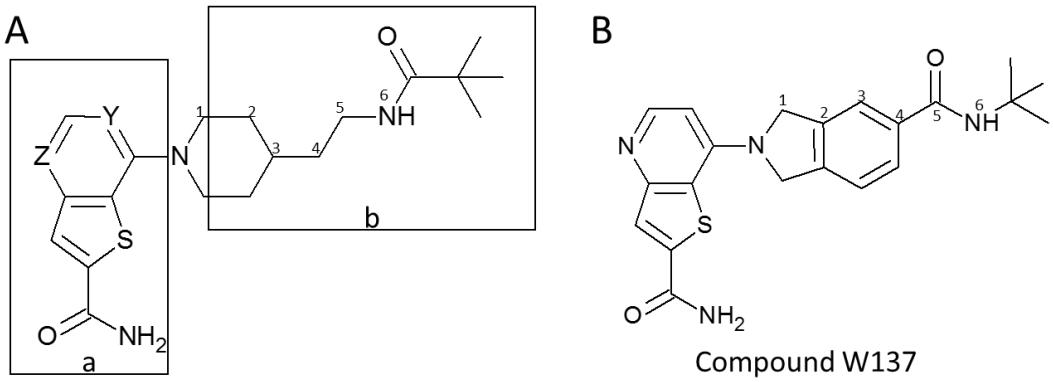

Figure 1.9: Structures of ligand 1NR from the 4jt8 protein structure from www.rcsb.org (A) and compound W137 (B). 1NR is a potent thieno carboximide pan SIRT 1, 2 and 3 inhibitor discovered by Disch *et al.* (2013) [177] . Figure is from the MSc of M Otto (2018) [178].

1.5.4 Ruxolitinib: JAK1/2 inhibitor

Ruxolitinib (Figure 1.10) is a US Food and Drug Administration approved drug for the treatment of myelofibrosis [179]. The drug has proven potent and selective dual inhibition of JAK1 and 2 [180]. Putatively, inhibition of JAK 1 and 2 cancer-associated proteins would cripple two of the hallmarks characteristically associated with cancer development and progression, namely: avoiding immune destruction, and tumour-promoting inflammation. Inclusion of this compound serves as part of a modified chemotherapeutic strategy in aim of complete cancer eradication through the inhibition of cancer stem cell conversion through reduced IL-6 expression.

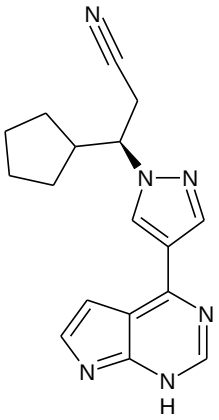

Figure 1.10: Chemical structure of Ruxolitinib. Structure was generated using ACD/ChemSketch (Freeware) version: 12.01.

The proposed multi-drug targeting of Hanahan and Weinberg's hallmarks of cancer [72] by each of the test compounds included in the study is presented in Figure 1.11.

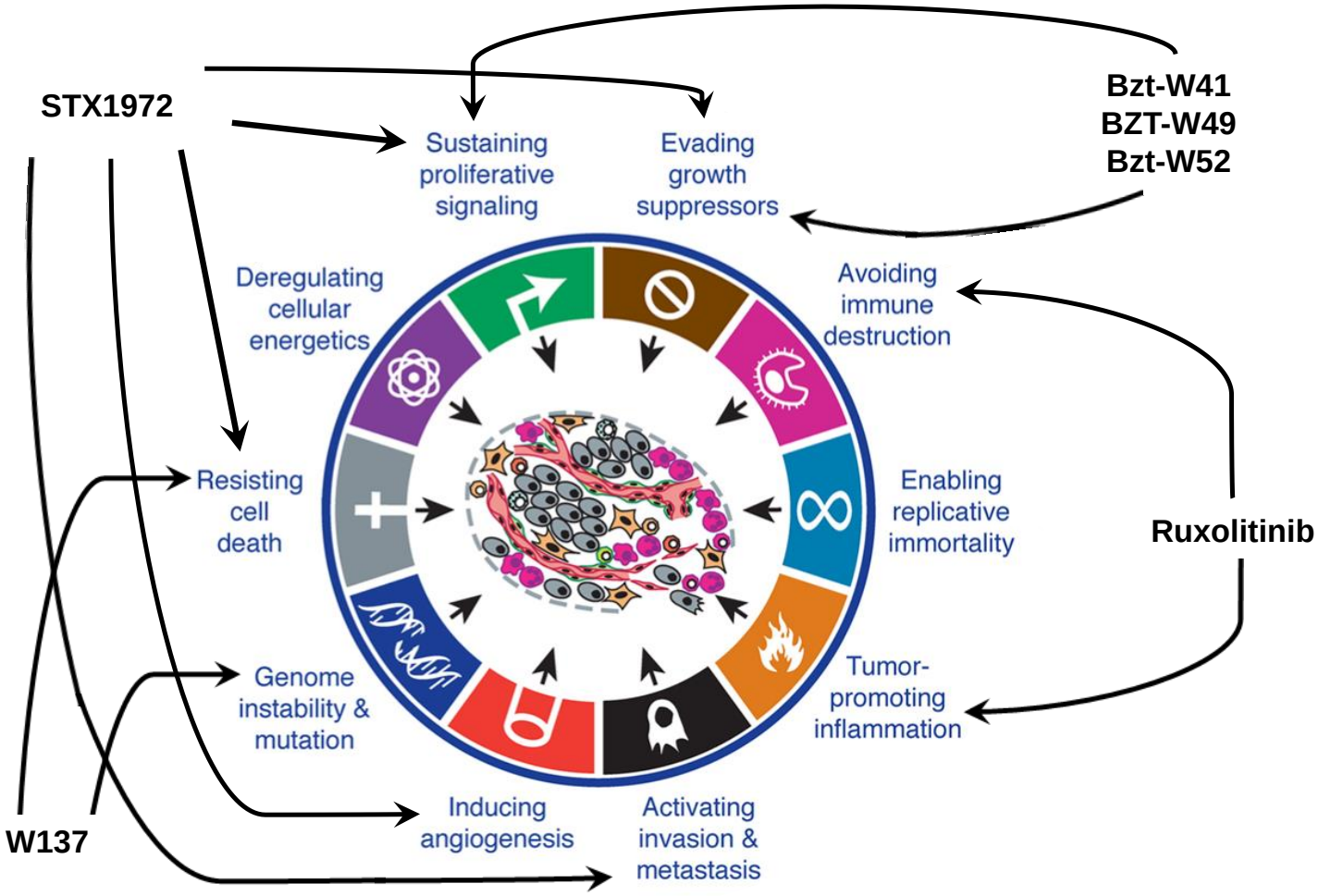

Figure 1.11: Proposed multi-drug targeting of Hanahan and Weinberg's hallmarks of cancer[72] (Adapted with permission). Six anticancer compounds from four distinct groups targeting various cancer-associated hallmarks. Four of the six compounds (W137, Bzt-W41, Bzt-W49 and Bzt-W52) are unique *in silico* designed molecules which have not been reported on before.

1.6 Combination therapy

The sobering reality of the 'magic bullet' approach is that it has not proven to be the miracle cure one would've hoped for. Tumours are mutable and adaptable and constantly devise mechanisms to circumvent the selective therapy being applied. Thus, just as the developmental barriers instigated the progression of the initial hallmarks, so again therapy is just another barrier that tumours manage to find a way around. The high degree of clonal and genetic heterogeneity of cancers, complex and multiple signalling pathways for survival, and the presence of chemoresistant cancer subpopulations strengthens resistance to single-targeted therapies [181]. Consequently, most clinical responses have been transitory and/or recurrent [72].

The hypothesis is that if one were to target several hallmarks concurrently, thereby presenting a multitude of barriers, tumours would not be able to decipher a means to bypass all of them simultaneously and therefore could be impaired in terms of the ability to progress. Combination therapy is a widely used therapeutic option for the treatment of cancer in order to reduce the dose and toxicity, minimize the development of resistance and achieve synergistic effects [182]. Synergism is achieved when the combination of compounds are less than the dosage needed for the same effect in the compounds alone [182].

1.7 Computer Aided Drug Design

Computer aided drug design (CADD), also known as *in silico* screening, is a group of techniques used in various phases of drug discovery in order to reduce time, cost and risk factors associated with drug development. CADD can be divided into two main approaches:

1) Ligand based drug design (LBDD)
2) Structure based drug design (SBDD)

LBDD is useful approach when there is no structural data available of the target. The technique relies on the assumption that structurally similar compounds will have similar biological effects. Therefore, compounds with known activities at the target site

are used as starting points to build a predictive model and new compounds are screened against this model. 1-Dimensional LBDD methods rely on ligand descriptors such molecular weight, lipophilicity, charge, molar refractivity, topological polar surface area (TPSA), number of hydrogen bond donors and acceptors, rotatable bonds, number of single, double and triple bonds, to name a few. 2-Dimensional LBDD methods look at the similarity between active compounds and test compounds based on various ligand fingerprints/patterns including MACCS, SMILES, SMARTS and ECFP6 [183]. 3-Dimensional LBDD methods build a pharmacophore model using the 3D positions of ligand descriptors such as hydrophobic centroids, hydrogen bond donors or acceptors, halides, aromatic rings, negative or positive charge, anion or cations. A single or a combination of the above-mentioned LBDD methods can then be used to screen a library of known or theoretical compounds for potential activity and in doing so reducing the number of compounds needed to test for biological activity.

With the increased availability of described 3D target protein structures including the active ligand binding sites, and for lipid and DNA structures, SBDD has become increasingly popular. Docking is a popular SBDD method commonly used to predict the interaction of potential ligands with proteins. *In silico* docking aims to predict the correct orientation or pose of a ligand in a protein and also predict the affinity of the ligand towards the protein. The latter is then used as a prediction of its biological activity.

Docking power refers to the ability of a docking program to reproduce the native binding pose of a ligand. RMSD (root mean square deviation) is used as the main parameter to evaluate Docking power. An RMSD below 2.0 Å is regarded as a successful prediction. Scoring power refers to the ability of a scoring function to produce binding scores in a linear correlation with experimental binding data. The most popular docking programs include AutoDock [184], Autodock Vina [185], DOCK[186], ICM [187], Glide [188] and GOLD [189]. Ideally, a good docking software suite will calculate a good docking and scoring power. Popular top-tier docking programs are able to reproduce the native docking pose (docking power) in 40-85% of the experiments depending on the dataset [190-192]. For the CASF 2016 benchmark suite Autodock Vina (the most used academically available software) has the best scoring power with an average Pearson

Correlation of 0.53 (R^2=0.28) and Glide SP, a popular commercial software package, has an average Pearson Correlation of 0.42 (R^2=0.176) [192].

Various machine learning techniques have successfully been applied to improve the scoring power of various docking programs. For Autodock Vina, Random Tree Forest (RTF) classification improved the scoring power to an average Pearson Correlation 0.73 (R^2=0.53) [192-193]. For Glide, the SIEVE-Score method was developed using RTF classification which considerably improved screening accuracy by separating active from inactive ligands [194].

For the present study the commercial docking software from Schrödinger, Glide, was used to predict the binding poses for the compounds and their various targets. Tubulin, CAII, CAIX and STS were used as targets for STX1972. BRD4 was used as the target of Bzt-W41, Bzt-W49 and Bzt-W52. Sirtuin 1, 2 and 3 were the targets of W137. JAK1 and JAK2 were the targets of Ruxolitinib. Additionally, a previously developed machine-learned RTF predictive model was used to predict the activity of the compounds against their corresponding targets.

1.8 Summary

Conventional cancer treatments have not proven entirely effective in the eradication of cancer with evidence suggesting that many of the cancer therapies augment cancerous cell adaptation and insensitivity to drugs and could potentially be the cause of cancer recurrence and reduced patient survival [14-15]. Therapeutic inefficacy is a particular dilemma associated with metastatic TNBC, with patients still facing poor prognosis. The design and development of novel anticancer agents specifically targeting cancer-associated pathways has been of particular therapeutic interest. The rationale is twofold: firstly, highly targeted therapy overcomes widespread toxicity and adverse effects of conventional methods due to the selectivity of the treatment modality. Secondly, synergistic combinations of different classes of targeted therapies could hold therapeutic promise to overcome resistance by simultaneously abolishing multiple cancer hallmarks. Furthermore, treatment with synergistically combined drugs allows administration at a reduced dose with efficacy superseding that of

monotherapy. A brief overview of the rationale behind the targeted drugs included in the study follows.

Antimitotics have shown promise as anticancer therapeutics because of their ability to effectively alter microtubule dynamics, causing cell cycle arrest and subversion of abnormally high cancer cell proliferation [85,88]. The mitosis-selective inhibitor (STX1972) used in this study is considered the most potent oestradiol antimitotic to date.

BRD4 is a pertinent therapeutic target because it is overexpressed in many cancers and plays a functional role in the induction of tumorigenesis. BRD4 erroneously permits transcription of key cancer-promoting genes resulting in increased expression of oncoproteins involved in anti-apoptosis, growth promotion and metastasis and invasion [109,112,167-168,195]. BRD4 has been shown to be fundamentally involved in the amplified expression of the c-MYC oncoprotein in breast tumours, making this a promising drug target for c-MYC sensitive breast cancers [167-168,196]. The BRD4 inhibiting compounds (Bzt-W41, Bzt-W49 and Bzt-W52) were designed to subvert transcription of proto-oncogenes by binding to the acetyl-lysine binding motif of the bromodomain protein.

SIRT1/2 proteins are deacetylases which cause the destabilization and inactivation of p53 [141,197]. The p53 protein plays a fundamental role in cell growth regulation and apoptosis. Acetylated p53 induces cell cycle arrest and pro-cell death pathways, whereas deacetylation leads to cell cycle progression, continued proliferation and survival of tumour cells [141]. Compound W137 is a novel, dual inhibitor of SIRT 1 and 2 proteins aimed at sensitizing cancer cells to apoptosis via p53 signalling.

The JAK1/2 inhibitor (ruxolitinib) has the potential to abrogate JAK/STAT signalling and thereby reduce IL-6 expression with the aim of preventing cancer stem cell conversion [78-79]. Therapeutic targeting of cancer stem cells appears to be a vital component of a multimodal treatment approach.

1.8.1 Study problem and overview

Obvious advances have been made in the field of breast cancer treatment which have led to improved prognosis and increased patient survival rate. However, this seems true only for early-stage, non-metastatic diagnoses. TNBC remains the most precarious subtype of breast cancer to treat, with limited and mostly ineffective therapeutic options available. Therapeutic resistance is owed to its highly aggressive and metastatic nature, induced by intra-tumour heterogeneity. The lack of successful conventional treatment options has prompted the development of novel drugs with potent cancer selectivity which are able to overcome chemotherapeutic resistance.

This study evaluated the selective antineoplastic activity of six *in silico* designed compounds using breast cancer cell lines as experimental models. Five of these compounds are novel, *in silico* designed agents to selectively target some of the aforementioned cancer hallmarks via inhibition of specific cancer-related proteins. The compounds include an antimitotic, three variants of BRD4 inhibitors, an inhibitor of SIRT1/2 and an inhibitor of JAK1/2. Possible synergism between paired combinations is also explored.

1.8.2 Study aim and objectives

The study aimed to mechanistically assess the *in vitro* antineoplastic activity of the novel test compounds and to investigate their potential combinatorial effects when combined. Two functionally distinct tumorigenic cell lines were included to investigate anti-tumour efficacy of compounds in hormone-dependent and TNBC models and compared to a non-cancerous transformed endothelial cell line.

The primary and related secondary objectives were:

- To establish the antiproliferative efficacy of each compound for each of the breast cancer cell lines by establishing the half maximal inhibitory concentration (IC_{50}) using cell culture techniques.

  Results from the antiproliferative studies were used to:

  - Initially identify feasible compounds for further experimental inclusion by comparing compound IC_{50} value to protein inhibition concentration.

    - Determine cell line selectivity by comparing antiproliferative potency of compounds between the two breast cancer models compared to a control cell line.
    - Screen for the lead BRD4 inhibitor compound(s) to include in combination studies.
- To use varying combinations of the most promising drugs and calculate the combination indexes of the paired drug combinations in order to assess drug interaction.

  Results from the combination studies will be used to:
    - Identify whether the paired combinations exhibit synergism.
    - Identify which of the paired combinations, and in which combination ratio, exhibit strongest synergism and would be most feasible for further investigation.
- To determine whether identified compounds and combinations exhibit cancer-specific selectivity by exposing a control cell line to the same concentrations.
- To assess the effects of individual compounds and the synergistic combinations on cell morphology.
- To evaluate the effects the drugs and drug combinations have on cell cycle progression, cell death, ROS generation and mitochondrial membrane potential using flow cytometry assays.
- To analyse specific gene expression changes induced by exposure to the drugs and drug combinations using quantitative reverse transcription polymerase chain reaction.
- To analyse specific changes in protein expression induced by exposure to the drugs and drug combinations using flow cytometry and enzyme-linked immunosorbent assay.

1.9 Concluding remarks

The study aimed to contribute towards deducing the mechanistic behaviours of the compounds and elucidate their combined effect during dual treatment. Novelty of the research lies in the incorporation of a chemomitotic agent combined with selective inhibitors of principal cancer associated proteins and epigenetic regulators which could

hold promise to induce synergistic effects due to simultaneous targeting of multiple cancer hallmarks.

Of note, although the study initially included six compounds designed as cancer-targeting drugs, cell growth and combination studies serve to screen for the most feasible lead compounds and drug combinations to include in further experimental procedures. Furthermore, since the tested compounds are novel and have not been reported on before, the anti-tumour efficacy of the drugs were tested on both hormone-dependent and TNBC cancer cell line models to determine selectivity. However, the primary focus was to determine whether the test compounds and compound pairs could be harnessed for their therapeutic potential to treat TNBC, since this remains one of the highest unmet needs in breast cancer treatment.

Chapter 2: Materials and methods

2.1 Cell lines

2.1.1 MDA-MB-231

MDA-MB-231 cells were purchased from Highveld Biological (Pty) Ltd, South Africa. The human breast carcinoma cell line was isolated from a metastatic site (pleural effusion) of a patient with invasive ductal carcinoma at the M.D Anderson Hospital and Tumor Institute, Houston, Texas [198]. The cell line is ER, PR and HER2 negative and is therefore commonly used to model TNBC with invasive and metastatic properties [199]. Genome profiling clusters MDA-MB-231 cells with the basal subtype of breast cancer [199]. These spindle-shaped epithelial cells grow randomly in an adherent manner and have been reported to exhibit an approximate population doubling time of 38 hours (h) [198,200] .

2.1.2 MCF-7

The MCF-7 cell line was supplied by Highveld Biological (Pty) Ltd, Johannesburg, South Africa. These breast cancer cells were derived from pleural effusion of a patient with metastatic adenocarcinoma at the Michigan Cancer Foundation (Detroit), from where their name derives [201]. MCF-7 cells are ER and PR positive and cluster with the Luminal A molecular subtype of breast cancer [201]. This cell line is non-invasive and displays low metastatic potential, thereby simulating a less aggressive breast cancer model than that of the MDA-MB-231 cell line [201]. The cells exhibit epithelial morphology and adherent growth properties with an estimated reported population doubling time of 38 h [202].

2.1.3 EA.hy926

Human endothelial-like EA.hy926 cells were derived from fusion of human umbilical vein endothelial cells (HUVECs) with epithelial lung adenocarcinoma cells A549-8 [203]. The result is an immortalized, well characterized somatic cell hybrid presenting endothelial properties [203]. The EA.hy926 cells were kindly provided by Ms. Margo Nell

(Department of Pharmacology, University of Pretoria). EA.hy926 served as the control cell line to elicit whether the drugs show cell line specific cytotoxicity.

EA.hy926 cells have been used by several researchers as a non-cancer or control or non-tumour cell line to compare the activity of compounds to cancer cell lines. For example, Arafath *et al.* (2017) tested their synthesized compounds on what they describe as the "normal human cell line (human endothelial cell line EA.hy926)" and compared it to MCF-7, HCT-116 and HeLa cells [204]. Buonannoa *et al.* (2008) tested the *in vitro* cytotoxicity of climacostol against what they describe as the "human non-tumour endothelial EA.hy926 cells" and compared it to human tumor squamous carcinoma A431 cells and human promyelocytic leukaemia HL60 cells [205]. Guo *et al.* (2020) performed *in vitro* cytotoxic activity of their synthesized compounds against what they describe as "normal EA.hy926 cells" and compared it to five other cancer cell lines including LLC (Lewis lung carcinoma), BGC-823 (gastric carcinoma), CT-26 (murine colon carcinoma), Bel-7402 (liver carcinoma), and MCF-7 (breast carcinoma) [206]. Figueiredo *et al.* (2016) describes the EA.hy926 cells as non-tumour cells when they compared the cytotoxicity of lignin-based nanoparticles to different cancer cell lines including MDA-MB-231, MCF-7, PC3-MM2 and Caco-2 cancer cells [207]. Jashari *et al.* (2014) tested the cytotoxicity of their novel isoxazolo- and thiazolo derivatives of coumarin on cancer cells (MCF-7, MDA-MB-231, LNCap, PC-3 and U936) and what they describe as "non-cancer cell lines such as the human endothelial cell line EA.hy926" [208]. The EA.hy926 cell line is described as non-cancerous in the article by Burger *et al.* (2018) when they compared the activity of a bioactive steroidal alkaloid isolated from *Solanum aculeastrum* on several cancer cells lines including MCF-7 and MDA-MB-231 cells [209]. Also, Cattin *et al.* (2018) showed that the EA.hy296 endothelial cells consistently inhibited 3D spheroid growth and also reduced growth *in vivo* of the SW620 and HCT116 colorectal cancer cells [210]. This supports the view that the EA.hy926 cell line is a valid non-cancerous and also non-tumorigenic cell line to compare the bio-activity of compounds to MCF-7 and MDA-MB-231 cells.

All three cell lines were cultured in Dulbecco's Modified Eagle's Medium (DMEM) (Sigma-Aldrich Pty Ltd., Johannesburg, South Africa). The original DMEM formulation containing 1000 mg/L of glucose was used to culture the MDA-MB-231 and MCF-7 tumorigenic cell lines, and the modified DMEM/High formulation containing 4500 mg/L

of glucose was used for EA.hy926 cell growth. To make the complete growth medium 13.5 grams of powder was reconstituted per litre and supplemented with the following: 3.7 g/L sodium bicarbonate, heat inactivated foetal bovine serum (FBS) to a final concentration of 10%, 100 IU/mL penicillin, 100 µg/mL streptomycin and 250 µg/L Fungizone. The cells were grown and maintained in sterile tissue culture flasks in a humidified atmosphere at 37°C, 5% CO_2 in a water-jacketed incubator.

Ethics approval for the use of these cell lines was obtained from the Faculty of Health Sciences Research Ethics Committee of the University of Pretoria. Ethics Reference No: 223/2016.

2.2 General material and culture maintenance

2.2.1 Reagents and consumables

DMEM and DMEM/High, Trypsin-EDTA, penicillin, streptomycin and Fungizone were purchased from Sigma-Aldrich Pty Ltd. (Johannesburg, South Africa). Heat-inactivated foetal bovine serum was bought from Celtic Molecular Diagnostics Pty Ltd. (Johannesburg, South Africa). Phosphate buffered saline (PBS) was prepared by diluting a ten times concentrated solution consisting of 80 g/l NaCl, 2 g/l KCl, 2 g/l KH_2PO_4 and 11.5 g/l Na_2HPO_4 (purchased from Merck (Johannesburg, South Africa)) to a 1X solution. The diluted PBS solution was pH adjusted to 7.4 followed by autoclaving (20 min, 120°C, 15 psi) before use. Sterile cell culture flasks, plates, centrifuge and microcentrifuge tubes, PCR tubes, pipette tips, 10 mL syringes and 0.22 µm syringe filters were obtained through Lasec SA Pty Ltd. (Cape Town, South Africa).

2.2.2 Cell culture procedures

Upon reaching between 70% - 90% confluence the cells were trypsinized by removing the medium, briefly rinsing the cell layer with sterile PBS and adding Trypsin-EDTA solution to the flask. To facilitate dissociation, cells were incubated at 37°C. Cells were observed under an inverted microscope every 2 to 3 minutes to check for cell rounding and detachment (usually 5 - 15 min). Fivefold fresh growth medium was added to inhibit trypsin and cells were aspirated by gently pipetting. The detached cells were

then either subcultured, cryopreserved at -80°C or seeded for an experiment. Medium renewal was done every two to three days and subcultivation twice a week, as required. For cryopreservation, cells were centrifuged at 125 *x g* for 5 minutes and resuspended in cryoprotectant medium (complete growth medium supplemented with 5% (v/v) DMSO).

For experimental procedures, cells were counted by staining with a 0.2% (m/v) solution of trypan blue and then counted by making use of a haemocytometer as described by Freshney (1994) [211]. If the percentage of blue stained (dead) cells was more than 5% the sample was discarded and not used for experiments. The number of viable cells per mL was determined by averaging the count of viable cells in the corner squares x dilution factor x 10^4. Hereafter, appropriate aliquots of the cell suspension were seeded into culture vessels required for experimentation. An inoculum of 5 X 10^4 viable cells per mL was maintained for experiments.

All of the operations were carried out under strict aseptic conditions, with all work being carried out in a Class II laminar flow cabinet from Esco (Centurion, South Africa). All sterile workspaces, including the surface of the laminar flow cabinet were cleaned with ethanol (70% v/v), sodium dodecyl sulphate (SDS) (0.1% m/v) and sodium hypochlorite (10% v/v) prior to every experiment. All solutions were sterilized by filtration (0.22 µm pore size) and all glassware and non-sterile equipment sterilized by autoclaving (20 min, 120°C, 15 psi).

All compounds were received as powder with purity of greater than 95%. The compounds in their powder format are stored at -20°C. Fresh aliquots of the compounds are made every six months and tested for activity in order to determine whether their activity remains stable. Dimethyl sulfoxide (DMSO) was used as solvent for stock solutions of each test compound to the following concentrations: STX1972 (100 µM), Bzt-W41 (50 mM), Bzt-W49 (50 mM), Bzt-W52 (50 mM), W137 (20 mM), and Ruxilitinib (20 mM). To minimize the effect of freeze/thaw cycles on the stability of the compounds, the stock solutions were split into aliquots of 10 to 20 µL and stored at -20°C. Immediately prior to use, each compound was fully thawed and thoroughly mixed and compounds were not allowed to go through more than 2 freeze thaw cycle. For combination studies the compounds were added to fresh cell culture medium on

the day of exposure. The final concentration of DMSO was never more than 0.05% v/v or 5 µL per 1 ml cell culture medium in the combination studies.

2.3 Methods

2.3.1 Computer Aided Drug Design

2.3.1.1 Receptor and Ligand preparation

Protein structures and conformations are solved by using static protein crystal analysis. In solution proteins are flexible and can undergo sidechain and backbone conformational changes [212]. Ensemble docking is a method whereby several rigid structures of the same protein are used to mimic side-chain and backbone flexibility without the additional computational costs of having to simulate these during docking [212]. This method is particularly useful if the receptor ligands have a similar structure to the compounds you want to dock. For this study, compounds similar in structure to the receptor ligands were chosen in order to determine the binding pose and subsequently the binding energy of the compounds in order to predict the biological activity of the compounds against their corresponding target receptors.

JQ1 was one of the first reported compounds to selectively target the BET bromodomains BRD2, 3 and 4 [123]. Filippakopoulos *et al.* (2010) tested JQ1 for activity against all the bromodomain subfamilies and reported their thermal stability shift (delta TM) based on differential scanning fluorimetry (DSF) [123]. For the present study the structures that are part of the bromodomain family was retrieved from the www.rcsb.org database and JQ1, Bzt-W41 and Bzt-W49 were docked into the receptors in order to determine if the docking could predict selectivity of the compounds. The BRD4 receptors with benzodiazepine and benzotriazepine analogues similar to the Bzt series of compounds were used to redock the native ligands in order to determine whether the Glide SP docking program could predict the correct docking pose (RMSD<2.0). The BRD4 receptors include 2YEL, 3MXF, 3P5O, 3U5K and 3ZYU.

The following CAII enzyme conformations were used for modelling: 1CIL, 1I91, 1TTM, 2X7S while 2X7T, 3IAI, 5FL6, 6FE2, 6G98 and 6RQN were the enzyme conformations

were used for CAIX. For STS only 1P49 was used. For SIRT the binding with the thienocarboximide moieties similar to W137 were used, as well as the open conformation of the SIRTs. 4IG9 and 4ZZI conformations were used for SIRT1 and for SIRT2 a homology model of 4ZZI was generated using SWISS-MODEL and Swiss-PDBViewer [213]. 4JSR, 4JT8, 4JT9 conformations were used for the SIRT3 receptors. The 1Z2B, 3DU7, 2E22, 1SA1, 5OSK and 6HX8 conformations were used for the tubulin receptors. The 5OSK and 6HX8 are recently solved conformations using structures containing potent sulfamates similar to STX1972 [214-215].

The Schrödinger package's *Protein preparation wizard* in Maestro was used to prepare protein structures [216]. Water molecules were kept in the protein structure when present. Hydrogen bond optimization was carried out with *ProtAssign* followed by energy minimization with *Impref* [216]. Ligands were prepared from Simplified Molecular Input Line Entry System (SMILES) notation using *LigPrep* [216]. Ionization states were predicted with Epik with a pH between 5-9 and at least 10 conformations were generated for each ligand.

2.3.1.2 Docking and Scoring

Molecular docking was done using Glide Standard Precision (SP) and all ligand structures were treated as flexible [216]. The docked poses presenting the best Glide score for each ligand-protein complex was used to predict binding affinity using a previously developed machine learning method employing a Random Tree Forest (RTF) regression model. Briefly, 11781 protein-ligand complexes with experimentally measured binding affinities (Ki, Kd and IC_{50}) from the PDBbind v2018 (http://www.pdbbind-cn.org/download.asp) general set was used to train a RTF regression model to predict Ki values of newly docked poses. The Smina package was used to extract 43 parameters of the bound ligands including the Vina docking score, 9 steric, 3 hydrophobic, 2 non-hydrophobic, 10 atom-type Gaussian, 4 non-direct hydrogen bond terms, 2 acceptor-acceptor, 2 donor-donor, 2 repulsion, 2 ad4 solvation, 1 electrostatic and 5 ligand descriptors [217]. Additionally Babel was used to extract 9 ligand descriptors including topological polar surface area (TPSA), octanol/water partition coefficient (logP), molar refractivity (MR), molecular weight (MW), number of aromatic bonds (abonds), number of double bonds (dbonds), number

of hydrogen bond acceptors 1 and 2 (HBA1 and HBA2), number of hydrogen bond donors (HBD) for a total number of 52 parameters to build a RTF predictive model trained against the Gibbs free energy estimates of the ligands. The Ranger package in R was used to build RTF models and the Caret package was used for cross-validation of the models [218-219]. An initial RTF model was built from the 11781 PDBbind v2018 protein-ligand complexes by using M = 2500 regression trees with m_{try} = 33 and a 10-fold cross validation. This RTF model was used to predict the binding affinities of the test compounds in this study.

The comparative assessment of scoring functions (CASF) benchmark was used to determine the scoring power of the newly developed RTF model. The scoring power indicates the ability of a program to correctly predict experimental ligand binding data. Briefly, Autodock Vina was used to redock the ligands in the benchmark, extract the scores and predict the binding affinity of the docked poses. The coefficient of determination (Pearson correlation squared or R-squared) and the standard deviation (in $\log K_a$ units) was reported.

2.3.2 Spectrophotometry: Cell growth

Quantification of fixated cells cultured as monolayers was determined spectrophotometrically by using crystal violet as a DNA stain. Staining the cell nuclei of fixed cells with crystal violet allows for accurate and reproducible quantification of cell number in cultures grown in 96-well plates [220-221]. Spectrophotometry was used to measure dye absorbance at 570 nm.

Dose-response curves were constructed in order to determine the growth inhibitory effect of the various test compounds on the two breast cancer cell lines and a control cell line. Time-dependent exposure studies were carried out at 48 h intervals in order to observe the progression of cell growth over time in response to exposure of various concentrations of the compounds.

Materials

Crystal violet, glutaraldehyde and Triton-X were purchased from Sigma-Aldrich Pty Ltd. (Johannesburg, South Africa).

Methods

Exponentially growing MCF-7, MDA-MB-231 cells were seeded in 96-well tissue culture plates at a cell density of 5 X 10^3 cells per well. Hereafter, cells were incubated in a humidified incubator at 37°C and 5% CO_2 for 24 h to allow for attachment. After 24 h attachment the medium was aspirated from the culture plate and the cells were exposed to the serial dilutions of each test compound in complete media (STX1972: 0 – 200 nM; Bzt-W41, Bzt-W49, Bzt-W52, W137, Ruxolitinib: 0 – 200 µM). A vehicle control, DMSO (< 0.01% v/v), was included in all experiments. The treated and control cells were then incubated for 48 h before the assay is performed.

After 48 h exposure, the medium was aspirated and cells were fixed by adding 100 µL of glutaraldehyde solution (1% v/v) to each well for 15 min at room temperature. The glutaraldehyde was discarded and 100 µL crystal violet solution (0.1% v/v) added and left at room temperature for 30 min. The crystal violet solution was aspirated and the plates repeatedly immersed under water until the supernatant was clear and then left overnight to air-dry. The stained cells were solubilized by adding 200 µL Triton X100 (0.2% v/v) to each well and incubated at room temperature for 45 min. Hereafter, well content was mixed thoroughly by gentle pipetting and 100 µL of the solution was transferred to a clean 96-well plate for reading. Optical density (OD) was read at 570 nm with an EL_x800 Universal Microplate Reader from Bio-Tek Instruments Inc. (Vermont, United States of America). Background was subtracted, based on the mean OD value of blank wells that had no added cells. The concentration of compound which results in 50% inhibition (IC_{50}) was determined as follows:

$$IC_{50} = \frac{OD\ of\ cells\ exposed\ to\ test\ condition\ (sample)}{OD\ of\ cells\ exposed\ to\ vehicle\ only\ condition\ (control)} * 100 = 50$$

The results obtained were used to plot dose-response curves. The mean IC_{50} values for each test compound for each cell line was extrapolated from a nonlinear regression model in GraphPad Prism version 6.01 for Windows, GraphPad Software, La Jolla California USA, www.graphpad.com. Three biological repeats were done for each experiment in triplicate.

2.3.3 Spectrophotometry: Combination Index

In the present study the IC_{50} after 48 h exposure describes the effect of a condition whereby 50% of the attached cells are present compared to the vehicle-treated control. This leaves enough cells to perform subsequent mechanistic experiments. Therefore, the present study looked at possible combinations of compounds that cause an IC_{50} after 48 h exposure and whether any of these combinations are synergistic.

According to the Chou-Talalay method the combination index (CI) is calculated by summing the combination fraction (CF) of each compound in the combination [222]. A CI less than 1 indicates synergism; equal to 1 indicates additive effect; and CI greater than 1 indicates antagonism. Drug interaction (synergism or antagonism) is more pronounced the farther a CI value deviates from 1.

The CI at IC_{50} is determined as follows:

$$CI = \frac{(D_1)_{[CF]}}{(D_1)_{[IC_{50}]}} + \frac{(D_2)_{[CF]}}{(D_2)_{[IC_{50}]}} = (CF)_1 + (CF)_2$$

Where $(D_1)_{[IC_{50}]}$ and $(D_2)_{[IC_{50}]}$ are the concentrations of Drug 1 alone and Drug 2 alone that inhibit cell growth by 50%, respectively. $(D_1)_{[CF]}$ and $(D_2)_{[CF]}$ are fractional concentrations of $(D_1)_{[IC_{50}]}$ and $(D_2)_{[IC_{50}]}$ that inhibit cell growth by 50% when used in combination. $(CF)_1$ and $(CF)_2$ refer to the subsequent combination fraction of Drug 1 and Drug 2, respectively, which is summed to deliver the CI.

Synergistic CIs of 0.95, 0.9, 0.85 and 0.8 at various CFs of two drugs on an isobologram whereby the CF of any drug is not less than 20% of its IC_{50} effect is plotted in Figure 2.1. These CIs and the respective ranges were used to test various combinations for synergism at the IC_{50} level. The reason for choosing CFs of any drug to be not less than 20% is to prevent one drug's mechanism from dominating the anti-proliferative effect and likely the overall mechanism of action. Furthermore, previous studies in our laboratory on various cell lines have identified that CIs of 0.8 to 0.95 as the optimal range for CIs that result in IC50 inhibition. For example, STX1972

combined with Bzt-W49 showed CI of 0.9 on SH-SY5Y neuroblastoma with CFs of 0.5 and 0.4 respectively [223]. W137 combined with Bzt-W41 showed a CI of 0.85 on SH-SY5Y neuroblastoma with CFs of 0.40 and 0.45 respectively [224]. Kapp *et al.* [138] identified a synergistic CI of 0.9 for Bzt-w41 combined with the antiglycolytic, 3-bromopyruvate on U937 myeloid leukemia cells with CFs of 0.5 and 0.4 respectively [138].

Cells were seeded as explained in Section 2.3.2 and exposed to paired drug combinations in various CF ratios with summed CI < 1. The cytotoxic effects of the drug combinations were measured using the crystal violet assay as described in Section 2.3.2 and statistically compared to the effects of the respective individual compounds.

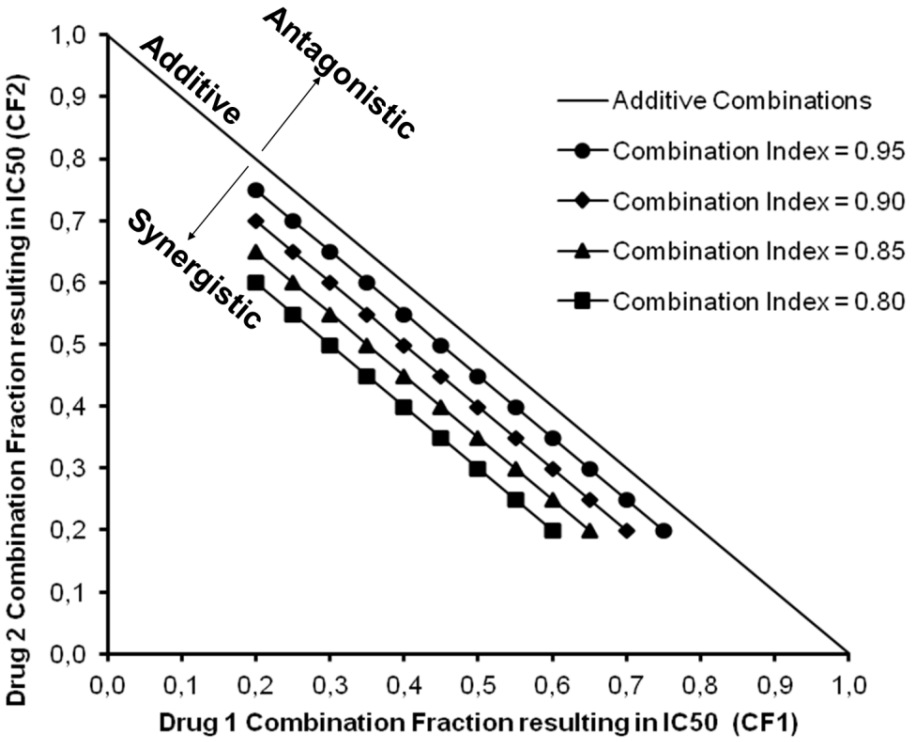

Figure 2.1: Normalized isobologram at IC_{50}. Synergistic CIs of 0.95, 0.9, 0.85 and 0.8 at various CFs of two drugs on an isobologram whereby the CF of any drug is not less than 25% of its IC_{50} effect.

2.3.4 Confocal microscopy: morphological observation of tubulin architecture

Confocal microscopy was used to observe the effects of the test compounds on the cytoskeletal microtubule architecture of treated EA.hy926, MCF-7 and MDA-MB-231 cells. Colchicine, a commercially used antimitotic known to cause tubulin disruption, was used as a positive control. Morphological observations of tubulin architecture were performed after 8 h of exposure to the test compounds. This time point was chosen based on results of a pilot experiment wherein treated cells were observed every 2 h by means of an inverted microscope to check for cell rounding. The 8 h cell cycle analysis results as per Section 2.3.6 validated the selected time point by quantifying the number of cells in the G_2/M phase of the treated versus vehicle-control samples.

Materials

R&D Systems Mouse anti-human Tubulin β-1 MAb (Clone 923425) and Goat F(ab)2 Anti-Mouse IgG (H+L) Fluorescein-conjugated antibodies from were purchased from Whitehead Scientific (Pty) Ltd, (Hillcrest, RSA). Methanol and 4', 6-diamidino-2-phenylindole (DAPI) was purchased from Sigma-Aldrich Pty Ltd. (St. Louis, MO, USA). Bovine serum albumin (BSA) and ProLong diamond antifade mountant, Molecular Probes were purchased from Life Technologies™ South Africa (Pty) Ltd. (Fairland, RSA). Cytoskeletal buffer was freshly prepared on the day of use (100 mL ddH_2O, 60 mM PIPES (1,4 piperazine diethanesulfonic acid), 27 mM HEPES (4-(2-hydroxyethyl)-1-piperazineethanesulfonic acid, 10 mM EGTA (ethylene glycol tetraacetic acid)) all purchased from Sigma-Aldrich Pty Ltd. (St. Louis, MO, USA).

Methods

Exponentially growing MCF-7, MDA-MB-231 and EA.hy926 cells were seeded at 50 000 cells per well in a 24-well plate. Sterile 12 mm glass coverslips were placed into the wells before adding the cells. After 24 h attachment the medium was discarded and the cells treated with STX1972 and the STX-Bzt-W41 combination, at IC_{50} and combination concentrations as determined in Sections 2.3.2 and 2.3.3. DMSO and colchicine-treated (100 nM) samples served as negative and positive controls respectively. After the 8 h treatment, media was discarded and cells were washed three times with cytoskeletal buffer (CB). Cells were fixed by adding 1 ml of ice-cold methanol and incubating the plate at -20˚C for 5 – 10 min. The coverslips were gently

washed three times with CB buffer for 5 min at room temperature. In order to stain the intracellular components, fixed cells were permeabilised with 0.2% Triton X100 diluted in 0.1 M PBS and incubated at room temperature for 5 min. After permeabilisation cells were washed three times in 0.1 M PBS for 5 min per wash. Non-specific binding was inhibited by immersing the coverslips in 500 µL blocking buffer (2% bovine serum albumin (BSA) in 0.1 M PBS) for 60 min at room temperature. Beta tubulin was located by incubating the cells with the primary mouse anti-β-1 tubulin antibody made up to 15 µg/mL in a 2% BSA solution for 60 min at 37°C. Cells were washed three times in cold 0.1 M PBS (5 min per wash) and counter stained with the secondary IgG (H+L) fluorescein-conjugated antibody, made up to 2 µg/mL in a 2% BSA solution for 60 min at 37°C in the dark. Following secondary staining, the coverslips were gently washed three times in cold 0.1 M PBS for 5 min per wash. Nuclei were stained with DAPI (1 µg/mL) for 5 min at room temperature. The coverslips were gently washed twice in cold 0.1 M PBS before being placed sample-side down onto a drop of ProLong® Diamond antifade mountant on a glass slide. The slides were left to cure for 24 h at room temperature in the dark. Stained cells were viewed and images captured using a ZEISS LSM 800 confocal laser scanning microscope (Carl Zeiss MicroImaging GmbH, Göttingen, Germany). The experiment was conducted in duplicate and a minimum of three representative images were captured from each sample at two magnifications (400x and 630x). The exposure time for each image captured was kept consistent to avoid deterioration of fluorescent signal.

2.3.5 Flow cytometry: Cell cycle progression

Flow cytometry was used to measure the DNA content of treated and control samples in order to monitor the effect on cell cycle progression. Analysis was conducted by ethanol fixation and propidium iodide staining of cells. Propidium iodide (PI), an intercalating dye, was used to stain the nucleus in order to quantify the amount of DNA present. Since PI also binds to double stranded RNA, RNAse is added to digest RNA present in the sample. The amount of DNA present correlates with the stages of the cell cycle during cell division, sorting the cells in four phases of the cycle (sub G_1, G_1, S and G_2/M). Time-dependent studies were conducted at intervals of 8 h and 48 h.

Materials

PI, RNAse A and Actinomycin D were purchased from Sigma-Aldrich Pty Ltd. (St. Louis, MO, USA). Absolute (99.9 %) ethanol was purchased from Merck (Darmstadt, Germany).

Methods

Exponentially growing MCF-7/MDA-MB-231/EA.hy926 cells were seeded at 1.5 X 10^4 cells per well in 6-well culture plates. After 24 h attachment in a humidified incubator at 37°C with 5% CO_2, cells were treated with the IC_{50} and combination concentrations as determined in Sections 2.3.2 and 2.3.3. An Actinomycin D-treated (0.2 µg/mL) sample was added as a positive control. The medium was discarded and the cells were exposed to the IC_{50} concentrations of the various compounds and combinations and incubated for 8 h and 48 h intervals. After the respective treatment times, cells were harvested by trypsinisation and centrifuged for 5 min at 300 x *g*. The supernatant was discarded and the cells were resuspended in 200 µL of ice-cold 0.1 M PBS containing 0.1% FBS. Fixation was performed by adding 4 mL of ice-cold 70% ethanol in a drop wise manner while gently vortex mixing and the samples were stored at 4ºC for 24 h. After 24 h, the cells were pelleted by centrifugation at 300 x *g* for 5 min. The supernatant was removed and the cells were resuspended in 600 µL of 0.1 M PBS containing PI (40 µg/mL) and RNAse A (100 µg/mL). The samples were incubated at 37ºC for 45 min in the dark.

The PI fluorescence (relative DNA content per cell) was measured by using the fluorescence activated cell sorting (FACS) FC500 flow cytometer (Beckman Coulter South Africa (Pty) Ltd) equipped with an air-cooled argon laser excited at 488 nm. Data from at least 10 000 events per sample was captured using CXP software (Beckman Coulter SA (Pty) Ltd). Experimental data from at least three biological repeats was acquired. Data from cell debris and cell aggregates was gated out when data analysis was performed. The data obtained was processed using a Java-based flow cytometry data analysis program WEASEL FC v3.0.2. (Walter and Elisa Hall Institute, Melbourne, Australia).

2.3.6 Flow cytometry: Apoptosis detection

Flow cytometry was used to analyse apoptosis in the three different cell lines exposed to the different treatments. Test compound treated cells were stained with Annexin V conjugated to a fluorochrome, fluorescein isothiocyanate (FITC), to measure the translocation of the membrane phosphatidylserine (PS) from the inner to the outer leaflet. PS translocation is associated with apoptotic processes. Cells were counter-stained with PI in order to distinguish between necrotic and early apoptotic cells. Fluorescence of both stains were analysed simultaneously by means of flow cytometry.

Materials

Annexin V binding buffer (pH7.4): HEPES 100 mM, NaCl 1.5 M, KCl 50 mM, $MgCl_2$ 10 mM, $CaCl_2$ 18 mM. Annexin V-FITC antibody (Sigma-Aldrich St. Louis, MO, USA).

Methods

Exponentially growing MCF-7/MDA-MB-231/EA.hy926 cells were seeded at 1.5 X 10^4 cells per well in 6-well culture plates. After 24 h for attachment the medium was discarded and the cells were treated with the IC_{50} or combination concentrations as set out in Sections 2.3.2 and 2.3.3 and incubated for 48 h. After the respective treatment times, cells were trypsinised and centrifuged for 5 min at 300 x *g*. Hereafter, supernatant was removed and cells were resuspended at a concentration of 1x10^6 cells in 1 mL Annexin V binding buffer. Cells in suspension (100 µL) were transferred and 5 µL of Annexin V-FITC was added. The samples were incubated for 15 min in the dark at room temperature. After 15 min 10 µL of propidium iodide (100 µg/mL) was added and gently mixed. Hereafter a further 400 µL of 1x binding buffer solution was added and cells were analysed.

Propidium iodide fluorescence (cell membrane compromised cells) and Annexin V fluorescence (apoptotic cells) were measured with a FACS FC500 flow cytometer (Beckman Coulter South Africa (Pty) Ltd) equipped with a 488 nm air-cooled argon laser. Data from at least 10 000 events per sample were captured using CXP software (Beckman Coulter SA (Pty) Ltd). Experimental data from at least three biological repeats was acquired. Data from cell debris and cell aggregates were gated out when

data analysis was performed. The data obtained was processed using a Java-based flow cytometry data analysis program WEASEL FC v3.0.2. (Walter and Elisa Hall Institute, Melbourne, Australia).

2.3.7 Flow cytometry: Acridine orange for autophagy detection

Acridine orange (AO) was used to measure the functional state of lysosomes. AO is lysosomotropic and emits red fluorescence when protonated and trapped in acidic vesicular organelles such as autolysosomes and green fluorescence when present in the cytosol [225]. The concentration-dependent metachromic shift to red fluorescence is correlated with autophagy induction [225]. Intracellular AO fluorescence was quantified by means of flow cytometry and the red-to-green fluorescence intensity ratio (R/GFIR) was used as ratiometric analysis of autophagy [225]. Two-parameter linear scale dot-plots were used to detect red fluorescence (y-axis) and green fluorescence (x-axis) and a R/GFIR-threshold (R/GFIR-T) was set according to the population axis.

Materials

Acridine orange was purchased from Sigma-Aldrich Pty Ltd. (St. Louis, MO, USA).

Methods

Exponentially growing cells were seeded into 6-well culture plates at 1.5 X 10^4 cells per well and left for 24 h in a humidified incubator at 37°C with 5% CO_2 to allow for attachment. Cells were treated with the DMSO control, IC_{50} values of compounds or combinations as detailed in Sections 2.3.2 and 2.3.3 at 37°C for 48 h. After the exposure time the cells were harvested by trypsinisation, centrifuged at 300 x *g* for 5 min and the supernatant discarded. Cells were resuspended in an AO staining solution at a final concentration of 1 µg/mL (diluted in pre-warmed 0.1 M PBS). Cells were incubated for 15 min at room temperature in the dark. After incubation cells were centrifuged at 300 x *g* for 5 min and the supernatant discarded. Samples were resuspended in 600 µL 0.1 M PBS and transferred to flow cytometry tubes for immediate data acquisition on the flow cytometer.

AO fluorescence, green (FL 1) versus red (FL 3), was measured with a FACS FC500 flow cytometer (Beckman Coulter South Africa (Pty) Ltd) equipped with a 488 nm air-cooled argon laser. Data from at least 10 000 events per sample was captured using CXP software (Beckman Coulter SA (Pty) Ltd). Experimental data from at least three biological repeats was acquired. Data from cell debris and cell aggregates was gated out when data analysis was performed. The data obtained was processed using a Java-based flow cytometry data analysis program WEASEL FC v3.0.2. (Walter and Elisa Hall Institute, Melbourne, Australia).

2.3.8 Flow cytometry: ROS generation assay

Increased intracellular production of reactive oxygen species (ROS) causes cell damage and eventually leads to cell death. To investigate whether exposure to the test compounds leads to oxidative stress, the cell permeable 2', 7'-dichlorodihydro fluorescein diacetate (H_2DCF-DA) was used as an intracellular ROS indicator. The principle of the assay is based on treating the cells with the reduced non-fluorescent H_2DCF-DA, which easily crosses the cell membrane where it becomes trapped due to esterase activity and is oxidized by intracellular ROS to the highly fluorescent 2', 7'-dichlorofluorescein (DCF). Flow cytometry was used for the rapid measurement of intracellular ROS production by quantification of H_2DCF-DA oxidation.

Materials

2', 7'-dichlorodihydrofluorescein diacetate (H_2DCF-DA), deferoxamine mesylate salt (DFO), and the antioxidant N-acetyl-L-cysteine (NAC), were purchased from Sigma-Aldrich Pty Ltd. (St. Louis, MO, USA).

Methods

Exponentially growing cells were seeded into 25 cm^2 culture flasks at 4 X 10^5 cells per flask and left for 24 h in a humidified incubator at 37°C with 5% CO_2 to allow for attachment. Cells were treated with the DMSO control, IC_{50} values of compounds or combinations as detailed in Sections 2.3.2 and 2.3.3 at 37°C for 48 h. After the exposure time the cells were harvested by trypsinisation, centrifuged at 300 x *g* for 5 min and the supernatant discarded, followed by three PBS wash steps. Cells were

resuspended in a 10 µM working solution of H_2DCF-DA in 0.1 M PBS, at a density of 1 X 10^6/mL and incubated for 20 min at 37°C, protected from light. After incubation, the cells were washed twice with PBS and resuspended in 500 µL pre-warmed PBS. For the control samples cells were exposed to 100 µM of the iron-chelator deferoxamine mesylate salt (DFO) for 48 h (parallel to treatment exposure) or pre-incubated with 5 mM of the ROS inhibitor N-acetyl-L-cysteine (NAC) for 1 h before termination.

The change in fluorescence intensity resulting from the oxidation of H_2DCF to DCF was measured using a flow cytometer. Flow cytometric data of FL1 Log versus count illustrated the x-mean shift. Data from at least 10 000 cells were analysed with CXP software (Beckman Coulter South Africa (Pty) Ltd).

2.3.9 Flow cytometry: Mitochondrial membrane depolarization

Mitochondrial transmembrane potential (ΔΨm) corresponds to mitochondrial membrane integrity and cell health. Mitochondrial membrane permeabilisation causes dissipation of ΔΨm and results in the initiation of the pro-apoptotic signal cascade [66]. A ΔΨm -sensitive probe 3,3'-dihexyloxacarbocyanine Iodide ($DiOC_6(3)$) is widely used as a cytofluorometric ΔΨm indicator [226]. $DiOC_6(3)$ is a lipophilic cationic dye that accumulates in the mitochondrial matrix of functional mitochondria to give green fluoresce due to aggregation [227]. In apoptotic cells the dye is unable to aggregate due to ΔΨm depolarization, resulting in decreased $DiOC_6(3)$ fluorescence [228]. Quantification of mitochondrial potential was done by means of flow cytometric analysis.

Materials

3, 3'-dihexyloxacarbocyanine iodide [$DiOC_6(3)$] was purchased from Merck (Pty) Ltd, (Darmstadt, Germany).

Methods

Exponentially growing cells were seeded into 25 cm^2 culture flasks at 4 X 10^5 cells per flask and left for 24 h in a humidified incubator at 37°C with 5% CO_2 to allow for

attachment. Cells were treated with the DMSO control, IC_{50} values of compounds or drug combinations as detailed in Sections 2.3.2 and 2.3.3 and 70% EtOH as positive control at 37°C for 48 h. After the exposure time the cells were harvested by trypsinisation, centrifuged at 300 x *g* for 5 min and the supernatant discarded, followed by three PBS wash steps. Cells were resuspended in a 10 nM working solution of $DiOC_6(3)$ in 0.1 M PBS, at a density of 1 X 10^6/mL and incubated for 30 min at 37°C. After incubation, the cells were washed twice with PBS and resuspended in 500 µL pre-warmed PBS.

$DiOC_6(3)$ fluorescence was measured with a FACS FC500 flow cytometer (Beckman Coulter South Africa (Pty) Ltd) equipped with a 488 nm air-cooled argon laser. Flow cytometric data of FL1 Log versus count illustrated the x-mean shift. Data from at least 10 000 events per sample was captured using CXP software (Beckman Coulter SA (Pty) Ltd). Experimental data from at least three biological repeats was acquired. Data from cell debris and cell aggregates was gated out when data analysis was performed. The data obtained was processed using a Java-based flow cytometry data analysis program WEASEL FC v3.0.2. (Walter and Elisa Hall Institute, Melbourne, Australia).

2.3.10 Protein expression analysis: Phosphorylation of Bcl-2 at Serine 70

Bcl-2 is a member of the Bcl-2 family which regulates mitochondrial membrane potential and mitochondrial mediated apoptosis induction. An increase in the phosphorylation of Bcl-2 at serine 70 only leads to inhibition of apoptosis while an increase in the multi-site phosphorylation status of Bcl-2 at serine-70, tryptophan-69 and serine-87 leads to induction of apoptosis [229]. Multi-site phosphorylation of Bcl-2 is associated with a G_2/M block in MCF-7 and MDA-MB-231 cells [229]. Dephosphorylation of Bcl-2 at serine 70 or an overall decrease in the protein expression of Bcl-2 are also associated with induction of apoptosis [229]. The test principle of the Muse™ Bcl-2 Activation Dual Detection Kit is based on the inclusion of two directly conjugated antibodies, anti-phospho-Bcl-2 (Ser70)-Alexa Fluor®555 and anti-Bcl-2-PECy5, which allows for the simultaneous measurement of Bcl-2 phosphorylation and total levels of Bcl-2 protein expression respectively. Flow cytometry was used to determine the extent of Bcl-2 activation by detecting the phospho-Bcl-2: total ratio within the MDA-MB-231 and EA.hy926 cell lines after treatment.

Materials

The Muse™ Bcl-2 Activation Dual Detection Kit from Millipore Corporation (Billerica, Massachusetts, USA) was purchased through Merck (Pty) Ltd. (Johannesburg, South Africa).

Methods

Exponentially growing cells were seeded into 25 cm^2 culture flasks at 4 X 10^5 cells per flask and left for 24 h in a humidified incubator at 37°C with 5% CO_2 to allow for attachment. Cells were treated with the DMSO control, IC_{50} values of compounds or drug combinations (as detailed in Sections 2.3.2 and 2.3.3) at 37°C for 48 h. After the exposure time the cells were harvested by trypsinisation, centrifuged at 300 x *g* for 5 min and the supernatant discarded. Cells were resuspended in 1 X Assay Buffer at a density of 1 X 10^6/mL after which equal parts of Fixation Buffer was added to cell suspension (1:1). Samples were mixed by gently pipetting up and down and incubated on ice for 5 min. Cells were then centrifuged at 300 x *g* for 5 min and the supernatant discarded. Cells were permeabilised by adding 1 mL ice-cold Permeabilisation Buffer per 1 X 10^6 cells and incubated on ice for 5 min. Once again, cells were centrifuged at 300 x *g* for 5 min and the supernatant discarded, after which cells were resuspended in 450 µL of 1 X Assay Buffer per 1 X 10^6 cells and 180 µL was aliquoted into 2 mL microcentrifuge tubes. For dual staining, 20 µL of the antibody working cocktail solution was added to each microcentrifuge tube containing the cell suspension. The antibody working cocktail solution is pre-mixed containing equal parts of antiphospho-Bcl-2 (Ser70), Alexa Fluor® 555 and anti-Bcl-2, PECy5 conjugated antibodies. Samples were incubated for 60 min at room temperature in the dark. Following the incubation step, 200 µL of 1 X Assay Buffer was added to each microcentrifuge testing sample and centrifuged at 300 x *g* for 5 min, supernatant was discarded. Samples were then resuspended in 500 µL of 1 X Assay Buffer and acquired directly.

Antiphospho-Bcl-2 (Ser70), Alexa Fluor® 555 (FL 2) and anti-Bcl-2, PECy5 (FL 4) fluorescence was measured with a FACS FC500 flow cytometer (Beckman Coulter South Africa (Pty) Ltd) equipped with a 488 nm air-cooled argon laser. Data from at least 10 000 events per sample were captured using CXP software (Beckman Coulter SA (Pty) Ltd). Experimental data from at least three biological repeats was acquired.

Data from cell debris and cell aggregates was gated out when data analysis was performed. The data obtained was processed using a Java-based flow cytometry data analysis program WEASEL FC v3.0.2. (Walter and Elisa Hall Institute, Melbourne, Australia).

2.3.11 Gene expression analysis: Reverse transcription quantitative polymerase chain reaction

Cancer pathogenesis and progression is often owed to altered expression of genes involved in cellular processes such as cell division and apoptosis. Three of the genes implicated in numerous cancers include *p53, bcl-2* and *c-myc* [230-231]. To investigate the effects of the compounds on the expression levels of these genes, quantitative reverse transcription polymerase chain reaction (RT-qPCR) was used. RT-qPCR technology is an accurate and practical method for gene level mRNA measurement [232]. The assay is based on isolation of total RNA which is enzymatically transcribed to complementary DNA (cDNA) by reverse transcriptase. The cDNA serves as the template for the polymerase reaction. A one-step RT-qPCR assay combines the reverse transcriptase and the DNA polymerase enzymes to catalyse cDNA synthesis and PCR in a single tube. The assay uses sequence specific primers for each target gene in a single tube. SYBR Green I, which fluoresces when bound to double-stranded DNA, is used for PCR product quantification. The change in fluorescence intensity is directly proportional to the quantity of PCR amplicons [233].

Materials

RNAzol® RT RNA isolation reagent, 2-propanol (Isopropanol), and TE buffer (10 mM Tris, pH 7.5 to 8.0, 1 mM EDTA), RNAse free water and sterile 0.1 mL 8-strip RNase- and DNase-free PCR tubes with caps were purchased from Sigma-Aldrich Pty Ltd. (St. Louis, MO, USA). 99.9 % Ethanol was purchased from Merck (Darmstadt, Germany). SensiFAST™ SYBR® No-ROX one-step kit from Bioline Reagents Ltd, was purchased from Celtic Molecular Diagnostics (Pty) Ltd, (Mowbray, RSA). LightCycler® 480 96-well plates and sealing foils were obtained from Roche Diagnostics Pty Ltd (Johannesburg, South Africa).

Methods

a) Isolation of total RNA

Exponentially growing cells were seeded at 1.5 X 10^4 cells per well in a 6-well culture plate. After allowing 24 h for attachment in a humidified incubator at 37°C with 5% CO_2, the medium was discarded and the cells exposed to IC_{50} or combination drug concentrations as determined in Sections 2.3.2 and 2.3.3. Cells were then incubated in a humidified incubator at 37°C with 5% CO_2 for 48 h. Total RNA from vehicle-control and individually isolated using RNAzol® RT RNA Isolation Reagent, as per manufacturer's protocol.

i. Sample preparation (Homogenization)

Cells were lysed directly in the culture dish by removing culture medium and adding 1 mL of RNAzol®RT isolation agent per surface area of 10 cm^2. To ensure a homogenous lysate, the cell lysate was repeatedly passed through a pipette tip.

ii. DNA, protein and polysaccharide precipitation

RNAse free water was added to the lysate at 0.4 mL per 1 mL of RNAzol®RT used for homogenization. The resulting mixture was shaken vigorously for 15 seconds and stored at room temperature for 15 min. Samples were then centrifuged at 12 000 x *g* for 15 min. DNA, proteins and polysaccharides form a semisolid pellet, RNA remains soluble in the supernatant. Samples were carefully handled and precaution was taken not to disrupt the semisolid pellet that would cause contamination of the RNA-containing supernatant.

iii. Precipitation of total RNA

The RNA-containing supernatant was transferred to a new RNAse free 2 mL microcentrifuge tube. RNA was precipitated by mixing 1 mL of the supernatant with 1 mL of 100% isopropanol. Samples were stored at room temperature for 10 min, followed by centrifugation at 12 000 x *g* for 10 min. Supernatant was aspirated and an RNA precipitate in the form of a small white pellet was left in the bottom of the tube

iv. RNA washes and solubilization

The RNA was washed by mixing the RNA pellet with 0.5 mL of 75% ethanol (v/v). The pellets were centrifuged at 8 000 x *g* for 3 min. This step was repeated twice. The alcohol solution was aspirated using a micropipette. The RNA pellet was dissolved, without drying, in 100 µL RNAse-free water to approach an RNA concentration of 1 - 2 µg/mL. For solubilization in water, the RNA pellet was vortex mixed at room temperature for 2 - 5 min. The RNA concentration of each sample was measured and the samples were stored at - 20°C.

b) Measuring RNA concentration

RNA content of each sample was checked for purity, concentration and integrity by adding 1.5 µL of homogenous sample onto a Nanodrop 2000 spectrophotometer. The RNAse free water used to solubilize the RNA was used to "blank" the system before sample reading began. RNA is considered pure of organic contamination with a 260/230 absorbance ratio greater than 1.5 and free of protein contamination with a 260/280 absorbance ratio greater than 2.

c) Primer preparation

Forward and reverse primers were synthesized by and purchased from Inqaba Biotechnical Industry, (Pretoria, South Africa). Oligomer sequences are shown in Table 2.1. Each tube was briefly centrifuged before opening to prevent loss of the lyophilized pellet. Stock solution of oligomers (100 µM) were prepared by adding sterile TE Buffer. Working solutions (4 µM) were diluted from the stock solution with sterile nuclease free water. Oligomers were divided into smaller aliquots and stored at -20°C.

Table 2.1: Forward and reverse primer sequences.

Gene	Forward Primer (5'→ 3')	Reverse Primer (5'→ 3')	Product Length
p53	GGAGCACTAAGCGAGCACT	TCTCGGAACATCTCGAAGCG	124 bp
c-myc	CGTCCTCGGATTCTCTGCTC	TTGTTCCTCCTCAGAGTCGC	116 bp
bcl-2	AGATTGATGGGATCGTTGCCT	AGTCTACTTCCTCTGTGATGTTGT	109 bp
GAPDH	CTCCTCCTGTTCGACAGTCA	CCCAATACGACCAAATCCGTTG	133 bp
β2M	AGATGAGTATGCCTGCCGTG	CGGCATCTTCAAACCTCCAT	104 bp

d) Quantitative real time PCR

The expression levels of the *p53, bcl-2* and *c-myc* genes in treated and untreated cells were determined using qPCR. The Roche LightCycler 480 (Roche Diagnostics) was used to perform the RT-qPCR using a SensiFAST™ SYBR No-ROX one-step kit. The reaction mix composition is shown in Table 2.2.

Table 2.2: Reaction mix composition.

Reagent	Volume	Final concentration
2x SensiFAST™ SYBR No-ROX One-Step Mix	10 µL	1x
F+R Primer mix (2 µM/strand)	3 µL	300 nM/strand
Reverse transcriptase	0.2 µL	-
RiboSafe RNase Inhibitor	0.4 µL	-
Template	6.4 µL	400 ng
Total volume	20 µl	

The Roche LightCycler 480 was set up to have one 10 min cycle at 45ºC for optimal reverse transcription and one 2 min cycle at 95ºC in order to activate the HotStart DNA polymerase. This was followed by 35 cycles at 95ºC for 5 seconds (for denaturation) and 60ºC for 20 seconds (for annealing) with a ramp rate of 1ºC/second. SYBR Green fluorescence was acquired at end step.

All samples and reagents were kept on ice prior to the PCR run. Quantitative gene expression for the target genes was normalized to the expression levels of two reference genes: glyceraldehyde-3-phosphate dehydrogenase (GAPDH) and beta-2-microglobulin (β2M). Each reaction was performed in triplicate. Control samples were included, one of which omitted reverse transcriptase and the other without RNA template (NTC). The data was captured using the LightCycler 480 software package.

The acceleration of the fluorescence signal at its maximum was considered as the crossing point (quantification cycle (Cq)) of the PCR reaction. The Second Derivative Maximum analysis method (set at high Confidence) available in the LightCycler 480 software package was used to identify the crossing point. Cq points were normalized to two reference genes (*GAPDH* and *β2M*) and to a treatment control (cells exposed to DMSO). Relative gene expression levels of genes of interest were determined from Cq values obtained from qPCR analysis using the ΔΔCq method [234]. Gene expression of the three genes of interest (*p53, c-myc* and *bcl-2*) were calculated as

target/reference ratio, and reported as fold increase relative to DMSO control, normalized to one.

2.3.12 Protein expression analysis: c-MYC expression by means of enzyme-linked immunosorbent assay

Gene expression data from the RT-qPCR experiments indicate relative mRNA levels of genes associated with apoptosis, cell cycle regulation and signal transduction at the time of termination. However, gene expression does not necessarily correlate with protein expression or activity. Therefore, protein levels of the c-MYC oncoprotein were quantified by means enzyme-linked immunosorbent assay (ELISA). Test principle is based on the Sandwich-ELISA method where the 96-well microplate is pre-coated with a capture antibody specific to Human c-MYC, added samples combine with the antibody after which detection antibodies conjugated to biotin and finally Avidin-Horseradish Peroxidase (HRP) conjugate is added, followed by the substrate reagent and stop solution. Results were obtained by means of spectrophotometry at a wavelength of 450 nm with OD values proportional to the concentration of c-MYC present. The concentration of c-MYC per sample was calculated by comparing the OD of the samples with the standard curve.

Materials

Elabscience® Human MYC ELISA Kits (Catalog No: E-EL-H0756) were purchased from BIOCOM AFRICA Pty Ltd, (Johannesburg, South Africa).

Methods

Exponentially growing MDA-MB-231 and EA.hy926 cells were seeded into 25 cm^2 flasks at 4 X 10^5 cells per flask and were exposed to the vehicle control or various compound test conditions (as per Section 2.3.2 and 2.3.3) at 37°C for 48 h. After the treatment time, sample collection and experimental procedures were followed as per manufacturer instructions set out below.

a) Sample collection

Culture medium was removed, cells were washed with pre-cooled PBS, harvested by means of trypsinisation, and centrifuged for 5 min at 1000 x *g*. Supernatant was discarded and cells were washed three times with pre-cooled PBS. Cells were resuspended in 250 µL of pre-cooled PBS for every 1 X 10^6 cells. This was followed by cell lysis by means of freeze-thaw process. The cell suspension was frozen in a dry ice/EtOH bath and thawed in incubator. Freeze-thaw cycles were repeated 3-5 times. To ensure that cells were fully lysed mechanical lysis was also implemented by passing the lysate though a disposable insulin syringe with fixed needle (29G – ½"). This was followed by 10 min centrifugation at 1500 x *g*. Cell fragments were removed and supernatant was collected to perform the assay.

b) Preparation of standard working solution

The standard was centrifuged at 10,000 x *g* for 1 min after which 1.0 mL of Reference Standard & Sample Diluent was added to prepare a 20 ng/mL reference standard. The solution was left to stand for 10 min at room temperature, inverted gently several times. After it dissolved fully, a ½ serial dilution was made by adding 500 µL reference standard to 500 µL diluent to create a detection range of 0.31 – 20 ng/mL.

c) Assay procedure

The different standard solutions were added to the first two columns, each concentration of the solution was added in duplicate, to one well each, side by side (100 µL for each well). The samples were added to the other wells in duplicate (100 µL for each well). The plate was covered with the sealer and incubated for 90 min at 37°C. Hereafter, the liquid was removed from each well and 100 µL of Biotinylated Detection Ab working solution was immediately added to each well. Plate was covered with the plate sealer and incubated for 1 hour at 37°C. The solution was aspirated from each well, 350 µL of wash buffer was added, allowed to soak for 1~2 min and decanted. The wash step was repeated 3 times. This was followed by adding 100 µL of HRP Conjugate working solution to each well. Plate was covered with the plate sealer and incubated for 30 min at 37°C. After incubation the solution was decanted and the previously mentioned wash step was repeated 5 times. Hereafter, 90 µL of Substrate Reagent was added to each well, the plate was covered with a new plate sealer and incubated in the dark for 15 min at 37°C. The process was terminated by adding 50 µL of Stop Solution to each well, in the same order as the substrate solution

was added. The OD value of each well was determined at once with a micro-plate reader set to 450 nm.

2.4 Statistics

Data was statistically analysed as per recommendation of the Biostatistician from the unit for Biostatistics, Faculty of Health Sciences, University of Pretoria. Data obtained from 3 independent experiments (minimum of two technical repeats per experiment) was statistically analysed for significance using the analysis of variance (ANOVA)-single factor model followed by a two-tailed Student's t-test. Means are presented in bar charts, with T-bars referring to standard errors of the mean (SEM). Results were compiled using Microsoft Excel 2013 and analysed statistically using GraphPad Prism version 6.01 for Windows (GraphPad Software, La Jolla California USA, www.graphpad.com) or Microsoft Excel 2013. The IC_{50} was determined using non-linear regression (normalized variable slope) to fit a dose response curve. Multiple comparisons were conducted by means of two-way ANOVA by using Tukey's, Dunnet's or Sidak's multiple comparisons test, subject to software recommendation and based on data input. In all analysis, statistical significance is indicated by *$p \leq 0.05$, **$p \leq 0.01$, ***$p \leq 0.001$, ****$p \leq 0.0001$.

Chapter 3: Results

3.1 Computer Aided Drug Design

3.1.1 Ligand-binding analysis of compounds

Glide SP was able to reproduce the native ligand pose for all the selected protein-ligand complexes (RMSD<2). This is a good indication that the best GlideScore likely corresponds to the best docking pose for the selected compounds. The machine-learning RTF predictive model was trained against the Gibbs free energy of the experimentally determined Ki values. The Gibbs free energy was calculated as follows: ΔG (kcal/mol) = -RT ln(Ki) (R=gas constant in kcal·K^{-1}·mol^{-1}, T=temperature in Kelvin (298°K)). The Glide SP score represents the ΔG (kcal/mol) for their scoring function.

The machine-learning RTF predictive model with native poses corresponds well with the experimentally determined ΔG values of the CASF database with a square of the Pearson product-moment correlation co-efficient (R^2) of 0.948 and a standard deviation of the error of 0.6 (Figure 3.1A). The CASF-2016 benchmark is composed of 285 complexes from 57 different targets [192]. When applying the model to the docked poses of the 285 complexes a correlation co-efficient of 0.845 and a standard deviation of the error of 1.21 was observed (Figure 3.1B). A possible reason for the decreased correlation co-efficient and standard deviation of the error for the CASF-2016 benchmark compared to the RTF predictive model with native poses is that the docking software does not always produce the native binding pose and thus likely underestimates the Gibbs free energy. The Glide SP program in the CASF-2016 benchmark showed a correlation co-efficient of 0.32 and a standard deviation of the error of 1.89 [192]. This translates to a standard error range in predicting the experimental Ki value of ± 18.6x the Ki for Glide SP and ± 7.7x the Ki for our model. Our model also improves on the best scoring function tested on CASF-2016 benchmark, the $\Delta VinaRF_{20}$, with a correlation co-efficient of 0.665 and a standard deviation of the error of 1.26 [192].

The docking of JQ1, Bzt-W41 and Bzt-W49 into receptors of the bromodomain family and subsequent prediction of activity indicate that these compounds will likely selectively inhibit the BET bromodomains BRD2, BRD3 and BRD4 compared to the

rest of the proteins of the bromodomain family (Table 3.1). Filippakopoulos, 2010 *et al.* used differential scanning fluorimetry and their thermal stability shift (delta TM) show that JQ1 is indeed selective towards BRD2-4, however, no selectivity between these BET proteins was observed [123]. Bzt-W49 is predicted to be more selective towards BRD4 compared to BRD2 and this was experimentally observed in Vishwa *et al.* (2017) (Table 3.1) [164]. Bzt-W49 is also predicted to be more selective towards bromodomain 1 of BRD2 (BRD2-BRD1) compared to bromodomain 2 of BRD2 (BRD2-BD2) (Table 3.1). No major selectivity is predicted between the bromodomain 1 and 2 proteins of BRD2 and BRD4 for JQ1 and Bzt-W41 (Table 3.1).

The binding pose of JQ1, Bzt-W41 and Bzt-W49 against BRD2, BRD3 and BRD4 show similar interactions for BD1 (Figure 3.2) and BD2 (Figure 3.3). The chloro-benzene of the ligands are in close proximity to TRP97 and MET165 (BRD2-BD1), TRP57 and MET125 (BRD3-BD1), TRP81 and MET149 (BRD4-BD1), TRP370 and MET438 (BRD2-BD2), TRP332 and MET400 (BRD3-BD2) and TRP374 and MET442 (BRD4-BD2) (Figure 3.2 and Figure 3.3). The selectivity of Bzt-W49 towards BRD4 compared to BRD2 was explained by Vishwa *et al.* (2017) as being due to a stable water network at the N-side before the AcK binding site between the ligand and the ASN140, LYS141 and ASP144 residues [164]. Three separate docking software packages were used in that study (Autodock Vina, rDOCK and Autodock) as well as the Gromacs molecular dynamics package [164]. The present study used the Glide SP package and a similar network was observed (Figure 3.2I) which further supports the view that the modifications to the Bzt-W49 ligand allows additional interactions with BRD4 (BD1) protein that is not observed in the BRD2 proteins and thus explains the selectivity.

The predicted pose for STX1972 against CAII and CAIX shows the classic zinc-sulfamate nitrogen interaction (Figure 3.4A and B). For CAII the ethyl group interacts with a hydrophobic pocket comprising of PRO201, PRO202 and LEU141 of CAII (Figure 3.4A) while the ethyl group interacts with a more hydrophilic pocket comprising of ASN62, HIS64 SER65 and GLN67 in CAIX (Figure 3.4B). A calcium-sulfamate nitrogen interaction is observed for STX1972 bound to STS (Figure 3.4C). The ethyl group of STX1972 occupies a hydrophobic region comprising of GLY100, VAL101, PHE102 and LEU103 (Error! Reference source not found.C). Additional hydrogen b

onds between the sulfamate oxygens of STX1972 and FLG75 (2-aminopropanedioic acid), THR165 and LYS368 were observed (Error! Reference source not found.C). T he RTF machine-learning prediction for the Ki of STX1972 against CAII, CAIX and STS is 75.5 nM, 194.3 nM and 305.7 nM respectively (Table 3.2).

Against tubulin the predicted binding pose of STX1972 is similar to the solved structure of the quinazolinone-based antimitotic compound from Dohle *et al.* (2018) (Figure 3.5A, B and C) [215]. Hydrophobic interactions with the ethyl group include LEU.B.131, PHE.B.404, VAL.B.315 and VAL.B.316 and hydrogen bond interactions include ASN.B.349, LYS.B.352 and ALA.A.180 (Figure 3.5A, B and C). The RTF machine-learning prediction for the Ki of STX1972 against tubulin is 301 nM (Table 3.2).

The W137 SIRT1/2 inhibitor shows a binding mode similar to the solved structures of the thieno pyridine-6-carboxamides 1NQ, 1NR and 1NS bound to SIRT1 (Figure 3.6) and SIRT3 (Figure 3.7) [177,235]. The carboxamide hydrogen bonds are preserved for all three SIRTs and these include hydrogen bonds with ASP (SIRT1: ASP348, SIRT2: ASP120, SIRT3: ASP231), backbone hydrogen bonds with ILE (SIRT1: ILE347, SIRT2: ILE119, SIRT3: ILE230) and a common water molecule interacting with ILE (SIRT1: ILE270, SIRT2: ILE43, SIRT3: ILE154) (Figure 3.6 and Figure 3.7). A hydrogen bond between the backbone nitrogen of PHE (SIRT1: PHE273, SIRT2: PHE46) with the thieno aromatic ring was observed between W137 and SIRT1 and 2, but not SIRT3 (Figure 3.6 and Figure 3.7). Additionally, an aromatic interaction was observed between HIS (SIRT1: HIS363, SIRT2: HIS137, SIRT3: HIS248) and W137 that is not observed in the 1NQ, 1NR and 1NS compounds (Figure 3.6 and Figure 3.7).

The predicted binding pose of Ruxolitinib shows that the compound occupies the ATP binding site and interacts via hydrogen bonds with subdomain V GLU (JAK1: GLU957, JAK2: GLU930) and backbone oxygen of LEU (JAK1: LEU959, JAK2: LEU932) of the kinase (Figure 3.8).

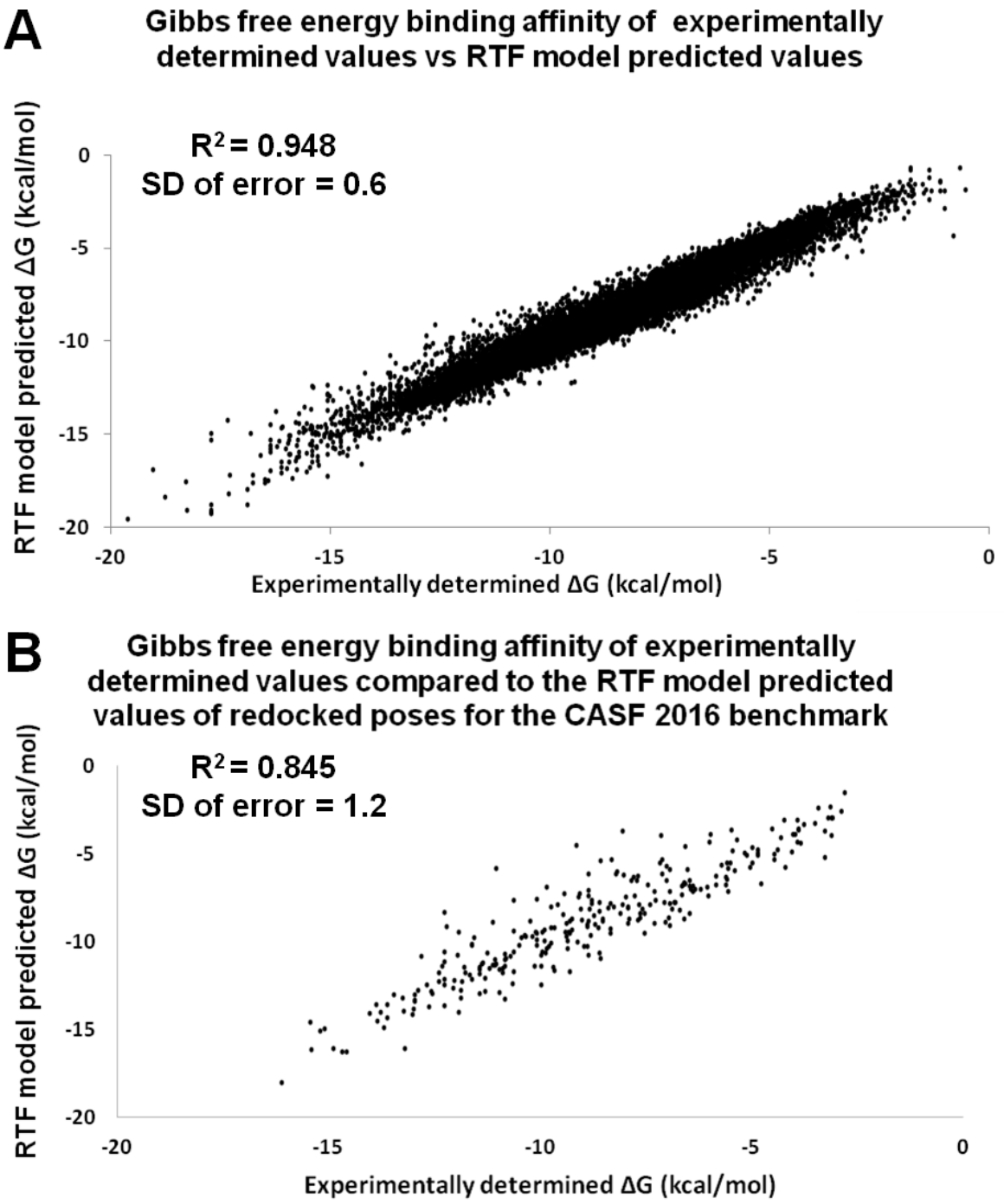

Figure 3.1: Plots of RTF model against experimentally determined Gibbs free energy (kcal/mol) from the CASF 2018 dataset (A) and the CASF-2016 benchmark set (B) [192].

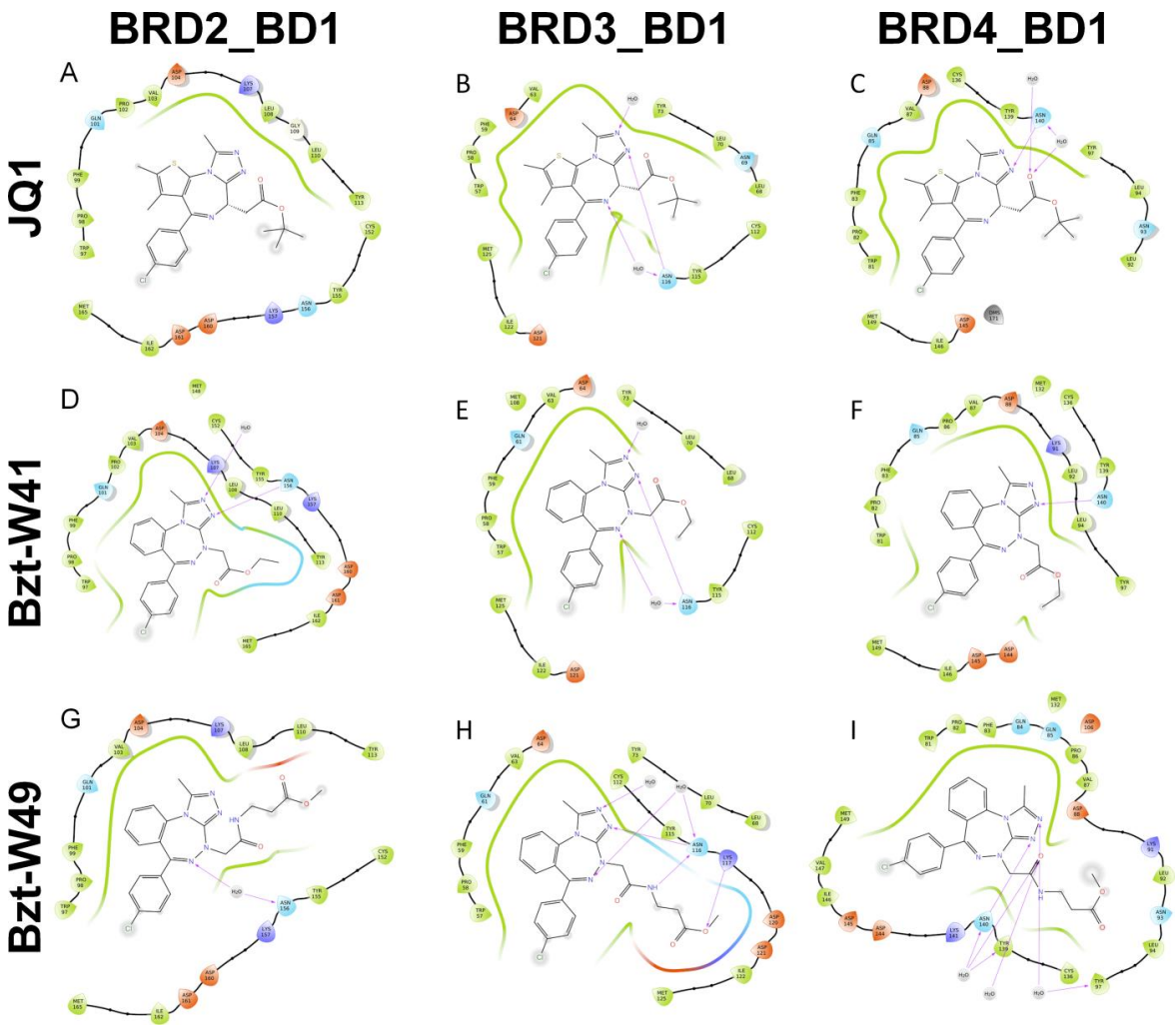

Figure 3.2: Docking of JQ1, Bzt-W41 and Bzt-W49 inhibitor compounds into the binding site of human bromodomain 1 of BRD2, BRD3 and BRD4. The triazolo nitrogens of JQ1, Bzt-W41 and Bzt-W49 are in close proximity to ASN156 (BRD2-BD1) (A, D and G), ASN116 (BRD3-BD1) (B, E and H) and ASN140 (BRD4-BD1) (C, F and J). The chloro-benzene of the ligands show close proximity to TRP97 and MET165 (BRD2-BD1) (A, D and G), TRP57 and MET125 (BRD3-BD1) (B, E and H) and TRP81 and MET149 (BRD4-BD1) (C, F and I). This indicates that the binding pose of all the ligands are similar between the BD1 of BRD2, 3 and 4. Also, a water network at the N-side before the AcK binding site with between the Bzt-W49 and the ASN140, LYS141 and ASP144 residues is observed (I).

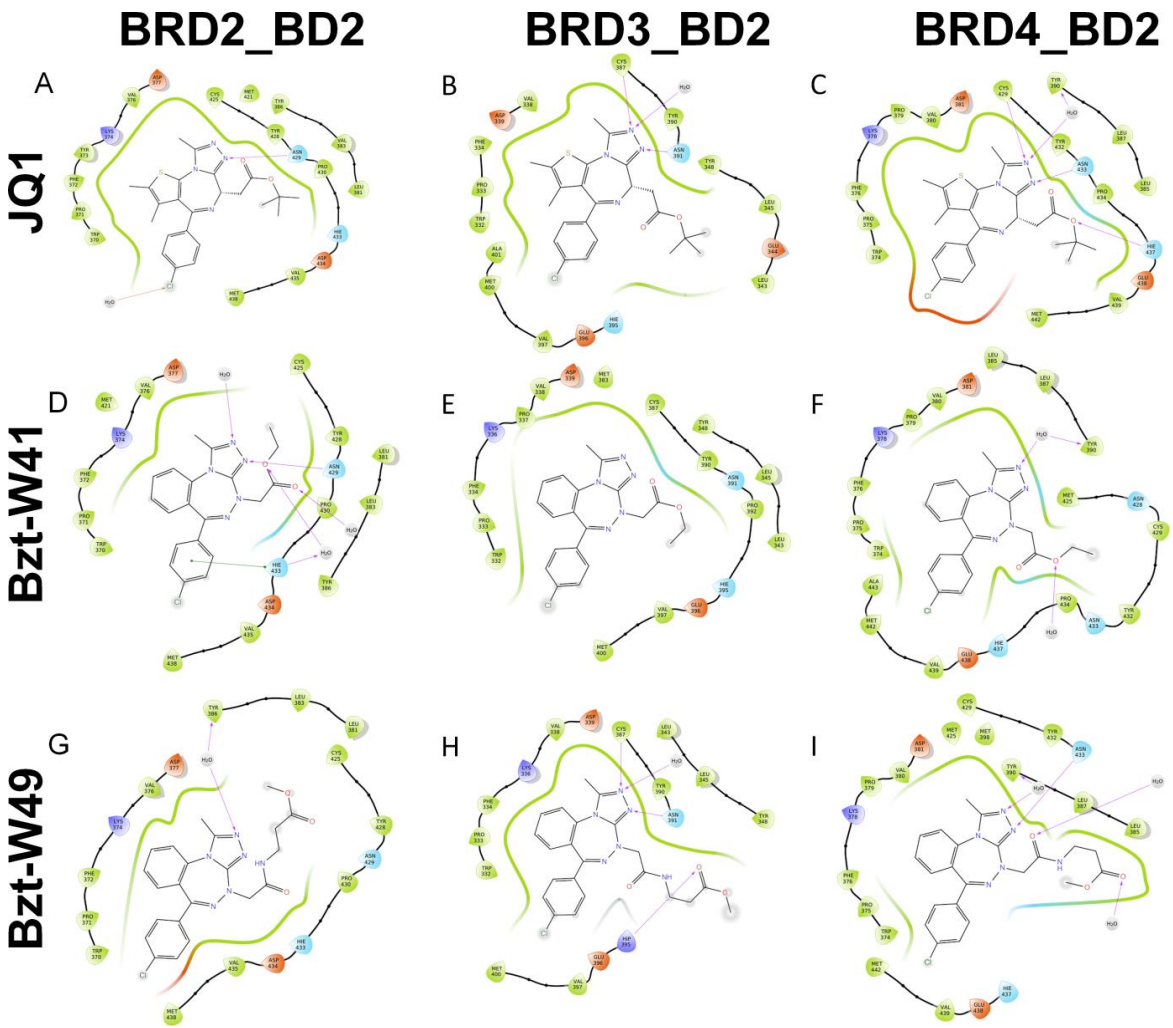

Figure 3.3: Docking of JQ1, Bzt-W41 and Bzt-W49 inhibitor compounds into the binding site of human bromodomain 2 of BRD2, BRD3 and BRD4. The triazolo nitrogens of JQ1, Bzt-W41 and Bzt-W49 are in close proximity to ASN429 (BRD2-BD2) (A, D and G), ASN391 (BRD3-BD2) (B, E and H), ASN433 (BRD4-BD2) (C, F and J). The chloro-benzene of the ligands show close proximity to TRP370 and MET438 (BRD2-BD2) (A, D and G), TRP332 and MET400 (BRD3-BD2) (B, E and H) and TRP374 and MET442 (BRD4-BD2) (C, F and I). This indicates that the binding pose of all the ligands are similar between the BD2 of BRD2, 3 and 4.

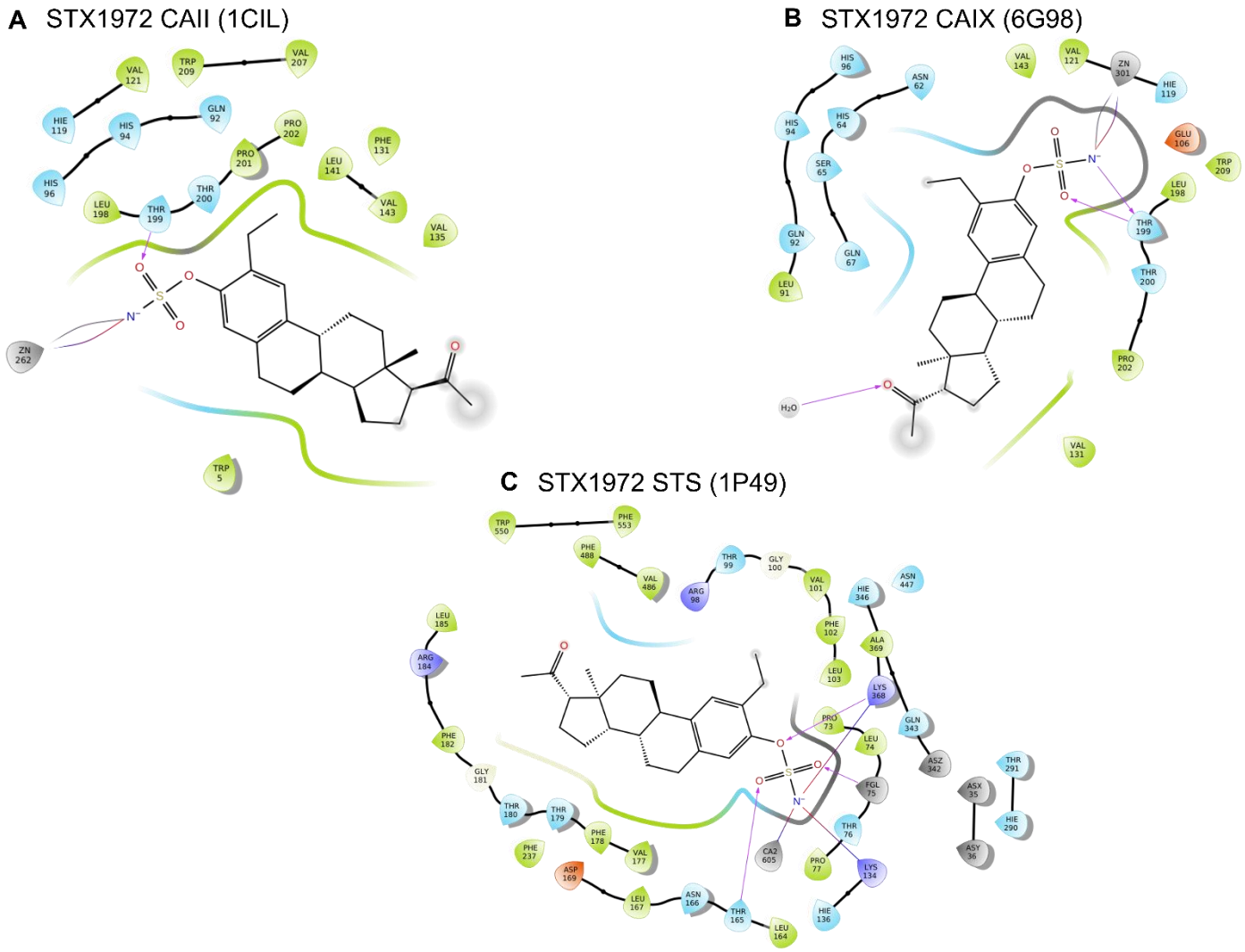

Figure 3.4: Ligand-receptor interactions between (A) STX1972-CAII (1CIL), (B) STX1972-CAIX (6G98) and (C) STX1972-STS (1P49). The predicted pose for STX1972 against CAII and CAIX shows the classic zinc-sulfamate nitrogen interaction (A and B). A calcium-sulfamate nitrogen interaction is observed for STX1972 bound to STS (C).

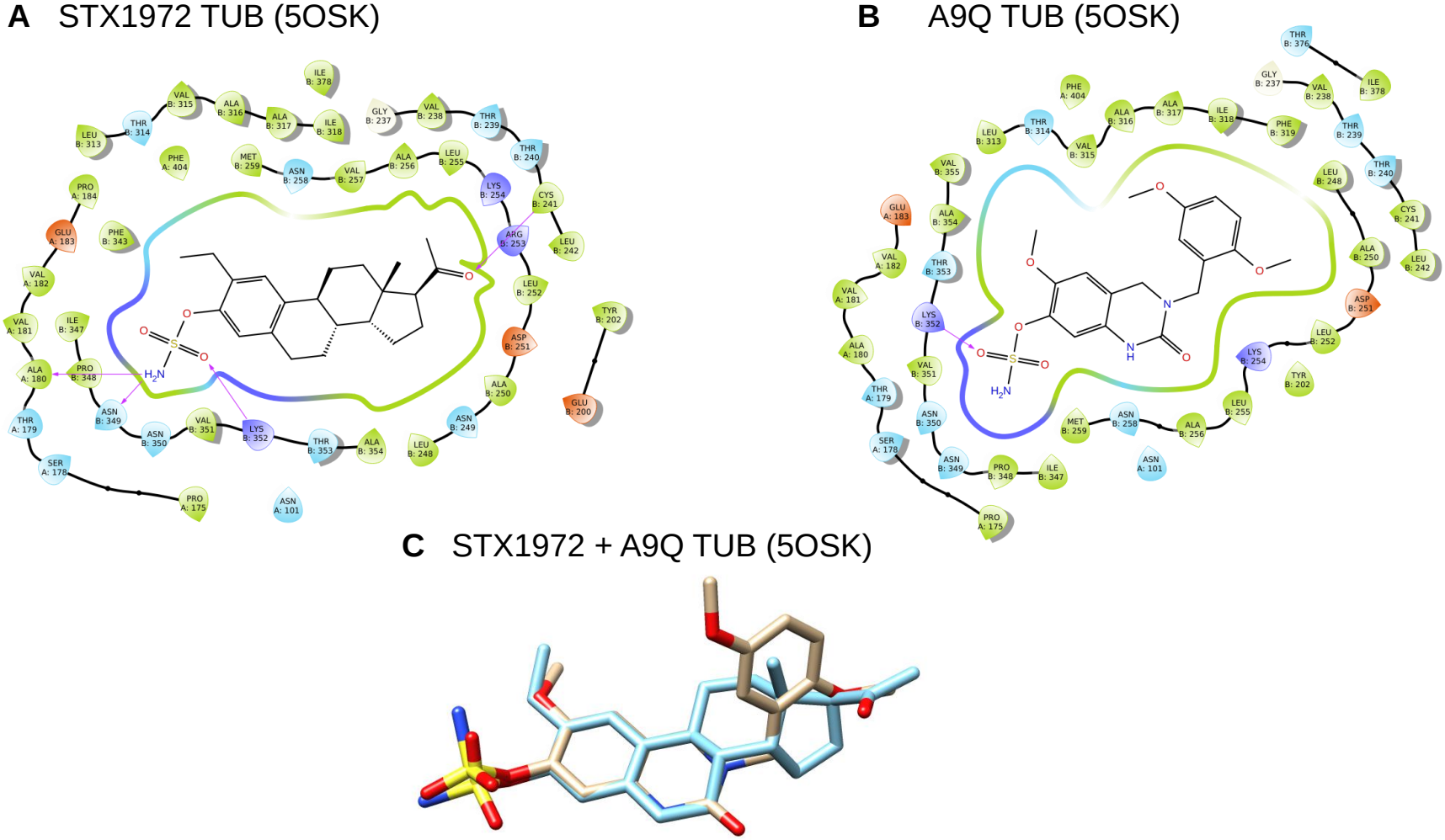

Figure 3.5: Ligand-receptor interactions between (A) STX1972-tubulin (5OSK) and (B) A9Q-tubulin (5OSK). (C) Superimposed binding pose of STX1972 (blue) and A9Q (brown). The predicted binding pose of STX1972 is similar to the solved structure of the quinazolinone-based antimitotic compound (A9Q) from Dohle *et al*. (2018).

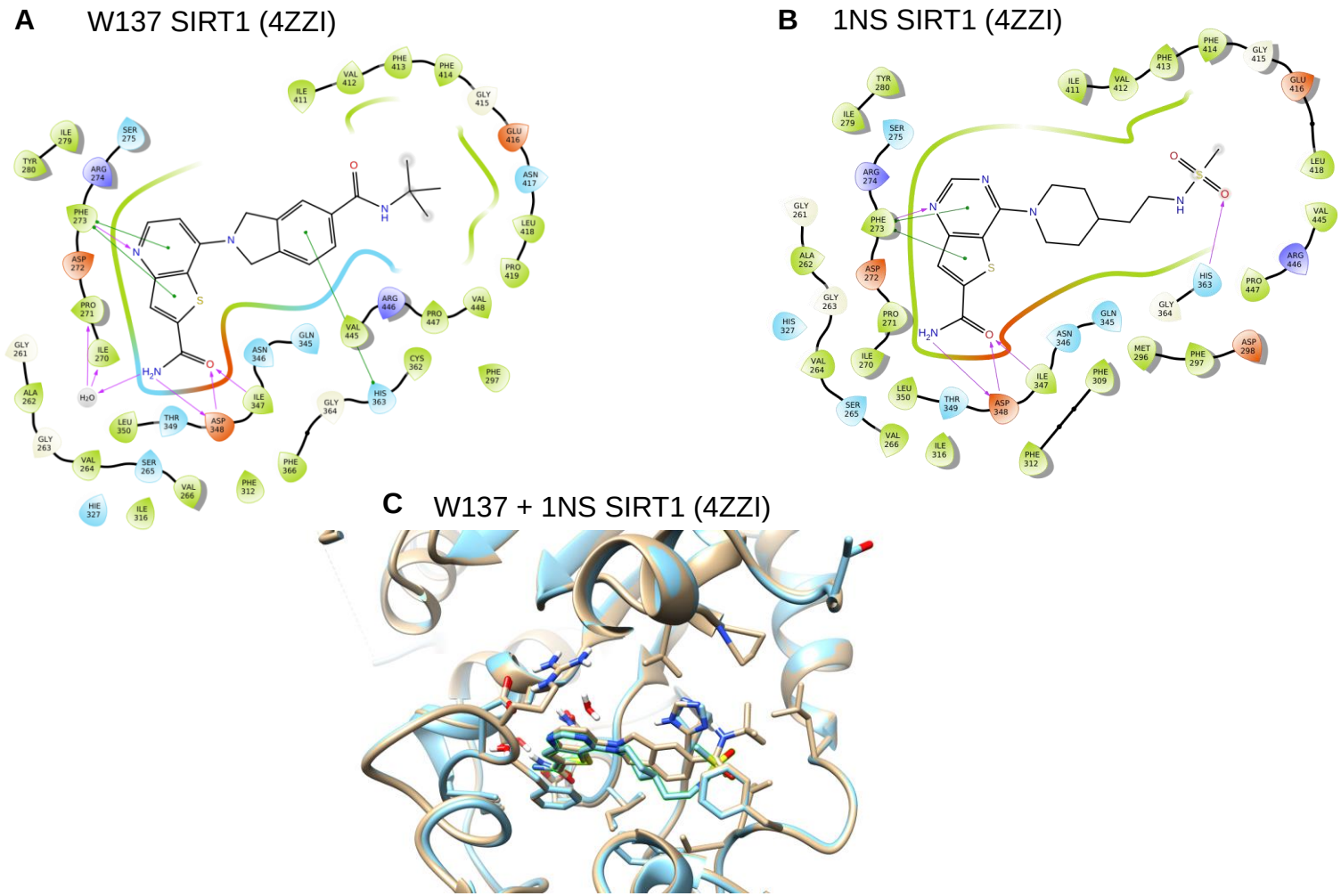

Figure 3.6: Ligand-receptor interactions between (A) W137-SIRT1 (4ZZI) and (B) 1NS-SIRT1 (4ZZI). (C) Superimposed binding pose of W137 (blue) and 1NS (brown) docked to SIRT1 (4ZZI) binding site. W137 SIRT1/2 inhibitor shows a binding mode similar to the solved structure of the thieno pyridine-6-carboxamide 1NS bound to SIRT1.

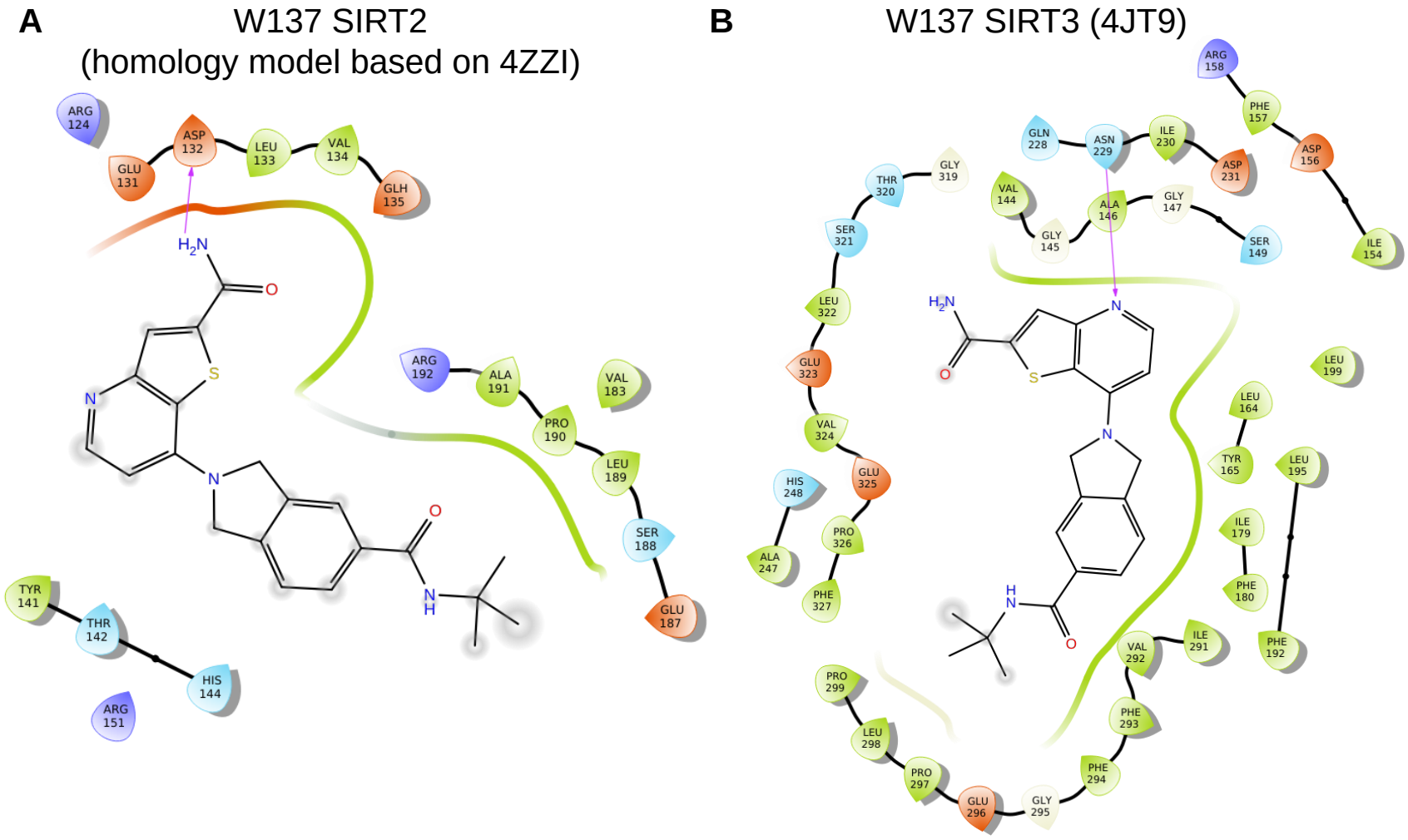

Figure 3.7: Ligand-receptor interactions between (A) W137-SIRT2 (homology model based on 4ZZI) and (B) W137-SIRT3 (4JT9).

A RUX JAK1 (3EYG)

B RUX JAK 2 (6BBV)

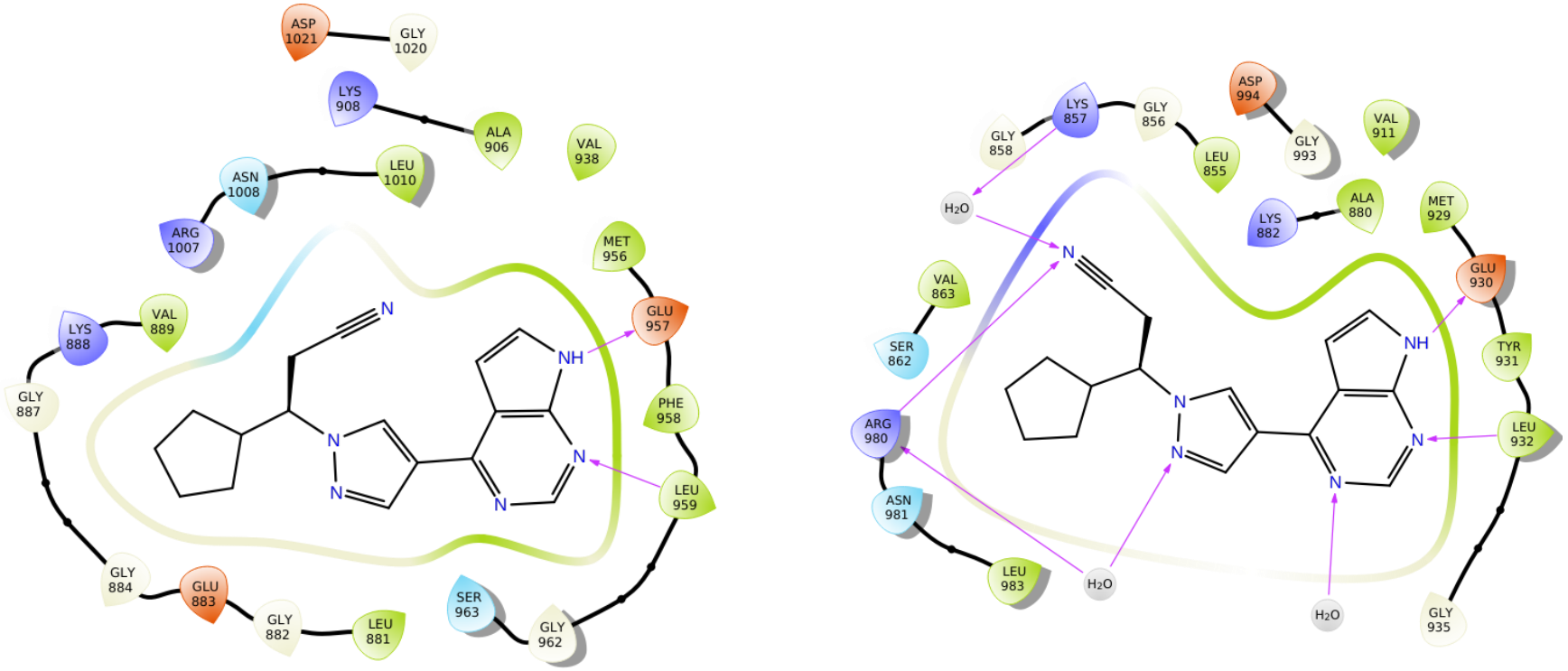

Figure 3.8: Ligand-receptor interactions between (A) Ruxolitinib-JAK1 (3EYG) and (B) Ruxolitinib-JAK2 (6BBV). Predicted binding pose of Ruxolitinib shows that the compound occupies the ATP binding site and interacts via hydrogen bonds with subdomain V GLU (JAK1: GLU957, JAK2: GLU930) and backbone oxygen of LEU (JAK1: LEU959, JAK2: LEU932) of the kinase.

Table 3.1: The Glide SP scores, RTF model predicted values and proteins with best docking pose of JQ1, Bzt-W41 and Bzt-W49 against members of the bromodomain protein family. JQ1, Bzt-W41 and Bzt-W49 are predicted to be most potent against the BET proteins BRD2, BRD3 and BRD4.

Gene name	UNIPROT	JQ1				Bzt-W41			Bzt-W49		
		Glide XP (kcal/mol)	RTF model (nM)	Delta TM [123]	Best docked PDB	Glide XP (kcal/mol)	RTF model (nM)	Best docked PDB	Glide XP (kcal/mol)	RTF model (nM)	Best docked PDB
ATAD2	**Q6PL18**	-3,45	1357	0	6hi4	-5,31	1199	4tu4	-5,32	5502	6s56
BAZ2A	**Q9UIF9**	-3,25	10323	0.18	6fkp	-5,2	5212	6fgg	-5,1	299932	5t8r
BPTF	**Q12830**	-3,22	389558	0	3qzv	-4,2	1472968	3qzv	-4,84	543257	3qzv
BRD2_1	**P25440**	-6,785	62	6.47	6mo9	-6,837	321	4uyf	-6,096	232	4a9n
BRD2_2	**P25440**	-7,709	39	7.97	5o3e	-6,224	253	6ffg	-6,69	753	4mr5
BRD3_1	**Q15059**	-6,292	197	8.27	3s91	-6,43	882	3s91	-7,946	718	3s91
BRD3_2	**Q15059**	-6,897	152	8.39	3s92	-7,669	392	5hjc	-7,621	505	3s92
BRD4_1	**O60885**	-7.805	48	9.35	3mxf	-7.297	205	4mxf	-7.682	155	3mxf
BRD4_2	**O60885**	-6,747	53	7.44	5uer	-7,186	200	5uer	-7,426	135	5uey
BRD9	**Q9H8M2**	-5,89	580	0	4z6i	-5,97	9329	4z6i	-6,19	3025	4z6i
BRDT_1	**Q58F21**	-6,792	158	3.93	4flp	-5,97	629	4flp	-6,185	296	5vbr
BRPF1	**P55201**	-4,7	3084	0	5myg	-4,67	42844	5myg	-4,56	1166	5myg
CBP	**Q92793**	-6,11	909	1.04	5mme	-6,09	1715	5mme	-5,35	5624	5i8b
CECR2	**Q9BXF3**	-5,49	580	0	5v84	-5,85	1794	5v84	-7,25	346	5v84
EP300	**Q09472**	-3,9	633	0.07	5lpm	-4,24	17689	5nu5	-5,12	443	5lpm
KAT2B	**Q92831**	-4,98	233129	0	2rnx	-6,69	8726	2rnx	-5,95	1474	2rnx
PB1	**Q86U86**	-4,37	27217	0	4q0o	-5,16	21427	4q0o	-5,36	5122	4q0o
SMCA2	**P51531**	-3,9	2780	0.93	6eg2	-5,51	4496	6eg2	-5,28	5670	6eg2
TIF1A	**O15164**	-3,93	14113	0	4yc9	-4,74	174226	4yax	-5,53	5187	4ybt

Table 3.2: GlideScores of docked ligands for several X-ray structures.

Compound	Protein	Best Docked PDB	Glide SP (kcal/mol)	Predicted Ki (nM)	Experimental Ki/IC_{50} (nM)
Bzt-W41	BRD2_BD1	4uyf	-6.837	321,2	1120,0 [138]
	BRD2_BD2	6ffg	-6.224	253,2	
	BRD4_BD1	3mxf	-7.297	204,8	490,0 [138]
	BRD4_BD1	5uer	-7.186	200,4	
Bzt-W49	BRD2_BD1	4a9n	-6.096	231,8	13230,0 [164]
	BRD2_BD2	4mr5	-6.69	753,2	
	BRD4_BD1	3mxf	-7.682	155,4	1270,0 [164]
	BRD4_BD1	5uey	-7.426	135,3	
W137	SIRT1	4zzi	-11.031	1815,0	14800,0 [178]
	SIRT2	4zzi (Homology model)	-10.906	1842,0	14600,0 [178]
	SIRT3	4jt9	-10.33	10180,0	>100000 [178]
STX1972	CAII	1cil	-7.212	76,0	*
	CAIX	6g98	-7.225	194,0	*
	TUB	5osk	-10.712	306,0	*
	STS	1p49	-7.225	301,0	*
RXT Ruxolitinib	JAK1	3eyg	-11.061	0,2	8,8
	JAK2	6bbv	-11.089	0,1	20,7

**Data for experimental Ki/IC_{50} (nM) of STX1972 unavailable*

3.2 Cell growth studies

3.2.1 Cell growth: IC_{50} determination

Dose-dependent cell growth inhibition studies were conducted in order to determine the growth inhibitory effect of a known antimitotic: STX1972; three Bromodomain 4 inhibitors: Bzt-W41, Bzt-W49, Bzt-W52; a JAK1 and 2 inhibitor: Ruxolitinib; and a Sirtuin 1 and 2 inhibitor: W137 on the two breast cancer cell lines (MCF-7 and MDA-MB-231). Cell growth studies were carried out after 48 h exposure to the test compounds in order to observe the cell growth characteristics in response to exposure to a range of concentrations of the six compounds. An exposure time of 48 h was chosen based on the reported population doubling time of approximately 38 h for both cell lines [200,202]. A 48 h interval allows at least one complete cell division for the cells.

Both cell lines were initially treated by means of two-fold serial dilutions, followed by a compound-specific exposure concentration series (STX1972: 0 – 200 nM; Bzt-W41, Bzt-W49, Bzt-W52, W137, Ruxolitinib: 0 – 200 µM) in order to establish concentrations required for half maximal growth inhibition (IC_{50}). Growth inhibition of treated samples were compared to a medium only and vehicle-treated control (DMSO < 0.01% v/v). No significant differences in cell growth were observed between the vehicle-treated and medium only controls, implying a negligible effect of the DMSO on cell growth. Unless indicated otherwise, the values reported are expressed as the percentage of surviving cells per well relative to the DMSO control.

Dose-response curves for each compound per cell line were generated by means of nonlinear regression (curve fit) XY analysis using GraphPad Prism version 6.0 for Windows (Figure 3.9, Figure 3.10). The IC_{50} values were extrapolated using the same software by means of the log [inhibitor] versus response – variable slope equation (Table 3.3).

STX1972 proved to be the most potent of the tested compounds since it is the only compound to display efficacy in the nanomolar range with an IC_{50} concentration of 37.5 ± 0.98 nM for MDA-MB-231 and 38.4 ± 0.16 nM for the MCF-7 cells. Bzt-W41 proved to be the most effective of the BRD-4 inhibitor compounds on both MDA-MB-

231 and MCF-7 cells with a mean IC_{50} of 20.4 ± 0.82 µM and 80.3 ± 0.73 µM respectively.

The IC_{50} concentrations of each compound were compared between the two cell lines in order to identify compounds which display selective toxicity towards the MDA-MB-231 cell line (Figure 3.11). No significant difference was found in the IC_{50} of STX1972 or W137 when comparing the MCF-7 and MDA-MB-231 cells. Ruxolitinib ($p \leq 0.05$) as well as all three the BRD-4 inhibitor compounds (Bzt-W41, Bzt-W49, Bzt-W52; $P \leq 0.0001$) showed selectivity towards the MDA-MB-231 cells. Bzt-W41 proved to be the most efficacious of the BRD-4 inhibitor compounds, with significantly lower IC_{50} concentrations than those of Bzt-W49 and Bzt-W52 ($p \leq 0.0001$) for both cell lines. Although less potent than Bzt-W41, Bzt-W49 was included in the combination studies due to its selectivity towards inhibition of BRD4 over BRD2 [164]. Bzt-W49 is 10.42x more selective for BRD4 inhibition in comparison to BRD2, whereas Bzt-W41 shows 2.28x BRD4 selectivity [164]. While Ruxolitinib showed anti-growth activity in the µM concentration range, evidence suggests JAK 1 and JAK 2 kinase inhibition in the low nanomolar concentration range [236]. Exposing cells to significantly higher concentrations (>1000-fold) than required for target protein inhibition may lead to non-specific binding instead of the intended kinase-specific inhibition. For this reason, Ruxolitinib was excluded from subsequent experiments.

In summary, completion and interpretation of the cell growth inhibition data led to only the following selected compounds being investigated further in combination studies: STX1972, Bzt-W41, Bzt-W49 and W137.

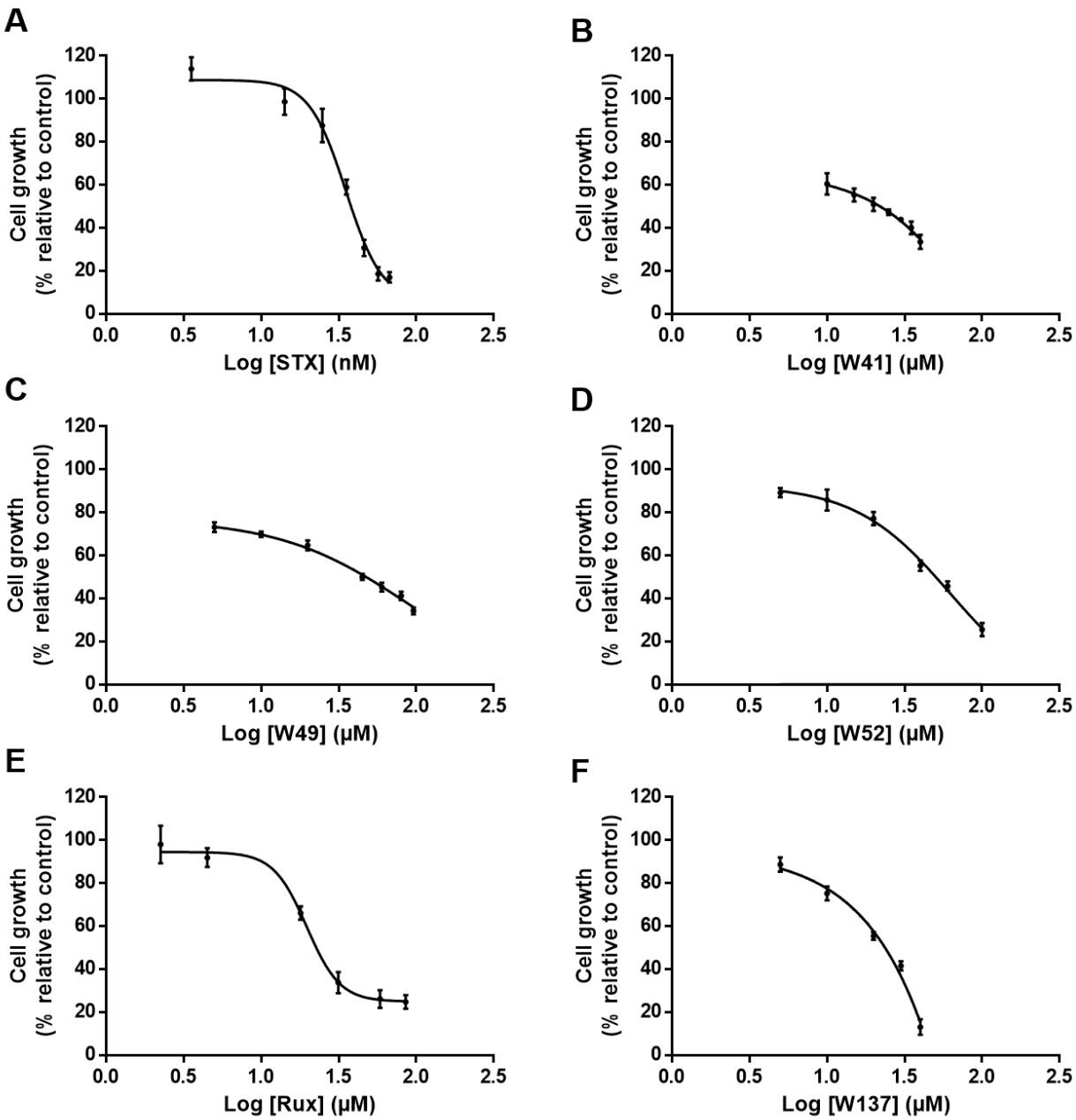

Figure 3.9: Dose-response curves of A) STX (STX1972), B) W41 (Bzt-W41), C) W49 (Bzt-W49), D) W52 (Bzt-W52), E) RUX (Ruxolitinib) and F) W137 on cell growth inhibition of MDA-MB-231 cells *in vitro*. Cell growth expressed as percentage relative to vehicle-treated control. Each point represents the mean ± SEM of at least three independent experiments done in triplicate. The IC_{50} values calculated from each dose-response curve are shown in Table 3.3. Note that the STX concentration is in nM.

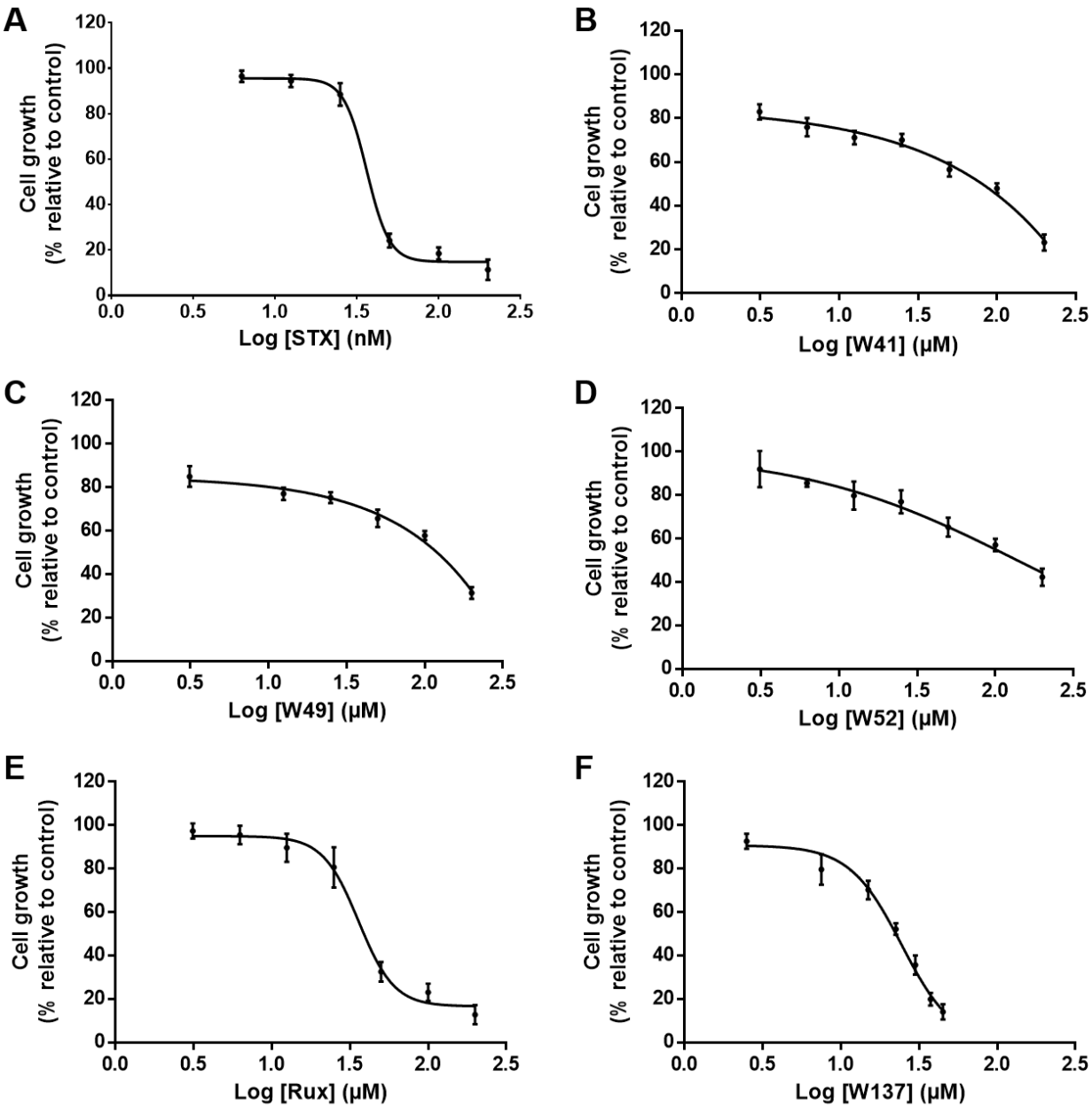

Figure 3.10: Dose- response curves of A) STX (STX1972), B) W41 (Bzt-W41), C) W49 (Bzt-W49), D) W52 (Bzt-W52), E) RUX (Ruxolitinib) and F) W137 on cell growth of MCF-7 cells *in vitro*. Cell growth expressed as percentage relative to vehicle-treated control. Each point represents the mean ± SEM of at least three independent experiments done in triplicate. The IC_{50} values calculated from each dose-response curve are shown in Table 3.3. Note that the STX concentration is in nM.

Table 3.3: Compound concentrations required for half maximal growth inhibition of MDA-MB-231 and MCF-7 cells exposed for 48 h summarized as the mean IC_{50} ± SEM.

Compound	Mean IC_{50} ± SEM	
	MDA-MB-231	MCF-7
STX1972 (nM)	37.5 ± 0.98	38.4 ± 0.16
Bzt-W41 (µM)	20.4 ± 0.82	80.3 ± 0.73
Bzt-W49 (µM)	45.0 ± 1.04	118.4 ± 1.1
Bzt-W52 (µM)	46.5 ± 1.4	139.1 ± 1.53
W137 (µM)	23.5 ± 0.28	24.1 ± 0.72
Ruxolitinib (µM)	25.2 ± 0.45	33.8 ± 1.43

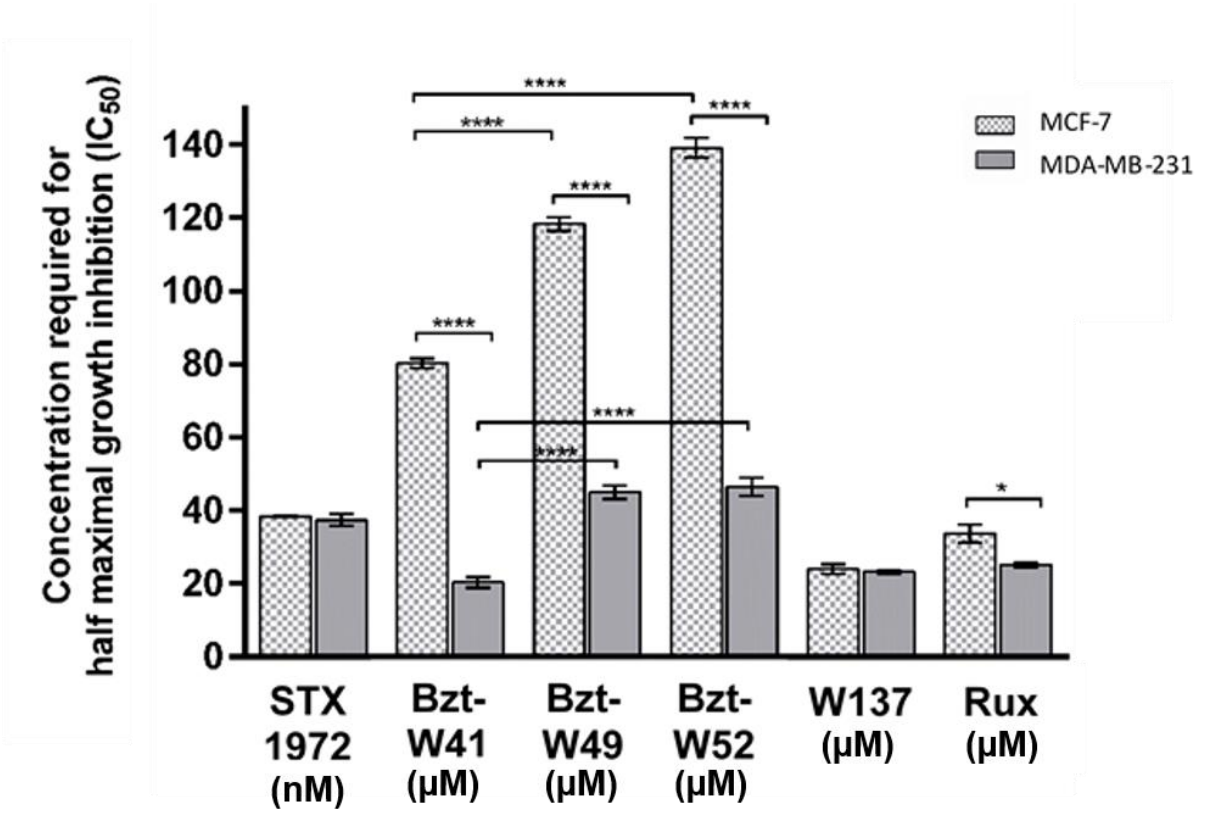

Figure 3.11: Comparison of concentrations required for half maximal growth inhibition of MCF-7 and MDA-MB-231 cells after 48 h exposure to STX1972 (nM), Bzt-W41 (µM), Bzt-W49 (µM), Bzt-W52 (µM), Rux (Ruxolitinib) (µM) and W137 (µM). Concentrations displayed are the mean IC_{50} ± SEM values (as shown in Table 3.3). * $p \leq 0.05$, **** $p \leq 0.0001$.

3.2.2 Cell growth: Inhibitor combination studies

Combination studies were based on the Chou-Talalay method for drug combinations which allows for quantification of drug-interactions [222]. The test compounds as detailed in Section 3.1.1 were grouped to into four binary combinations. Combination 1 (C1): STX1972 + Bzt-W41; combination 2 (C2): Bzt-W41 + W137; combination 3 (C3): STX1972 + W137; and combination 4 (C4): STX1972 + Bzt-W49. Since Bzt-W49 proved less potent than Bzt-W41 (Section 3.2.1), it was not included in a second combination with W137. The reason for including the less potent BRD-4 inhibitor paired with STX and not W137 is that STX has nM IC_{50} activity while W137 has µM activity. The effects on attached cell numbers of the four combinations were investigated on MDA-MB-231 and MCF-7 cell lines using the crystal violet assay.

Compounds were paired at concentrations as described in Section 2.3.3. Both cell lines were exposed to the four drug pairs in their varying combination ratios for 48 h in order to identify the most synergistic combinations (i.e. lowest CI) resulting in half maximal growth inhibition.

Figure 3.12 and Figure 3.13 summarize the best combination ratios per drug pair for MDA-MB-231 and MCF-7 cells respectively. Only the lowest CI ratios (indicating highest synergism) are displayed per cell line for each of the combinations (C1 - C4), measured as percentage cell growth relative to control.

3.2.2.1 Combination 1: STX1972 + Bzt-W41

A CI of 0.85 proved to be the lowest value showing the highest relative growth inhibition for both MDA-MB-231 and MCF-7 cell lines. For the MDA-MB-231 cell line a 0.55 + 0.3 ratio (0.55 * STX1972 [IC_{50}] + 0.3 * Bzt-W41 [IC_{50}]) was found to be the most effective, reducing cell growth to 51.16 ± 2.12% in comparison to vehicle control (Figure 3.12). Individual compound concentrations for STX1972 and Bzt-W41 at the above-mentioned fractions are 20.625 nM and 6.12 µM respectively. For the MCF-7 cells a 0.6 + 0.25 combination ratio (0.6 * STX1972 [IC_{50}] + 0.25 * Bzt-W41 [IC_{50}]) appeared to be most efficacious, reducing cell growth to 52.99 ± 1.55% (Figure 3.13). Drug concentrations for these fractions in the combination are calculated as 23.04 nM and 20.075 µM for STX1972 and Bzt-41 respectively. The most effective combination

for both cell lines contain higher concentration ratios of the antimitotic drug (STX1972) and lower concentration ratios of the BRD-4 inhibitor drug (Bzt-W41). It should be noted that although the Bzt-W41 CF is low for both cell lines, the CF concentration is derived from the IC_{50} of the compound, which in the case of Bzt-W41 is distinctly cell line specific with selectivity towards the MDA-MB-231 cell line. Therefore, even though synergism is proven for the BRD-4 inhibitor and antimitotic combination, the MCF-7 cell line is ultimately exposed to a much higher concentration of the BRD-4 inhibitor in order to achieve the same antiproliferative effect.

3.2.2.2 Combination 2: Bzt-W41 + W137

For the Bzt-W41 + W137 combination a CI of 0.9 proved most effective. Lower CI values of 0.8 and 0.85 did not reduce cell growth to the desired end-point (IC_{50}). A combination ratio of 0.7 * W137 [IC_{50}] + 0.2 * Bzt-W41 [IC_{50}] resulted in IC_{50} in both MDA-MB-231 (49.44 ± 1.25%) and MCF-7 (53.45 ± 3.35%) cell lines, seen in Figure 3.12 and Figure 3.13 respectively. The exposure concentration of W137 at a CF of 0.7 for MDA-MB-231 and MCF-7 cells equals 16.45 µM and 16.87 µM respectively. A CF of 0.2 for Bzt-W41 corresponds to treatment concentrations of 4.08 µM and 16.06 µM for MDA-MB-231 and MCF-7 cells respectively. For the Bzt-W41 + W137 pair, it was evident that combining a higher concentration of the sirtuin inhibitor (W137) with a lower concentration of the BRD-4 inhibitor (Bzt-W41) led to the best inhibitory drug interaction.

3.2.2.3 Combination 3: STX1972 + W137

The STX1972 + W137 combination did not successfully reduce cell growth to 50%, even at the highest tested CI of 0.95 (i.e. least pronounced synergistic drug interaction) and regardless of the combination ratios applied (Figure 3.12 and Figure 3.13). This implies that the combined drug treatment of the antimitotic (STX1972) and sirtuin inhibitor (W137) has either additive (CI = 1) or antagonistic (CI > 1) effect. Since the aim was to identify synergistic drug interactions, this combination was not explored further.

3.2.2.4 Combination 4: STX1972 + Bzt-W49

The STX1972 + Bzt-W49 combination showed sufficient synergism in both cell lines at a CI of 0.85. For the MDA-MB-231 cell line a 0.55 + 0.3 combination ratio (0.55 * STX1972 [IC_{50}] + 0.3 * Bzt-W49 [IC_{50}]) resulted in a growth inhibition effect of 59.49 ± 6.99% (Figure 3.12). Individual drug concentrations at these CFs amounts to 20.625 nM for STX1972 and 13.5 µM for Bzt-W49. A ratio 0.6 + 0.25 (0.6 * STX1972 [IC_{50}] + 0.25 * Bzt-W49 [IC_{50}]) was found to be most effective against the MCF-7 cell line (Figure 3.13). These CFs, at individual concentrations of 23.04 nM for STX1972 and 29.6 µM for Bzt-W49, inhibited cell growth to 53.39 ± 2.66%.

Based on the results it was concluded that C1 (STX1972 + Bzt-W41) and C2 (Bzt-W41 + W137) would be included in further experiments. Although C4 (STX1972 + Bzt-W49) did show synergism, it was decided to continue with the Bzt-W41 combination based on its selectivity towards the MDA-MB-231 cell line. C3 (STX1972 + W137) was also omitted from further experimental procedures since combined drug interactions did not prove to be synergistic.

Regarding the combination ratios of C1 and C2, it was concluded that C1 at a CF ratio of 0.55 * STX1972 [IC_{50}] combined with 0.3 * Bzt-W41 [IC_{50}]; and C2 at a CF ratio of 0.7 * W137 [IC_{50}] and 0.2 * Bzt-W41 [IC_{50}] would be included in further investigation (Figure 3.14). These were the most effective ratios on the MDA-MB-231 cell line, implying MDA-MB-231 selectivity. Unless indicated otherwise, all further data represents effects of C1 at individual drug concentrations of 20.625 nM for STX1972 and 6.12 µM for Bzt-W41; and C2 at drug concentrations of 16.45 µM for W137 and 4.08 µM for Bzt-W41.

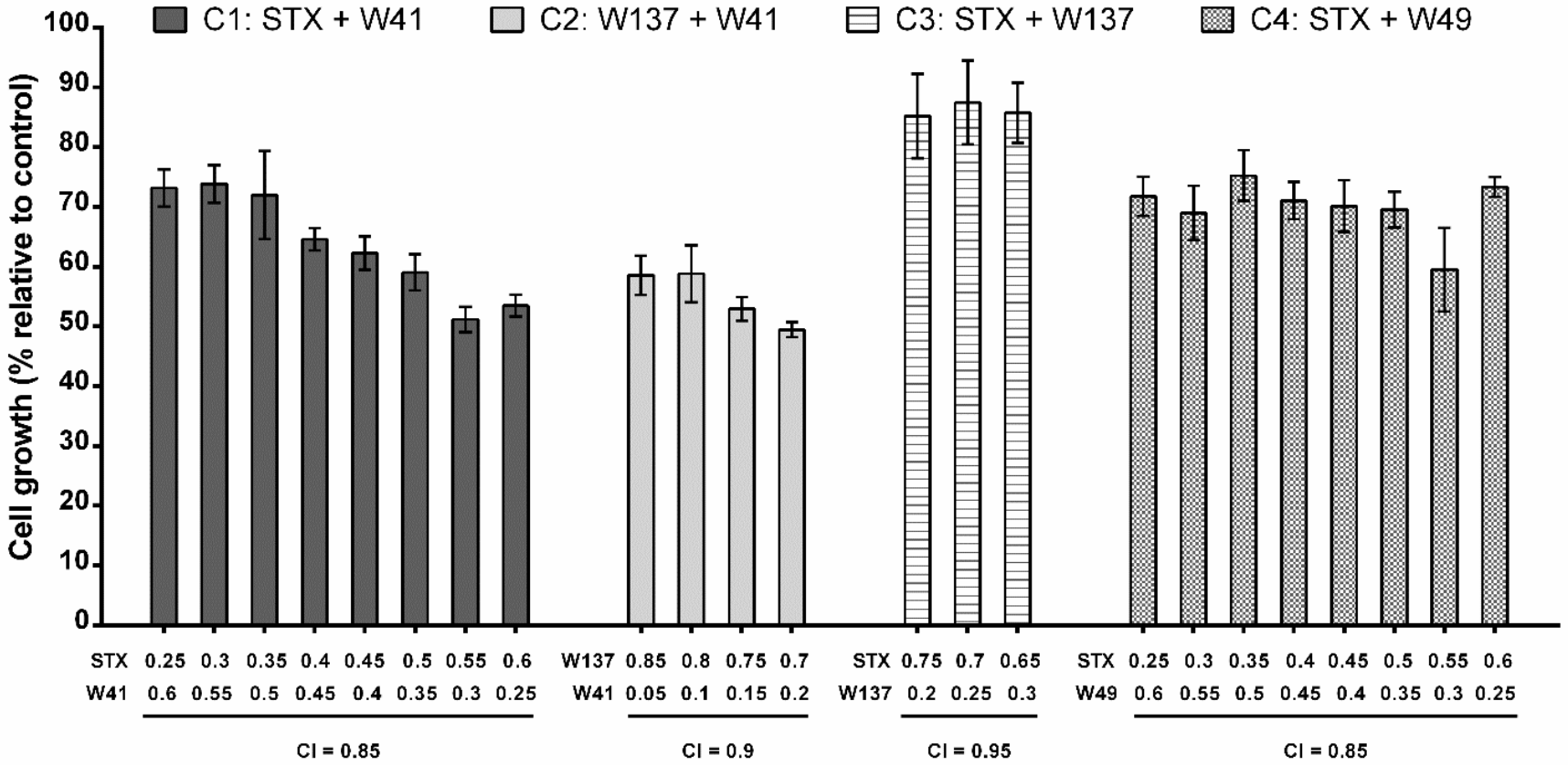

Figure 3.12: Relative cell growth inhibition of MDA-MB-231 cells after 48 h exposure to four combinations (C1:STX1972 + Bzt-W41; C2: Bzt-W41 + W137; C3: STX1972 + W137; C4: STX1972 + Bzt-W49) in a series of compound ratios with CI < 1. Cell growth expressed as percentage relative to vehicle-treated control. Ratios on the X-axis refer to the CF per compound. The CFs are summed to calculate the CI. Exposure concentration is calculated as CF * IC_{50} of compound. STX = STX1972, W41 = Bzt-W41; W49 = Bzt-W49

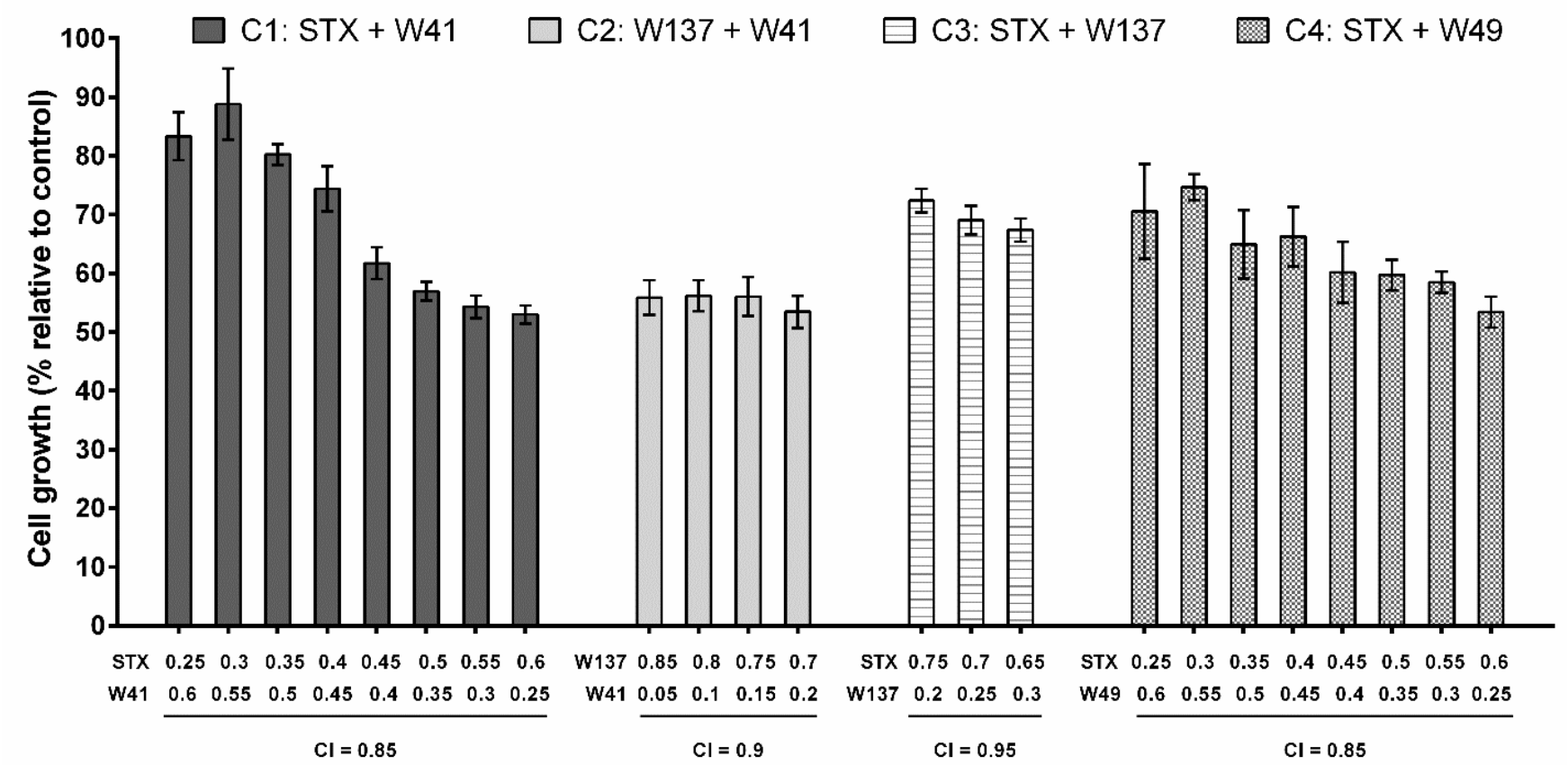

Figure 3.13: Relative cell growth inhibition of MCF-7 cells after 48 h exposure to four combinations (C1:STX1972 + Bzt-W41; C2: Bzt-W41 + W137; C3: STX1972 + W137; C4: STX1972 + Bzt-W49) in a series of compound ratios with CI < 1. Cell growth expressed as percentage relative to vehicle-treated control. Ratios on the X-axis refer to the CF per compound. The CFs are summed to calculate the CI. Exposure concentration is calculated as CF * IC_{50} of compound. STX = STX1972, W41 = Bzt-W41; W49 = Bzt-W49.

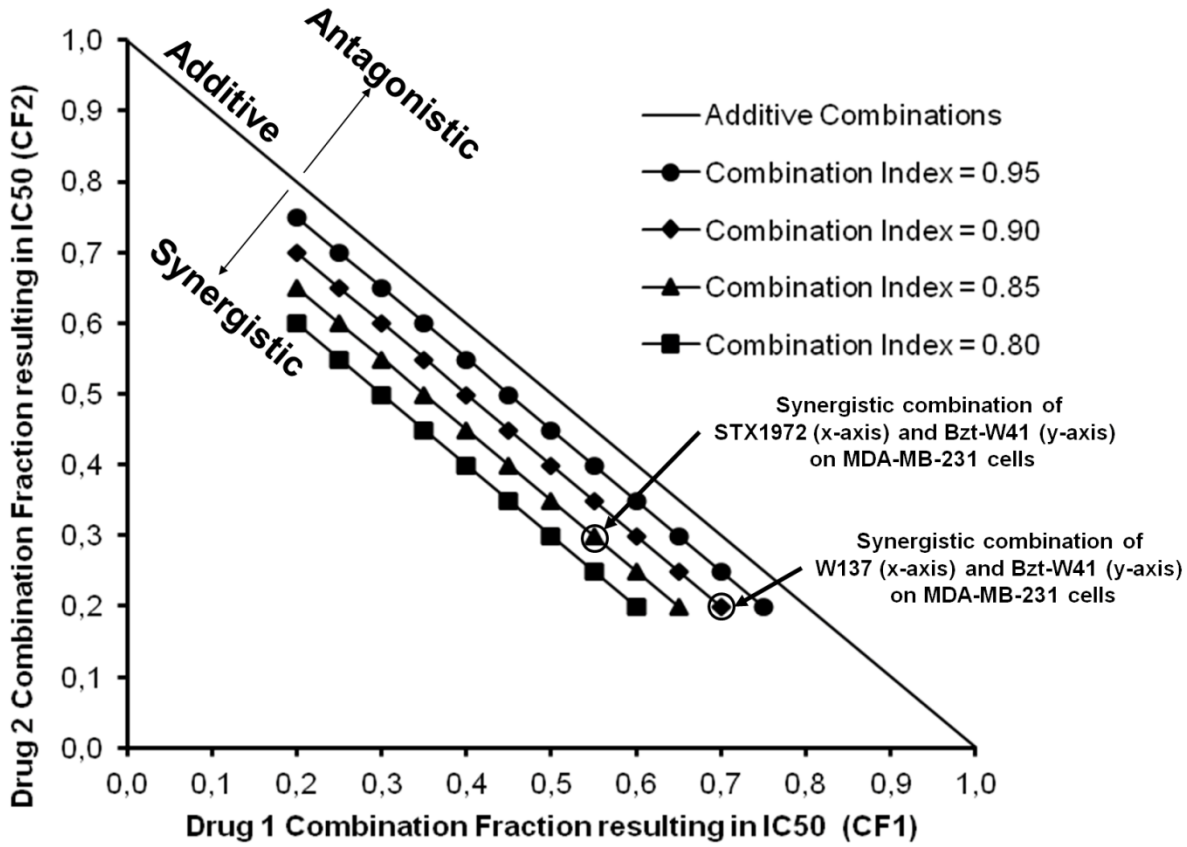

Figure 3.14: Normalized isobologram at IC_{50}. Showing the synergistic combinations. A synergistic, CI of 0.85 and 0.9 was identified for STX1972 (0.55, x-axis) + Bzt-W41 (0.3, y-axis) and W137 (0.7, x-axis) + Bzt-W41 (0.2, y-axis) combinations respectively.

3.2.3 Cell growth: Selectivity of inhibitor combinations

As deduced from the results of the combination studies, only C1 and C2 would be included in further experiments. Therefore, only the three drugs included in these combinations were further investigated, namely STX1972, Bzt-W41 and W137. All further experiments were conducted with the single drug IC_{50} concentrations (Section 3.2.1), and the combination treatment concentrations (Section 3.2.3) most selective for the MDA-MB-231 cell line. In order to compare relative cell growth inhibition, both the MCF-7 and EA.hy926 cell lines were exposed to these concentrations (Figure 3.15).

No significant selectivity was seen between MDA-MB-231 and MCF-7 cell lines following treatment with single drug IC_{50} concentrations of STX1972 and W137. However, Bzt-W41 treatment did show to be significantly more selective towards the MDA-MB-231 cell line in comparison to MCF-7. Since treatment conditions were standardized to concentrations determined for the MDA-MB-231 cell line, it implies that the MCF-7 cells were treated with much lower concentrations of Bzt-W41 (as required for IC_{50}), but similar concentrations of STX1972 and W137. Exposure to the IC_{50} concentrations of STX1972, Bzt-W41 and W137 resulted in significantly reduced antiproliferation in EA.hy926 cells when compared to MDA-MB-231 cells, with Bzt-W41 showing the most pronounced selectivity for the MDA-MB-231 cell line. Both of the combination treatments: STX + Bzt-W41 and Bzt-W41 + W137 proved significantly more selective towards the MDA-MB-231 cell line in comparison to both the MCF-7 and EA.hy926 cell lines.

The antiproliferative effects of the test compounds and their combinations is summarised in Figure 3.15. Since CF concentrations only constitute a fraction of the single drug IC_{50} concentration, CF exposures proved significantly less effective at reducing cell growth when compared to the corresponding IC_{50} treatment within the cell line. Significance was seen throughout, with the exception of the Bzt-W41 CF exposure in the EA.hy926 cell line, which did not differ significantly when compared to the Bzt-W41 IC_{50} treatment.

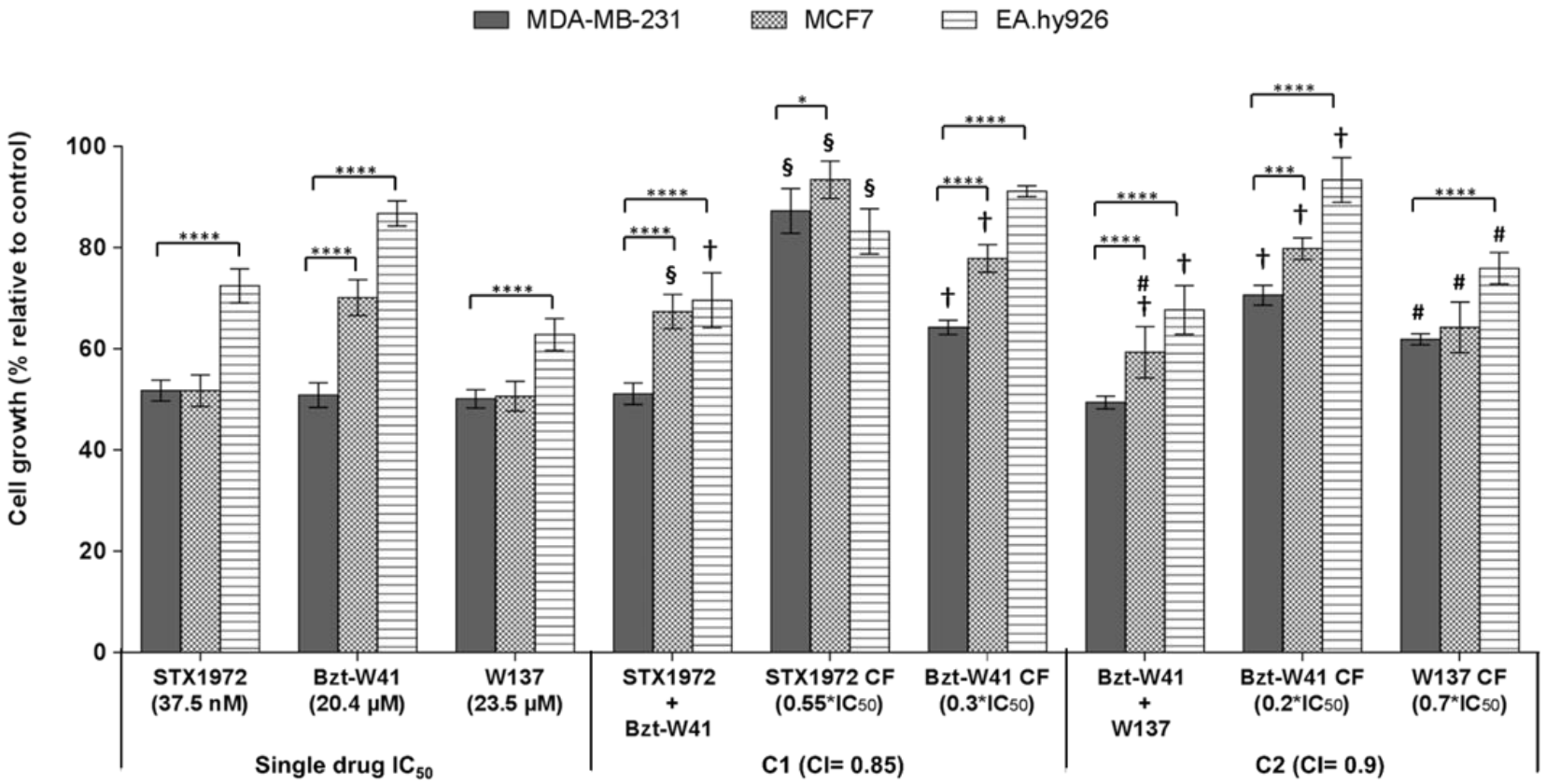

Figure 3.15: Comparison of relative cell growth inhibition of MDA-MB-231, MCF-7 and EA.hy926 cell lines after 48 h exposure to single compounds at their IC_{50} concentrations or test compound combination treatments at concentrations most selective for MDA-MB-231 cells. C1 at a CF ratio of 0.55 * STX1972 [IC_{50}] combined with 0.3 * Bzt-W41 [IC_{50}], CI = 0.85; and C2 at a CF ratio of 0.7 * W137 [IC_{50}] and 0.2 * Bzt-W41 [IC_{50}], CI = 0.7. Individual effect of treatment with each compounds' CF concentration, as used in the binary combinations, is also reported. C1: STX1972 [CF] = 20.625 nM; Bzt-W41 [CF] = 6.12 µM. C2: Bzt-W41 [CF] = 4.08 µM; W137 [CF] = 16.45 µM. * $p \leq 0.05$, *** $p \leq 0.001$, **** $p \leq 0.0001$ indicates significant difference when compared to MDA-MB-231 cell line; § $p \leq 0.05$ when compared to STX1972 IC_{50} within the cell line; † $p \leq 0.05$ when compared to Bzt-W41 IC_{50} within the cell line; # $p \leq 0.05$ when compared to W137 IC_{50} within the cell line.

3.3 Tubulin morphology

Confocal microscopy was used to determine whether the antimitotic drug STX1972 disrupts normal microtubule dynamics similar to that of other tubulin-binding agents, such as colchicine. Cells were treated with STX1972 as well as the STX + Bzt-W41 combination to observe morphological differences induced by the individual and combinations of the test compounds following 8 h exposure. Microtubule staining of beta-tubulin subunits was done using a primary anti-β-tubulin antibody, counter stained with a secondary fluorescein-conjugated antibody (green fluorescence), while nuclei were stained with DAPI (blue fluorescence). Figure 3.16, Figure 3.17 and Figure 3.18 are representative confocal micrographs of the results obtained for the MDA-MB-231, MCF-7 and EA.hy926 cell lines respectively.

Vehicle-treated control MDA-MB-231, MCF-7 and EA.hy926 cells presented with normal, intact tubulin architecture signified by intact spindle formations. After 8 h exposure to test compound, microtubule interference evident by the diffuse arrangement of the stained tubulin proteins was apparent in both MCF-7 and MDA-MB-231 cells, mimicking the effects of the colchicine (100 nM), the positive control for microtubule interference. Decreased tubulin polymerization was seen in both MCF-7 and MDA-MB-231 cell lines for the STX1972 and STX + Bzt-W41 treated samples, although less obvious in the latter. For the EA.hy926 cells, no microtubule disruption is evident and spindle fibres remained intact.

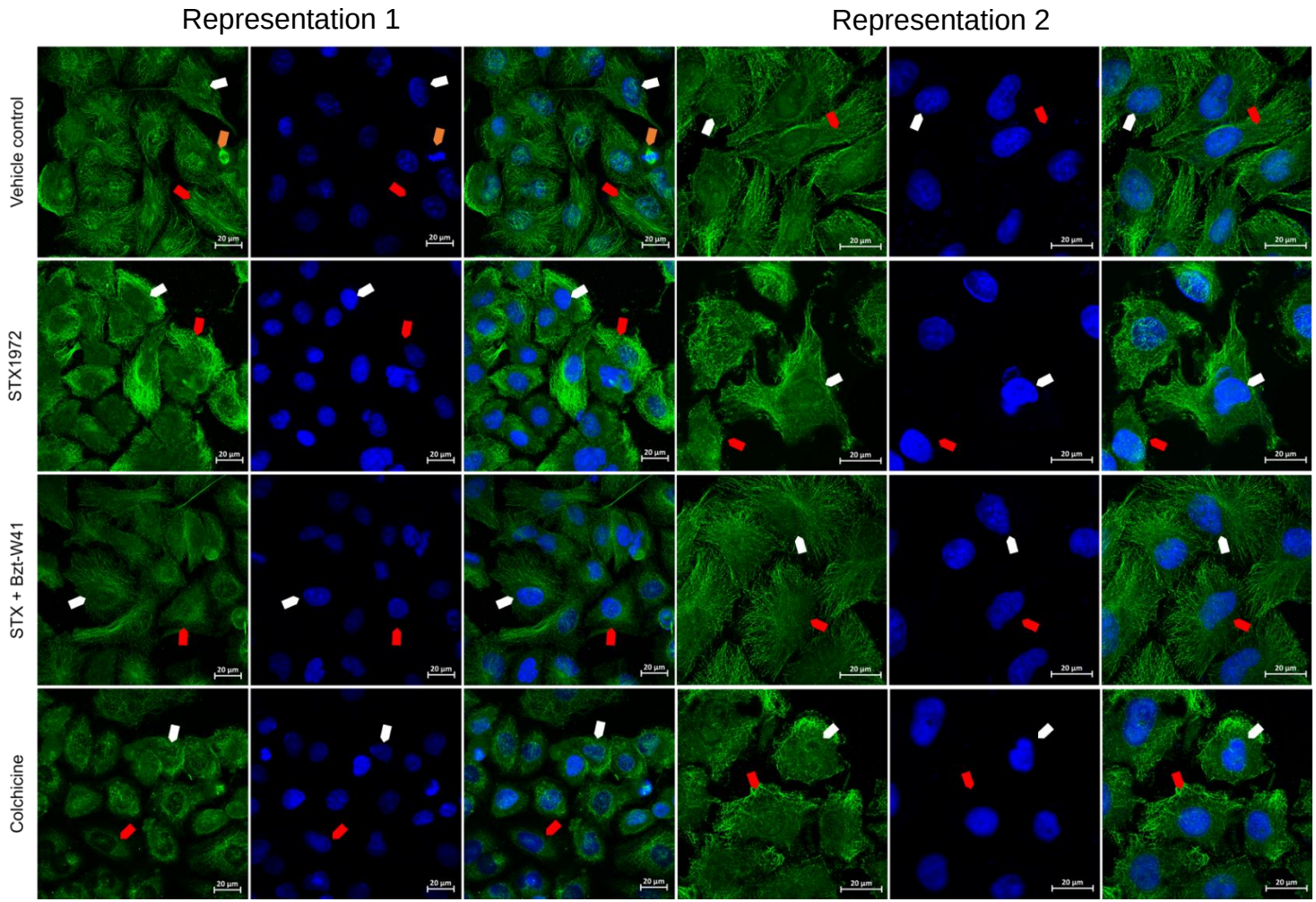

Figure 3.16: Laser scanning confocal micrographs of MDA-MB-231 cells stained with DAPI (blue - nuclei) and anti-β-tubulin (green) after 8 h exposure. Vehicle treated cells displayed no evidence of microtubule disruption and spindle fibres remained intact. Cells treated with STX1972 IC_{50} (37.5 nM) and the STX + Bzt-W41 combination (STX1972 [CF] = 20.625 nM; Bzt-W41 [CF] = 6.12 µM) showed evidence of microtubule disruption similar to that of colchicine-treated (100 nM) positive control sample. Representation 1 magnification 400x; representation 2 magnification 630x. (Arrow colour key: white = nucleus; orange = metaphase; red = microtubules, organized and intact in the vehicle control, and depolymerized in treated samples).

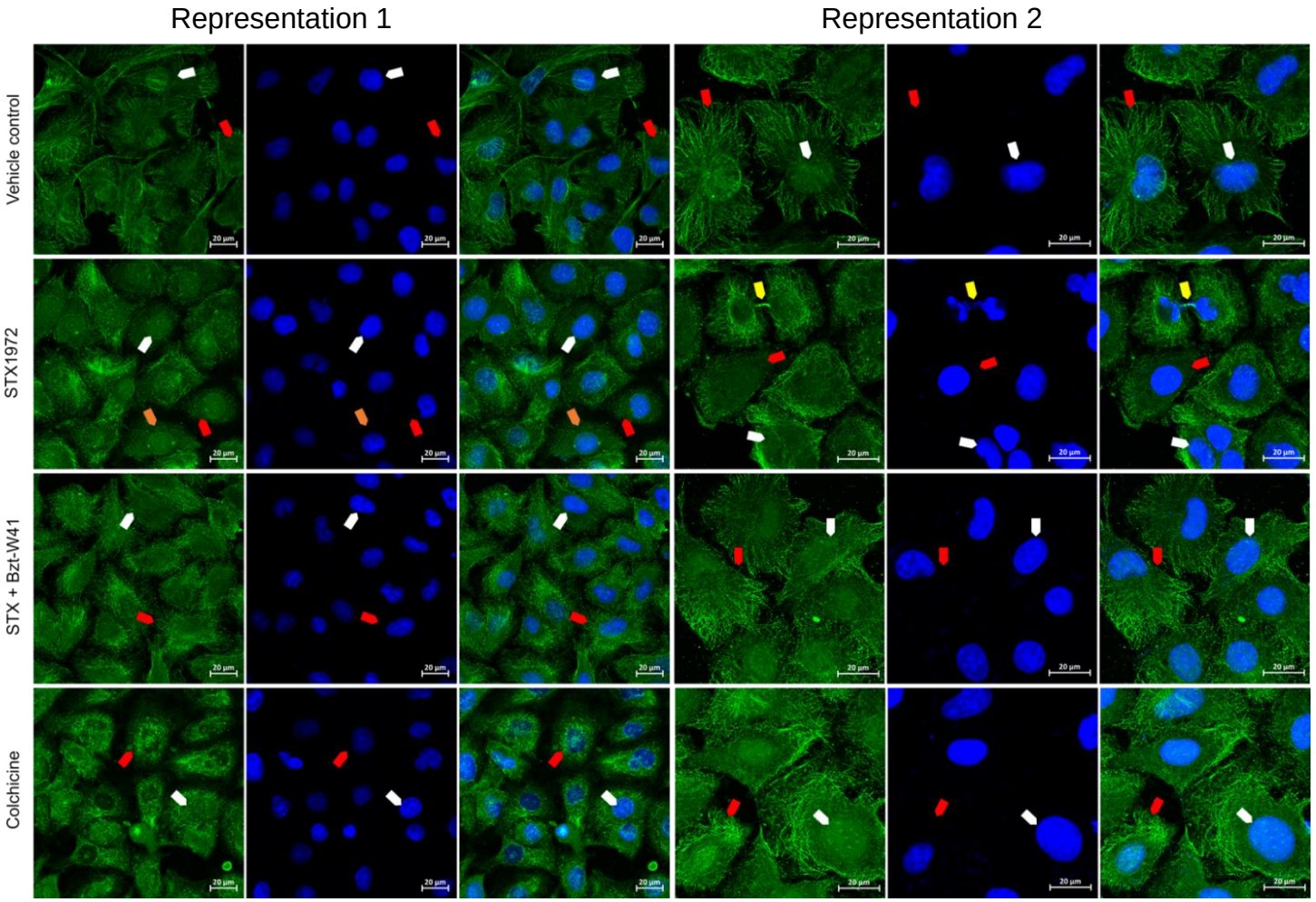

Figure 3.17: Laser scanning confocal micrographs of MCF-7 cells stained with DAPI (blue) and anti-β-tubulin (green) after 8 h exposure. Vehicle treated cells displayed no evidence of microtubule disruption and spindle fibres remained intact. Cells treated with STX1972 IC_{50} (37.5 nM) and the STX + Bzt-W41 combination (STX1972 [CF] = 20.625 nM; Bzt-W41 [CF] = 6.12 µM) showed evidence of microtubule disruption similar to that of colchicine-treated (100 nM) positive control sample. Representation 1 magnification 400x; representation 2 magnification 630x. (Arrow colour key: white = nucleus; orange = prophase; yellow: midbody; red = microtubules, organized and intact in the vehicle control, and depolymerized in treated samples).

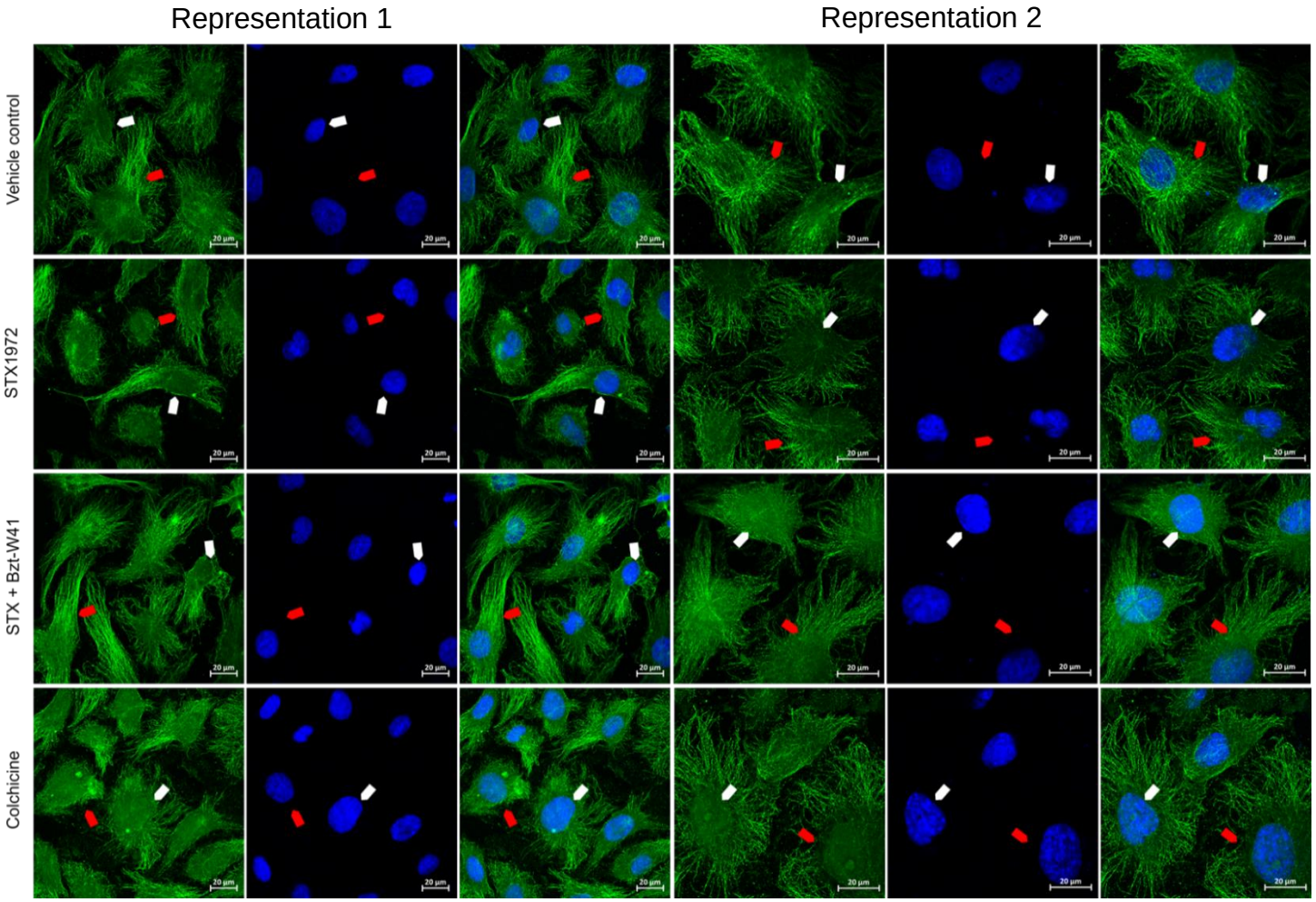

Figure 3.18: Laser scanning confocal micrographs of EA.hy926 cells stained with DAPI (blue) and anti-β-tubulin (green) after 8 h exposure. Vehicle treated cells as well as samples exposed to STX1972 IC_{50} (37.5 nM) and the STX + Bzt-W41 combination (STX1972 [CF] = 20.625 nM; Bzt-W41 [CF] = 6.12 µM) displayed no evidence of microtubule disruption and spindle fibres remained intact. Cells treated with 100 nM colchicine (positive control) showed evidence of microtubule disruption. Representation 1 magnification 400x; representation 2 magnification 630x. (Arrow colour key: white = nucleus; red = microtubules, organized and intact in the vehicle control treated samples, and depolymerized in colchicine treated samples).

3.4 Cell cycle progression

DNA content of cells was measured at 8 h and 48 h to determine the effect of STX1972 at IC_{50} (37.5 nM), Bzt-W41 at IC_{50} (20.4 µM), W137 at IC_{50} (23.5 µM), STX + Bzt-W41 combination (STX1972 [CF] = 20.625 nM; Bzt-W41 [CF] = 6.12 µM), and Bzt-W41 + W137 combination (Bzt-W41 [CF] = 4.08 µM; W137 [CF] = 16.45 µM) on cell cycle progression at specific phases. Actinomycin D (0.2 µg/mL µM) was used as positive control. Figure 3.19, Figure 3.20 and Figure 3.21 illustrate time-dependent flow cytometry histograms for MDA-MB-231, MCF-7 and EA.hy926 cell lines respectively. Quantitative representations of 8 h and 48 h cell cycle data for each cell line comparing the different treatment conditions to the vehicle control is displayed in Figure 3.22, Figure 3.23 and Figure 3.24. Table 3.4, Table 3.5 and Table 3.6 display mean ± SEM values for cell cycle phases per cell line.

For the MDA-MB-231 cell line a significant increase in sub-G_1 is evident after 48 h treatment with both STX1972 (10.33 ± 1.75%) and W137 (23.28 ± 7.07%), when compared to that of the vehicle control (3.08 ± 0.66%) (Figure 3.19, Figure 3.22 and Table 3.4). The sub-G_1 increase is already notable for W137-treated cells after 8 h exposure, significantly increased to 9.23 ± 0.44% compared to that of vehicle control (2.23 ± 0.48%) (Figure 3.19, Figure 3.22 and Table 3.4). After 8 h exposure to STX1972 and the STX + Bzt-W41 combination the G_2/M phase is respectively increased to 47.39 ± 1.99% and 39.50 ± 1.51%, significantly higher than that of the vehicle control (29.89 ± 3.07%) (Figure 3.19, Figure 3.22 and Table 3.4). This indicates that the antimitotic effects of STX1972 are evident after 8 h exposure. The G_2/M phase was also significantly increased after 48 h exposure to STX1972 (22.98 ± 0.43%) and the Bzt-W41 + W137 combination (26.21 ± 1.13%). For the G_1 phase, following 48 h exposure to the STX + Bzt-W41 combination showed significant increase (72.47 ± 1.63%) compared to the vehicle control (57.32 ± 1.67%). Bzt-W41 exposed cells showed an evident but non-significant increase (64.31 ± 3.47%), while W137-treated cells were found to be significantly decreased (36.62 ± 4.35%) in the G_1 phase (Figure 3.19, Figure 3.22 and Table 3.4).

For the MCF-7 cell line, W137-treated cells once again proved the most prominent increase in sub-G_1 after 8 h (6.67 ± 1.67%) and 48 h (27.91 ± 8.97%) exposure, significantly increased compared to the vehicle control (1.07 ± 0.15% (8 h); 4.12 ± 0.34% (48 h)) (Figure 3.20, Figure 3.23 and Table 3.5). After 8 h treatment with STX1972 the cells showed a significant increase in the G_2/M phase (44.96 ± 0.90%), mirroring results from the MDA-MB-231 cells and signifying cytotoxic effect at this time point. However, only the Bzt-W41 + W137 combination treated cells showed a significant G_2/M increase (22.49 ± 1.05%) after 48 h treatment. There was no significant increase in the G_1 phase for any of the treatment conditions after 48 h exposure. However, W137-treated cells again showed a significant decrease (40.79 ± 3.71%) compared to the vehicle control sample (69.83 ± 3.9%) (Figure 3.20, Figure 3.23 and Table 3.5).

For the EA.hy926 cell line 8 h treatment with W137 and the Bzt-W41 + W137 combination significantly increased sub-G_1 to 8.57 ± 1.04% and 9.45 ± 1.03% respectively, while W137 treatment also resulted in a significant decrease in G_2/M (8.99 ± 2.38%) (Figure 3.21, Figure 3.24 and Table 3.6). After 48 treatment, the only notable difference was a significant decrease in G_1 (64.21 ± 2.08%) for the STX+ Bzt-W41 combination treated sample (Figure 3.21, Figure 3.24 and Table 3.6).

The effects of single compound IC_{50} treatment was compared to combination treatment within a cell line for a respective phase (Figure 3.25). From the MDA-MB-231 cell line comparisons it is evident that the STX + Bzt-W41 combination treatment resulted in a significant increase in the G_1 cell cycle phase (72.47 ± 1.63%) when compared to isolated STX1972 IC_{50} exposure (56.83 ± 1.87%). Although non-significant, the G_1 arrest seen for combination treatment was also evidently higher than of Bzt-W41 mono-treatment (64.31 ± 3.47%). The Bzt-W41 + W137 combination treatment led to a significantly reduced percentage of cells in the sub-G_1 phase when compared to single drug treatment with W137 in MDA-MB-231 (2.01 ± 25% versus 23.28 ± 7.07%) and MCF-7 (6.37 ± 0.85% versus 27.91 ± 8.97%) cells.

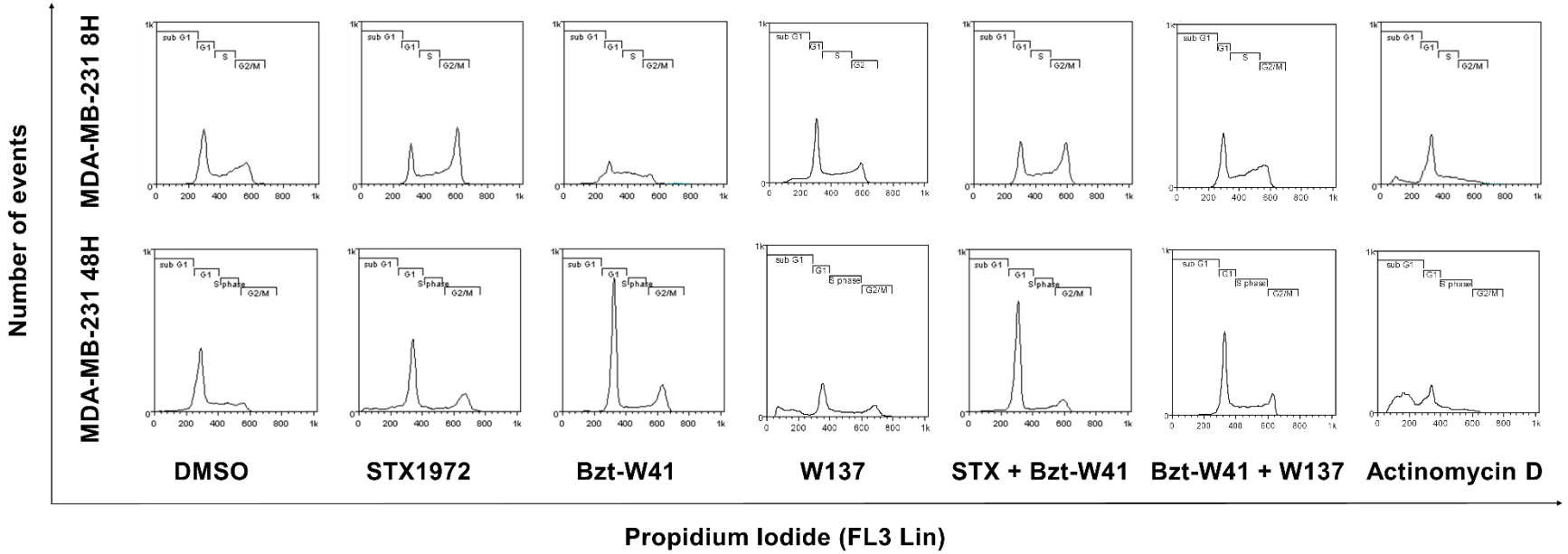

Figure 3.19: Flow cytometry histograms for cell cycle analysis in MDA-MB-231 cells. Cells in the different phases of the cell cycle (sub-G_1, G_1, S and G_2/M) were analysed using WEASEL v3.0.2 software. The results show the cell cycle progression after 8 h and 48 h treatment with STX1972 at IC_{50} (37.5 nM), Bzt-W41 at IC_{50} (20.4 µM), W137 at IC_{50} (23.5 µM), STX + Bzt-W41 combination (STX1972 [CF] = 20.625 nM; Bzt-W41 [CF] = 6.12 µM), and Bzt-W41 + W137 combination (Bzt-W41 [CF] = 4.08 µM; W137 [CF] = 16.45 µM). Actinomycin D (0.2 µg/mL) was used as positive control.

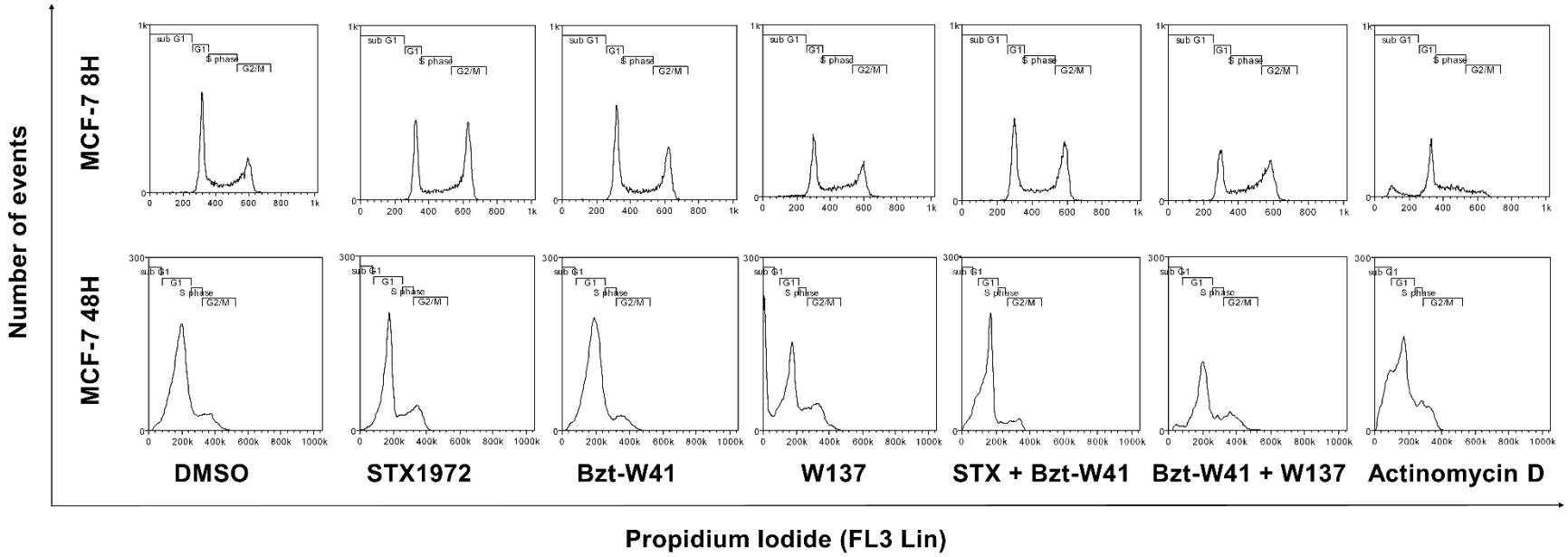

Figure 3.20: Flow cytometry histograms for cell cycle analysis in MCF-7 cells. Cells in the different phases of the cell cycle (sub-G_1, G_1, S and G_2/M) were analysed using WEASEL v3.0.2 software. The results show the cell cycle progression after 8 h and 48 h treatment with STX1972 at IC_{50} (37.5 nM), Bzt-W41 at IC_{50} (20.4 µM), W137 at IC_{50} (23.5 µM), STX + Bzt-W41 combination (STX1972 [CF] = 20.625 nM; Bzt-W41 [CF] = 6.12 µM), and Bzt-W41 + W137 combination (Bzt-W41 [CF] = 4.08 µM; W137 [CF] = 16.45 µM). Actinomycin D (0.2 µg/mL) was used as positive control.

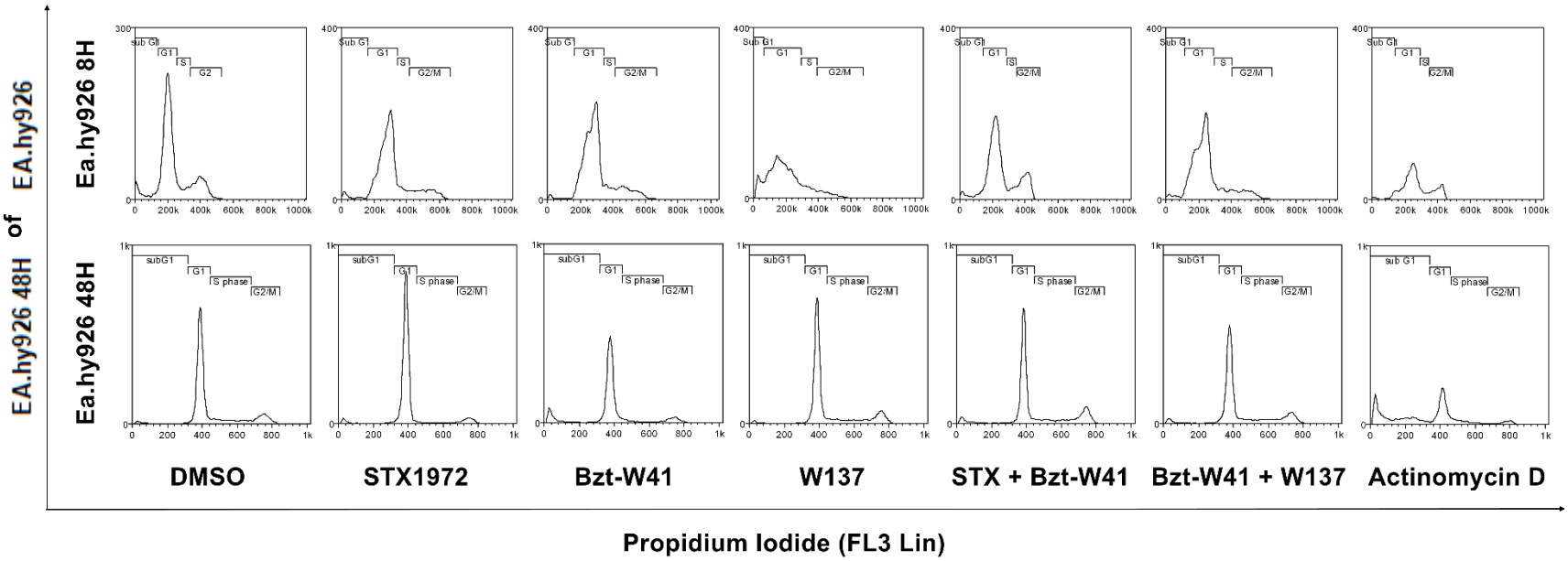

Figure 3.21: Flow cytometry histograms for cell cycle analysis in EA.hy926 cells. Cells in the different phases of the cell cycle (sub G1, G1, S and G2/M) were analysed using WEASEL v3.0.2 software. The results show the cell cycle progression after 8 h and 48 h treatment with STX1972 IC_{50} (37.5 nM), Bzt-W41 IC_{50} (20.4 µM), W137 IC_{50} (23.5 µM), STX + Bzt-W41 combination (STX1972 [CF] = 20.625 nM; Bzt-W41 [CF] = 6.12 µM), and Bzt-W41 + W137 combination (Bzt-W41 [CF] = 4.08 µM; W137 [CF] = 16.45 µM). Actinomycin D (0.2 µg/mL) was used as positive control.

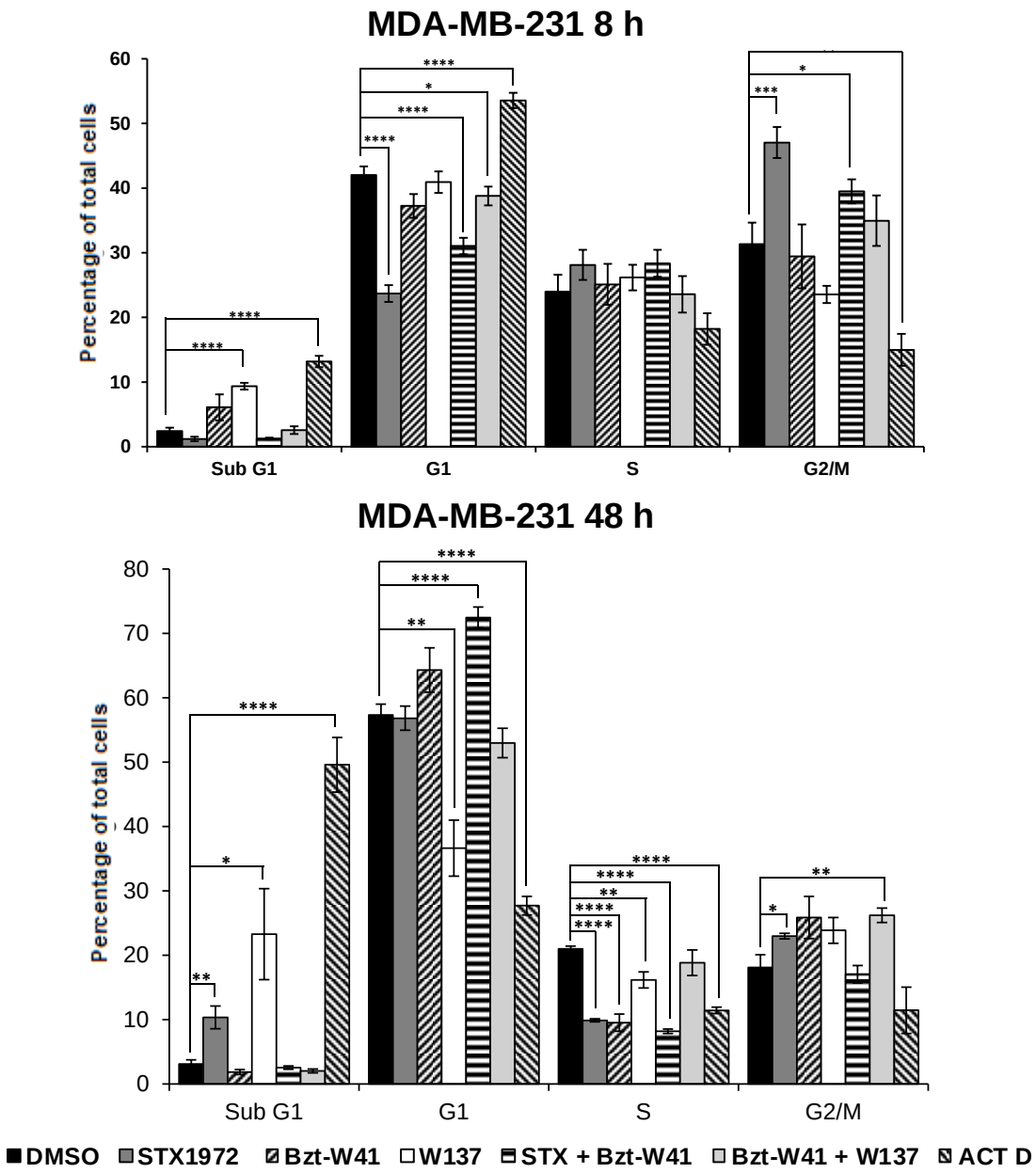

Figure 3.22: Quantitative representation of percentage of MDA-MB-231 cells in the different phases of the cell cycle (sub-G_1, G_1, S and G_2/M) in response to 8 h and 48 h treatment with STX1972 at IC_{50} (37.5 nM), Bzt-W41 at IC_{50} (20.4 µM), W137 at IC_{50} (23.5 µM), STX + Bzt-W41 combination (STX1972 [CF] = 20.625 nM; Bzt-W41 [CF] = 6.12 µM), and Bzt-W41 + W137 combination (Bzt-W41 [CF] = 4.08 µM; W137 [CF] = 16.45 µM). Actinomycin D (0.2 µg/mL) was used as positive control. The bar graphs represent the mean ± SEM values averaged from three biological replicates for each treatment condition. *p ≤ 0.05, **p ≤ 0.01, ***p ≤ 0.001, ****p ≤ 0.0001 indicate significant differences between the vehicle control and treatment groups within the respective phase.

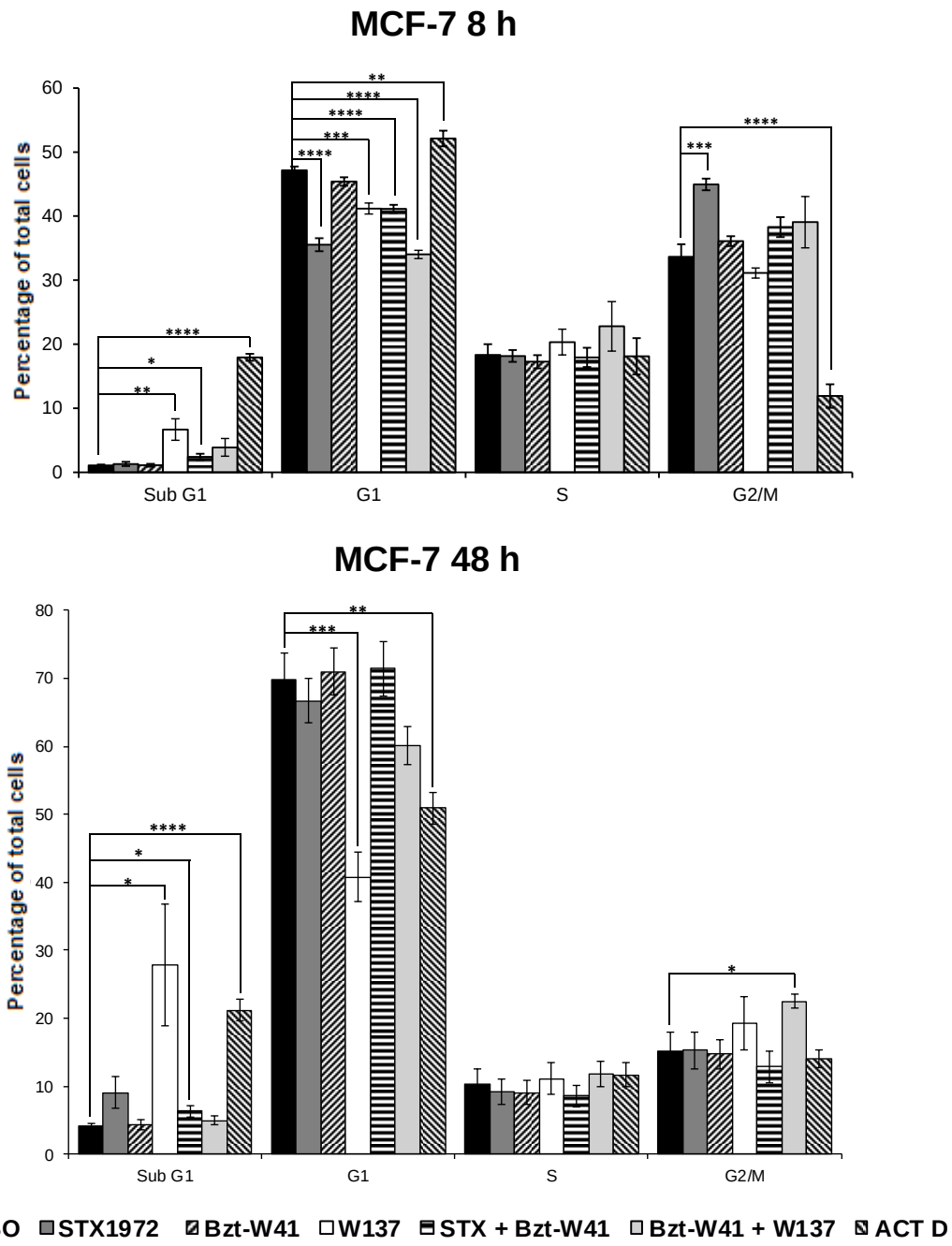

Figure 3.23: Quantitative representation of percentage of MCF-7 cells in the different phases of the cell cycle (sub-G_1, G_1, S and G_2/M) in response to 8 h and 48 h treatment with STX1972 at IC_{50} (37.5 nM), Bzt-W41 at IC_{50} (20.4 µM), W137 at IC_{50} (23.5 µM), STX + Bzt-W41 combination (STX1972 [CF] = 20.625 nM; Bzt-W41 [CF] = 6.12 µM), and Bzt-W41 + W137 combination (Bzt-W41 [CF] = 4.08 µM; W137 [CF] = 16.45 µM). Actinomycin D (0.2 µg/mL) was used as positive control. The bar graphs represent the mean ± SEM values averaged from three biological replicates for each treatment condition. *p ≤ 0.05, **p ≤ 0.01, ***p ≤ 0.001, ****p ≤ 0.0001 indicate significant differences between the vehicle control and treatment groups within the respective phase.

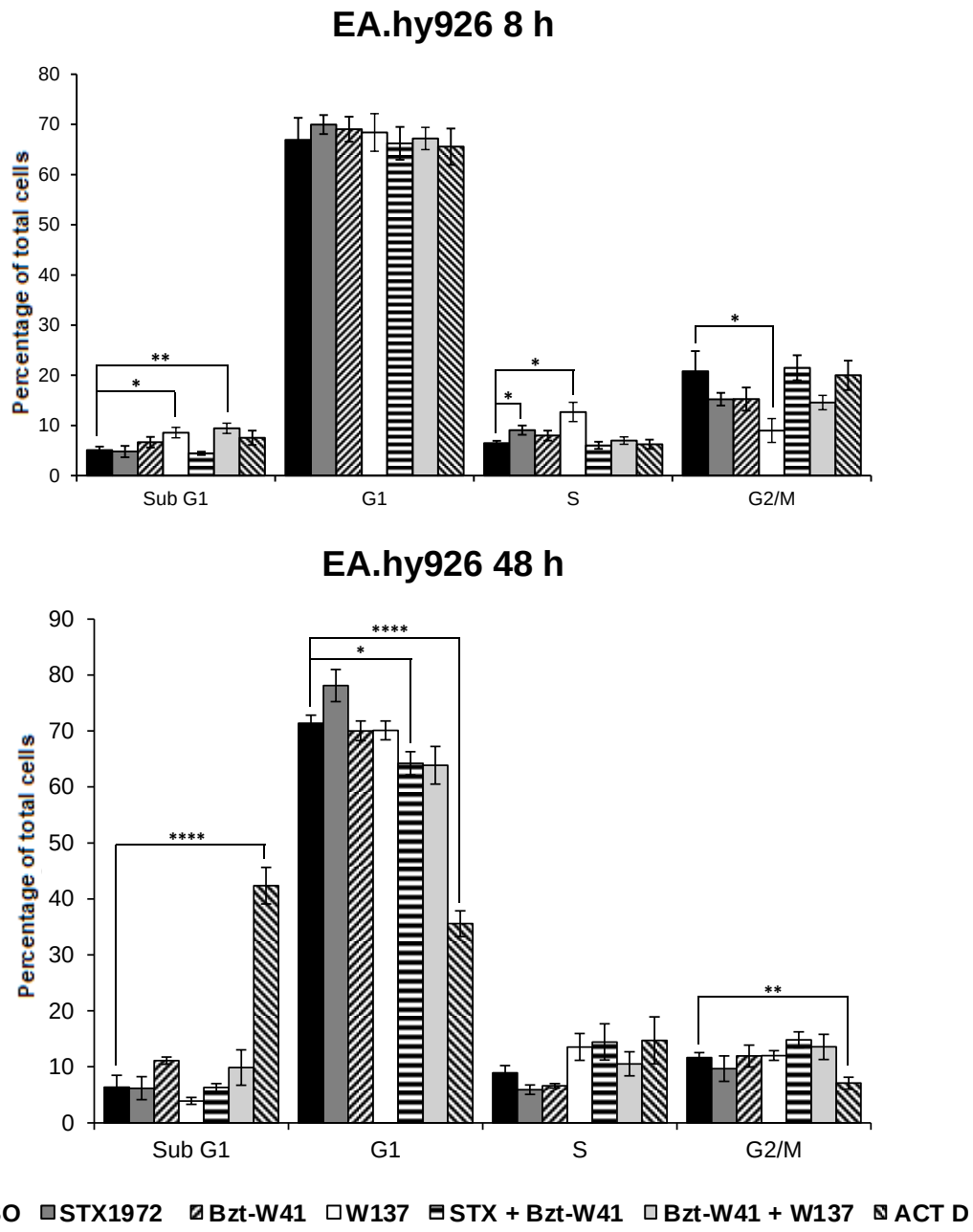

Figure 3.24: Quantitative representation of percentage of EA.hy926 cells in the different phases of the cell cycle (sub-G_1, G_1, S and G_2/M) in response to 8 h and 48 h treatment with STX1972 at IC_{50} (37.5 nM), Bzt-W41 at IC_{50} (20.4 µM), W137 at IC_{50} (23.5 µM), STX + Bzt-W41 combination (STX1972 [CF] = 20.625 nM; Bzt-W41 [CF] = 6.12 µM), and Bzt-W41 + W137 combination (Bzt-W41 [CF] = 4.08 µM; W137 [CF] = 16.45 µM). Actinomycin D (0.2 µg/mL) was used as positive control. The bar graphs represent the mean ± SEM values averaged from three biological replicates for each treatment condition. *p ≤ 0.05, **p ≤ 0.01, ****p ≤ 0.0001 indicate significant differences between the vehicle control and treatment groups within the respective phase.

Table 3.4: Percentage of MDA-MB-231 cells in the different phases of the cell cycle (sub G_1, G_1, S and G_2/M) after 8 h and 48 h treatment with STX1972 IC_{50} (37.5 nM), Bzt-W41 IC_{50} (20.4 µM), W137 IC_{50} (23.5 µM), STX + Bzt-W41 combination (STX1972 [CF] = 20.625 nM; Bzt-W41 [CF] = 6.12 µM), and Bzt-W41 + W137 combination (Bzt-W41 [CF] = 4.08 µM; W137 [CF] = 16.45 µM). Actinomycin D (0.2 µg/mL) was used as positive control. The means ± SEM values are averaged from three biological replicates for each treatment condition.

		DMSO		STX1972		Bzt-W41		W137		STX + Bzt-W41		Bzt-W41 + W137		Actinomycin D	
		Mean	SEM	Mean	SEM	Mean	SEM	Mean	SEM	Mean	SEM	Mean	SEM	Mean	SEM
8 h	Sub G_1	2.23	0.48	1.07	0.31	5.33	1.82	9.23	0.44	1.12	0.18	2.29	0.56	13.31	0.73
	G_1	42.47	1.16	23.59	1.06	37.98	1.67	41.38	1.44	31.21	1.06	38.71	1.19	53.51	0.97
	S phase	25.28	2.52	28.04	1.89	26.57	2.98	26.27	1.62	28.53	1.71	26.02	3.36	19.37	2.31
	G_2/M	29.89	3.07	47.39	1.99	28.39	4.17	23.21	1.13	39.50	1.51	32.98	3.75	13.81	2.34
48 h	Sub G_1	3.08	0.66	10.33	1.75	1.85	0.39	23.28	7.07	2.54	0.25	2.01	0.30	49.59	4.25
	G_1	57.32	1.67	56.83	1.87	64.31	3.47	36.62	4.35	72.47	1.63	52.97	2.30	27.70	1.44
	S phase	21.00	0.40	9.88	0.23	9.52	1.33	16.16	1.25	8.19	0.35	18.84	1.99	11.43	0.49
	G_2/M	18.08	2.00	22.98	0.43	25.86	3.26	23.85	1.99	17.04	1.36	26.21	1.13	11.44	3.59

Table 3.5: Percentage of MCF-7 cells in the different phases of the cell cycle (sub G_1, G_1, S and G_2/M) after 8 h and 48 h treatment with STX1972 IC_{50} (37.5 nM), Bzt-W41 IC_{50} (20.4 µM), W137 IC_{50} (23.5 µM), STX + Bzt-W41 combination (STX1972 [CF] = 20.625 nM; Bzt-W41 [CF] = 6.12 µM), and Bzt-W41 + W137 combination (Bzt-W41 [CF] = 4.08 µM; W137 [CF] = 16.45 µM). Actinomycin D (0.2 µg/mL) was used as positive control. The means ± SEM values are averaged from three biological replicates for each treatment condition.

		DMSO		STX1972		Bzt-W41		W137		STX + Bzt-W41		Bzt-W41 + W137		Actinomycin D	
		Mean	SEM	Mean	SEM	Mean	SEM	Mean	SEM	Mean	SEM	Mean	SEM	Mean	SEM
8 h	Sub G_1	1.07	0.15	1.29	0.33	1.09	0.22	6.67	1.67	2.40	0.49	3.89	1.37	17.95	0.54
	G_1	47.17	0.60	35.54	1.00	45.41	0.66	41.18	0.85	41.14	0.63	34.03	0.64	52.11	1.23
	S phase	18.32	1.67	18.16	0.93	17.26	1.04	20.33	2.01	17.94	1.51	22.79	3.87	18.12	2.84
	G_2/M	33.63	1.97	44.96	0.90	36.10	0.78	31.11	1.95	38.29	1.56	39.07	4.01	11.91	1.84
48 h	Sub G_1	4.12	0.34	9.11	2.41	4.44	0.75	27.91	8.97	6.37	0.85	4.96	0.68	21.23	1.60
	G_1	69.83	3.90	66.72	3.34	70.98	3.51	40.79	3.71	71.41	4.07	60.12	2.78	50.88	2.26
	S phase	10.40	2.14	9.18	1.82	9.11	1.79	11.14	2.38	8.56	1.50	11.77	1.83	11.71	1.78
	G_2/M	15.22	2.73	15.27	2.67	14.71	2.09	19.33	3.89	12.90	2.30	22.49	1.05	14.04	1.24

Table 3.6: Percentage of EA.hy926 cells in the different phases of the cell cycle (sub G_1, G_1, S and G_2/M) after 8 h and 48 h treatment with STX1972 IC_{50} (37.5 nM), Bzt-W41 IC_{50} (20.4 µM), W137 IC_{50} (23.5 µM), STX + Bzt-W41 combination (STX1972 [CF] = 20.625 nM; Bzt-W41 [CF] = 6.12 µM), and Bzt-W41 + W137 combination (Bzt-W41 [CF] = 4.08 µM; W137 [CF] = 16.45 µM). Actinomycin D (0.2 µg/mL) was used as positive control. The means ± SEM values are averaged from three biological replicates for each treatment condition.

		DMSO		STX1972		Bzt-W41		W137		STX + Bzt-W41		Bzt-W41 + W137		Actinomycin D	
		Mean	SEM	Mean	SEM	Mean	SEM	Mean	SEM	Mean	SEM	Mean	SEM	Mean	SEM
8 h	Sub G_1	5.09	0.69	4.81	1.13	6.68	1.05	8.57	1.04	4.46	0.33	9.45	1.03	7.55	1.43
	G_1	66.91	4.39	69.95	1.90	69.04	2.48	68.39	3.73	66.22	3.28	67.20	2.22	65.56	3.63
	S phase	6.50	0.44	9.08	0.92	7.99	1.00	12.68	1.91	6.05	0.74	6.98	0.74	6.25	0.92
	G_2/M	20.80	4.01	15.24	1.28	15.25	2.31	8.99	2.38	21.50	2.51	14.58	1.42	20.02	2.93
48 h	Sub G_1	6.35	2.16	6.18	2.06	11.11	0.64	3.91	0.61	6.31	0.69	9.88	3.18	42.35	3.26
	G_1	71.37	1.47	78.11	2.85	70.02	1.74	70.11	1.67	64.21	2.08	63.85	3.36	35.57	2.29
	S phase	8.94	1.28	5.92	0.82	6.62	0.39	13.56	2.42	14.45	3.24	10.54	2.13	14.73	4.19
	G_2/M	11.66	0.89	9.67	2.29	11.94	1.96	12.02	0.87	14.83	1.41	13.57	2.24	7.08	1.07

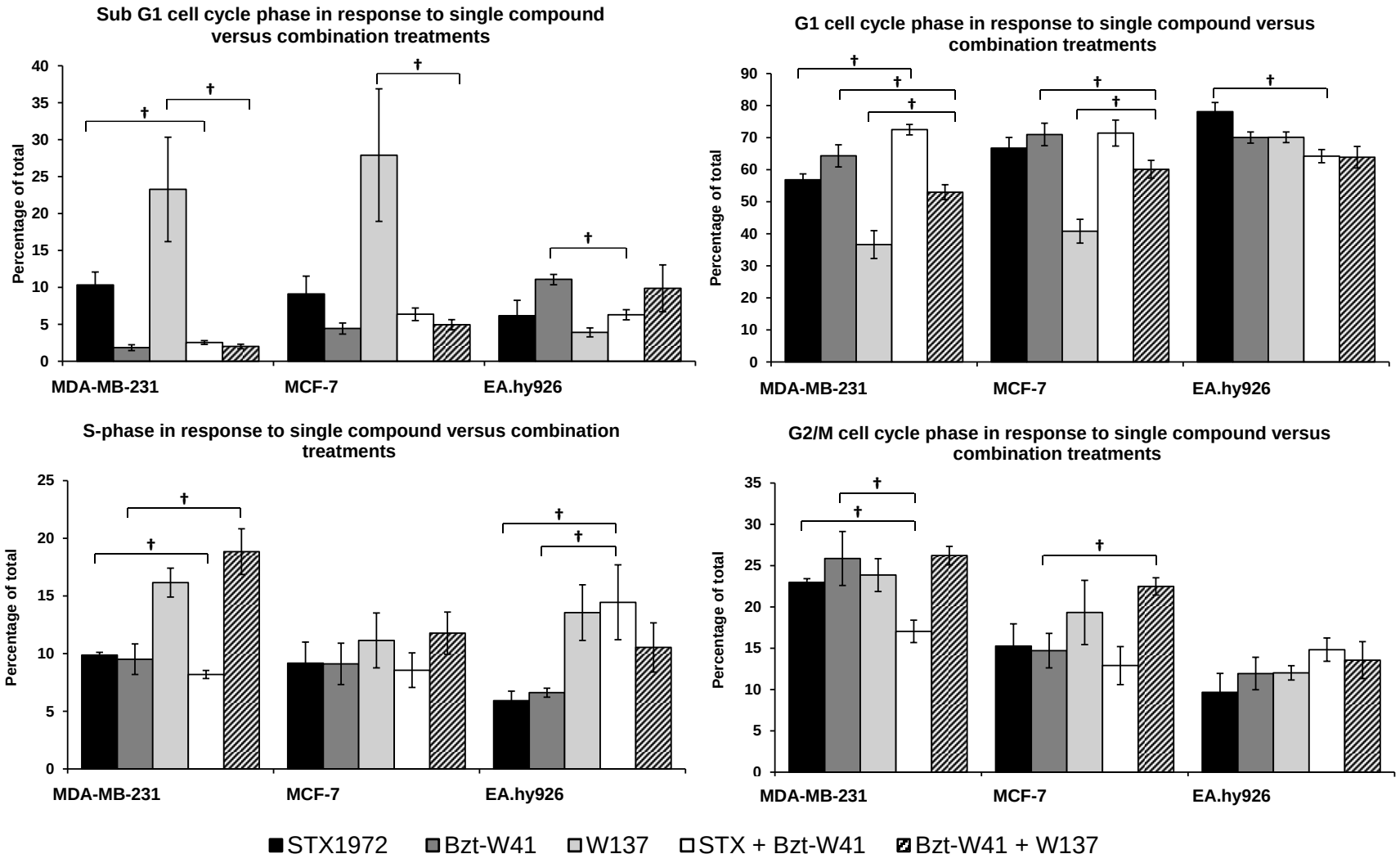

Figure 3.25: Comparison of single compound versus combination treatments on percentage of MDA-MB-231, MCF-7 and EA.hy926 cells in each of the four cell cycle phases. Bar graphs represent the mean ± SEM values from three biological replicates for each treatment condition.
† $p \leq 0.05$ indicates significant difference between single compound versus combination treatment within the respective cell cycle phase.

3.5 Cell death

Apoptosis was quantified by means of flow cytometric analysis of dual stained Annexin V-FITC and PI cells, following 48 h exposure to STX1972 at IC_{50} (37.5 nM), Bzt-W41 at IC_{50} (20.4 µM), W137 at IC_{50} (23.5 µM), STX + Bzt-W41 combination (STX1972 [CF] = 20.625 nM; Bzt-W41 [CF] = 6.12 µM), and Bzt-W41 + W137 combination (Bzt-W41 [CF] = 4.08 µM; W137 [CF] = 16.45 µM). Actinomycin D (0.2 µg/mL) was used as positive control. Dot-plots created from the data are used to sort cells into one of four quadrants, each representing a different stage of cell death. Viable cells at lower-left quadrant, FITC(-)/PI(-); necrotic cells at lower-right quadrant, FITC(-)/PI(+); late apoptotic cells at upper-right quadrant, FITC(+)/PI(+); and early apoptotic cells at upper-left quadrant, FITC(+)/PI(-).

Representative dot-plot diagrams for each treatment condition and for each cell line is shown in Figure 3.26. Bar graphs quantifying each of the quadrants (viable, early apoptotic, late apoptotic and necrotic cells) within each cell line, represented as the mean ± SEM is shown in Figure 3.27. Table 3.7 summarizes the mean ± SEM percentages of cells per quadrant for each treatment condition for all three cell lines. The between cell line comparison for each treatment condition for a respective quadrant is illustrated in Figure 3.28. Figure 3.29 compares single compound versus combination treatment effect on all three cell lines for the respective quadrants.

STX1972 treatment resulted in a significant decrease in the viable population for both MDA-MB-231 (74.14 ± 2.53%) and MCF-7 (63.44 ± 4.85%) cells in comparison to the vehicle control (≈ 95%) (Figure 3.26, Figure 3.27 and Table 3.7). However this effect was not seen for the STX1972-treated EA.hy926 cells (86.38 ± 3.76%) in comparison to the vehicle control (93.03 ± 0.53%) indicating cancer-selective toxicity of the antimitotic compound (Figure 3.26, Figure 3.27 and Table 3.7). To the opposite end, W137 and Bzt-W41 + W137 combination treatment did not exhibit the same selectivity and significantly reduced the viable population in all three cell lines. W137 decreased the viable population to 26.58 ± 4.46% in MDA-MB-231 cells, 28.56 ± 5.92% in MCF-7 cells, and most prominently decreased the EA.hy926 viable population to 21.86 ± 3.83% (Figure 3.26, Figure 3.27 and Table 3.7). Although not as pronounced as W137

treatment alone, the Bzt-W41 + W137 combination treatment significantly reduced the viable population to 54.00 ± 2.61%, 65.23 ± 4.21% and 43.23 ± 4.6% for MDA-MB-231, MCF-7 and EA.hy926 cells, respectively. Again, causing the most pronounced reduction in the control cell line. For the MDA-MB-231 cell line, treatment with Bzt-W41 and the STX + Bzt-W41 combination also resulted in significantly reduced viability (Figure 3.26, Figure 3.27 and Table 3.7).

Treatment with STX1972 significantly increased the early apoptotic population in comparison to vehicle control of MDA-MB-231 (12.76 ± 1.4 versus 2.81 ± 0.23%) and MCF-7 (12.91 ± 2.59% versus 1.10 ± 0.34%) cells. This increase was not evident in the control cell line (2.66 ± 1.66% versus 1.12 ± 0.4%) (Figure 3.26, Figure 3.27 and Table 3.7). Similar observations were made for STX + Bzt-W41 combination treatment with slight but significant increase in early apoptosis in MDA-MB-231 (5.09 ± 0.47%) and MCF-7 (3.42 ± 0.88%) cells.

Treatment with W137 and the Bzt-W41 + W137 combination significantly increased early apoptosis in all three cell lines. For MDA-MB-231 cells the early apoptotic population increased from 2.81 ± 0.23% (vehicle control) to 9.41 ± 1.28% and 20.80 ± 2.32% for W137 and Bzt-W41 + W137 treatment, respectively. The effect was not as strong but still significant for MCF-7 cells with W137 and Bzt-W41 + W137 treatment resulting in an early apoptosis increase to 5.41 ± 1.75% and 9.59 ± 2.53%, respectively in comparison to the vehicle control (1.10 ± 0.34%). The EA.hy926 results more closely resembled that of the MDA-MB-231 results, with W137 treatment increasing early apoptosis to 8.82 ± 1.65% and combination treatment strongly expanding the same population to 20.57 ± 2.81% when compared to the vehicle control (1.12 ± 0.43%). STX1972 treatment increased late apoptosis in the MDA-MB-231 (10.64 ± 1.33%) and MCF-7 (17.06 ± 3.05%) cell lines, in comparison to vehicle control samples (≈ 1.2%). Treatment with W137 and Bzt-W41 + W137 lead to significantly increased late apoptosis in all three cell lines. W137 strongly increased the MDA-MB-231, MCF-7 and EA.hy926 late apoptotic cell population to 62.88%, 64.54% and 67.15% respectively. Similarly, Bzt-W41 + W137 combined treatment significantly expanded the late apoptotic population of MDA-MB-231, MCF-7 and EA.hy926 cells to 24.04%, 22.60%, and 33.01% respectively.

A slight but significant increase in late apoptosis was observed after treatment with Bzt-W41 (2.03 ± 0.14%) and STX + Bzt-W41 (3.27 ± 0.21%), however this was only evident in the MDA-MB-231 cell line (Figure 3.26, Figure 3.27 and Table 3.7).

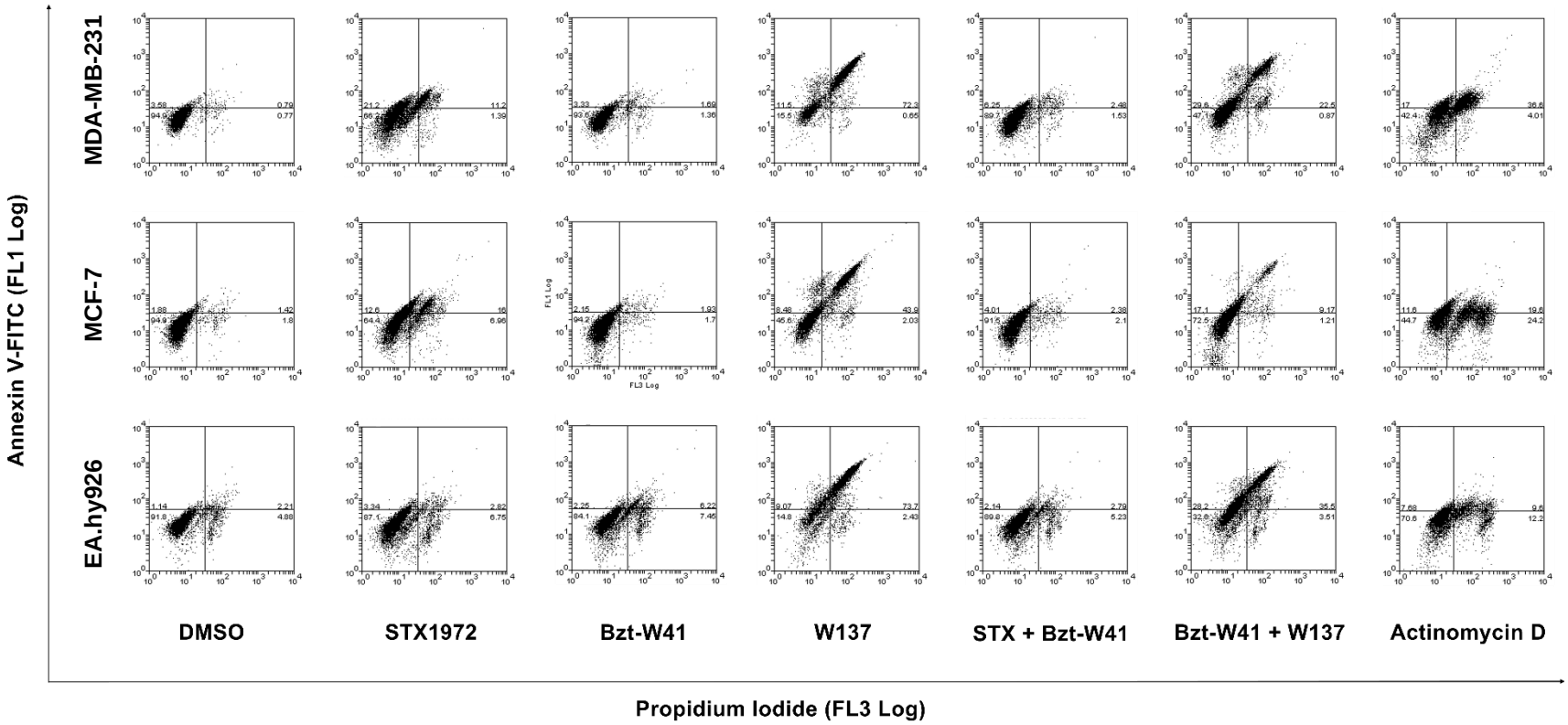

Figure 3.26: PI (FL3 Log) versus Annexin V-FITC (FL1 Log) dot-plots for MDA-MB-231, MCF-7 and EA.hy926 cells. The dot-plots indicate the percentage of viable, early apoptotic, late apoptotic and necrotic cells after 48 h treatment with STX1972 IC_{50} (37.5 nM), Bzt-W41 IC_{50} (20.4 µM), W137 IC_{50} (23.5 µM), STX + Bzt-W41 combination (STX1972 [CF] = 20.625 nM; Bzt-W41 [CF] = 6.12 µM), and Bzt-W41 + W137 combination (Bzt-W41 [CF] = 4.08 µM; W137 [CF] = 16.45 µM). Actinomycin D (0.2 µg/mL) was used as positive control. Viable cells at lower-left quadrant, FITC(-)/PI(-); necrotic cells at lower-right quadrant, FITC(-)/PI(+); late apoptotic cells at upper-right quadrant, FITC(+)/PI(+); and early apoptotic cells at upper-left quadrant, FITC(+)/PI(-).

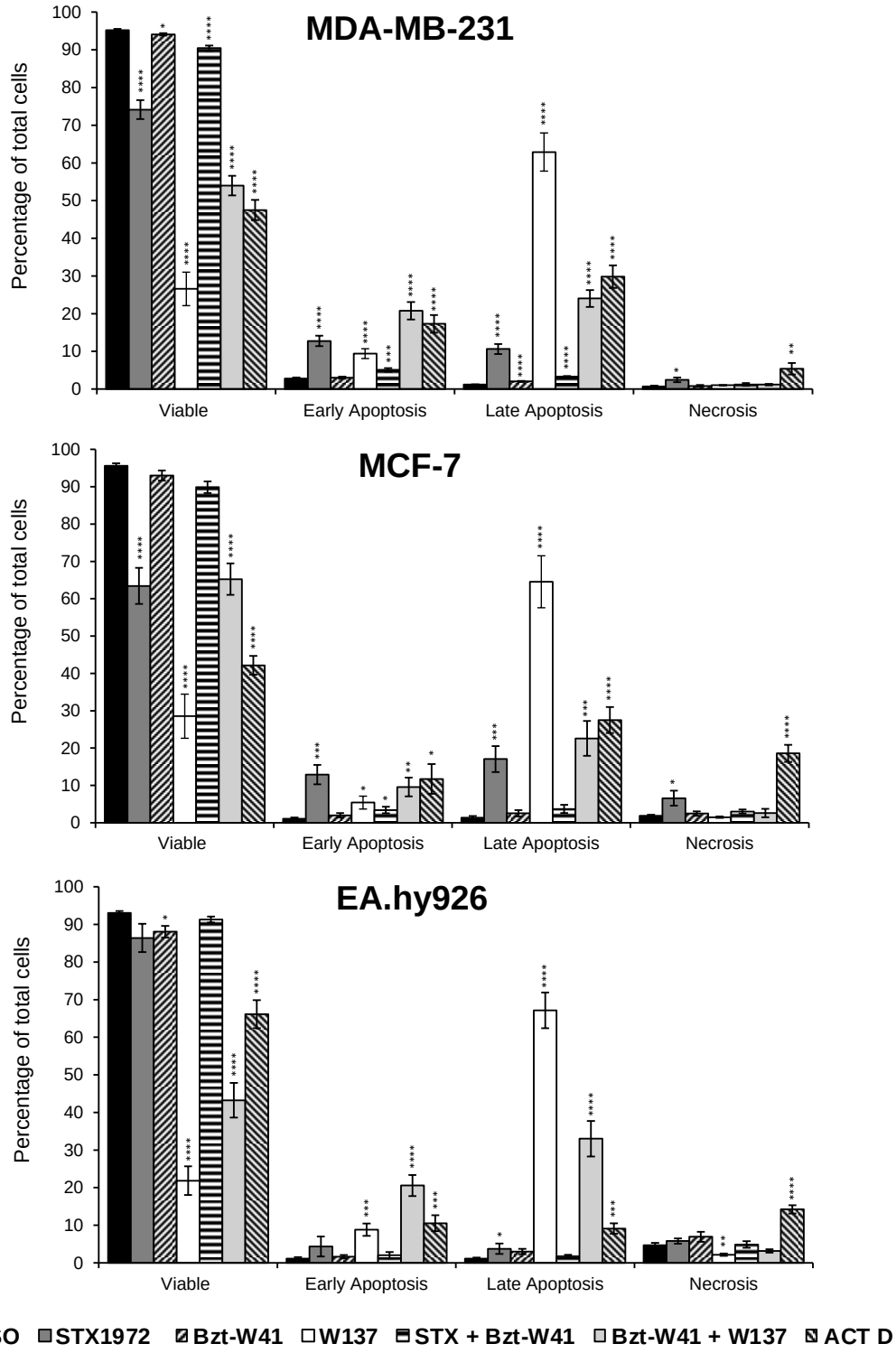

Figure 3.27: Apoptosis quantification in MDA-MB-231, MCF-7 and Ea.hy926. Bar graphs represent the mean ± SEM percentage of cells in each of the four quadrants (viable, early apoptosis, late apoptosis and necrosis) of the dot plots in Figure 3.26 after 48 h of respective drug treatment, averaged from three biological repeats.*p ≤ 0.05, **p ≤ 0.01, ***p ≤ 0.001, ****p ≤ 0.0001 indicate significant differences in the respective quadrants between the vehicle controls and treatment groups.

Table 3.7: Apoptosis quantification in MDA-MB-231, MCF-7 and EA.hy926. Values represent the mean ± SEM percentage of cells in each of the four quadrants (viable, early apoptosis, late apoptosis and necrosis) of the dot plots in Figure 3.26 after 48 h of respective drug treatment, averaged from three biological repeats. The means ± SEM values are averaged from three biological replicates for each treatment condition.

		DMSO		STX1972		Bzt-W41		W137		STX + Bzt-W41		Bzt-W41 + W137		Actinomycin D	
		Mean	SEM	Mean	SEM	Mean	SEM	Mean	SEM	Mean	SEM	Mean	SEM	Mean	SEM
MDA-MB-231	Viable	95.24	0.32	74.14	2.53	94.10	0.31	26.58	4.46	90.44	0.69	54.00	2.61	47.48	2.69
	Early apoptosis	2.81	0.23	12.76	1.40	3.02	0.30	9.41	1.28	5.09	0.47	20.80	2.32	17.31	2.34
	Late apoptosis	1.22	0.07	10.64	1.33	2.03	0.14	62.88	5.07	3.27	0.21	24.04	2.25	29.82	2.99
	Necrosis	0.72	0.18	2.46	0.63	0.83	0.24	1.01	0.14	1.21	0.37	1.18	0.21	5.39	1.54
MCF-7	Viable	95.62	0.64	63.44	4.85	92.98	1.35	28.56	5.92	89.87	1.55	65.23	4.21	42.15	2.51
	Early apoptosis	1.10	0.34	12.91	2.59	1.99	0.60	5.41	1.75	3.42	0.88	9.59	2.53	11.74	3.96
	Late apoptosis	1.38	0.44	17.06	3.50	2.54	0.85	64.54	6.94	3.69	1.10	22.60	4.69	27.52	3.46
	Necrosis	1.90	0.26	6.59	1.99	2.49	0.60	1.49	0.24	3.02	0.53	2.59	1.13	18.59	2.29
EA.hy926	Viable	93.03	0.53	86.38	3.76	88.06	1.56	21.86	3.83	91.32	0.79	43.23	4.60	66.11	3.74
	Early apoptosis	1.12	0.43	4.37	2.66	1.66	0.45	8.82	1.65	2.03	0.85	20.57	2.81	10.55	2.14
	Late apoptosis	1.14	0.27	3.74	1.39	3.03	0.68	67.15	4.74	1.78	0.36	33.01	4.74	9.12	1.39
	Necrosis	4.71	0.64	5.81	0.72	6.94	1.31	2.17	0.31	4.87	0.87	3.19	0.46	14.23	1.09

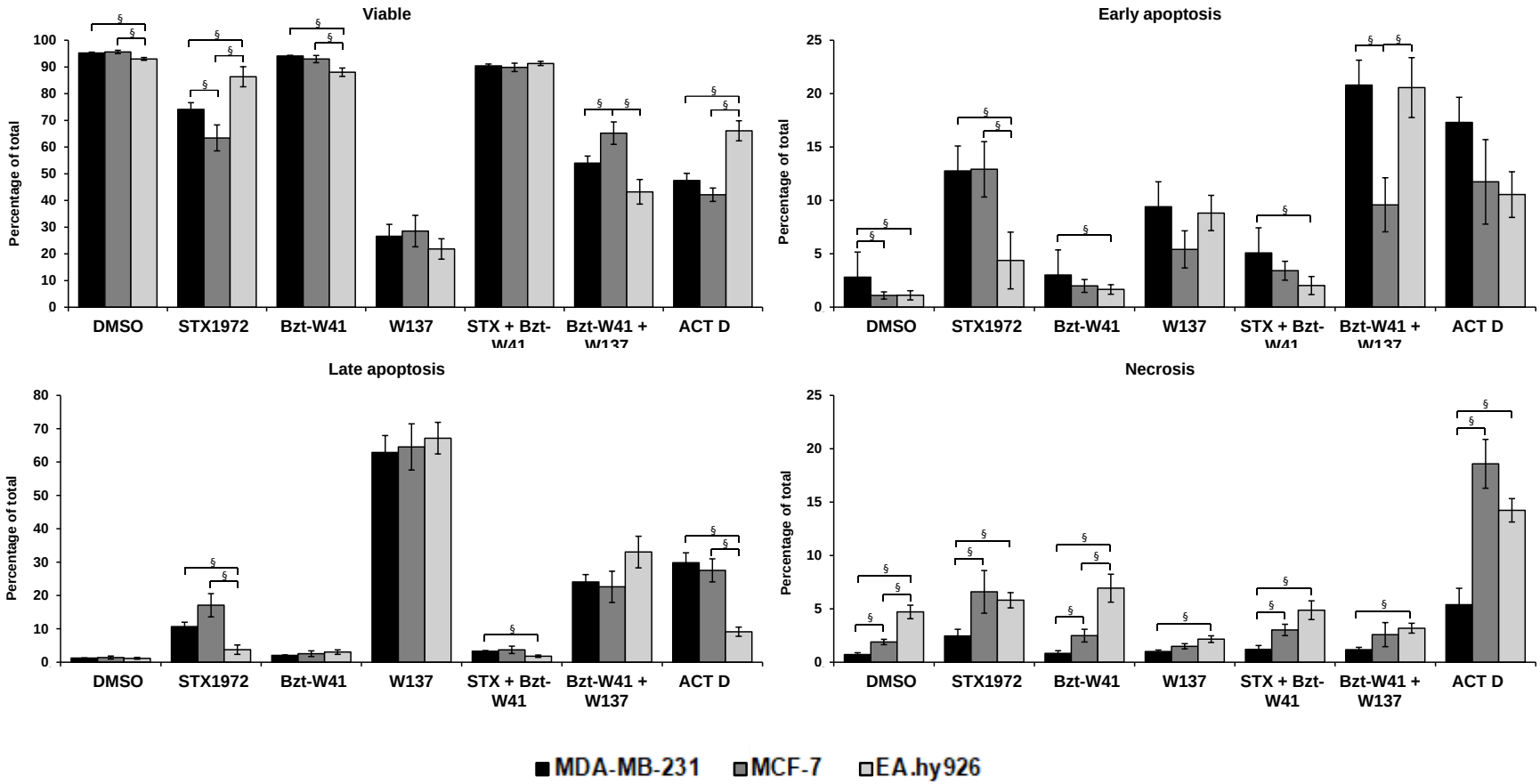

Figure 3.28: Comparison of the mean proportion of cells in each of the four quadrants (viable, early apoptosis, late apoptosis and necrosis) between MDA-MB-231, MCF-7 and EA.hy926 cells. Bar graphs represent the mean ± SEM values averaged from three biological replicates for each treatment condition. § $p \leq 0.05$ indicates significant difference between cell lines for a specific treatment condition.

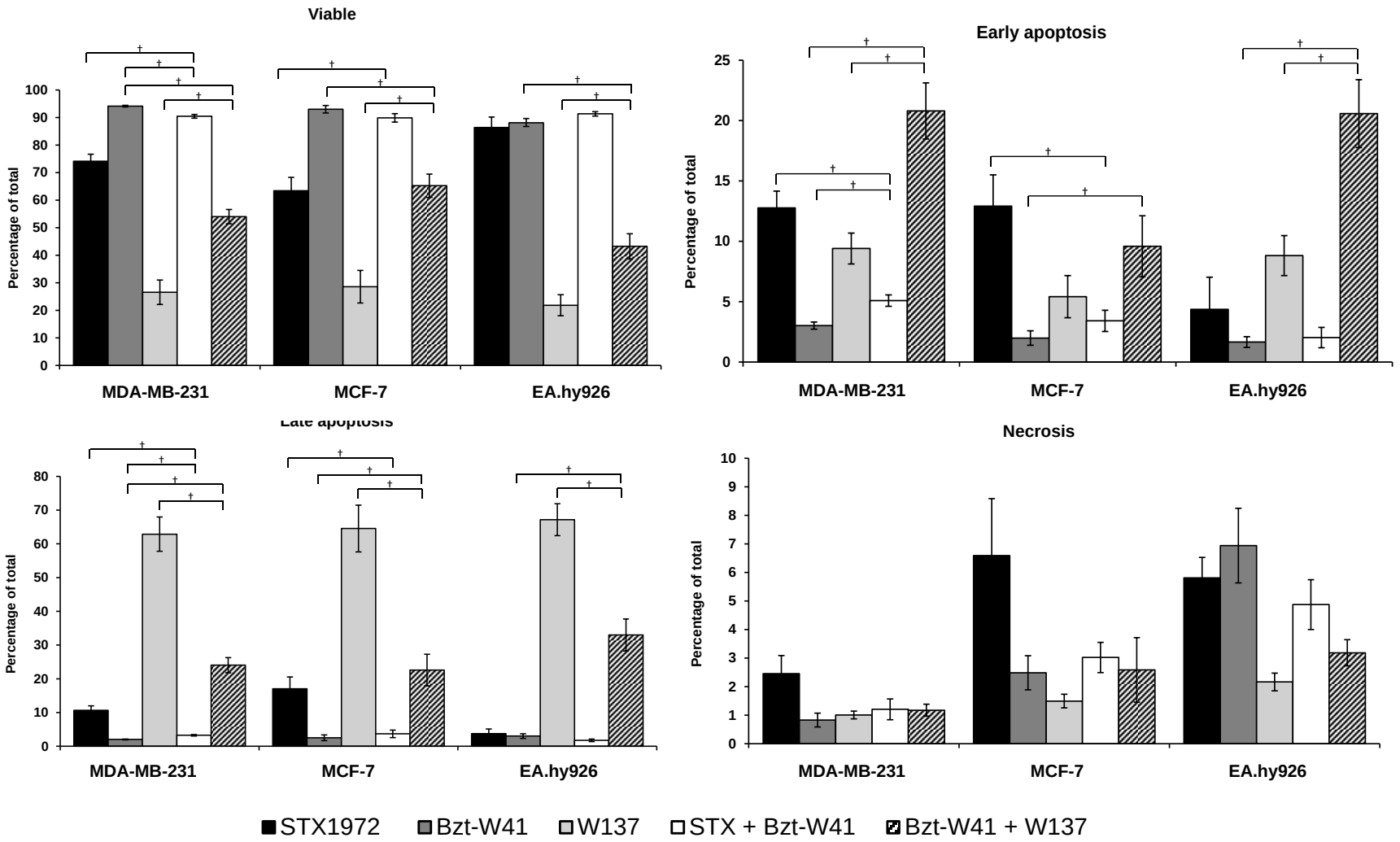

Figure 3.29: Comparison of single compound versus combination treatments on percentage of MDA-MB-231, MCF-7 and EA.hy926 cells in each of the four quadrants (viable, early apoptosis, late apoptosis and necrosis).Bar graphs represent the mean ± SEM values averaged from three biological replicates for each treatment condition. † $p \leq 0.05$ indicates significant difference between single compound versus combination treatment within the quadrant.

3.6 Autophagy

Results from the cell death assay suggest that W137 and Bzt-W41 + W137 combination treatment does not exhibit cancer-specific selectivity, resulting in significant decreases in cell viability and increases in early and late apoptosis populations in the EA.hy926 cell line, often with more pronounced effects than those in the cancer cells. For this reason, it was decided to proceed further experiments with the antimitotic (STX1972) and BRD-4 inhibitor (Bzt-W41) and their synergistic, and cancer selective combination (STX + Bzt-W41). Moreover, treatment with these compounds and their paired combination showed to be more selective toward the TNBC cell line model (MDA-MB-231), in comparison to the hormone-dependent model (MCF-7). For the purpose of this project, individual and combined effects of the drugs on the MCF-7 cell line was satisfactorily concluded. All further experiments were performed on MDA-MB-231 and EA.hy926 cells and included the following treatment conditions: STX1972 at IC_{50} (37.5 nM), Bzt-W41 at IC_{50} (20.4 µM) and STX + Bzt-W41 combination (STX1972 [CF] = 20.625 nM; Bzt-W41 [CF] = 6.12 µM).

Acridine orange (AO), an acidotropic dye, was used to stain cells after 48 h test compound treatment. Actinomycin D (0.2 µg/mL) was used as positive control. AO fluoresces green in the cytosol but undergoes a concentration-dependent metachromic shift to red fluorescence when concentrations are high due to protonation and trapping in acidic vesicular organelles such as autolysosomes, implying correlation with autophagy induction [225]. AO fluorescence was quantified by means of flow cytometry and the red-to-green fluorescence intensity ratio (R/GFIR) was used as ratiometric analysis of autophagy [225]. Two-parameter linear scale dot-plots were used to detect red fluorescence (y-axis) and green fluorescence (x-axis) and a R/GFIR-threshold (R/GFIR-T) was set along the population axis (Figure 3.30). The proportion of cells above the threshold defines the positive population and is reported as fold change relative to control (Figure 3.31 A) and percentage of cell population above threshold (Figure 3.31 B).

For the MDA-MB-231 cell line, a significant increase in the AO positive (red) population in terms of fold-change after 48 h treatment with STX1972 (6.83-fold), Bzt-W41 (10.62-

fold) and STX + Bzt-W41 (11.50-fold) was seen. Also, when reporting the results as percentage above threshold (Figure 3.31 B) for STX1972 (38.32%); Bzt-W41 (59.24%) and STX + Bzt-W41 (64.06%) in relation to the vehicle control sample (5.62%). Although all three treatment conditions lead to increased AO fluorescence, it is clear that the combination treatment is most efficacious. According to Thomé *et al.* (2016) this would imply an increase of the volume of acidic organelles such as autolysosomes and lysosomes, and could be correlated with autophagy in MDA-MB-231 cells [225]. The effect of the combination treatment, STX + Bzt-W41, significantly exceeds that of individual compounds in isolation, confirming synergistic effect of dual treatment (Figure 3.32).

For the EA.hy926 cell line, significant increase in the fold-change in relation to the control sample was seen for only in the STX1972-treated sample (2.34-fold) (Figure 3.31 A).

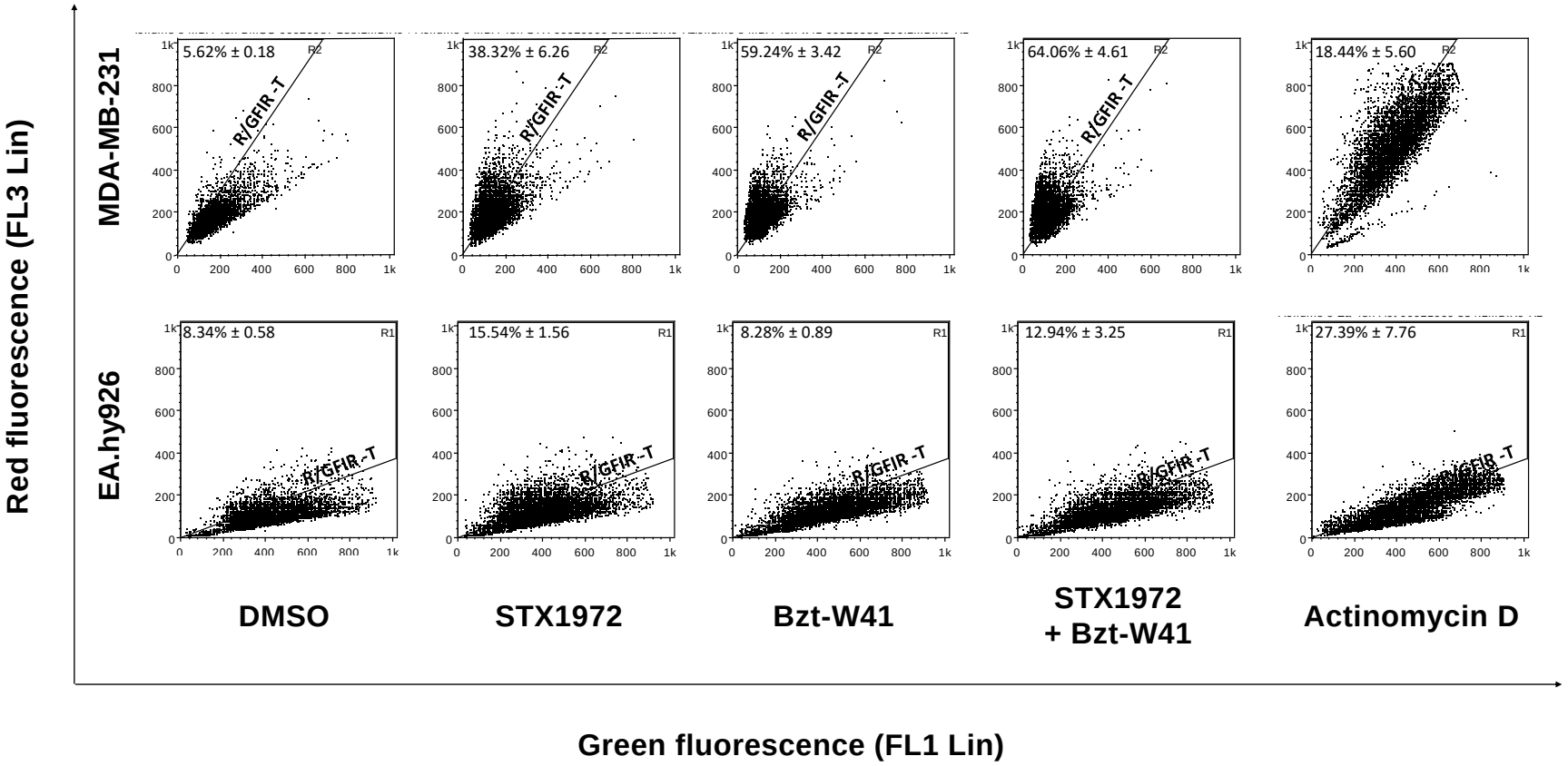

Figure 3.30: Detection of autophagy induction in AO-stained MDA-MB-231 and EA.hy926 cells. Representative plots of flow cytometric detection of red (FL3) and green (FL1) fluorescence after 48 h treatment with STX1972 at IC_{50} (37.5 nM), Bzt-W41 at IC_{50} (20.4 µM), and STX + Bzt-W41 combination (STX1972 [CF] = 20.625 nM; Bzt-W41 [CF] = 6.12 µM). Actinomycin D (0.2 µg/mL) was used as positive control. Ratiometric analysis of autophagy induction by means of red-to-green fluorescence intensity ratio threshold (R/GFIR-T) setting. Percentages represent the mean ± SEM proportion of events above the set threshold (positive population) for three independent experiments.

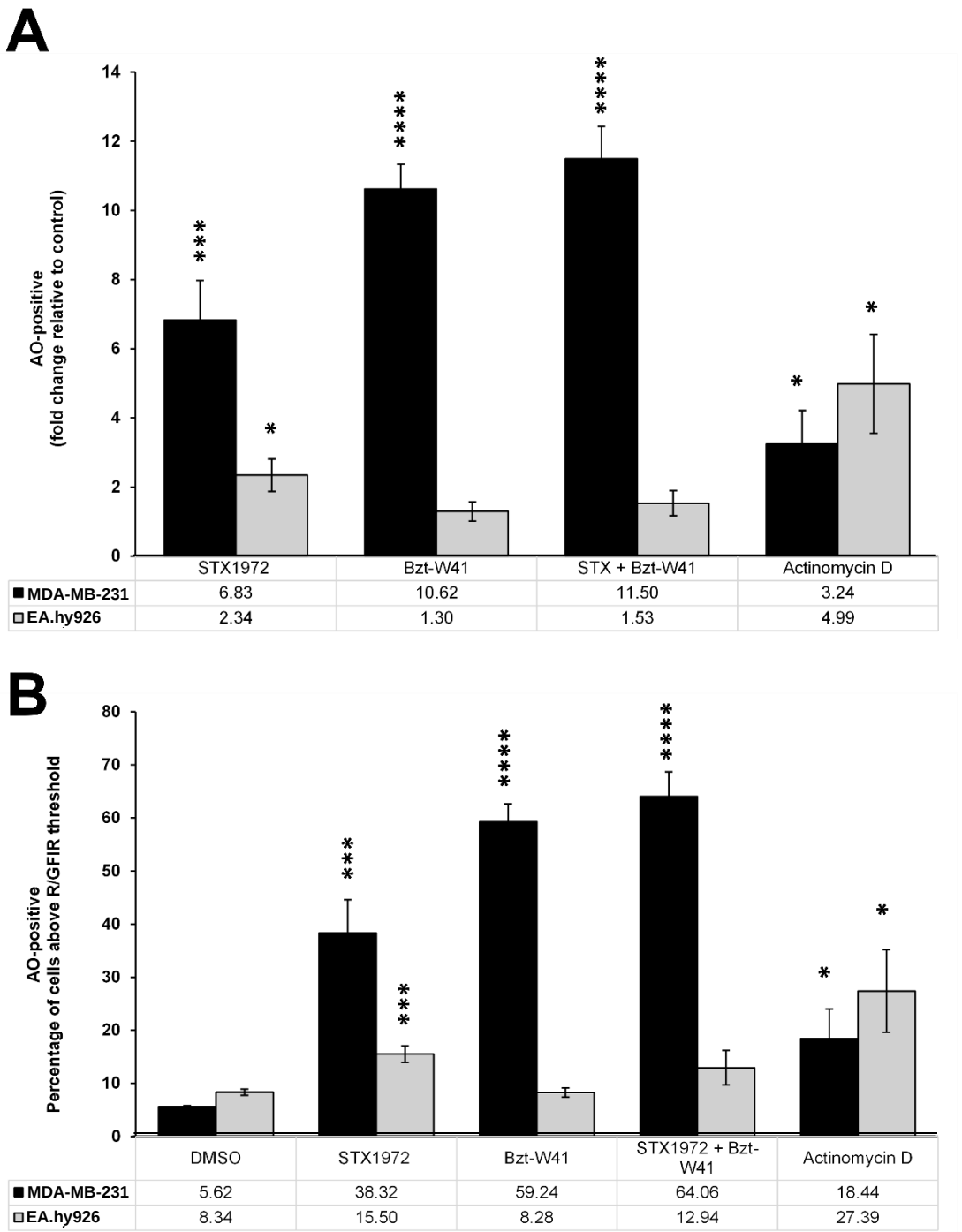

Figure 3.31: Red and green fluorescence of AO-stained cells analysed with the R/GFIR-T setting.(A) The proportion of events above the R/GFIR-T in relation to vehicle-treated control, is represented as the fold change. Values were normalized to the averaged control, set to one. (B) The percentage of AO stained cells above the R/GFIR-T. Bar graphs represent the mean ± SEM for three independent experiments. *p ≤ 0.05, **p ≤ 0.01, ***p ≤ 0.001, ****p ≤ 0.0001 indicate significant differences between the vehicle controls and treatment groups.

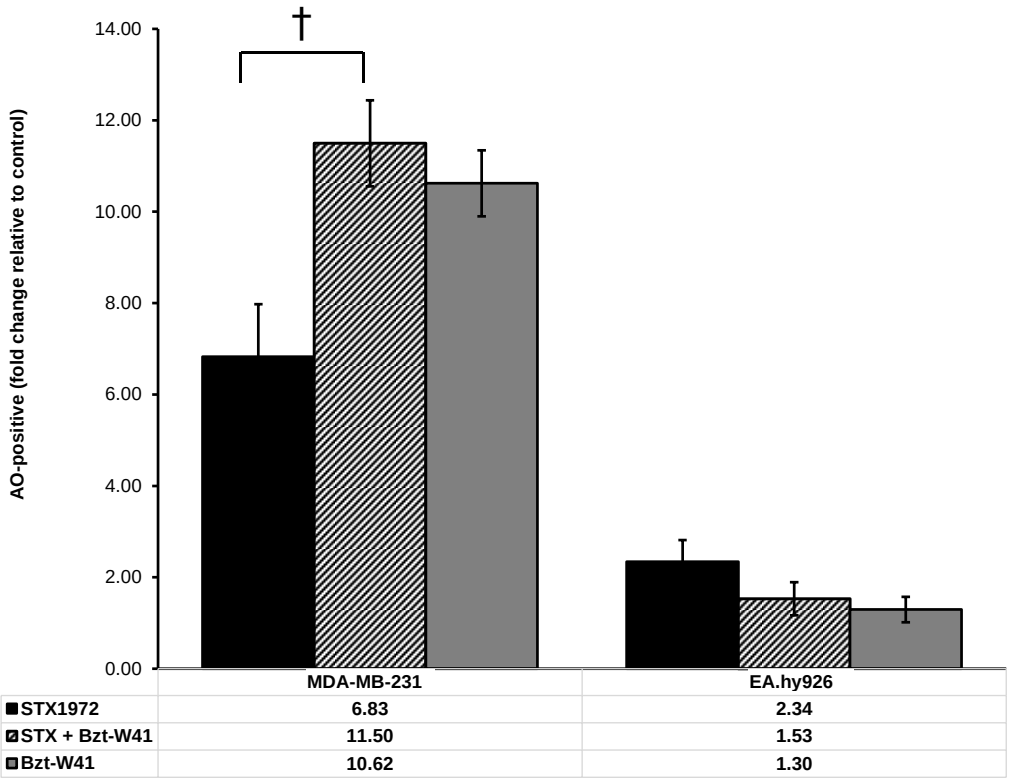

	MDA-MB-231	EA.hy926
STX1972	6.83	2.34
STX + Bzt-W41	11.50	1.53
Bzt-W41	10.62	1.30

Figure 3.32: Comparison of effects of single compound versus combination treatment on mean proportion of AO-stained cells analysed with the R/GFIR-T setting. The proportion of events above the R/GFIR-T in relation to vehicle-treated control, represented as the fold of change. Values were normalized to the averaged control, set to one. Bar graphs represent the mean ± SEM for three independent experiments. † $p \leq 0.05$ indicates significant difference between single compound versus combination treatment.

3.7 ROS generation

Intracellular ROS generation was evaluated after 48 h treatment of MDA-MB-231 and EA.hy926 cell lines with STX1972 at IC_{50} (37.5 nM), Bzt-W41 at IC_{50} (20.4 µM) and STX + Bzt-W41 combination (STX1972 [CF] = 20.625 nM; Bzt-W41 [CF] = 6.12 µM). Flow cytometry was used to quantify DCF fluorescence as an indication of ROS formation. The DCF reaction requires the involvement of iron, therefore the iron-chelator DFO (100 µM) was used as a negative control. The ROS inhibitor NAC (5 mM) was also included as a negative control. A column chart showing the mean DCF fluorescence intensity of treated samples represented as the fold of change relative to vehicle control, set to one, is shown if Figure 3.33. Representative flow cytometric histograms of DCF fluorescence intensity (FL1 Log) versus event count is shown in Figure 3.34.

Results indicate that only STX1972 treatment induces a significant increase (>1.4-fold) in ROS production, and this is seen only in MDA-MB-231 cells. Interestingly, combination treatment (STX + Bzt-W41) shows a significantly attenuated effect (≈ 0.8-fold) when compared to STX1972 treatment alone.

None of the treatment conditions resulted in significantly increased ROS formation in EA.hy926 cells and no significant difference in ROS production is notable when comparing the MDA-MB-231 and this control cell line.

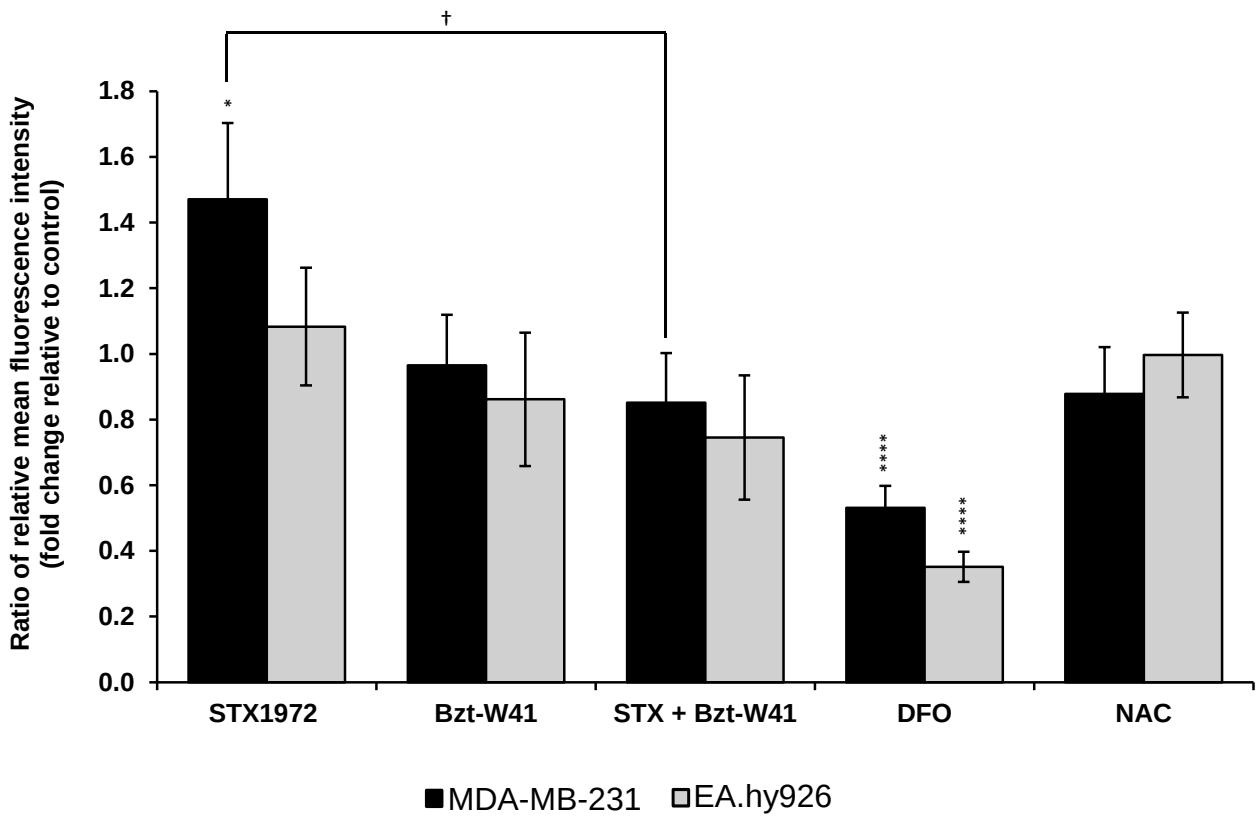

Figure 3.33: DCF fluorescence as an indication of ROS formation. Relative mean fluorescence represented as the fold of change. Values were normalized to the averaged vehicle control, set to one. Bar graphs represent the mean ± SEM values averaged from three biological replicates for each treatment condition. * $p \leq 0.05$, ** $p \leq 0.01$, *** $p \leq 0.001$, **** $p \leq 0.0001$ indicates significant differences between the vehicle controls and treatment groups; † $p \leq 0.05$ indicates significant difference between individual compound versus combination exposure

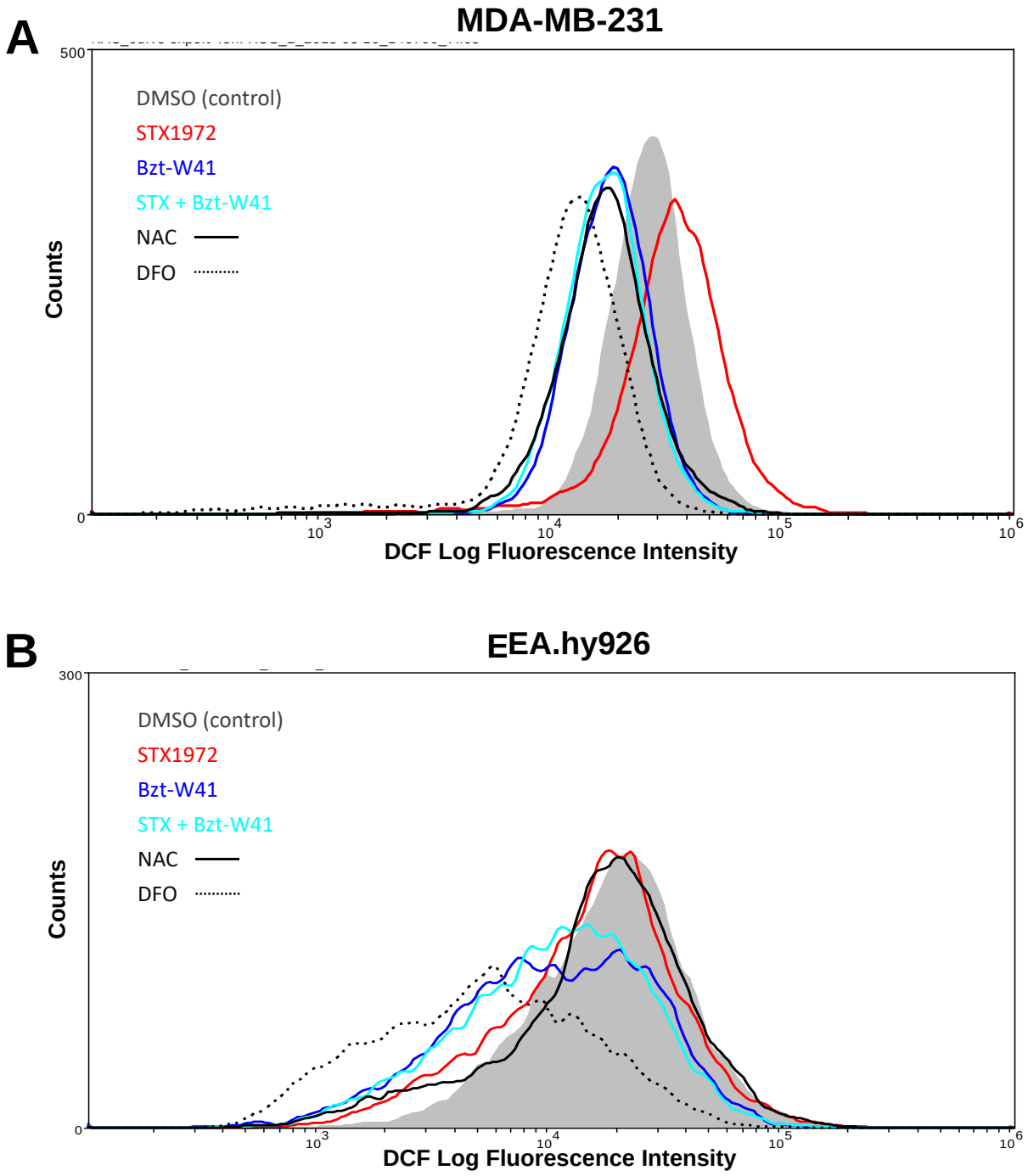

Figure 3.34: Histograms of DCF fluorescence intensity as measure ROS formation. FL1 Log versus event count illustrating the x-axis mean shift in response to different treatments in MDA-MB-231 (A) and EA.hy926 (B) cells.

3.8 Mitochondrial membrane depolarization

Depolarization of mitochondrial membrane potential (ΔΨm) was detected in MDA-MB-231 and EA.hy926 cells following 48 h exposure to STX1972 at IC_{50} (37.5 nM), Bzt-W41 at IC_{50} (20.4 µM) and STX + Bzt-W41 combination (STX1972 [CF] = 20.625 nM; Bzt-W41 [CF] = 6.12 µM). Mitochondrial transmembrane potential corresponds to mitochondrial membrane integrity and cell health. Mitochondrial membrane permeabilisation causes dissipation of ΔΨm and results in the initiation of the proapoptotic signal cascade [66]. The ΔΨm -sensitive probe $DiOC_6(3)$ was used as a cytofluorometric ΔΨm indicator [226]. $DiOC_6(3)$ is a lipophilic cationic dye that accumulates in the mitochondrial matrix of functional mitochondria to fluoresce as green light [227]. In apoptotic cells the dye is unable to aggregate due to ΔΨm depolarization, resulting in decreased $DiOC_6(3)$ fluorescence [228]. Flow cytometry was used to quantify mitochondrial depolarization by measuring $DiOC_6(3)$ fluorescence intensity. Data is expressed as the proportion of cells with depolarized mitochondrial potential in treated groups compared to vehicle control (Figure 3.35). Representative histograms of $DiOC_6(3)$ fluorescence in MDA-MB-231 and EA.hy926 cells is shown in Figure 3.36 A and B respectively.

For the MDA-MB-231 cell line, all three treatment conditions resulted in a significant increase in the percentage cell population with depolarized mitochondrial membrane potential. STX1972 treatment had the most pronounced effect (13.23%), followed by Bzt-W41 (10.1%) and the combination treatment (7.3%), which proved significantly lower than that of STX1972 treatment in isolation. For the EA.hy926 cell line STX1972 alone and in combination treatment proved to significantly increase the percentage of cells displaying mitochondrial depolarization to 3.64% and 5.2%, respectively, in relation to the vehicle control (1.37%). Overall, the increase in mitochondrial membrane depolarization seen in the EA.hy926 cell line was less prominent for all three treatment conditions than that seen in MDA-MB-231 cells, with STX1972 and Bzt-W41 treatment being significantly lower.

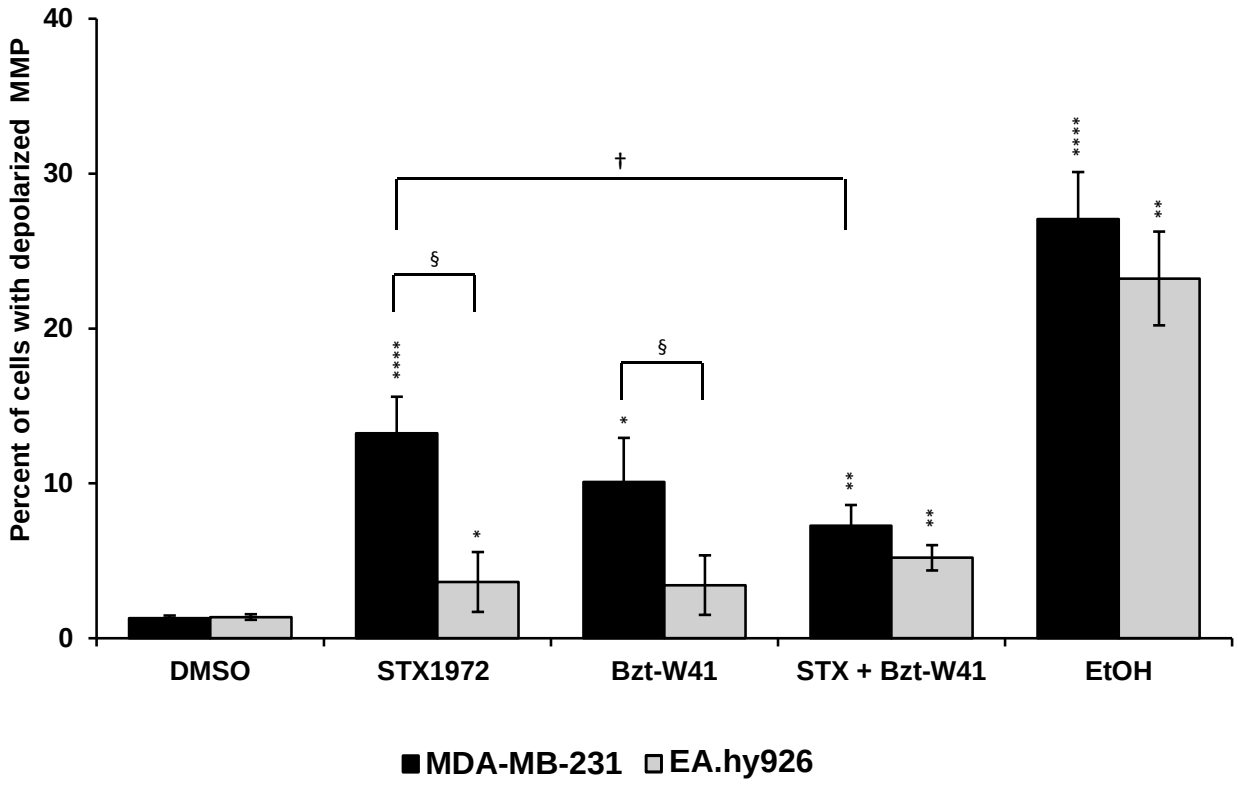

Figure 3.35: Mitochondrial membrane depolarization in MDA-MB-231 and EA.hy926 cells. Data from both cell lines are expressed in percentage of cells displaying mitochondrial depolarization in the different treatment groups compared with the vehicle control. Bar graphs represent the mean ± SEM values averaged from three biological replicates for each treatment condition. * $p \leq 0.05$, ** $p \leq 0.05$, *** $p \leq 0.05$, **** $p \leq 0.05$ indicates significant differences between the vehicle controls and treatment groups; § $p \leq 0.05$ indicates significant difference between MDA-MD-231 and EA.hy926 for a treatment condition; † $p \leq 0.05$ indicates significant difference between individual compound versus combination exposure

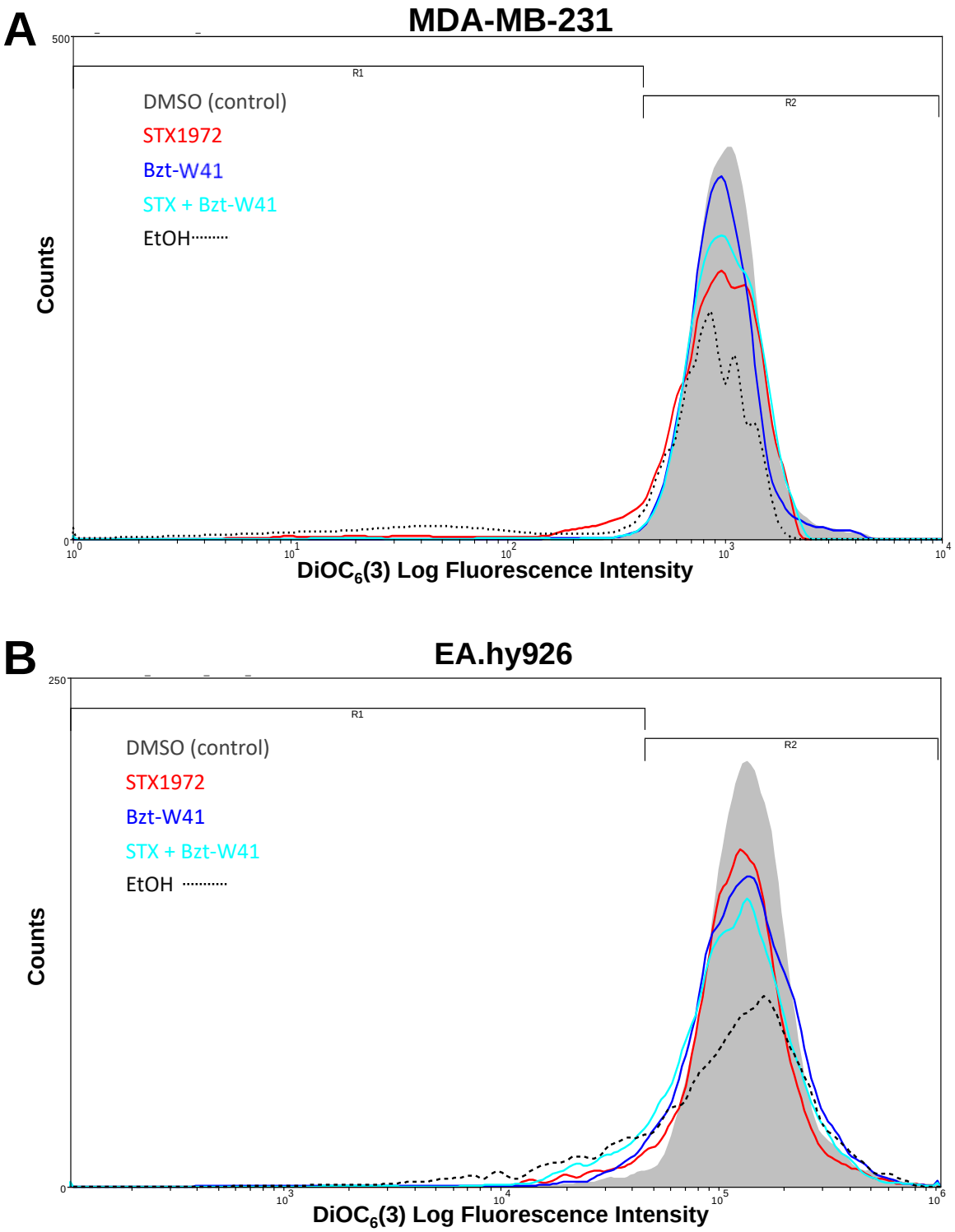

Figure 3.36: Representative flow cytometry histograms generated from $DiOC_6(3)$ fluorescence intensity detection in MDA-MB-231 (A) and EA.hy926 (B) cells. Cells with altered MMP were gated by R1 and R2 for depolarized and polarized MMP, respectively. EtOH (70%) was used as positive control.

3.9 Bcl-2 protein expression and phosphorylation

Flow cytometry was used to evaluate the phosphorylation status of Bcl-2 at Ser 70 (p-Bcl-2 (ser70)) in the MDA-MB-231 and EA.hy926 cell lines after 48 h exposure to STX1972 at IC_{50} (37.5 nM), Bzt-W41 at IC_{50} (20.4 µM) and STX + Bzt-W41 combination (STX1972 [CF] = 20.625 nM; Bzt-W41 [CF] = 6.12 µM) compared to the vehicle-treated control. The Muse™ Bcl-2 Activation Dual Detection Kit allowed for the simultaneous measurement of Bcl-2 phosphorylation and total levels of Bcl-2 protein expression. Flow cytometry was used to determine the extent of Bcl-2 activation by detecting the p-Bcl-2 (ser70): total Bcl-2 ratio within the MDA-MB-231 and EA.hy926 cell lines after 48 h exposure to treatment. Representative flow cytometry dot-plots for both cell lines are shown in Figure 3.37. Bar graphs quantifying activated (p-Bcl-2 (ser70)), inactivated (dephosphorylated Bcl-2) and non-expressing populations can be seen in Figure 3.38.

For the MDA-MB-231 cell line, STX1972 treatment only resulted in significant effects, reducing the relative percentage p-Bcl-2 (ser70) cell population (83.02 ± 1.49%) while increasing the percentage dephosphorylated Bcl-2 cells (16.98 ± 1.49%). Dephosphorylation of Bcl-2 at serine 70 is associated with apoptosis [229]. No significant effects were seen for the EA.hy926 cell line following any of the equivalent treatments.

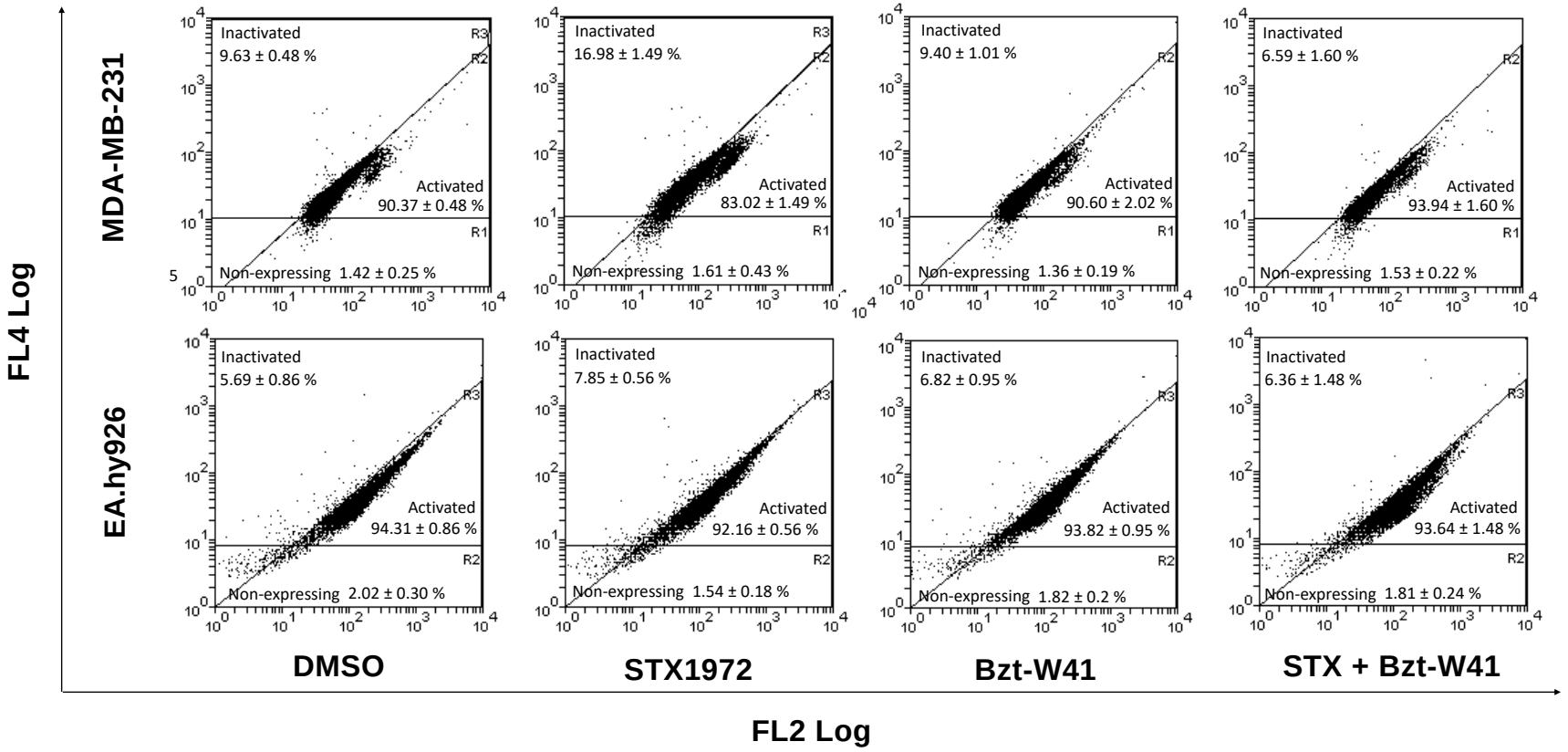

Figure 3.37: Representative flow cytometry dot-plots of Bcl-2 phosphorylation (FL2 Log) and expression (FL4 Log). The quadrants represent the activated (p-Bcl-2 (ser70)), inactivated (dephosphorylated Bcl-2) and non-expressing populations as shown. Numbers represent mean percentage per quadrant ± SEM of three independent experiments following 48 h treatment with STX1972 at IC_{50} (37.5 nM), Bzt-W41 at IC_{50} (20.4 µM) and STX + Bzt-W41 combination (STX1972 [CF] = 20.625 nM; Bzt-W41 [CF] = 6.12 µM).

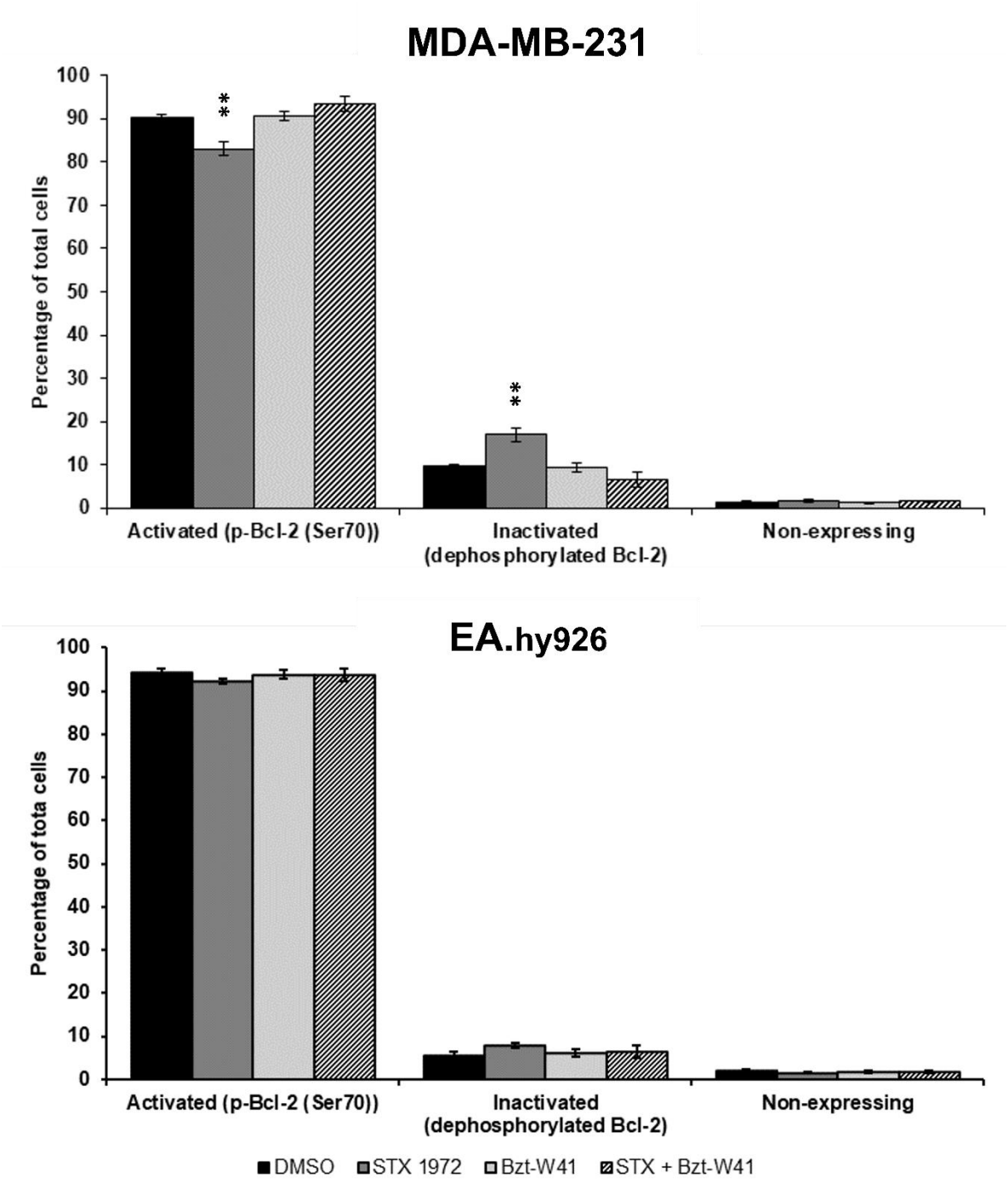

Figure 3.38: Bcl-2 protein expression in MDA-MB-231 and EA.hy926 cells. Bar graphs quantify activated (p-Bcl-2 (ser70)), inactivated (dephosphorylated Bcl-2) and non-expressing populations, expressed as mean percentage ± SEM of three independent experiments following 48 h treatment with STX1972 at IC_{50} (37.5 nM), Bzt-W41 at IC_{50} (20.4 µM) and STX + Bzt-W41 combination (STX1972 [CF] = 20.625 nM; Bzt-W41 [CF] = 6.12 µM). ** $p \leq 0.01$ indicates significant differences between the vehicle controls and treatment groups.

3.10 c-MYC gene expression

Cell death was observed when exposing MDA-MB-231 cells to the STX + Bzt-W41 combination. Both Bcl-2 and p53 are known to play a mechanistic role in inducing cell death. The JQ1 bromodomain inhibitor has been implicated in p53-mediated cell death and also affects the expression of *c-myc* and *Bcl-2* [237]. Furthermore, antimitotic compounds are known to activate the p53 and Bcl-2 pathways to cause cell death [238-239]. Therefore, *p53, c-myc* and *bcl-2* were chosen as genes of interest that may provide information about the mechanism of the combination and single agents.

Relative quantification of mRNA transcription levels in both MDA-MB-231 and EA.hy926 cell lines after 48 h exposure to STX1972 at IC_{50} (37.5 nM), Bzt-W41 at IC_{50} (20.4 µM) and STX + Bzt-W41 combination (STX1972 [CF] = 20.625 nM; Bzt-W41 [CF] = 6.12 µM) were calculated. The LightCycler 480 software package was used to identify the crossing point (CT). CT points obtained from the software were normalized to two reference genes (*GAPDH* and *β2M*) and to a treatment control (cells exposed to DMSO). Relative gene expression levels of genes of interest were determined from CT values obtained from qPCR analysis using the ΔΔCT method [234]. Gene expression of the three genes of interest (*p53, c-myc* and *bcl-2*) were calculated as target/reference ratio, and displayed as fold increase relative to vehicle control, normalized to one, as seen in Figure 3.39.

No significant changes in *p53* mRNA levels were observed for any of the treatment conditions. For the MDA-MB-231 cell line Bzt-W41 treatment resulted in significantly decreased relative expression of *bcl-2* (≈0.6-fold) and *c-myc* (≈0.5-fold) relative to the vehicle control. STX1972 treatment alone resulted in significantly increased *bcl-2* (≈1.7-fold) and decreased *c-myc* (≈0.5-fold) mRNA expression, whilst the combination treatment (STX + Bzt-W41) only significantly reduced c-*myc* (≈0.5-fold) mRNA transcription levels. This indicates that while BRD-4 inhibitor and antimitotic treatment had opposing effects on *bcl-2* expression, all three treatment conditions showed similar effects on *c-myc* expression.

For the EA.hy926 cell line p53 expression was significantly increased (≈1.5-fold) for all three treatment conditions. Bzt-w41 and STX1972 again showed opposing effects on *bcl-2* expression, resulting in significant decrease (≈0.6-fold) and increase (≈1.8-fold) respectively that is similar to the effect seen for the MDA-MB 231 cell line. Relative expression of *c-myc* was significantly decreased (≈0.8-fold) following Bzt-W41 treatment and significantly increased in response to STX1972 (≈1.4-fold) and STX + Bzt-W41 (≈1.2-fold) treatment compared to the vehicle control.

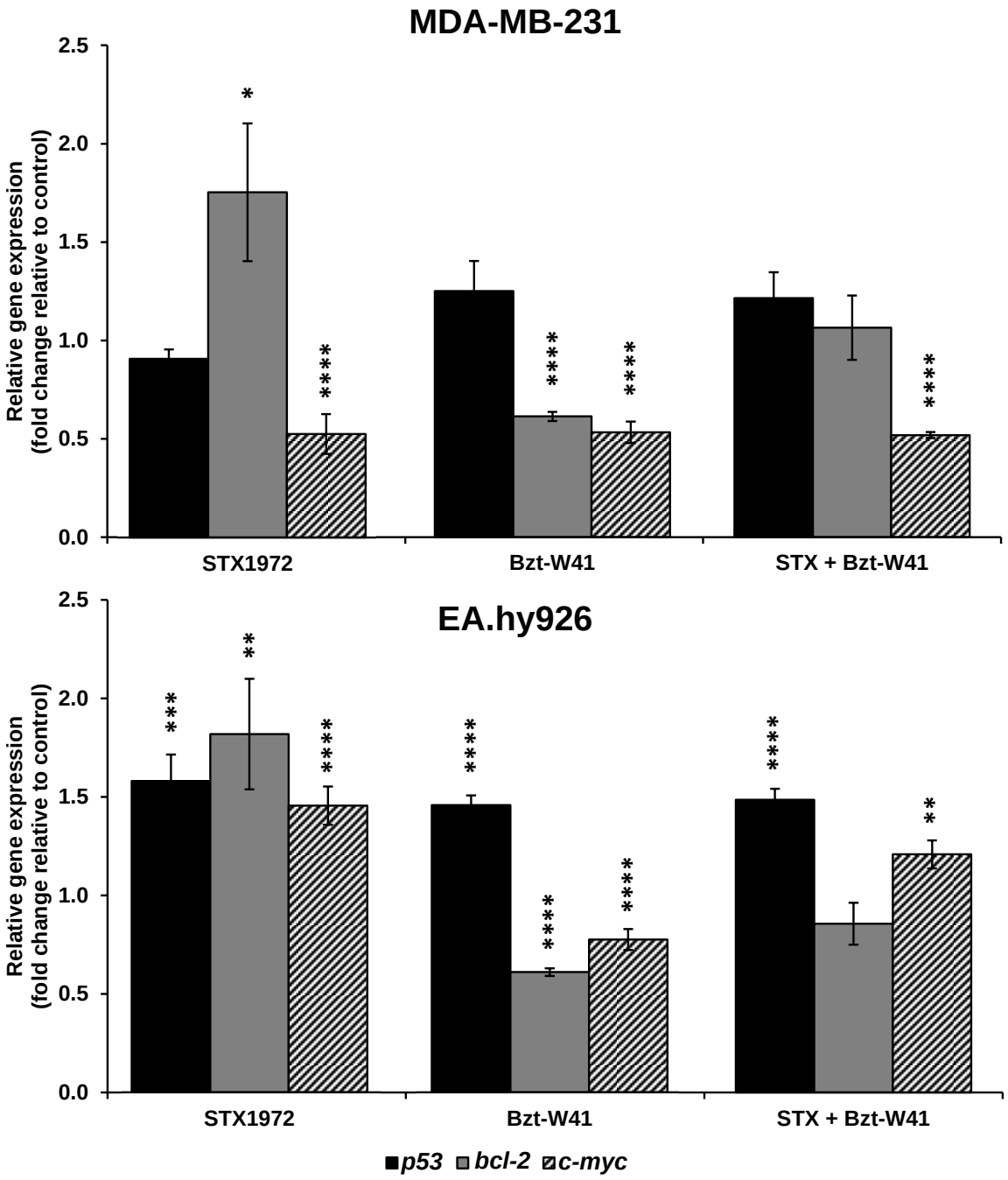

Figure 3.39: Real time qPCR analysis of the relative expression of *p53, bcl-2* and *c-myc* genes in MDA-MB-231 and EA.hy926 cells After 48 h exposure to STX1972 at IC_{50} (37.5 nM), Bzt-W41 at IC_{50} (20.4 µM) and STX + Bzt-W41 combination (STX1972 [CF] = 20.625 nM; Bzt-W41 [CF] = 6.12 µM). Results are expressed as fold change relative to vehicle control (normalized to one) and represent the mean ± SEM of three biological repeats. *p ≤ 0.05, **p ≤ 0.01, ***p ≤ 0.001, ****p ≤ 0.0001 indicates a significant difference between the relative gene expression in vehicle control versus treated cells.

3.11 c-MYC protein expression

Since gene expression does not necessarily correlate with protein expression or activity, the Sandwich ELISA method was used for the *in vitro* quantitative determination of the *c-myc* proto-oncogene protein, c-MYC, after 48 h exposure to STX1972 at IC_{50} (37.5 nM), Bzt-W41 at IC_{50} (20.4 µM) and STX + Bzt-W41 combination (STX1972 [CF] = 20.625 nM; Bzt-W41 [CF] = 6.12 µM). Results were obtained by means of spectrophotometry with OD values proportional to the concentration of c-MYC present. The concentration of c-MYC per sample was calculated by comparing the OD of the samples with the standard curve.

For the MDA-MB-231 cell line c-MYC protein expression was significantly decreased after treatments with STX1972 (≈0.5-fold), Bzt-W41 (≈0.2-fold) or the STX + Bzt-W41 combination (≈0.5-fold). These results mirror relative gene expression of *c-myc* in MDA-MD-231 cells. It is notable that the Bzt-W41 treatment resulted in greater reduction in protein expression versus that of the mRNA transcription level.

Bzt-W41 was the only treatment demonstrating a significant effect in the EA.hy926 cell line, reducing c-MYC expression (≈0.8-fold). Although significant, the decrease in protein concentration is much less pronounced than that observed for MDA-MB-231 cells treated with Bzt-W41, implying selectivity towards the TNBC cell line. When correlating these results to that of the RT-qPCR results (Section 3.10) it is evident that the significant increase in *c-myc* gene expression seen in STX1972 alone and combination-treated cells (Figure 3.40) was not equivalently translated to overexpression of the c-MYC oncoprotein.

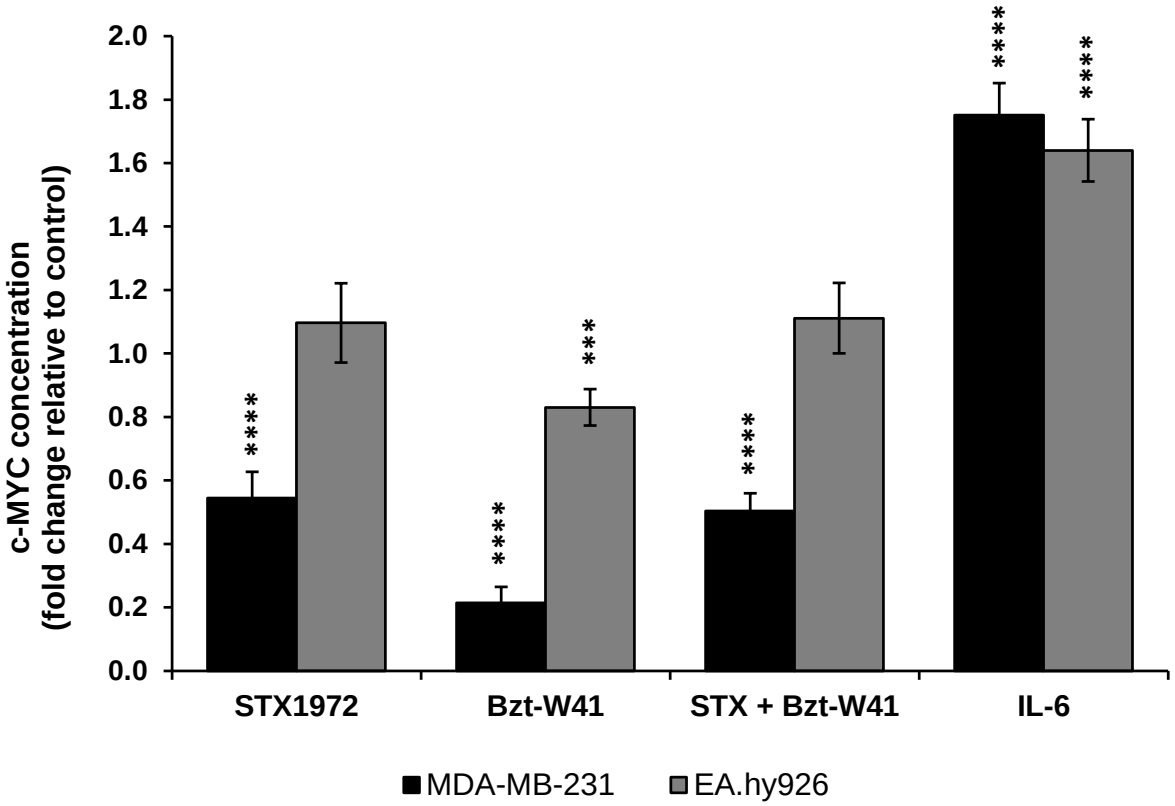

Figure 3.40: Relative c-MYC concentration in MDA-MB-231 and EA.hy926 cells after 48 h treatment with STX1972 at IC_{50} (37.5 nM), Bzt-W41 at IC_{50} (20.4 µM) and STX + Bzt-W41 combination (STX1972 [CF] = 20.625 nM; Bzt-W41 [CF] = 6.12 µM). IL-6 (50 ng/mL) was used as positive control. Results are expressed as fold change relative to vehicle control (normalized to one) and represent the mean fold change ± SEM of three biological repeats. *p ≤ 0.05, **p ≤ 0.01, ***p ≤ 0.001, ****p ≤ 0.0001 indicates a significant difference between the c-MYC concentration in vehicle control versus treated cells.

Chapter 4: Discussion

In the present study the *in vitro* antineoplastic activity of four classes of compounds each targeting different cancer-associated proteins was assessed using breast cancer cell lines as an experimental model. The initial test compounds included an antimitotic (STX1972), three variants of BRD4 inhibitors (Bzt-W41, Bzt-W49 and Bzt-W52), an inhibitor of SIRT1/2 (W137) and an inhibitor of JAK1/2 (Ruxolitinib). Following an initial screening study, three compounds (STX1972, Bzt-W41 and W137) were chosen and included in two combinations (C1: STX + Bzt-W41; C2: Bzt-W41 + W137) to test for synergy. Furthermore, the selectivity of the synergistic combinations was tested against a control cell line, EA.hy926, and the mechanism of action of the synergistic combination was probed using various methods.

4.1 STX1972

STX1972 is multi-targeted antimitotic compound designed to inhibit several cancer-associated proteins: CAII, CAIX, tubulin and STS. Molecular modelling and ligand-binding studies demonstrated that STX1972 successfully docks to binding sites on each of the intended target proteins (CAII, CAIX, tubulin and STS), validating that it is a polypharmacological agent. Glide SP docking software (Schrödinger-Maestro v12.1.013) proved effective STX1972-carbonic anhydrase binding, with the Zinc atom of CAII (PDB ID: 1CIL) and CAIX (PDB ID: 5FL6) interacting with the sulfonamide functional group of the ligand. For the STS target receptor (PDB ID: 1P49), the calcium ion in the active binding site interacts with the sulfonamide group of STX1972. The next protein, tubulin, is targeted at the colchicine binding site which is located at the edge of α- and β-tubulin monomers [240]. The colchicine binding site can accommodate a range of ligands with no apparent scaffold resemblance, however, even a slight change to a potent colchicine ligand can result in compromised binding and significantly reduced cytotoxic efficacy [240]. The STX1972-tubulin (PDB ID: 5OSK) binding pose superimposes well with that of A9Q, a similar antimicrotubule agent with potent inhibitory activity [215]. Separate studies have shown crosslinking of colchicine analogues to peptides in β-tubulin, including residues 1-36 and 216-243, as well as the Cys356 residue [90]. Other studies on colchicine binding site inhibitors have shown

interactions at Cys239, Leu246, Ala314, Asn256 and Lys350 residues of β-tubulin [240]. The RTF machine learning model predicts STX1972 to have sub-micromolar activity for all the tested enzymes, further supporting the notion that the compound is a polypharmacological agent.

Since cancer is a disease of hyperproliferation, selective inhibition of cell cycle progression has long been a relevant and amenable chemotherapeutic strategy [65,85-86]. Given the fundamental role of microtubules during cell division, mitosis-selective anticancer strategies are centralized around disrupting normal microtubule dynamics [85,87-88]. Microtubule-targeted agents are designed to suppress and/or disrupt microtubule function, thereby inducing mitotic arrest and eventually culminating in cell death [86,88]. To date, several oestrogen analogues have proven antimitotic activity [91-94]. 2-methoxyestradiol (2ME2, Panzem®), an endogenous metabolite of oestradiol exerts antimitotic and antiangiogenic effects but has low bioavailability and rapid metabolic breakdown [91,241]. The anticancer success of 2ME2 has encouraged the design of multiple oestradiol derivatives with the aim of increasing bioavailability for enhanced antitumour efficacy [93-95,160,242-243]. The effects of STX1972, a sulphamoylated 2ME2 derivative, on cell proliferation, morphology, cell cycle progression and cell death induction were investigated with the aim of elucidating the mechanistic mode of action of the compound. The research team involved in the synthesis of STX1972 reported on the compound's potent *in vitro* antiproliferative effects and *in vivo* anti-angiogenic activity [95]. Although there is consensus regarding the cellular outcomes of colchicine binding site inhibitors, i.e.: disruption of microtubule dynamics resulting in G_2/M cell cycle arrest and ultimately apoptosis induction; the precise pathways driving the cytotoxicity is not universally concurred.

Treatment with STX1972 single drug at the IC_{50} concentration significantly reduced growth of hormone-dependent and hormone-independent cancer cell lines in comparison to the non-cancerous control cell line, signifying cancer-specific targeting (see Section 3.2.3). Antiproliferative activity of the compound showed slight but non-significant selectivity for the TNBC cell line compared to the hormone responsive MCF-7 cell line, as similarly reported by the STX1972 founders [95]. Cancer-specific antiproliferative potency was observed at nanomolar concentrations, resembling results reported by the founding research group and making this one of the most potent

antimitotic compounds to date [95]. Several analogues of 2-substituted oestradiol-3,17-O,O-bis-sulfamates (E2bisMATEs) have also shown excellent *in vitro* antiproliferative activity against numerous tumorigenic cell lines [95]. Confocal microscopy demonstrated antimitotic effects of STX1972 on actively dividing MDA-MB-231 and MCF-7 cells comparable to that of the positive control, colchicine (see Section 3.3). This implies that STX1972 binds and inhibits tubulin in a similar manner to that of colchicine, namely inhibition of tubulin polymerization. Analogous anti-microtubule activity has been reported after treatment with 2-methoxyoestradiol-bis-sulphamate (2MEBM) and its parent analogue 2ME2 [244]; as well as other bis-sulphamate oestrone derivatives [242].

Cell cycle analysis revealed that STX1972 caused MDA-MB-231 and MCF-7 cells to arrest in the G_2/M phase, with the increased significance detectable after 8 h treatment (see Section 3.4). Similar cell cycle progression results have been found in studies with related oestradiol analogues, including 2-methoxyoestrone-3-O-sulphamate (2-MeOEMATE) [245], 2-ethyl-3-O-sulphamoyl-oestra-1,3,5(10),15-tetraen–17-ol (ESE-15-ol) [93] and STX140 [246]. After 48 h treatment the G_2/M block was still significant but less prominent in the MDA-MB-231 cell line; and negligible in the MCF-7 cell line. The observed reduction in G_2/M arrest after longer treatment could possibly be owed to the induction of cell death after the initial G_2/M block, implying incomplete cell cycle progression and less cells available to reach the subsequent G_2/M phase. Similar results have been reported by Stander *et al.* who found that MDA-MB-231 and MCF-7 cells exhibited an increase in the percentage cells in the G_2/M phase after 12 h and 24 h treatment with the oestradiol analogue, ESE-15-ol, but not after 48 h treatment [93]. The reduction of the G_2/M fraction for the MDA-MB-231 cell line after 48 h treatment was accompanied by a significant increase in the sub-G_1 population. The sub-G_1 phase corresponds to cells undergoing cell death and strengthens the aforementioned reasoning behind the plausible cause for G_2/M arrest reduction. For the MCF-7 cells there was a relative but non-significant increase in the sub-G_1 population. For the EA.hy926 cell line there was no evident G_2/M phase block after 8 h or 48 h treatment and negligible difference in the sub-G1 population in comparison to the DMSO control, signifying cancer cell selectivity. Annexin V analysis confirmed that STX1972 induced apoptosis after 48 h treatment. The assay revealed a significant increase in the proportion of MDA-MB-231 and MCF-7 cells in early and late apoptosis. The effect

was more pronounced in the cancer cell lines compared to the EA.hy926 control cell line. The ability of antimitotic compounds to induce apoptosis in tumorigenic cell lines *in vitro* has been shown in previous studies [94,241,245,247]. In summary, the cell cycle and Annexin V results indicate that STX1972 treatment is able to induce a mitotic block, followed by apoptosis. It also indicates that the tumorigenic cell lines are preferentially targeted for apoptosis with the EA.hy926 control cell line showing less cytotoxic sensitivity to this compound.

Quantitation of AO-stained cells revealed a significant increase in the AO-positive population in STX1972-treated MDA-MB-231 cells, with the effect being less pronounced in the EA.hy926 cells (see Section 3.6). The red AO-positive population was determined by means of the ratiometric R/GFIR method as described by Thomé *et al.* [225]. According to this method an increased red AO-positive population correlates with an increased volume of acidic organelles such as autolysosomes and could be correlated with autophagy induction [225]. The authors validate the ratiometric analysis of AO as a quantitative measure of late stage autophagy, however, this study did not confirm the increased red AO population as an exclusive measure of autophagy. This initial method of AO evaluation needs to be complemented by further methods in order to confirm the extent of autophagy induction and explore the possibility that the increased AO could be caused by other phenomena such as increased lysosomal activity without autophagy induction; and/or early stages of lysosomal rupture. Lysosomal injury is a form of cell death and has been reported to be induced by oestradiol analogue ESE-16 in breast cancer cells [94]. Separate studies have also proven the ability of antimitotic analogues to induce autophagy *in vitro* in tumorigenic cell lines [248-249].

Evaluation of intracellular ROS generation after 48 h STX1972 treatment demonstrated a significant increase (>1.4-fold) in ROS production in MDA-MB-231 cells, an effect not seen in the control cell line (see Section 3.7). This is in accordance with results from Stander *et al.* who reported that 24 h treatment with the oestradiol analogue, ESE-16 (200 nM), resulted in a significant and prominent increase in ROS in MDA-MB-231 tumorigenic cells [94]. Treatment of MCF-7 cells with 2ME2 have also revealed similar results to the current findings, increasing ROS generation by ≈1.5-fold in comparison to the vehicle-treated control [250]. ROS generation has been

implicated in the activation and mediation of apoptotic and autophagic processes culminating in cell death [241]. However, intracellular ROS does not exclusively culminate in cell death induction since transient signalling is paradoxically associated with pro-survival pathways [65,251]. Apoptotic signalling initiated via ROS overload leads to the programmed demise of cells via intrinsic mitochondrial and/or ER-regulated signalling pathways [65]. Furthermore, although it is widely accepted that ROS participates in the regulation of autophagy, the exact mechanisms involved in switching from pro-survival to pro-death autophagy remains to be fully elucidated [251].

Mitochondrial membrane permeabilisation and subsequent depolarization is associated with apoptosis induction [94]. Stander *et al.* (2012) and Stander *et al.* (2013) reported that oestradiol analogues ESE-15-ol [93] and ESE-16 [94] induced mitochondrial membrane dissipation and associated apoptotic signalling in MDA-MB-231 and MCF-7 cells. Results from the current study are in accordance with these findings, demonstrating STX1972-induced mitochondrial membrane depolarization after 48 h treatment, with more pronounced effects in the tumorigenic versus the control cell line (see Section 3.8). Bcl-2 is a member of the Bcl-2 family which regulates mitochondrial membrane potential and mitochondrial mediated apoptosis induction. Dephosphorylation of Bcl-2 at serine 70 is associated with initiation of apoptosis and an overall decrease in the protein expression of Bcl-2 is also considered pro-apoptotic [229]. Stander *et al.* reported that ESE-15-ol treatment (50 nM) abrogates the phosphorylation status of Bcl-2, culminating in intrinsic apoptosis induction in MDA-MB-231 cells [93]. In accordance with these findings, the current study found STX1972 treatment to significantly reduce the p-Bcl-2 (ser70) cell population and increase the number of dephosphorylated Bcl-2 cells in comparison to the vehicle control in the TNBC cell line (see Section 3.9). An increase in the phosphorylation of Bcl-2 at serine 70 inhibits apoptosis, while dephosphorylation is pro-apoptotic [229]. The phosphorylation status of the control cell line (EA.hy926) remained the same as that of the vehicle control. This indicates that STX1972 has a similar mechanism of action to that of antimitotic oestradiol analogues. Inhibiting the phosphorylation of Bcl-2 is one of the many suggested mechanisms of apoptosis induction of microtubule inhibitors [252].

Relative quantification of mRNA transcription levels in MDA-MB-231 cell lines after 48 h exposure to STX1972 revealed a significant increase in *bcl-2* expression, whilst significantly downregulating *c-myc* expression. Since gene expression does not necessarily correlate with protein expression or activity, the sandwich ELISA method was used for the *in vitro* quantitation of the *c-myc* proto-oncogene protein, c-MYC, after exposure to STX1972. ELISA results mirror that of *c-myc* gene expression in MDA-MB-231 cells, with significantly decreased c-MYC protein expression. For the EA.hy926 cell line it was evident that the significant increase in *c-myc* gene expression seen in the STX1972-treated sample was not equally translated to overexpression of the c-MYC oncoprotein (see Section 3.10 and 3.11).

4.2 BRD4 inhibitors (Bzt-W41, Bzt-W49 and Bzt-W52)

Epigenetic regulators have received considerable interest as amenable anticancer targets. BRD proteins are involved in transcriptional regulation and also play a key role in cell cycle progression [111]. BRD4, a member of the BRD epigenetic regulator family, is overexpressed in many cancers and is notoriously implicated in tumorigenesis [109,111-112,115]. BRD4 permits excessive transcription of key cancer-promoting genes, including *cdk9*, *c-myc* and *bcl-2* resulting in increased expression of oncoproteins involved in anti-apoptosis, growth promotion and metastasis and invasion [109,112,167-168,195]. BRD inhibiting agents such as JQ1, I-BET151 and IBET762 have proven therapeutic potential for the treatment of various cancers and has provided impetus to the design and development of novel BRD inhibitors with clinically translatable anticancer efficacy [115,124-131,163,253]. This study investigated the effects of three novel BRD4 inhibitors (Bzt-W41, Bzt-W49 and Bzt-W52) which were designed to subvert transcription of proto-oncogenes by binding to the acetyl-lysine binding motif of the bromodomain protein. Molecular modelling studies by means of Glide SP docking software (Schrödinger-Maestro v12.1.013) proved acceptable ligand docking of Bzt-W41 and Bzt-W49 to the BRD4 active site. Of the six X-ray crystallographic structures screened, BRD4 (PDB ID: 2yel) delivered the best binding pose with the lowest energy for both ligands. The BRD4 - Bzt-W41 complex superimposes well with that of JQ1, a similar BRD4 inhibitor agent currently being tested in several clinical trials. Hydrogen interaction and close association with Tyr139 and Asn140 residues as well as two

amino acid regions: residues 81 - 87 and 145 - 149 are important for optimal binding to the active site of BRD4 (see Section 3.1.1).

Following an initial screen for antiproliferative effects, the most potent benzotriazepine analogue(s) were included in morphology change, cell cycle progression, and apoptosis induction studies. With the aim of deducing the possible mechanism of action, effects on the expression of *c-myc* and *bcl-2* genes and proteins was also investigated. Cell proliferation studies revealed sufficient antiproliferative effects for all three BRD4 inhibitors at µM concentrations ranging between 20 µM – 140 µM (see Section 3.2.1). Bzt-W41 proved to be the most potent of the three analogues, reducing cell growth to 50% at significantly lower concentrations than that of Bzt-W49 and Bzt-W52 in both MDA-MB-231 and MCF-7 cell lines. This corresponds to results obtained from the chemiluminescent binding assay wherein Bzt-W41 demonstrated the most effective BRD2 and BRD4 protein inhibition at the lowest concentration in comparison to Bzt-W49 and Bzt-W52 [138,164]. All three BRD-4 inhibitor compounds show significant antiproliferative selectivity towards the TNBC cell line in comparison to the hormone-dependent cell line. Bzt-W41 is approximately 4-fold more selective towards the MDA-MB-231 cell line compared to the MCF-7 cell line, proving the highest selectivity of the three analogues. These data confirm that data from Mqoco *et al.* (2019) whereby, Bzt-W41 (ITH-47 in Mqoco *et al.* (2019)) shows selectivity towards MDA-MB-231 cells at similar concentration ranges (MDA-MB-231 GI_{50}: 15 µM, MCF-7 GI_{50}: 75 µM) [254]. Preferential sensitivity of TNBCs to BRD protein inhibition in comparison to ER^+ luminal and $Her2^+$ subtypes has also been reported by Shu *et al.* [255].

Cell cycle analysis revealed an apparent but non-significant increase in the proportion of MDA-MB-231 cells in the G_1 phase after 48 h exposure to Bzt-W41, while a negligible difference was seen in MCF-7 and EA.hy926 cells in the same phase. Furthermore, in all three cell lines, Bzt-W41 exposure did not result in an increased sub-G_1 population, implicating possible cytostatic rather than cytotoxic effect of the inhibitor (see Section 3.4). JQ1, the class prototype BET inhibitor, has been reported to deliver more pronounced G_1 cell cycle arrest, but similar sub-G_1 effects after 48 h of treatment [256]. Trabucco *et al*. found that nanomolar exposure of four diffuse large B-cell lymphoma (DLBCL) cell lines to JQ1 significantly increased the G_1 population but resulted in nonsignificant sub-G_1 population expansion, suggesting cell cycle

arrest with minimal cell death after 48 h treatment [256]. The same study investigated the effects of longer JQ1 treatment on cell cycle progression and found that 96 h exposure increased the sub-G_1 population in two of the four DLBCL lines, whilst 7-days of treatment was still insufficient to cause significant sub-G_1 increase in one of the cell lines [256]. The researchers further reported that initial G_1 cell-cycle arrest was followed by either apoptosis or senescence after longer (7-day) treatment with JQ1 [256]. Shu *et al.* found that 72 h treatment of the TNBC line (SUM159) with JQ1 (500 nM) resulted in G_1 arrest and apoptosis [255]. Similar results were reported by Vázquez *et al.* who showed that the BRD-4 inhibitor OTX015 induced an increase in the percentage of cells in G_1 phase after 72 h exposure, but with no evidence of senescence or apoptosis in any of the three TNBC lines tested [257]. Likewise, the apoptosis assay results from the current study revealed no significant increase in early or late stage apoptosis in either of the cell lines (see Section 3.5), corresponding to the cell cycle analysis results for the sub-G_1 phase. Results propose the possibility that BRD inhibitors have slow onset of action and that longer exposure to Bzt-W41 could deliver more evident G_1 arrest and perhaps increase the likelihood of apoptotic cell death or senescence. Varied results found in literature suggests that BRD inhibitors are distinctly specific. Related BRDi analogues show differential results when effects are compared within a specific TNBC line and when comparing the effects of a single BRD inhibitor across multiple TNBC cell lines preferential sensitivity of TNBC subtypes is evident [255,257]. Furthermore, preferential selectivity of the BRD inhibitor towards BRD4 versus BRD2 could also contribute to the varied effects observed for this class of inhibitors. Chemiluminescent assay results reveal no significant BRD4 selectivity compared to that of BRD2 for the JQ1 compound. However, Bzt-W41 is 2.28-fold more selective towards BRD4 in comparison to BRD2, but more than 10-fold less potent than JQ1 [138]. It is plausible to argue that the differences in potency and selectivity of these two BRD-4 inhibitor compounds contribute towards their differential effects.

AO quantitation after 48 h exposure of the MDA-MB-231 cell line to Bzt-W41 showed a significant increase in percentage cells in the red AO-positive population (10.62-fold) when compared to the DMSO control treatment (see Section 3.6). Although the ratiometric increase of AO could be correlated with increased autolysosomes and therefore possible autophagy activation [225], further assays need to complement this analysis in order to confirm autophagy and/or lysosomal stress. However, BRD4 is a

recognized transcriptional repressor of autophagy and lysosomal function and BRD4 inhibition promotes autophagy gene activation which induces several types of autophagy [258]. Sakamaki *et al.* reported that BRD4 silencing leads to increased autophagosome accumulation and autophagic flux *in vitro* and *in vivo* [258]. Consistent with BRD4 knockdown results, BRD4 inhibition by JQ1 was found to activate autophagy *in vitro* and *in vivo* while exposure to the BET degrader ARV-825 also induced autophagic flux [258-259]. Collectively, these results implicate BRD4 as a negative regulator of autophagy and validates the use if BRD4 inhibitors for autophagy modulation as a plausible therapeutic strategy for cancer [258,260].

Flow cytometric analysis of mitochondrial membrane potential revealed that 48 h exposure to Bzt-W41 results in significant mitochondrial membrane depolarization in MDA-MB-231 cells but not in the control cell line (see Section 3.8). Likewise, Ishida *et al.* reported that T98G glioblastoma cells showed mitochondrial membrane potential dissipation following 72 h treatment with BRD inhibitors JQ1 (5 µM) and the derivative OTX015 (5 µM) [261]. The mitochondrial membrane depolarization observed in the MDA-MB-231 cells could possibly be linked as a causative factor for the increased late apoptosis observed. Both JQ1 and OTX015 have also been found to downregulate *c-myc* transcriptional activity in several cancer models including TNBCs [262]. Preferential c-MYC overexpression in basal-like TNBCs correlates to tumorigenesis and poor prognosis, thereby validating the therapeutic potential of *c-myc* repression and subsequent inhibition of c-MYC oncoprotein expression [125,262]. BRD4 has also been implicated in the transcriptional regulation of *bcl-2* and subsequent downstream effectors, which is equally associated with cancer cells [263]. Relative gene expression results from the current study revealed that Bzt-W41 treatment significantly reduced both *c-myc* and *bcl-2* oncogene expression in MDA-MB-231 cells. Although less prominently so, *c-myc* expression was inhibited in the EA.hy926 cell line and *bcl-2* inhibition was similar in both cell lines. Protein expression results revealed a likewise decrease in c-MYC oncoprotein expression in MDA-MB-231 cells after Bzt-W41 exposure, again proving less prominent in the EA.hy926 cell line. Despite significantly reduced *bcl-2* mRNA levels, Bcl-2 protein levels appeared unaffected in both cell lines. These results are in part contradictory to the findings of Wu *et al.* who reported that BRD4 inhibition by JQ1 and BRD4 knockdown suppressed *bcl-2* and *c-myc* mRNA expression and protein levels in renal cell carcinoma cells [263]. Tan *et al.* similarly

reported that *c-myc* and *bcl-2* genes were downregulated in prostate cancer cells in response to treatment with BRD4 inhibitor JQ1 [264]. Mertz *et al.* investigated the effects of JQ1 on several leukemia and lymphoma cell lines, reporting a reduction in *c-myc* transcript and protein levels resulting in G_1 arrest and an extensive increase in apoptosis [125]. In the same study, authors revealed somewhat different results for the MDA-MB-231 cell line indicating that although there was significant reduction in c-MYC protein levels, no cytotoxic effects were observed, irrespective of high-dose JQ1 treatment [125]. This is in line with the findings in this study, indicating a possible mechanistic overlap in the distinct antiproliferative action of Bzt-W41 and JQ1 on MDA-MB-231 breast cancer cells. The antitumor activity of BRD inhibitors is unequivocal, however, the drivers behind the downstream responses to these inhibitors vary depending on tumour type, with notable variation even within a defined sub-type such as TNBC [265]. Therefore, when probing to deduce the mechanism of action of BRD inhibitors the distinct TNBC model investigated has to be taken into consideration. Nonetheless, the anticancer advantage of this class of inhibitor is two-fold. First, its preferential selectivity towards various TNBC subtypes renders it a viable treatment option for this heterogeneous and highly aggressive form of breast cancer, as shown by our own and other's work [262,265-266]. Second, BRD inhibitors have been implicated in overcoming acquired resistance to FDA-approved therapies [267].

4.3 W137

Of late, sirtuins (SIRTs) have evoked interest as plausible cancer targets due to their putative roles in conferring cancer cells the abilities of survival, proliferation, angiogenesis and drug resistance [139,141]. SIRT 1/2 have been particularly implicated in breast cancer and identified as novel molecular therapeutic targets [268]. To date, the effects of several SIRT-specific inhibitors have been investigated, including spitomicin [269], sirtinol [270], cambinol [271], dihydrocoumarin [272] and a series of indole derivatives [273]. Although these SIRT inhibitors show mutual anticancer activity, their mechanisms of action vary and remain to be fully elucidated [268]. In this study the effects of a novel sirtuin inhibitor, W137, on cell growth, morphology, cell cycle progression and apoptosis were investigated.

W137 was designed to target SIRT 1/2-mediated p53 deacetylation with preferential SIRT1/2 compared to SIRT3 targeting. Molecular modelling studies proved successful ligand docking of W137 to SIRT 1, 2 and 3 active sites as performed by means of Glide SP docking software (Schrödinger-Maestro v12.1.013) (see Section 3.1.1). Of the six X-ray crystallographic structures screened, SIRT1 (PDB ID: 4ZZI) delivered the best binding pose with the lowest Glide score and lowest predicted Ki for the ligand. The thieno carboxamide hydrogen bonds are preserved for all three SIRTs similar to previously described thieno carboxamide pan-SIRT inhibitors 1NQ, 1NR and 1NS [177,235]. Unlike these pan-SIRT inhibitors, W137 is at least 7 times more selective towards inhibiting SIRT1 and 2 compared to SIRT3 [274]. A major difference between the docking poses of W137 against SIRT1-3 is the presence of a hydrogen bond between PHE (SIRT1: PHE273, SIRT2: PHE46) and the thieno aromatic ring which is absent for the W137-SIRT3 binding pose. This in part can explain the selectivity found in the RTF predictive model and the biological data.

Cell viability studies revealed that W137 significantly reduced the growth of MDA-MB-231 and MCF-7 cells in a concentration dependent manner. The IC_{50} values after 48 h of W137 exposure were 23.5 µM and 24.1 µM respectively, implicating no preferential selectivity between the hormone-dependent and hormone-independent cell models (see Section 3.2.1). Likewise, Sirtinol has been reported to reduce MCF-7 cell growth to 50% after 48 h treatment at a concentration of 43.5 µM [268]; and 100 µM Salermide treatment reduced MDA-MB-231 cell growth to 50% after 24 h treatment [275]. To probe the mechanistic action driving the cytotoxicity of the W137 compound, cell cycle analysis and apoptosis assays were performed (see Section 3.4). Quantitation of cell cycle phases revealed that MDA-MB-231 and MCF-7 cells treated with W137 for 8 h and 48 h showed a significant increase in the sub-G_1 fraction of cells. The increased sub-G_1 population was also apparent in the control cell line after 8 h treatment. The second evident influence of W137 on cell progression was a significantly reduced G_1 population in both MDA-MB-231 and MCF-7 cell lines after 48 h treatment, but not in the EA.hy926 cell line. The deacetylation of p53 by SIRT1, leading to its subsequent deactivation and loss of function has been implicated in desensitization to cell death tumorigenesis [276-277]. SIRT1 inhibition therefore aims to abrogate the deacetylation of p53, allowing activation of apoptotic pathways. Supporting studies within the research team have conducted p53 protein expression

studies on W137 and have reported significantly increased p53 acetylation after 48 h treatment of SH-SY5Y neuroblastoma cells, validating the involvement of p53-related apoptotic pathways in the antitumor effects of W137 [274]. In the current study, the apoptosis assay revealed that 48 h treatment with W137 induced strong apoptosis (see Section 3.5). Early apoptosis was significantly increased in MDA-MB-231 and MCF-7 cells but not in the control cell line. However, the notoriously prominent late apoptosis induction was not cancer specific. In part contradictory to these findings, Lara *et al.* found that Salermide induced strong apoptosis without any evident effect on the cell cycle in all the cancer cell lines analysed but not in non-tumorigenic MRC5 cells [275]. Contrary to this, the parent molecule (sirtinol) was reported to significantly increase the sub-G_1 phase of the cell cycle and induce both apoptotic and autophagic cell death in MCF-7 cells [268]. Conflicting results found in the literature could possibly be attributed to the varied activity of sirtuins in distinct cell types and cell states; the ubiquitous expression of some SIRTs; and their diverse effects on pathologies via multiple downstream and often overlapping targets [278]. Moreover, much of the research focussed on the effect of SIRT modulators on SIRTs in isolation, but not exploring the possibility that other SIRT proteins contributed to the mechanistic effects, although not intentionally targeted [278]. For instance, molecular docking and *in vitro* studies render the SIRT inhibitor Salermide most effective against SIRT2, however, results suggest that it's *in vivo* biological role is independent of SIRT2 [275]. Since the SIRT protein family shares a conserved catalytic core it poses a challenge in the design and development of novel compounds aimed at interacting with a single SIRT isoform [279-280]. To further add to the confusion both SIRT activation and SIRT inhibition have been reported to confer beneficial effects in pathologies, hence SIRT activators and SIRT inhibitors are in various stages of investigation and development [278]. Adding to the complexity of SIRT modulation, and as mentioned previously, SIRTs have been observed to induce varied responses across cell types. More specifically to breast cancer, SIRT1 has been implicated as both a tumour promoter and suppressor depending on the breast cancer subtype [143,281]. This implies that successful pharmacological targeting of breast cancer by means of SIRT inhibitors requires investigation of the distinct molecular tumour subtype.

The current study reveals that the antiproliferative capacity of the novel SIRT1/2 inhibitor, W137, is attributed to prominent apoptosis induction which is likely due to

p53 stabilization and activation. However, the compound's lack of selective toxicity deemed it infeasible for further study. This warrants that the compound be tested against other cell lines and also being further refined to deliver cancer-targeting analogues with similar apoptotic potency.

4.4 Combination studies

Conventional therapeutic strategies fail to induce highly cancer-selective cytotoxicity and are often overcome by acquired resistance. Targeted therapy preferentially sensitizes cancer cells to their dysfunction and/or demise, addressing one of the pitfalls of traditional treatment approaches. However, therapeutic resistance remains a concern, especially in TNBC subtypes having complex intratumor heterogeneity. The lack of successful conventional and targeted treatment options for this precarious subtype prompted the investigation into combination therapy as a possible treatment option. The advantages of combination therapy include reduced toxicity with more potent anticancer effects and circumventing drug resistance by concurrently targeting several cancer hallmarks. The current study screened four paired combination options, each combined in various combination ratios of the single drug IC_{50} concentrations. Results revealed that two of these combinations, STX + Bzt-W41 and Bzt-W41 + W137, exhibited slight to moderate synergism [182] with CI of 0.85 and 0.9, respectively, for inhibiting 50% growth in MDA-MB-231 cells. This is similar to the CI reported by Mcoqo *et al.* (2019) whereby a CI of 0.7 was reported against MDA-MB-231 cells for the less potent estradiol antimitotic, ESE-15-ol and Bzt-W41/ITH-47 [254]. In the present study the 0.55 * STX1972 [IC_{50}] + 0.3 * Bzt-W41 [IC_{50}] ratio with CFs of 20.625 nM for STX1972 and 6.12 µM for Bzt-W41 was found to be the most effective. These ratios reported by Mcoqo *et al.* (2019) against MDA-MB-231 cells are 0.2 * ESE-15-ol [GI_{50}] + 0.5 * Bzt-W41/ITH-47 [GI_{50}] ratio with CFs of 14 nM for ESE-15-ol and 6.12 µM for Bzt-W41/ITH-47. It is interesting to note that in our study the antimitotic CF ratio (0.55) was higher compared to the BRD4 inhibitor CF ratio (0.3) while the ratios reported by Mcoqo *et al.* (2019) the BRD4 inhibitor CF ratio (0.5) was higher compared to the antimitotic CF ratio (0.2) [254].

The third combination (STX + W137) did not show synergism in any of the combination ratios for any of the combination indexes tested, including the highest CI of 0.95. This combination is therefore presumed to be additive (CI 0.95 – 1.05) or, most probably, antagonistic (CI >1.05) [182], although this was not further explored since the goal of the study was to test synergistic drug combinations. Of note, determination of the CI can be done for any chosen effect level or growth inhibitory concentration, i.e: low growth inhibition of 25% or high growth inhibition of 75% or even 100%. Chou suggests effect levels may influence drug interactions, with drug combinations presenting as antagonistic or synergistic at low or high effect levels, respectively [222]. Since the goal of dual therapy is cancer eradication, synergism at high effect levels ($IC_{>75}$) is more relevant to cancer treatment. However, mechanistic *in vitro* evaluation at these high effect levels is not feasible and therefore the chosen effect level for the paired drug combinations in this study was 50% growth inhibition (IC_{50}). After the initial screen for antiproliferative effects, only two synergistic combinations were further investigated, probing to elucidate the probable mechanism of action driving the growth inhibition.

4.4.1 Bzt-W41 + W137

The effects of the Bzt-W41 + W137 combination on morphology, cell cycle progression and apoptosis in both MDA-MB-231 and MCF-7 cells were compared to effects induced in EA.hy926 cells. Combining a BRD-4 inhibitor and a SIRTi implies dual targeting of two groups of epigenetic regulators. The literature does not report on the combined anticancer effects of these two classes of drugs. However, the first functional connection between BRD inhibitors and the histone deacetylase (HDAC), SIRT1, was reported by Kokkola *et al.* wherein they reported that BRD inhibition upregulates SIRT1 and inhibits an inflammatory response [282]. The authors found that JQ1 treatment activated SIRT1 in cancerous A549 and MCF-7 cells, as well as in non-cancerous (HEK293) cells [282]. Sakamaki *et al.* have also implicated SIRT1 to play a role in the dissociation of BRD4 from autophagy gene promoters leading to de-repression of autophagy related transcription during starvation [258]. The aforementioned studies only focus on the interaction of SIRT1 and BRD4, however, HDACs are ubiquitously expressed and often share substrates, and many of their biological roles are not fully understood, implying the possibility of more elaborate overlap between these epigenetic classes than currently known. It has also been

debated whether the clinical development of multi-potent HDAC inhibitors may hold more anticancer potential than that of highly selective HDAC suppressors, although the latter will aid to decipher the biological activities of the HDACs [283]. Nonetheless, the combination of two major classes of epigenetic regulators provides a novel anticancer strategy for the targeting and regulation of gene activity. In the current study the Bzt-W41 + W137 combination proved significant antiproliferative effects with preferential TNBC cell line selectivity. In probing the mechanism of action behind the cytotoxic effects of the combination, cell cycle progression was analysed and results revealed only one significant effect of 48 h treatment on both of the cancer cell lines namely, increased proportion of cells in the G_2/M fraction. This effect was not seen in the EA.hy926 cell line, instead a significant increase in the sub-G_1 population was evident after 8 h of combined test compound treatment of the control cell line. These findings do not resemble the cell cycle effects reported for either of the single-treated samples implying the possibility of a different mechanism of action for the combination. Results from the apoptosis analysis was similar to that of W137 as a single drug treatment, revealing prominent apoptosis in both early and late stages, with the latter being most evident. Among the three cell lines, the control cell line showed the largest late apoptotic population. These findings indicate this specific BRDi-SIRTi combination as not being a cancer-selective therapeutic option. As with the W137 compound in isolation, the W137-combination was also deemed infeasible for further investigation.

4.4.2 STX + Bzt-W41

The effects of the STX + Bzt-W41 combination on morphology, cell cycle progression, and apoptosis induction and expression of *p53*, *c-myc* and *bcl-2* genes in both MDA-MB-231 and MCF-7 cell lines were investigated. The literature suggests that co-treatment of BRD inhibitors with other targeted epigenetic therapies may induce a more durable antitumor response [267,284]. Liu *et al*. undertook a chemical library screening with the aim of identifying small molecule compounds which exert high synergistic anticancer effects when combined with BRD-4 inhibitor JQ1 [284]. The authors reported anti-microtubule drugs as one of two major classes of agents which showed the best synergistic antitumour effect with JQ1 [284]. Of the nine antimitotic drugs screened, vincristine, an FDA-approved agent with a similar mechanism of action to that of STX1972, proved to have the strongest synergistic activity [284]. Their

results suggest that JQ1 and vincristine synergistically induce apoptosis in neuroblastoma cells, but not in normal cells, by means of G_2/M cell cycle arrest and destabilization of microtubules [284]. In this study the STX + Bzt-W41 combination did result in a G_2/M arrest in MDA-MB-231 cells after 8 h treatment, implying that the effect of the STX1972 CF concentration resembles that of STX1972 single treatment. Of note, the G_2/M arrest was not translated to the 48 h treatment results. Instead, cell cycle analysis revealed a significant increase in the G_1 population in MDA-MB-231 cells after 48 h, indicating a more pronounced G_1 arrest than that of Bzt-W41 alone. Furthermore, neither of the cell cycle arrests seen at 8 h or 48 h treatment was accompanied by an increase in the sub-G_1 cell population. For the MCF-7 cells, however, the only notable effect was an increase in sub-G_1 population, but with none of the cell cycle arrests noted for the TNBC line. For the EA.hy926 cell line, 48 h treatment with STX + Bzt-W41 resulted in a significant reduction in the G_1 phase cell population, but no increase in the sub-G_1 cell population. Apoptosis results show significant increase in early apoptosis for both cancer cell lines; an increase in late apoptosis only in the TNBC line; and no significant increase in early or late apoptosis in the control cell line. These results resemble that of STX1972 treatment alone and are consistent with the findings of Liu *et al.* [284]. Quantitation of AO revealed a significant increase in red AO-positive cells in the MDA-MB-231 cell line in comparison to the EA.hy926 cell line. The increase seen for the combination treatment exceeds that of compounds in isolation, confirming synergistic effect of dual treatment. This suggests that combined treatment leads to the activation of pathways which possibly induce autophagy, in addition to apoptosis, as a second mechanism of cell death. Combination treatment was found to induce mitochondrial membrane depolarization in both MDA-MB-231 and EA.hy926 cells, however, more prominently so in the cancer cells. The depolarization caused by single drug treatments surpassed that of the combination treatment. ROS formation was not significantly increased in MDA-MB-231 or EA.hy926 cells following combination treatment and the effect was found to be similar to that of Bzt-W41 treatment alone, but significantly lower in comparison to STX1972 treatment alone. This implies that synergistic effects are not translatable to ROS-induced pathways and that STX1972-induced formation of ROS is possibly constrained to a concentration threshold. Investigation of the phosphorylation status of Bcl-2 at serine-70 showed no significant difference for either of the cell lines after combination treatment. This is in contrast to STX1972 treatment alone, which led to

significant Bcl-2 dephosphorylation in MDA-MB-231 cells. Again, implying that STX1972 related activity is possibly concentration dependent. Furthermore, gene expression studies revealed no significant change in *bcl-2* expression in MDA-MB-231 or EA.hy926 cells. This implies that the apoptosis seen in the MDA-MB-231 cells is unrelated to *bcl-2* or downstream protein expression. In contrast, *c-myc* mRNA expression was significantly reduced following combination treatment of MDA-MB-231 cells. Interestingly, *c-myc* mRNA levels were significantly increased in the EA hy926 cell line but did not translate to significantly altered c-MYC protein expression as seen from the ELISA results. Combination treatment resulted in significantly decreased c-MYC protein expression in MDA-MB-231 cells with inhibition less than that of Bzt-W41 treatment but similar to that of STX1972 treatment alone. Previous studies have found that the inhibition of c-MYC activity leads to G_1 arrest through loss of cyclin E/CDK 2 kinase activity [285]. Furthermore, *c-myc* repression through inhibition or transcriptional inactivation has been linked to mitotic catastrophe and cell death *in vivo* [286]. The International Nomenclature Committee on Cell Death describes mitotic catastrophe as an intrinsic oncosuppressive mechanism which drives mitosis-incompetent cells to a form of regulated cell death or cellular senescence [62,286]. Mitotic catastrophe could be implicated as a possible mediator of the synergistic interaction between STX1972 and Bzt-W41. STX1972 is an antimitotic which interferes with microtubule dynamics, leading to abrogated mitosis, mitotic catastrophe and ultimately mitotic death. Likewise, Bzt-W41 potently inhibits *c-myc* mRNA expression that leads to mitotic catastrophe-induced cellular demise. An interesting connection has been noted between BRD4 dynamics and drug-induced mitotic stress which could further explain the synergism observed for the STX + Bzt-W41 combination treatment. During mitosis BRD4 localizes to chromosomes and predominantly resides along the long axis of the mitotic chromosomes [172,176]. However, BRD4 is rapidly released from chromosomes upon treatment with antimicrotubule drugs, including Nocodazole [176]. Nocodazole has a similar antimitotic effect to STX1972, causing microtubule depolymerization and mitotic arrest. Although the exact mechanism and biological relevance of the BRD4 release remains to be elucidated, it is thought to mediate protection from drug-induced mitotic stress [176,287] and possibly play a role in antimitotic resistance. This implies that antimitotic treatment with simultaneous inhibition of BRD4 release could enhance mitotic arrest and halt cell division, ultimately sensitizing cells to death. Whether or not the Bzt-W41 compound is able to cause BRD4 dissociation and partake in the

chromatin dynamics during STX1972 exposure is beyond the scope of this study but undoubtedly worthy of future investigation when aiming to fully elucidate the synergistic interaction. Another possible synergistic connection was highlighted by da Motta *et al.* who recently reported that JQ1 is able to target the hypoxic response of TNBC via epigenetic downregulation of hypoxia-induced genes, including CAIX [288]. Since CAIX is one of the STX1972 targets this provides another explorable connection between STX1972 and Bzt-W41 and the synergism observed. Furthermore, da Motta *et al*. also found that the BRD-4 inhibitor JQ1 inhibited xenograft vascularization, proving its anti-angionenic effect [288]. Similarly, Jourdan *et al.* reported that STX1972 exhibits significant *in vivo* anti-angiogenesis [95]. Again, aligning the anticancer effects of these two drug classes and highlighting the possible augmented anticancer potential of dual therapy as opposed to monotherapy.

4.5 Proposed mechanism of action of STX1972 on MDA-MB-231 cells

STX1972 has proven to be a polypharmacological agent, however, the focus of the current study was on the anti-tubulin activity of the antimitotic compound. The compound showed potent and preferential antiproliferative effects against the TNBC breast cancer cell line in comparison to the control cell line. Results imply the possibility that the cytotoxic consequences of STX1972 treatment are induced by both apoptotic and autophagy/lysosomal related pathways. STX1972 appears to induce these cell death pathways via multiple initiation points, namely: microtubule depolymerisation, G_2/M arrests, increased ROS formation, mitochondrial membrane depolarization, Bcl-2 dephosphorylation and suppression of *c-myc* transcription and translation (Figure 4.1). STX1972 targets the colchicine binding site of tubulin, resulting in the inhibition/disruption of tubulin polymerization in actively dividing cells which marks a G_2/M cell cycle arrest and related cell death, a familiar phenomenon among antimitotic agents [93,289]. The mitotic block and associated prolonged CDK1/cyclin B activity has been correlated with ROS signalling, implicating the G_2/M block and resulting cell stress as the source of ROS accumulation [65,94]. However, some studies have also implicated ROS as a causative factor in cell cycle arrest, rather than a result thereof. Park *et al.* found that scavenging of intracellular ROS permitted G_2/M cell cycle departure and concluded that ROS induced G_2/M arrest and apoptosis

via inhibition of the PI3K/Akt pathway [290]. Whether the ROS accumulation seen in the current study was caused by the mitotic block, or whether it contributed to the G_2/M cell cycle arrest remain to be elucidated, however, STX1972 was shown to be a ROS-stimulating compound. Excess ROS formation is known to induce caspase-mediated apoptosis via several mitochondrial and endoplasmic reticulum-regulated pathways [65]. The mitochondrial-related pro-apoptotic consequences of ROS include permeablization and subsequent depolarization of the mitochondrial membrane; release of cytochrome c; and activation of caspases 9, 3 and 7 [65]. ROS has also been implicated as a critical integration factor between mitochondrial and lysosomal death pathways [291]. ROS-dependent inhibition of the pro-survival PI3/Akt signalling pathway could be another mechanism to induce cell death via both apoptosis and autophagy [65,290,292]. STX1972 was found to increase the amount of dephosphorylated Bcl-2. The pro- and anti-apoptotic function of Bcl-2 is complex and closely related to its phosphorylation status. Studies have proven that phosphorylation at serine-70 enhances Bcl-2's potent anti-apoptotic function and that dephosphorylation, and thereby deactivation, of Bcl-2 is correlated with apoptosis and cell death [65,229,293]. However, in contrast to the findings of the current study there are reports of antimitotic chemotherapeutic agents such as paclitaxel, vincristine and vinblastine which cause serine phosphorylation of Bcl-2 [294]. The phosphorylation dynamics induced by these drugs are reportedly different and involve multisite Bcl-2 phosphorylation at sites including thr69, ser70, ser87, thr56 and thr74 [294]. Nonetheless, although treatment with these antimitotic drugs induces cell death, it has been suggested that the cells with dephosphorylated Bcl-2 status actually undergo apoptosis [294]. The source of STX1972-induced Bcl-2 dephosphorylation is suspected to be secondary to the production of ceramide. Ceramide is a membrane sphingolipid and is considered a potent apoptotic second messenger [295]. Antimitotic-induced ceramide generation is associated with increased toxicity and possibly reduced treatment resistance in breast cancer cells [296]. Apoptotic stress stimuli, including chemotherapeutic drugs, increases ceramide production resulting from activation of protein phosphatase 2A (PP2A) and indirect inactivation of protein kinase C (PKCα), ultimately resulting in deactivation of Bcl-2 function via dephosphorylation and induction of apoptosis [295,297-298]. Studies have also revealed that the ceramide-induced dephosphorylated form of Bcl-2 favours the formation of the Bcl-2/p53 complex and apoptotic cell death [297]. Furthermore, ceramide and redox signalling is coupled: ceramide triggers ROS generation; and

ROS is involved in sphingomyelinase (SMase) activation which is required for ceramide production in the lysosomes [299]. This cross-talk highlights a possible indirect link between ROS and Bcl-2 dephosphorylation. STX1972 was also found to downregulate c-MYC expression, implying abrogation of the oncoprotein-related tumorigenic pathways including proliferation and pro-survival [163,167-169]. Recently, c-MYC has also been linked to the regulation of autophagy and lysosomal biogenesis [300]. Annunziata *et al.* discovered that c-MYC inhibition frees lysosomal and autophagy gene promoter sites, thereby allowing binding of the microphthalmia family of transcription factors (MiT/TFE) and/or the forkhead box protein H1 (FOXH1) transcriptional activator [300]. In summary, STX1972 culminates in cancer cell cytotoxicity via activation of several apoptotic and autophagy/lysosomal related pathways.

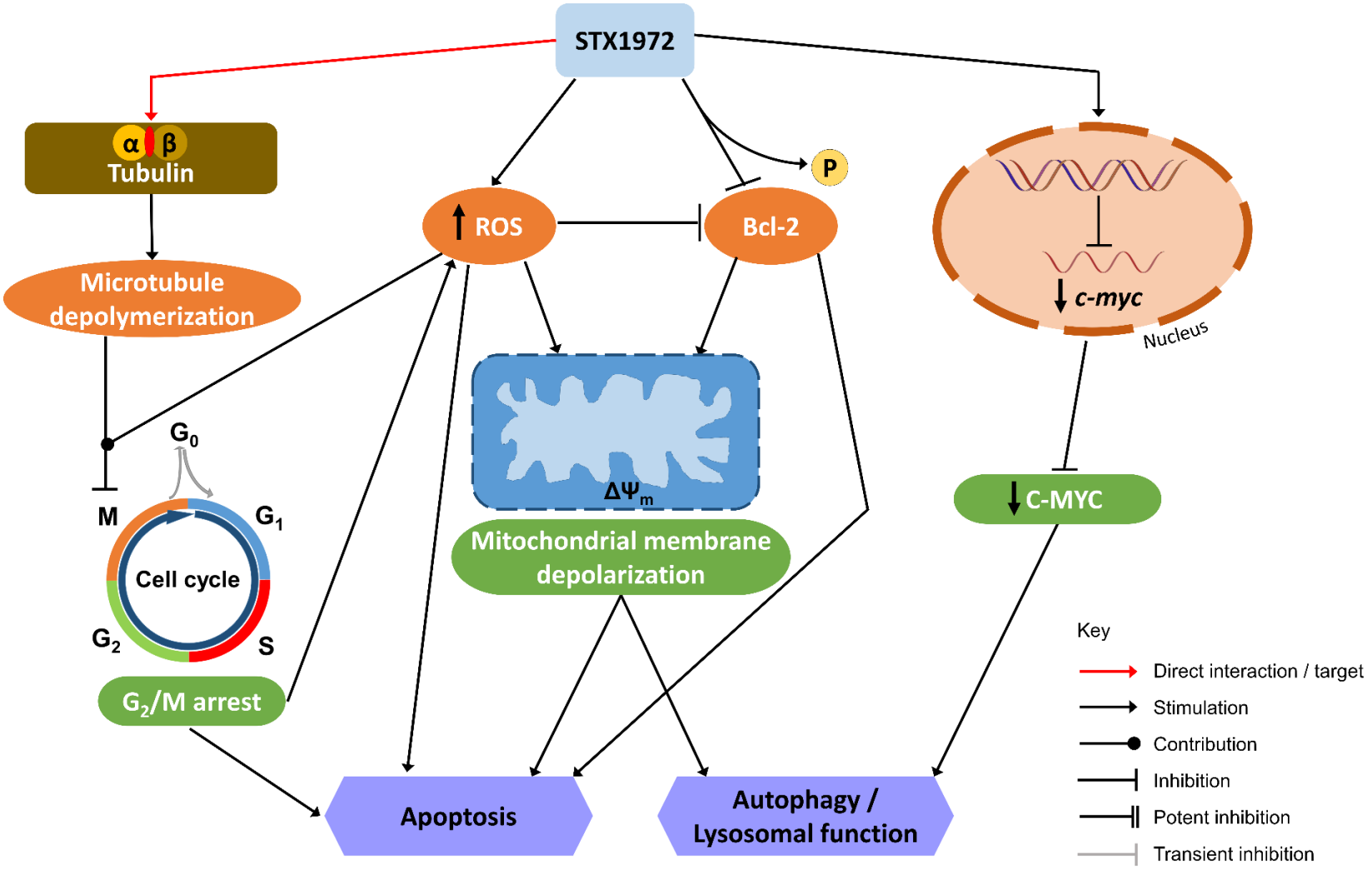

Figure 4.1: Proposed mechanisms of action of STX1972. Cytotoxic consequences of STX1972 treatment are induced by both apoptotic and autophagy/lysosomal related pathways. STX1972 appears to induce these cell death pathways via multiple points of initiation, namely: microtubule depolymerization, G_2/M arrest, increased ROS formation, mitochondrial depolarization, Bcl-2 dephosphorylation and suppression of *c-myc* transcription and translation.

4.6 Proposed mechanism of action of Bzt-W41 on MDA-MB-231 cells

Bzt-W41 demonstrated TNBC-selective antiproliferative activity. Treatment of the MDA-MB-231 cell line with the BRD4 inhibitor resulted in an evident but non-significant increase in the G_1 population; dissipated mitochondrial membrane potential; suppression of *c-myc* and *bcl-2* mRNA expression; a potent reduction in c-MYC expression; ultimately leading to increased autophagy/lysosomal activity and late apoptosis culminating in cellular demise (Figure 4.2). BRD4 inhibitors have been found to induce G_1 cell cycle arrest to varying extent in several malignant cell types [264,301-304]. However, the downstream pathways which drive the related apoptotic events remain to be fully elucidated. A study by Tan *et al.* demonstrated that BRDi-induced G_1 cell cycle arrest and apoptosis is associated with upregulation of p21 and forkhead box protein O1 (FOXO1), and suppression of *c-myc* and *bcl-2* [264]. Partly similar to these findings, Gallagher *et al.* found that G_1 arrest was associated with p21 upregulation in some melanoma cell lines, while p27 upregulation was linked to other cancers [303]. However they concluded that involvement of c-MYC in cell cycle arrest was unlikely and attributed apoptosis to the loss of mitochondrial potential and upregulation of the BH3 pro-apoptotic BIM protein [303]. Other studies have concluded that the apoptotic response to BRD inhibition in TNBC is caused by the suppression of Aurora kinases A and B (AURKA/B) and is induced independently from c-MYC suppression [265]. Here, we speculate that the mechanism driving apoptosis involves several pathways, including G_1 arrest; *bcl-2* and *c-myc* downregulation; and c-MYC oncoprotein suppression. c-MYC suppression is also implicated in the activation of autophagy and lysosomal biogenesis by allowing MiT/TFE and/or FOXH1 to bind to the gene promoter regions and permitting transcriptional activation [300]. BRD4 itself is a recognized negative transcriptional regulator of autophagy and lysosomal function, and both BRD4 inhibition and silencing have been associated with several types of autophagy [258-260,305]. Several autophagy-related genes and related proteins, including mammalian target of rapamycin (mTOR), AMP activated protein kinase (AMPK) and UNC-51-like kinase 1 (ULK1) are downregulated in breast cancer, with some associated with poor prognosis [306]. Ouyang *et al.* identified a direct BRD4-AMPK interaction and designed a BRD4 inhibitor (9f) which was found to induce autophagy associated cell death via activation of the AMPK-mTOR-ULK pathway [306]. This implies

the possibility that Bzt-W41 regulates two separate pathways for the modulation of autophagy associated cell death, namely: c-MYC downregulation and dissociation from autophagy and lysosomal promotor regions; as well as the direct inhibition of BRD4 and related AMPK activation.

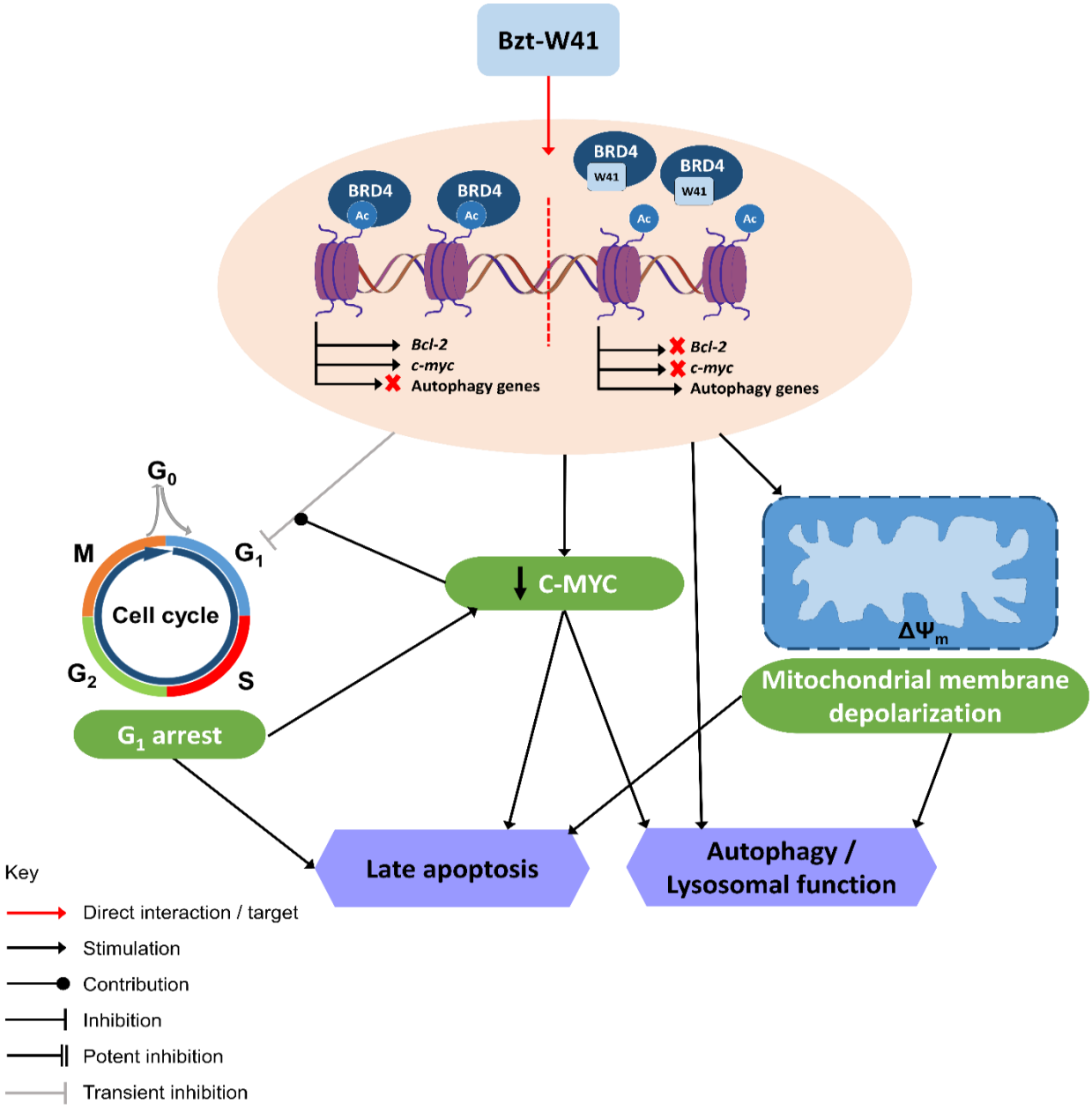

Figure 4.2: Proposed mechanisms of action of Bzt-W41. Treatment of the MDA-MB-231 cell line with the BRD4 inhibitor resulted in an evident but non-significant increase in the G_1 population; dissipated mitochondrial membrane potential; repression of *c-myc* and *bcl-2* mRNA expression; a potent reduction in c-MYC expression; ultimately leading to increased autophagy/lysosomal activity and late apoptosis culminating in cellular demise

4.7 Proposed mechanism of action of STX1972 + Bzt-W41 combination on MDA-MB-231 cells

The STX + Bzt-W41 combination revealed some overlap of the two compounds' individual mechanistic action. The combination treatment resulted in an initial G_2/M arrest, followed by a strong G_1 arrest; decreased mitochondrial membrane depolarization; repression of *c-myc* mRNA levels; downregulation of c-MYC oncoprotein expression; finally leading to increased autophagy/lysosomal activity and activation of both early and late apoptosis and cell death (Figure 4.3). The G_2/M arrest is transient but evident and indicates that the STX1972 contribution is capable of inducing an initial mitotic block similar to that of the individual treatment. However, unlike individual treatment which led to reduced G_2/M fraction and increased sub-G_1 population after 48 h; the combination treatment resulted in a reduced G_2/M fraction and a corresponding increase in the G_1 population which is attributed to the Bzt-W41 modulation. It could be speculated that the cells which escape the temporary STX1972-induced G_2/M block get arrested in the Bzt-W41-induced G_1 block, eventually culminating in cell death via activation of apoptotic pathways, possibly via mitotic catastrophe. Dissipation of mitochondrial outer membrane potential is possibly related to both STX1972 and Bzt-W41 and further drives downstream caspase-dependent apoptosis. Since autophagy and lysosomal activation was implicated as possible additional modes of cell death following single compound treatment, we venture to deduce that combination treatment surpasses monotreatment autophagy effects possibly culminating in the activation of several of the aforementioned autophagic pathways through mediation by both STX1972 and Bzt-W41.

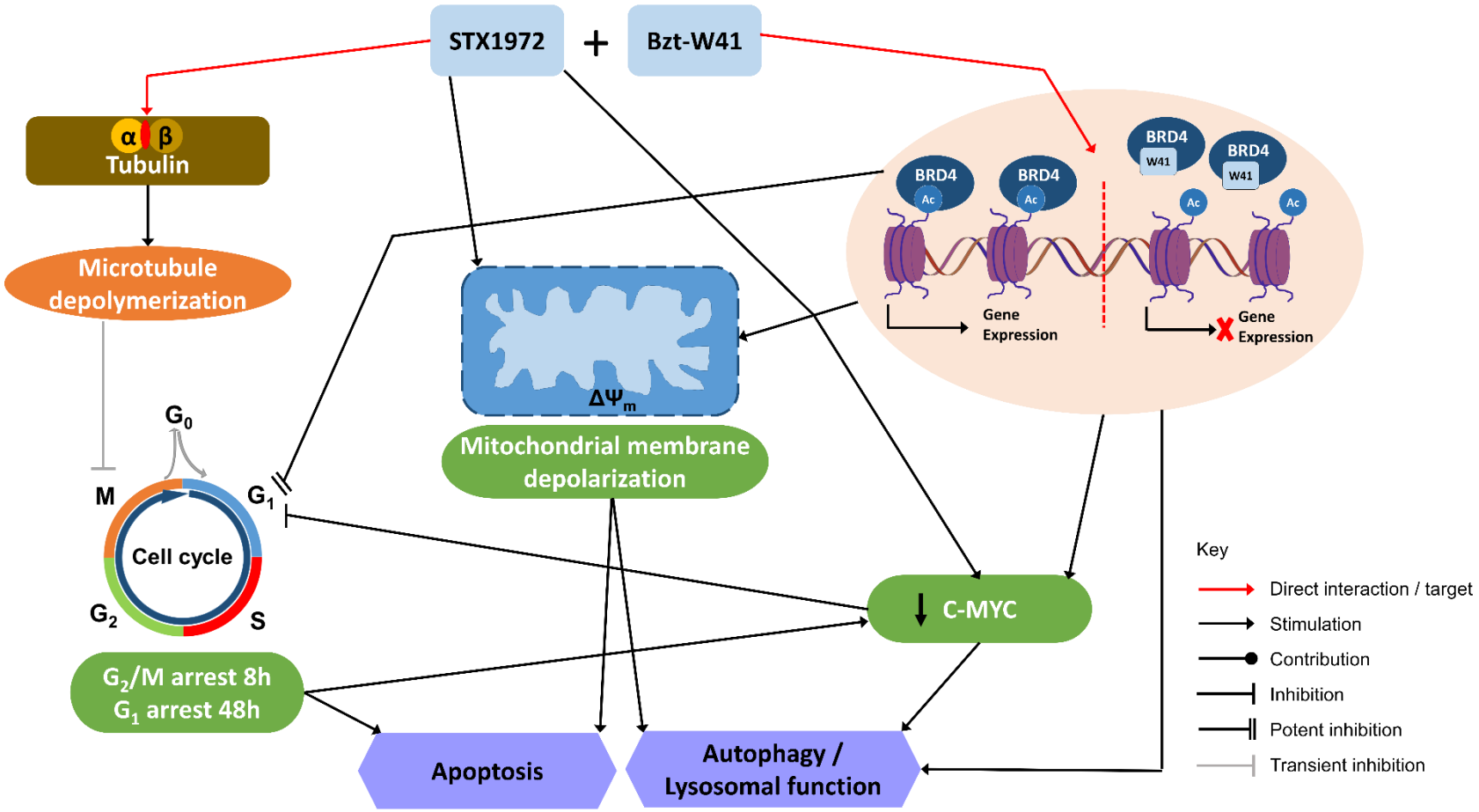

Figure 4.3: Proposed mechanisms of action of STX1972 + Bzt-W41 combination. The combination treatment resulted in an initial G_2/M arrest, followed by a strong G_1 arrest; decreased mitochondrial membrane depolarization; repression of *c-myc* mRNA levels; downregulation of c-MYC oncoprotein expression; finally leading to increased autophagy/lysosomal activity and activation of both early and late apoptosis and cell death.

Chapter 5: Conclusion

In conclusion, *in silico* screening by means of structure-based drug design was used to predict receptor-ligand interactions, docking poses and affinity. Glide SP software was able to reproduce the native ligand pose for all the selected receptors with ligands (RMSD<2) and the machine-learning RTF predictive model corresponded well with the experimentally determined Ki values of the CASF database.

In vitro screening for the antiproliferative capacity of the six cancer-targeting compounds via cell growth and combination studies allowed for the identification of the most feasible test compounds and combinations to include in further mechanistic experimental procedures. The initial screening identified three test compounds for further investigative inclusion, namely the antimitotic (STX1972), the BRD-4 inhibitor (Bzt-W1) and the SIRTi (W137). All three these compounds showed cancer-selective antiproliferative effects when compared to the EA.hy926 control cell line. STX1972 was found to inhibit cell growth in the nanomolar range, whilst the other test compounds showed growth inhibition in the lower micromolar range. Of the BRD-4 inhibitor analogues, Bzt-W41 was found to be the most potent in comparison to Bzt-W49 and Bzt-W52. The benzotriazepine derivative also showed significant preferential selectivity for the TNBC cell line versus the hormone-dependent MCF-7 cell line, while STX1972 and W137 exhibited only slight differential selectivity. Synergistic interactions of the three compounds were probed by measuring the cytotoxic effects of paired combinations. Two combinations (STX + Bzt-W41 and Bzt-W41 + W137) exhibited synergism, whilst the STX + W137 combination exhibited antagonistic interaction. Cell cycle and apoptosis analysis revealed that STX1972 and Bzt-W41, alone and in combination, selectively induced cell cycle arrest and apoptosis in cancer cells. However, W137 and the Bzt-W41 + W137 combination did not show preferential targeting of breast cancer cell lines, with apoptosis induced equally or even more so in the EA.hy926 cell line. STX1972 and Bzt-W41, as well as their paired combination, was further probed in aim of deciphering their individual and combined mode of action.

The cytotoxic consequences of STX1972 was found to be induced via several initiators, namely: microtubule depolymerisation, G_2/M cell cycle arrest, increased

ROS formation, dissipated mitochondrial membrane potential, Bcl-2 dephosphorylation and suppression of *c-myc* transcription and translation. These molecular changes lead to downstream pathway activation which culminate in both apoptotic an autophagy related cellular demise. Bzt-W41 induces a slight G_1 block; causes mitochondrial membrane depolarization; suppresses *c-myc* and *bcl-2* mRNA expression; potently downregulates c-MYC expression and ultimately results in increased autophagy/lysosomal activity and apoptosis. In combination, STX1972 + Bzt-W41 mirrored some effects of individual treatment and also induced some responses surpassing that of mono-treatment. Combination treatment resulted in transient G_2/M arrest, tailed by a potent G_1 block (superior to single treatment); decreased mitochondrial outer membrane depolarization; suppression of *c-myc* and inhibition of c-MYC oncoprotein. These factors contributed to the downstream activation of autophagy/lysosomal function and induction of apoptosis.

Plausible sources for the initiator events, role-players in the mediation of the effector pathways and cross-talk between the signalling modes have been speculated but the key drivers remain to be pinpointed and the intricate pathways remain to be fully deciphered. Nonetheless, the objectives of this study were satisfactorily met: antiproliferative effects of novel compounds were determined; novel drug combinations were probed; synergistic combinations were identified; and results from the study were used to generate various testable hypotheses for the mechanism of action of individual and combination treatments, providing a foundation for future studies.

6. References

1. Ferlay J, Soerjomataram I, Ervik M, Dikshit R, Eser S, Mathers C, et al. Globocan 2012 v1.0, cancer incidence and mortality worldwide: Iarc cancer base no. 11 [internet]. Lyon, france: International agency for research on cancer; 2013.

2. IARC World cancer report 2014. [Internet]: International Agency for Research on Cancer; 2015 [cited Access 2015 Access Date]. Available from: https://www.who.int/cancer/publications/WRC_2014/en/.

3. Ferlay J, Soerjomataram I, Dikshit R, Eser S, Mathers C, Rebelo M, et al. Cancer incidence and mortality worldwide: Sources, methods and major patterns in globocan 2012. Int J Cancer. 2015; 136(5):E359-E86. doi:10.1002/ijc.29210

4. WHO. World health organization - cancer country profiles. 2014.

5. Cheung-Ong K, Giaever G, Nislow C. DNA-damaging agents in cancer chemotherapy: Serendipity and chemical biology. Chem Biol. 2013; 20(5):648-59.

6. Connell PP, Hellman S. Advances in radiotherapy and implications for the next century: A historical perspective. Cancer Res. 2009; 69(2):383-92.

7. Niederhuber JE. Surgical interventions in cancer. In: Abeloff MD, Armitage JO, Niederhuber JE, Kastan MB, McKenna WG, editors. Abeloff's clinical oncology. 4th ed: Churchill Livingstone/Elsevier Philadelphia; 2008. p. 407 - 16.

8. Wust P, Hildebrandt B, Sreenivasa G, Rau B, Gellermann J, Riess H, et al. Hyperthermia in combined treatment of cancer. Lancet Oncol. 2002; 3(8):487-97.

9. Schlom J. Therapeutic cancer vaccines: Current status and moving forward. J Natl Cancer Inst. 2012; 104(8):599-613.

10. Brunstein C, Weisdorf D. Future of cord blood for oncology uses. Bone Marrow Transplant. 2009; 44(10):699-707.

11. Brown SB, Brown EA, Walker I. The present and future role of photodynamic therapy in cancer treatment. Lancet Oncol. 2004; 5(8):497-508.

12. Bjordal JM, Bensadoun R-J, Tunèr J, Frigo L, Gjerde K, Lopes-Martins RA. A systematic review with meta-analysis of the effect of low-level laser therapy (lllt) in cancer therapy-induced oral mucositis. Support Care Cancer. 2011; 19(8):1069-77.

13. National cancer institute. Cancer treatment.

14. Gatenby RA. A change of strategy in the war on cancer. Nature. 2009; 459(7246):508-9.

15. Parkin DM, Bray F, Ferlay J, Pisani P. Global cancer statistics, 2002. CA Cancer J Clin. 2005; 55(2):74-108.

16. Longley D, Johnston P. Molecular mechanisms of drug resistance. J Pathol. 2005; 205(2):275-92.

17. Gorlick R, Bertino JR. Clinical pharmacology and resistance to dihydrofolate reductase inhibitors. In: Jackman AL, editor. Antifolate drugs in cancer therapy: Springer; 1999. p. 37-57.

18. Yang R, Sowers R, Mazza B, Healey JH, Huvos A, Grier H, et al. Sequence alterations in the reduced folate carrier are observed in osteosarcoma tumor samples. Clin Cancer Res. 2003; 9(2):837-44.

19. Laverdiere C, Chiasson S, Costea I, Moghrabi A, Krajinovic M. Polymorphism g80a in the reduced folate carrier gene and its relationship to methotrexate plasma levels and outcome of childhood acute lymphoblastic leukemia. Blood. 2002; 100(10):3832-4.

20. Thomas H, Coley HM. Overcoming multidrug resistance in cancer: An update on the clinical strategy of inhibiting p-glycoprotein. Cancer Control. 2003; 10(2):159-65.

21. Meijer C, Mulder NH, Timmer-Bosscha H, Sluiter WJ, Meersma GJ, de Vries EG. Relationship of cellular glutathione to the cytotoxicity and resistance of seven platinum compounds. Cancer Res. 1992; 52(24):6885-9.

22. Reed E. Platinum-DNA adduct, nucleotide excision repair and platinum based anti-cancer chemotherapy. Cancer treatment reviews. 1998; 24(5):331-44.

23. Breast cancer facts and figures 2015 - 2016. Atlanta: American Cancer Society, Inc, 2015.

24. Dieci MV, Orvieto E, Dominici M, Conte P, Guarneri V. Rare breast cancer subtypes: Histological, molecular, and clinical peculiarities. Oncologist. 2014; 19(8):805-13.

25. Yang XR, Chang-Claude J, Goode EL, Couch FJ, Nevanlinna H, Milne RL, et al. Associations of breast cancer risk factors with tumor subtypes: A pooled analysis from the breast cancer association consortium studies. J Natl Cancer Inst. 2011; 103(3):250-63.

26. Barnard ME, Boeke CE, Tamimi RM. Established breast cancer risk factors and risk of intrinsic tumor subtypes. Biochimica et Biophysica Acta (BBA)-Reviews on Cancer. 2015; 1856(1):73-85.

27. Perou CM, Sorlie T, Eisen MB, van de Rijn M, Jeffrey SS, Rees CA, et al. Molecular portraits of human breast tumours. Nature. 2000; 406(6797):747-52. doi:http://www.nature.com/nature/journal/v406/n6797/suppinfo/406747a0_S1.html

28. Kim H, Cho J, Kwon SY, Kang SH. Biologic subtype is a more important prognostic factor than nodal involvement in patients with stages i and ii breast carcinoma. Ann Surg Treat Res. 2016; 90(1):1-9.

29. Network CGA. Comprehensive molecular portraits of human breast tumours. Nature. 2012; 490(7418):61-70.

30. Peintinger F. Using molecular profiles to tailor treatment in breast cancer: Are they ready for prime time? Curr Opin Obstet Gynecol. 2014; 26(1):21-6.

31. Anderson WF, Rosenberg PS, Prat A, Perou CM, Sherman ME. How many etiological subtypes of breast cancer: Two, three, four, or more? J Natl Cancer Inst. 2014; 106(8):dju165.

32. Anderson WF, Rosenberg PS, Katki HA. Tracking and evaluating molecular tumor markers with cancer registry data: Her2 and breast cancer. J Natl Cancer Inst. 2014; 106(5):dju093.

33. Cheang MC, Martin M, Nielsen TO, Prat A, Voduc D, Rodriguez-Lescure A, et al. Defining breast cancer intrinsic subtypes by quantitative receptor expression. Oncologist. 2015; 20(5):474-82.

34. Cubasch H, Dickens C, Joffe M, Duarte R, Murugan N, Chih MT, et al. Breast cancer survival in soweto, johannesburg, south africa: A receptor-defined cohort of women diagnosed from 2009 to 11. Cancer Epidemiol. 2018; 52:120-7.

35. Blows FM, Driver KE, Schmidt MK, Broeks A, Van Leeuwen FE, Wesseling J, et al. Subtyping of breast cancer by immunohistochemistry to investigate a relationship between subtype and short and long term survival: A collaborative analysis of data for 10,159 cases from 12 studies. PLoS Med. 2010; 7(5):e1000279.

36. Effects of chemotherapy and hormonal therapy for early breast cancer on recurrence and 15-year survival: An overview of the randomised trials. Lancet: Elsevier; 2005. p. 1687-717.

37. Bianchini G, Balko JM, Mayer IA, Sanders ME, Gianni L. Triple-negative breast cancer: Challenges and opportunities of a heterogeneous disease. Nature reviews Clinical oncology. 2016; 13(11):674.

38. Gonzalez-Angulo AM, Morales-Vasquez F, Hortobagyi GN. Overview of resistance to systemic therapy in patients with breast cancer. Breast cancer chemosensitivity: Springer; 2007. p. 1-22.

39. Domenyuk V, Gatalica Z, Santhanam R, Wei X, Stark A, Kennedy P, et al. Poly-ligand profiling differentiates trastuzumab-treated breast cancer patients according to their outcomes. Nat Commun. 2018; 9(1):1219. doi:10.1038/s41467-018-03631-z

40. Ellis MJ, Coop A, Singh B, Mauriac L, Llombert-Cussac A, Jänicke F, et al. Letrozole is more effective neoadjuvant endocrine therapy than tamoxifen for erbb-1–and/or erbb-2–positive, estrogen receptor–positive primary breast cancer: Evidence from a phase iii randomized trial. J Clin Oncol. 2001; 19(18):3808-16. doi:10.1200/jco.2001.19.18.3808

41. Crown J, O'Leary M, Ooi W-S. Docetaxel and paclitaxel in the treatment of breast cancer: A review of clinical experience. Oncologist. 2004; 9(Supplement 2):24-32.

42. Burrell RA, McGranahan N, Bartek J, Swanton C. The causes and consequences of genetic heterogeneity in cancer evolution. Nature. 2013; 501(7467):338-45.

43. Lord CJ, Ashworth A. The DNA damage response and cancer therapy. Nature. 2012; 481(7381):287-94.

44. Zardavas D, Irrthum A, Swanton C, Piccart M. Clinical management of breast cancer heterogeneity. Nat Rev Clin Oncol. 2015; 12(7):381-94.

45. Ding L, Ley TJ, Larson DE, Miller CA, Koboldt DC, Welch JS, et al. Clonal evolution in relapsed acute myeloid leukaemia revealed by whole-genome sequencing. Nature. 2012; 481(7382):506-10.

46. Bosch F, Rosich L. The contributions of paul ehrlich to pharmacology: A tribute on the occasion of the centenary of his nobel prize. Pharmacology. 2008; 82(3):171-9.

47. Strebhardt K, Ullrich A. Paul ehrlich's magic bullet concept: 100 years of progress. Nat Rev Cancer. 2008; 8(6):473-80.

48. Li Y, Barbash O, Diehl JA. 11 - regulation of the cell cycle. In: Mendelsohn J, Gray JW, Howley PM, Israel MA, Thompson CB, editors. The molecular basis of cancer (fourth edition). Philadelphia: Content Repository Only!; 2015. p. 165-78.e2.

49. Li Y, Barbash O, Diehl JA. Part ii: Cancer biology - regulation of the cell cycle. In: Mendelsohn J, Gray JW, Howley PM, Israel MA, Thompson CB, editors. The molecular basis of cancer Fourth ed. Philadelphia: Elsevier; 2015. p. 165-78.

50. Chapter 40 - introduction to the cell cycle. In: Pollard TD, Earnshaw WC, Lippincott-Schwartz J, Johnson GT, editors. Cell biology (third edition): Elsevier; 2017. p. 697-711.

51. Casem ML. Chapter 13 - cell cycle. In: Casem ML, editor. Case studies in cell biology. Boston: Academic Press; 2016. p. 299-326.

52. Malumbres M. Cyclin-dependent kinases. Genome Biol. 2014; 15(6):122. doi:10.1186/gb4184

53. Roskoski R. Cyclin-dependent protein kinase inhibitors including palbociclib as anticancer drugs. Pharmacol Res. 2016; 107:249-75. doi:https://doi.org/10.1016/j.phrs.2016.03.012

54. Schaal C, Pillai S, Chellappan SP. Chapter four - the rb–e2f transcriptional regulatory pathway in tumor angiogenesis and metastasis. In: Tew KD, Fisher PB, editors. Adv cancer res: Academic Press; 2014. p. 147-82.

55. Nakayama KI, Nakayama K. Ubiquitin ligases: Cell-cycle control and cancer. Nat Rev Cancer. 2006; 6(5):369-81. doi:10.1038/nrc1881

56. Diehl JA, Ponugoti B. Ubiquitin-dependent proteolysis in g1/s phase control and its relationship with tumor susceptibility. Genes Cancer. 2010; 1(7):717-24. doi:10.1177/1947601910382902

57. Santo L, Siu KT, Raje N. Targeting cyclin-dependent kinases and cell cycle progression in human cancers. Semin Oncol. 2015; 42(6):788-800. doi:https://doi.org/10.1053/j.seminoncol.2015.09.024

58. Elledge SJ. Cell cycle checkpoints: Preventing an identity crisis. Science. 1996; 274(5293):1664-72.

59. Niederhuber JE, Armitage JO, Doroshow JH, Kastan MB, Tepper JE. Abeloff's clinical oncology e-book: Elsevier Health Sciences; 2019.

60. OpenSTax [Internet]. Control of the cell cycle. Openstax CNX; Jun 4, 2013 [cited 2019 Nov 9]. Available from: http://cnx.org/contents/69b8e2ee-f350-4202-8085-878c433e1cd5@6.

61. Gorbsky GJ. The mitotic spindle checkpoint. Curr Biol. 2001; 11(24):R1001-R4.

62. Galluzzi L, Vitale I, Aaronson SA, Abrams JM, Adam D, Agostinis P, et al. Molecular mechanisms of cell death: Recommendations of the nomenclature committee on cell death 2018. Cell Death Differ. 2018; 25(3):486-541.

63. Galluzzi L, Bravo-San Pedro JM, Kepp O, Kroemer G. Regulated cell death and adaptive stress responses. Cell Mol Life Sci. 2016; 73(11-12):2405-10.

64. Galluzzi L, Bravo-San Pedro J, Vitale I, Aaronson S, Abrams J, Adam D, et al. Essential versus accessory aspects of cell death: Recommendations of the nccd 2015. Cell Death Differ. 2015; 22(1):58.

65. Stander BA. In silico design, synthesis and in vitro evaluation of antimitotic agents: University of Pretoria; 2012.

66. Galluzzi L, Kepp O, Kroemer G. Mitochondria: Master regulators of danger signalling. Nat Rev Mol Cell Biol. 2012; 13(12):780-8. doi:10.1038/nrm3479

67. Matsuzawa A, Ichijo H. Redox control of cell fate by map kinase: Physiological roles of ask1-map kinase pathway in stress signaling. Biochimica et Biophysica Acta (BBA) - General Subjects. 2008; 1780(11):1325-36. doi:https://doi.org/10.1016/j.bbagen.2007.12.011

68. Lopez-Lazaro M. Dual role of hydrogen peroxide in cancer: Possible relevance to cancer chemoprevention and therapy. Cancer Lett. 2007; 252(1):1-8. doi:S0304-3835(06)00592-1 [pii]
10.1016/j.canlet.2006.10.029

69. Rabinowitz JD, White E. Autophagy and metabolism. Science. 2010; 330(6009):1344-8. doi:10.1126/science.1193497

70. Castedo M, Perfettini J-L, Roumier T, Andreau K, Medema R, Kroemer G. Cell death by mitotic catastrophe: A molecular definition. Oncogene. 2004; 23(16):2825-37. doi:10.1038/sj.onc.1207528

71. Golstein P, Kroemer G. Cell death by necrosis: Towards a molecular definition. Trends Biochem Sci. 2007; 32(1):37-43.

72. Hanahan D, Weinberg RA. Hallmarks of cancer: The next generation. Cell. 2011; 144(5):646-74.

73. Hanahan D, Weinberg RA. The hallmarks of cancer. Cell. 2000; 100(1):57-70.

74. Charafe-Jauffret E, Monville F, Ginestier C, Dontu G, Birnbaum D, Wicha MS. Cancer stem cells in breast: Current opinion and future challenges. Pathobiology. 2008; 75(2):75-84.

75. Reya T, Morrison SJ, Clarke MF, Weissman IL. Stem cells, cancer, and cancer stem cells. Nature. 2001; 414(6859):105-11.

76. Sun H, Jia J, Wang X, Ma B, Di L, Song G, et al. Cd44+/cd24− breast cancer cells isolated from mcf-7 cultures exhibit enhanced angiogenic properties. Clin Transl Oncol. 2013; 15(1):46-54.

77. Iliopoulos D, Hirsch HA, Wang G, Struhl K. Inducible formation of breast cancer stem cells and their dynamic equilibrium with non-stem cancer cells via il6 secretion. Proc Natl Acad Sci U S A. 2011; 108(4):1397-402. doi:10.1073/pnas.1018898108 1018898108 [pii]

78. Marotta LL, Almendro V, Marusyk A, Shipitsin M, Schemme J, Walker SR, et al. The jak2/stat3 signaling pathway is required for growth of cd44+ cd24–stem cell–like breast cancer cells in human tumors. J Clin Invest. 2011; 121(7):2723.

79. Kim S-Y, Kang JW, Song X, Kim BK, Yoo YD, Kwon YT, et al. Role of the il-6-jak1-stat3-oct-4 pathway in the conversion of non-stem cancer cells into cancer stem-like cells. Cell Signal. 2013; 25(4):961-9.

80. Korkaya H, Kim G-i, Davis A, Malik F, Henry NL, Ithimakin S, et al. Activation of an il6 inflammatory loop mediates trastuzumab resistance in her2+ breast cancer by expanding the cancer stem cell population. Mol Cell. 2012; 47(4):570-84.

81. Drost J, Agami R. Transformation locked in a loop. Cell. 2009; 139(4):654-6. doi:http://dx.doi.org/10.1016/j.cell.2009.10.035

82. Iliopoulos D, Hirsch HA, Struhl K. An epigenetic switch involving nf-κb, lin28, let-7 microrna, and il6 links inflammation to cell transformation. Cell. 2009; 139(4):693-706. doi:http://dx.doi.org/10.1016/j.cell.2009.10.014

83. Chang C-J, Chien Y, Lu K-H, Chang S-C, Chou Y-C, Huang C-S, et al. Oct4-related cytokine effects regulate tumorigenic properties of colorectal cancer cells. Biochem Biophys Res Commun. 2011; 415(2):245-51.

84. Sawyers C. Targeted cancer therapy. Nature. 2004; 432(7015):294-7. doi:10.1038/nature03095

85. Chan K, Koh CG, Li H. Mitosis-targeted anti-cancer therapies: Where they stand. Cell Death Dis. 2012; 3(10):e411.

86. Nepali K, Ojha R, Sharma S, MS Bedi P, L Dhar K. Tubulin inhibitors: A patent survey. Recent Pat Anticancer Drug Discov. 2014; 9(2):176-220.

87. Rieder CL, Maiato H. Stuck in division or passing through: What happens when cells cannot satisfy the spindle assembly checkpoint. Dev Cell. 2004; 7(5):637-51. doi:http://dx.doi.org/10.1016/j.devcel.2004.09.002

88. Jordan MA, Wilson L. Microtubules as a target for anticancer drugs. Nat Rev Cancer. 2004; 4(4):253-65.

89. van Vuuren RJ, Visagie MH, Theron AE, Joubert AM. Antimitotic drugs in the treatment of cancer. Cancer Chemother Pharmacol. 2015; 76(6):1101-12.

90. Downing KH. Structural basis for the interaction of tubulin with proteins and drugs that affect microtubule dynamics. Annu Rev Cell Dev Biol. 2000; 16(1):89-111.

91. Bruce JY, Eickhoff J, Pili R, Logan T, Carducci M, Arnott J, et al. A phase ii study of 2-methoxyestradiol nanocrystal colloidal dispersion alone and in combination with sunitinib malate in patients with metastatic renal cell carcinoma progressing on sunitinib malate. Invest New Drugs. 2012; 30(2):794-802.

92. Harrison MR, Hahn NM, Pili R, Oh WK, Hammers H, Sweeney C, et al. A phase ii study of 2-methoxyestradiol (2me2) nanocrystal® dispersion (ncd) in patients with taxane-refractory, metastatic castrate-resistant prostate cancer (crpc). Invest New Drugs. 2011; 29(6):1465-74.

93. Stander BA, Joubert F, Tu C, Sippel KH, McKenna R, Joubert AM. In vitro evaluation of ese-15-ol, an estradiol analogue with nanomolar antimitotic and carbonic anhydrase inhibitory activity. PLoS One. 2012; 7(12):e52205. doi:10.1371/journal.pone.0052205

94. Stander BA, Joubert F, Tu C, Sippel KH, McKenna R, Joubert AM. Signaling pathways of ese-16, an antimitotic and anticarbonic anhydrase estradiol analog, in breast cancer cells. PLoS One. 2013; 8(Suppl 1):e53853.

95. Jourdan F, Leese MP, Dohle W, Ferrandis E, Newman SP, Chander S, et al. Structure–activity relationships of c-17-substituted estratriene-3-o-sulfamates as anticancer agents. J Med Chem. 2011; 54(13):4863-79.

96. Ho YT, Purohit A, Vicker N, Newman SP, Robinson JJ, Leese MP, et al. Inhibition of carbonic anhydrase ii by steroidal and non-steroidal sulphamates. Biochem Biophys Res Commun. 2003; 305(4):909-14. doi:https://doi.org/10.1016/S0006-291X(03)00865-9

97. Supuran CT, Scozzafava A. Carbonic anhydrase inhibitors and their therapeutic potential. Expert Opin Ther Pat. 2000; 10(5):575-600. doi:10.1517/13543776.10.5.575

98. Supuran CT, Scozzafava A. Carbonic anhydrases as targets for medicinal chemistry. Bioorg Med Chem. 2007; 15(13):4336-50.

99. Elger W, Hedden A, Reddersen G, Schneider B. Sulfamates of various estrogens are prodrugs with increased systemic and reduced hepatic estrogenicity at oral application. J Steroid Biochem Mol Biol. 1995; 55:395-403.

100. Lloyd MD, Thiyagarajan N, Ho YT, Woo LL, Sutcliffe OB, Purohit A, et al. First crystal structures of human carbonic anhydrase ii in complex with dual aromatase−steroid sulfatase inhibitors. Biochemistry. 2005; 44(18):6858-66.

101. Vicker N, Ho Y, Robinson J, Woo LLW, Purohit A, Reed MJ, et al. Docking studies of sulphamate inhibitors of estrone sulphatase in human carbonic anhydrase ii. Bioorg Med Chem Lett. 2003; 13(5):863-5. doi:https://doi.org/10.1016/S0960-894X(03)00009-X

102. Thiry A, Dogné J-M, Masereel B, Supuran CT. Targeting tumor-associated carbonic anhydrase ix in cancer therapy. Trends Pharmacol Sci. 2006; 27(11):566-73. doi:https://doi.org/10.1016/j.tips.2006.09.002

103. Švastová E, Hulíková A, Rafajová M, Zat'ovičová M, Gibadulinová A, Casini A, et al. Hypoxia activates the capacity of tumor-associated carbonic anhydrase ix to acidify extracellular ph. FEBS Lett. 2004; 577(3):439-45. doi:10.1016/j.febslet.2004.10.043

104. McDonald PC, Winum J-Y, Supuran CT, Dedhar S. Recent developments in targeting carbonic anhydrase ix for cancer therapeutics. Oncotarget. 2012; 3(1):84-97. doi:10.18632/oncotarget.422

105. Reed M, Purohit A, Woo L, Potter B. The development of steroid sulphatase inhibitors. Endocrine-Related Cancer. 1996; 3(1):9-23.

106. Stanway SJ, Delavault P, Purohit A, Woo LL, Thurieau C, Potter BV, et al. Steroid sulfatase: A new target for the endocrine therapy of breast cancer. Oncologist. 2007; 12(4):370-4.

107. Purohit A, Woo LW, Barrow D, Hejaz HA, Nicholson RI, Potter BV, et al. Non-steroidal and steroidal sulfamates: New drugs for cancer therapy. Mol Cell Endocrinol. 2001; 171(1-2):129-35. doi:S0303-7207(00)00428-7 [pii]

108. Woo LWL, Purohit A, Malini B, Reed MJ, Potter BVL. Potent active site-directed inhibition of steroid sulphatase by tricyclic coumarin-based sulphamates. Chem Biol. 2000; 7(10):773-91. doi:https://doi.org/10.1016/S1074-5521(00)00023-5

109. Chung C-W. Small molecule bromodomain inhibitors: Extending the druggable genome. In: Lawton G, Witty DR, editors. Progress in medicinal chemistry: Elsevier B.V; 2012. p. 1 - 56.

110. Annunziato A. DNA packaging: Nucleosomes and chromatin. Nat Educ. 2008; 1(1):26.

111. Doroshow DB, Eder JP, LoRusso PM. Bet inhibitors: A novel epigenetic approach. Ann Oncol. 2017; 28(8):1776-87. doi:10.1093/annonc/mdx157

112. Sanchez R, Meslamani J, Zhou M-M. The bromodomain: From epigenome reader to druggable target. Biochimica et Biophysica Acta (BBA)-Gene Regulatory Mechanisms. 2014; 1839(8):676-85.

113. Denis GV. Bromodomain coactivators in cancer, obesity, type 2 diabetes, and inflammation. Discovery medicine. 2010; 10(55):489.

114. Sanchez R, Zhou M-M. The role of human bromodomains in chromatin biology and gene transcription. Curr Opin Drug Discov Devel. 2009; 12(5):659.

115. Chung C, Coste H, White JH, Mirguet O, Wilde J, Gosmini RL, et al. Discovery and characterization of small molecule inhibitors of the bet family bromodomains. J Med Chem. 2011;

116. Crawford NP, Alsarraj J, Lukes L, Walker RC, Officewala JS, Yang HH, et al. Bromodomain 4 activation predicts breast cancer survival. Proceedings of the National Academy of Sciences. 2008; 105(17):6380-5.

117. Yang Z, He N, Zhou Q. Brd4 recruits p-tefb to chromosomes at late mitosis to promote g1 gene expression and cell cycle progression. Mol Cell Biol. 2008; 28(3):967-76.

118. Dey A, Nishiyama A, Karpova T, McNally J, Ozato K. Brd4 marks select genes on mitotic chromatin and directs postmitotic transcription. Molecular Biology of the Cell. 2009; 20:4899–909.

119. Shu S, Lin CY, He HH, Witwicki RM, Tabassum DP, Roberts JM, et al. Response and resistance to bet bromodomain inhibitors in triple-negative breast cancer. Nature. 2016; 529(7586):413.

120. Pérez-Pena J, Páez R, Nieto-Jiménez C, Sánchez VC, Galan-Moya EM, Pandiella A, et al. Mapping bromodomains in breast cancer and association with clinical outcome. Scientific reports. 2019; 9(1):1-10.

121. Walsh L, Haley KE, Moran B, Mooney B, Tarrant F, Madden SF, et al. Bet inhibition as a rational therapeutic strategy for invasive lobular breast cancer. Clinical Cancer Research. 2019; 25(23):7139-50.

122. Murakami S, Li R, Nagari A, Chae M, Camacho CV, Kraus WL. Distinct roles for bet family members in estrogen receptor α enhancer function and gene regulation in breast cancer cells. Molecular Cancer Research. 2019; 17(12):2356-68.

123. Filippakopoulos P, Qi J, Picaud S, Shen Y, Smith WB, Fedorov O, et al. Selective inhibition of bet bromodomains. Nature Reviews. 2010; (468):1067-73.

124. Zuber J, Shi J, Wang E, Rappaport AR, Herrmann H, Sison EA. Rnai screen identifies brd4 as a therapeutic target in acute myeloid leukaemia. Nature. 2011; 478:524-8.

125. Mertz JA, Conery AR, Bryant BM, Sandy P, Balasubramanian S, Mele DA, et al. Targeting myc dependence in cancer by inhibiting bet bromodomains. Proc Natl Acad Sci. 2011; 108(40):16669-74.

126. Delmore Jake E, Issa Ghayas C, Lemieux Madeleine E, Rahl Peter B, Shi J, Jacobs Hannah M, et al. Bet bromodomain inhibition as a therapeutic strategy to target c-myc. Cell. 146(6):904-17. doi:10.1016/j.cell.2011.08.017

127. Henssen AG, Thor T, Odersky A, Heukamp L, El-Hindy N, Beckers A, et al. Bet bromodomain protein inhibition is a therapeutic option for medulloblastoma. Oncotarget. 2013; 4(11):2080-95.

128. Wyce A, Degenhardt Y, Bai Y, Le B, Korenchuk S, Crouthamel M-C, et al. Inhibition of bet bromodomain proteins as a therapeutic approach in prostate cancer2013.

129. Da Costa D, Agathanggelou A, Perry T, Weston V, Petermann E, Zlatanou A, et al. Bet inhibition as a single or combined therapeutic approach in primary paediatric b-precursor acute lymphoblastic leukaemia. Blood Cancer J. 2013; 3:e126. doi:10.1038/bcj.2013.24

130. Ott CJ, Kopp N, Bird L, Paranal RM, Qi J, Bowman T, et al. Bet bromodomain inhibition targets both c-myc and il7r in high-risk acute lymphoblastic leukemia. Blood. 2012; 120(14):2843-52. doi:10.1182/blood-2012-02-413021

131. Chaidos A, Caputo V, Gouvedenou K, Liu B, Marigo I, Chaudhry MS, et al. Potent antimyeloma activity of the novel bromodomain inhibitors i-bet151 and i-bet762. Blood. 2014; 123(5):697-705. doi:10.1182/blood-2013-01-478420

132. Khandekar D, Tiriveedhi V. Role of bet inhibitors in triple negative breast cancers. Cancers. 2020; 12(4):784.

133. Lee DH, Qi J, Bradner JE, Said JW, Doan NB, Forscher C, et al. Synergistic effect of jq 1 and rapamycin for treatment of human osteosarcoma. Int J Cancer. 2015; 136(9):2055-64.

134. Baker EK, Taylor S, Gupte A, Sharp PP, Walia M, Walsh NC, et al. Bet inhibitors induce apoptosis through a myc independent mechanism and synergise with cdk inhibitors to kill osteosarcoma cells. Sci Rep. 2015; 5:10120.

135. Sun B, Shah B, Fiskus W, Qi J, Rajapakshe K, Coarfa C, et al. Synergistic activity of bet protein antagonist-based combinations in mantle cell lymphoma cells sensitive or resistant to ibrutinib. Blood. 2015:blood-2015-04-639542.

136. Shahbazi J, Liu PY, Atmadibrata B, Bradner JE, Marshall GM, Lock RB, et al. The bromodomain inhibitor jq1 and the histone deacetylase inhibitor panobinostat synergistically reduce n-myc expression and induce anticancer effects. Clin Cancer Res. 2016;

137. Tinsley S, Meja K, Shepherd C, Khwaja A. Synergistic induction of cell death in haematological malignancies by combined phosphoinositide-3-kinase and bet bromodomain inhibition. Br J Haematol. 2015; 170(2):275-8.

138. Kapp N, Stander XX, Stander BA. Synergistic in-vitro effects of combining an antiglycolytic, 3-bromopyruvate, and a bromodomain-4 inhibitor on u937 myeloid leukemia cells. Anticancer Drugs. 2018; 29(5):429-39.

139. Kozako T, Suzuki T, Yoshimitsu M, Arima N, Honda S-i, Soeda S. Anticancer agents targeted to sirtuins. Molecules. 2014; 19(12):20295-313.

140. Roth M, Chen W. Sorting out functions of sirtuins in cancer. Oncogene. 2014; 33(13):1609-20.

141. Peck B, Chen C-Y, Ho K-K, Di Fruscia P, Myatt SS, Coombes RC, et al. Sirt inhibitors induce cell death and p53 acetylation through targeting both sirt1 and sirt2. Molecular cancer therapeutics. 2010; 9(4):844-55.

142. Wang Y, Yang J, Hong T, Chen X, Cui L. Sirt2: Controversy and multiple roles in disease and physiology. Ageing research reviews. 2019:100961.

143. Chung YR, Kim H, Park SY, Park IA, Jang JJ, Choe J-Y, et al. Distinctive role of sirt1 expression on tumor invasion and metastasis in breast cancer by molecular subtype. Hum Pathol. 2015; 46(7):1027-35. doi:https://doi.org/10.1016/j.humpath.2015.03.015

144. Kim H, Lee K-H, Park IA, Chung YR, Im S-A, Noh D-Y, et al. Expression of sirt1 and apoptosis-related proteins is predictive for lymph node metastasis and disease-free survival in luminal a breast cancer. Virchows Archiv. 2015; 467(5):563-70.

145. Chung SY, Jung YY, Park IA, Kim H, Chung YR, Kim JY, et al. Oncogenic role of sirt1 associated with tumor invasion, lymph node metastasis, and poor disease-free survival in triple negative breast cancer. Clinical & experimental metastasis. 2016; 33(2):179-85.

146. Jin M-S, Hyun CL, Park IA, Kim JY, Chung YR, Im S-A, et al. Sirt1 induces tumor invasion by targeting epithelial mesenchymal transition-related pathway and is a prognostic marker in triple negative breast cancer. Tumor Biology. 2016; 37(4):4743-53.

147. Jackson SP, Bartek J. The DNA-damage response in human biology and disease. Nature. 2009; 461(7267):1071-8.

148. Thornberry NA, Lazebnik Y. Caspases: Enemies within. Science. 1998; 281(5381):1312-6.

149. Harris CC. P53 tumor suppressor gene: From the basic research laboratory to the clinic—an abridged historical perspective. Carcinogenesis. 1996; 17(6):1187-98.

150. Fiskus W, Coothankandaswamy V, Chen J, Ma H, Ha K, Saenz DT, et al. Sirt2 deacetylates and inhibits the peroxidase activity of peroxiredoxin-1 to sensitize breast cancer cells to oxidant stress-inducing agents. Cancer research. 2016; 76(18):5467-78.

151. Zhou W, Ni TK, Wronski A, Glass B, Skibinski A, Beck A, et al. The sirt2 deacetylase stabilizes slug to control malignancy of basal-like breast cancer. Cell reports. 2016; 17(5):1302-17.

152. Li Y, Matsumori H, Nakayama Y, Osaki M, Kojima H, Kurimasa A, et al. Sirt2 down-regulation in hela can induce p53 accumulation via p38 mapk activation-dependent p300 decrease, eventually leading to apoptosis. Genes to Cells. 2011; 16(1):34-45.

153. Schwarz-Cruz-y-Celis Á, Meléndez-Zajgla J. Cancer stem cells. Cancer. 2011; 7:11.

154. Nor C, Zhang Z, Warner KA, Bernardi L, Visioli F, Helman JI, et al. Cisplatin induces bmi-1 and enhances the stem cell fraction in head and neck cancer. Neoplasia. 2014; 16(2):137-46. doi:10.1593/neo.131744

155. Rizzo S, Hersey JM, Mellor P, Dai W, Santos-Silva A, Liber D, et al. Ovarian cancer stem cell-like side populations are enriched following chemotherapy and overexpress ezh2. Mol Cancer Ther. 2011; 10(2):325-35. doi:10.1158/1535-7163.MCT-10-0788
1535-7163.MCT-10-0788 [pii]

156. Alvero AB, Craveiro V, Holmberg J, Yang Y, Mor G. Paclitaxel selects and enriches for cd44+/myd88+ ovarian cancer stem cells. Cancer Res. 2012; 72(8 Supplement):3471.

157. Bao S, Wu Q, McLendon RE, Hao Y, Shi Q, Hjelmeland AB, et al. Glioma stem cells promote radioresistance by preferential activation of the DNA damage response. Nature. 2006; 444(7120):756-60. doi:10.1038/nature05236

158. Phillips TM, McBride WH, Pajonk F. The response of cd24−/low/cd44+ breast cancer–initiating cells to radiation. J Natl Cancer Inst. 2006; 98(24):1777-85. doi:10.1093/jnci/djj495

159. Grivennikov SI, Greten FR, Karin M. Immunity, inflammation, and cancer. Cell. 2010; 140(6):883-99. doi:10.1016/j.cell.2010.01.025

160. Jourdan F, Leese MP, Dohle W, Hamel E, Ferrandis E, Newman SP, et al. Synthesis, antitubulin, and antiproliferative sar of analogues of 2-methoxyestradiol-3,17-o,o-bis-sulfamate. J Med Chem. 2010; 53(7):2942-51. doi:10.1021/jm9018806

161. Ireson CR, Chander SK, Purohit A, Perera S, Newman SP, Parish D, et al. Pharmacokinetics and efficacy of 2-methoxyoestradiol and 2-methoxyoestradiol-bis-sulphamate in vivo in rodents. Br J Cancer. 2004; 90(4):932-7. doi:10.1038/sj.bjc.6601591

162. Filippakopoulos P, Picaud S, Fedorov O, Keller M, Wrobel M, Morgenstern O, et al. Benzodiazepines and benzotriazepines as protein interaction inhibitors targeting bromodomains of the bet family. Bioorganic & medicinal chemistry. 2012; 20(6):1878-86.

163. Filippakopoulos P, Qi J, Picaud S, Shen Y, Smith WB, Fedorov O, et al. Selective inhibition of bet bromodomains. Nature. 2010; 468(7327):1067-73.

164. Deepak V, Wang B, Koot D, Kasonga A, Stander XX, Coetzee M, et al. In silico design and bioevaluation of selective benzotriazepine brd 4 inhibitors with potent antiosteoclastogenic activity. Chem Biol Drug Des. 2017; 90(1):97-111.

165. You L, Nie J, Sun W-J, Zheng Z-Q, Yang X-J. Lysine acetylation: Enzymes, bromodomains and links to different diseases. Essays in biochemistry. 2012; 52:1-12.

166. Jung M, Philpott M, Müller S, Schulze J, Badock V, Eberspächer U, et al. Affinity map of bromodomain protein 4 (brd4) interactions with the histone h4 tail and the small molecule inhibitor jq1. J Biol Chem. 2014; 289(13):9304-19.

167. Naidu R, Wahab NA, Yadav M, Kutty MK. Protein expression and molecular analysis of c-myc gene in primary breast carcinomas using immunohistochemistry and differential polymerase chain reaction. Int J Mol Med. 2002; 9(2):189-96.

168. Xu J, Chen Y, Olopade OI. Myc and breast cancer. Genes Cancer. 2010; 1(6):629-40.

169. Kadota M, Sato M, Duncan B, Ooshima A, Yang HH, Diaz-Meyer N, et al. Identification of novel gene amplifications in breast cancer and coexistence of gene amplification with an activating mutation of pik3ca. Cancer Res. 2009; 69(18):7357.

170. Zuber J, Shi J, Wang E, Rappaport AR, Herrmann H, Sison EA, et al. Rnai screen identifies brd4 as a therapeutic target in acute myeloid leukaemia. Nature. 2011;

171. Dubik D, Shiu R. Transcriptional regulation of c-myc oncogene expression by estrogen in hormone-responsive human breast cancer cells. J Biol Chem. 1988; 263(25):12705-8.

172. Dey A, Nishiyama A, Karpova T, McNally J, Ozato K. Brd4 marks select genes on mitotic chromatin and directs postmitotic transcription. Mol Biol Cell. 2009; 20(23):4899-909.

173. You J, Croyle JL, Nishimura A, Ozato K, Howley PM. Interaction of the bovine papillomavirus e2 protein with brd4 tethers the viral DNA to host mitotic chromosomes. Cell. 2004; 117(3):349-60.

174. Dey A, Chitsaz F, Abbasi A, Misteli T, Ozato K. The double bromodomain protein brd4 binds to acetylated chromatin during interphase and mitosis. Proc Natl Acad Sci. 2003; 100(15):8758-63.

175. Devaiah BN, Singer DS. Two faces of brd4: Mitotic bookmark and transcriptional lynchpin. Transcription. 2013; 4(1):13-7.

176. Nishiyama A, Dey A, Miyazaki J-i, Ozato K. Brd4 is required for recovery from antimicrotubule drug-induced mitotic arrest: Preservation of acetylated chromatin. Mol Biol Cell. 2006; 17(2):814-23.

177. Disch JS, Evindar G, Chiu CH, Blum CA, Dai H, Jin L, et al. Discovery of thieno [3, 2-d] pyrimidine-6-carboxamides as potent inhibitors of sirt1, sirt2, and sirt3. J Med Chem. 2013; 56(9):3666-79.

178. Otto M. In vitro study of in silico designed sirtuin 1 and bromodomain 4 inhibitors on human neuroblastoma sh-sy5y and acute myeloid leukemia u937 cells: University of Pretoria; 2018.

179. Mesa RA, Yasothan U, Kirkpatrick P. Ruxolitinib. Nature Publishing Group; 2012.

180. Harrison C, Kiladjian J-J, Al-Ali HK, Gisslinger H, Waltzman R, Stalbovskaya V, et al. Jak inhibition with ruxolitinib versus best available therapy for myelofibrosis. New Engl J Med. 2012; 366(9):787-98. doi:10.1056/NEJMoa1110556

181. Bozic I, Reiter JG, Allen B, Antal T, Chatterjee K, Shah P, et al. Evolutionary dynamics of cancer in response to targeted combination therapy. Elife. 2013; 2:e00747. doi:10.7554/eLife.00747

182. Chou T-C. Theoretical basis, experimental design, and computerized simulation of synergism and antagonism in drug combination studies. Pharmacol Re. 2006; 58(3):621. doi:10.1124/pr.58.3.10

183. Berenger F, Vu O, Meiler J. Consensus queries in ligand-based virtual screening experiments. J Cheminform. 2017; 9(1):60.

184. Huey R, Morris GM. Using autodock 4 with autodocktools: A tutorial. The Scripps Research Institute, USA. 2008:54-6.

185. Trott O, Olson AJ. Autodock vina: Improving the speed and accuracy of docking with a new scoring function, efficient optimization, and multithreading. J Comput Chem. 2010; 31(2):455-61.

186. Venkatachalam CM, Jiang X, Oldfield T, Waldman M. Ligandfit: A novel method for the shape-directed rapid docking of ligands to protein active sites. J Mol Graphics Model. 2003; 21(4):289-307.

187. Abagyan R, Totrov M, Kuznetsov D. Icm—a new method for protein modeling and design: Applications to docking and structure prediction from the distorted native conformation. J Comput Chem. 1994; 15(5):488-506.

188. Friesner RA, Murphy RB, Repasky MP, Frye LL, Greenwood JR, Halgren TA, et al. Extra precision glide: Docking and scoring incorporating a model of hydrophobic enclosure for protein− ligand complexes. J Med Chem. 2006; 49(21):6177-96.

189. Verdonk ML, Cole JC, Hartshorn MJ, Murray CW, Taylor RD. Improved protein–ligand docking using gold. Proteins. 2003; 52(4):609-23.

190. Pagadala NS, Syed K, Tuszynski J. Software for molecular docking: A review. Biophys Rev. 2017; 9(2):91-102.

191. Gaillard T. Evaluation of autodock and autodock vina on the casf-2013 benchmark. J Chem Inf Model. 2018; 58(8):1697-706.

192. Su M, Yang Q, Du Y, Feng G, Liu Z, Li Y, et al. Comparative assessment of scoring functions: The casf-2016 update. J Chem Inf Model. 2018; 59(2):895-913.

193. Wang C, Zhang Y. Improving scoring-docking-screening powers of protein–ligand scoring functions using random forest. J Comput Chem. 2017; 38(3):169-77.

194. Yasuo N, Sekijima M. Improved method of structure-based virtual screening via interaction-energy-based learning. J Chem Inf Model. 2019; 59(3):1050-61.

195. Delmore JE, Issa GC, Lemieux ME, Rahl PB, Shi J, Jacobs HM, et al. Bet bromodomain inhibition as a therapeutic strategy to target c-myc. Cell. 2011; 146(6):904-17.

196. Dang CV, Le A, Gao P. Myc-induced cancer cell energy metabolism and therapeutic opportunities. Clin Cancer Res. 2009; 15:6479–83.

197. Li L, Wang L, Li L, Wang Z, Ho Y, McDonald T, et al. Activation of p53 by sirt1 inhibition enhances elimination of cml leukemia stem cells in combination with imatinib. Cancer Cell. 2012; 21(2):266-81.

198. Cailleau R, Olive M, Cruciger QV. Long-term human breast carcinoma cell lines of metastatic origin: Preliminary characterization. In Vitro. 1978; 14(11):911-5.

199. Welsh J. Animal models for studying prevention and treatment of breast cancer. Animal models for the study of human disease: Elsevier; 2013. p. 997-1018.

200. ATCC®. Thawing, propagating, and cryopreserving protocol nci-pbcf-htb26 (mda-mb-231) breast adenocarcinoma (atcc®htb-26™). 2012.

201. Comşa Ş, Cimpean AM, Raica M. The story of mcf-7 breast cancer cell line: 40 years of experience in research. Anticancer Res. 2015; 35(6):3147-54.

202. ATCC®. Thawing, propagating, and cryopreserving protocol mcf-7 breast adenocarcinoma nci-pbcf-htb22 (atcc® htb-22™). 2012.

203. Bouïs D, Hospers GA, Meijer C, Molema G, Mulder NH. Endothelium in vitro: A review of human vascular endothelial cell lines for blood vessel-related research. Angiogenesis. 2001; 4(2):91-102.

204. Arafath MA, Adam F, Razali MR, Ahmed Hassan LE, Ahamed MBK, Majid AMSA. Synthesis, characterization and anticancer studies of ni(ii), pd(ii) and pt(ii) complexes with schiff base derived from n-methylhydrazinecarbothioamide and 2-hydroxy-5-methoxy-3-nitrobenzaldehyde. Journal of Molecular Structure. 2017; 1130:791-8. doi:https://doi.org/10.1016/j.molstruc.2016.10.099

205. Buonanno F, Quassinti L, Bramucci M, Amantini C, Lucciarini R, Santoni G, et al. The protozoan toxin climacostol inhibits growth and induces apoptosis of human tumor cell lines. Chemico-Biological Interactions. 2008; 176(2):151-64. doi:https://doi.org/10.1016/j.cbi.2008.07.007

206. Guo L, Chen X, Chen W, Ma Q, Fan W, Zhang J, et al. Molecular hybrid design, synthesis, in vitro and in vivo anticancer evaluation, and mechanism of action of n-acylhydrazone linked, heterobivalent β-carbolines. Bioorganic Chemistry. 2020; 96:103612. doi:https://doi.org/10.1016/j.bioorg.2020.103612

207. Figueiredo P, Lintinen K, Kiriazis A, Hynninen V, Liu Z, Bauleth-Ramos T, et al. In vitro evaluation of biodegradable lignin-based nanoparticles for drug delivery and enhanced antiproliferation effect in cancer cells. Biomaterials. 2017; 121:97-108. doi:https://doi.org/10.1016/j.biomaterials.2016.12.034

208. Jashari A, Imeri F, Ballazhi L, Shabani A, Mikhova B, Dräger G, et al. Synthesis and cellular characterization of novel isoxazolo- and thiazolohydrazinylidene-chroman-2,4-diones on cancer and non-cancer cell growth and death. Bioorganic & Medicinal Chemistry. 2014; 22(9):2655-61. doi:https://doi.org/10.1016/j.bmc.2014.03.026

209. Burger T, Mokoka T, Fouché G, Steenkamp P, Steenkamp V, Cordier W. Solamargine, a bioactive steroidal alkaloid isolated from solanum aculeastrum induces non-selective cytotoxicity and p-glycoprotein inhibition. BMC complementary and alternative medicine. 2018; 18(1):137.

210. Cattin S, Ramont L, Rüegg C. Characterization and in vivo validation of a three-dimensional multi-cellular culture model to study heterotypic interactions in colorectal cancer cell growth, invasion and metastasis. Frontiers in bioengineering and biotechnology. 2018; 6:97.

211. Freshney RI. Culture of animal cells: A manual of basic technique Third ed. New York: John Wiley and Sons, Inc.; 1994.

212. Totrov M, Abagyan R. Flexible ligand docking to multiple receptor conformations: A practical alternative. Curr Opin Struct Biol. 2008; 18(2):178-84. doi:S0959-440X(08)00008-0 [pii]
10.1016/j.sbi.2008.01.004

213. Guex N, Peitsch MC, Schwede T. Automated comparative protein structure modeling with swiss-model and swiss-pdbviewer: A historical perspective. Electrophoresis. 2009; 30(S1):S162-S73.

214. Dohle W, Prota AE, Menchon Gg, Hamel E, Steinmetz MO, Potter BV. Tetrahydroisoquinoline sulfamates as potent microtubule disruptors: Synthesis, antiproliferative and antitubulin activity of dichlorobenzyl-based derivatives, and a tubulin cocrystal structure. ACS Omega. 2019; 4(1):755-64. doi:doi: 10.1021/acsomega.8b02879

215. Dohle W, Jourdan FL, Menchon G, Prota AE, Foster PA, Mannion P, et al. Quinazolinone-based anticancer agents: Synthesis, antiproliferative sar, antitubulin activity, and tubulin co-crystal structure. J Med Chem. 2018; 61(3):1031-44.

216. Sastry GM, Adzhigirey M, Day T, Annabhimoju R, Sherman W. Protein and ligand preparation: Parameters, protocols, and influence on virtual screening enrichments. J Comput-Aided Mol Des. 2013; 27(3):221-34.

217. Koes DR, Baumgartner MP, Camacho CJ. Lessons learned in empirical scoring with smina from the csar 2011 benchmarking exercise. J Chem Inf Model. 2013; 53(8):1893-904.

218. Wright MN, Ziegler A. Ranger: A fast implementation of random forests for high dimensional data in c++ and r. arXiv preprint arXiv:1508.04409. 2015;

219. Kuhn M. Building predictive models in r using the caret package. J Stat Softw. 2008; 28(5):1-26.

220. Gillies RJ, Didier N, Denton M. Determination of cell number in monolayer cultures. Anal Biochem. 1986; 159(1):109-13. doi:0003-2697(86)90314-3 [pii]

221. Kueng W, Silber E, Eppenberger U. Quantification of cells cultured on 96-well plates. Anal Biochem. 1989; 182(1):16-9. doi:0003-2697(89)90710-0 [pii]

222. Chou T-C. Drug combination studies and their synergy quantification using the chou-talalay method. Cancer Res. 2010; 70(2):440-6.

223. Jacinto CS, Grobbelaar C, Hlophe Y, Potter BV, Stander A, du Toit P. Synergistic anticancer potential of an antimitotic compound and an in silico-designed bromodomain 4 inhibitor on human neuroblastoma cells. Faculty of Health Sciences Health Sciences. 2015;

224. Riekert C, Grobbelaar C, Hlophe Y, Stander A, du Toit P. In vitro effects of combining novel in silico-designed sirtuin 1 and bromodomain 4 inhibitors on human neuroblastoma cells. Faculty of Health Sciences Health Sciences. 2015;

225. Thomé MP, Filippi-Chiela EC, Villodre ES, Migliavaca CB, Onzi GR, Felipe KB, et al. Ratiometric analysis of acridine orange staining in the study of acidic organelles and autophagy. J Cell Sci. 2016; 129(24):4622-32.

226. Cottet-Rousselle C, Ronot X, Leverve X, Mayol JF. Cytometric assessment of mitochondria using fluorescent probes. Cytometry Part A. 2011; 79(6):405-25.

227. Guthrie H, Welch G. Determination of high mitochondrial membrane potential in spermatozoa loaded with the mitochondrial probe 5,5',6,6'-tetrachloro-1,1',3,3'-tetraethylbenzimidazolyl-carbocyanine iodide (jc-1) by using fluorescence-activated flow cytometry. Methods Mol Biol. 2008; 477:89-97.

228. Mandy F, Bergeron M, Minkus T. Principles of flow cytometry. Transfus Sci. 1995; 16(4):303-14.

229. Letai A, Kutuk O. Regulation of bcl-2 family proteins by posttranslational modifications. Current Molecular Medicine. 2008; 8(2):102-18.

230. Yip KW, Reed JC. Bcl-2 family proteins and cancer. Oncogene. 2008; 27(50):6398-406. doi:10.1038/onc.2008.307

231. Ryan JJ, Prochownik E, Gottlieb CA, Apel IJ, Merino R, Nuñez G, et al. C-myc and bcl-2 modulate p53 function by altering p53 subcellular trafficking during the cell cycle. Proc Natl Acad Sci. 1994; 91(13):5878. doi:10.1073/pnas.91.13.5878

232. Provenzano M, Mocellin S. Complementary techniques: Validation of gene expression data by quantitative real time pcr. Adv Exp Med Biol. 2007; 593:66-73. doi:10.1007/978-0-387-39978-2_7

233. Coleman WB, Tsongalis GJ. Diagnostic molecular pathology: A guide to applied molecular testing: Academic Press; 2016.

234. Livak KJ, Schmittgen TD. Analysis of relative gene expression data using real-time quantitative pcr and the 2− δδct method. Methods. 2001; 25(4):402-8.

235. Dai H, Case AW, Riera TV, Considine T, Lee JE, Hamuro Y, et al. Crystallographic structure of a small molecule sirt1 activator-enzyme complex. Nat Commun. 2015; 6:7645.

236. Eghtedar A, Verstovsek S, Estrov Z, Burger J, Cortes J, Bivins C, et al. Phase 2 study of the jak kinase inhibitor ruxolitinib in patients with refractory leukemias, including postmyeloproliferative neoplasm acute myeloid leukemia. Blood. 2012; 119(20):4614-8. doi:10.1182/blood-2011-12-400051

237. Stewart HJS, Horne GA, Bastow S, Chevassut TJT. Brd 4 associates with p53 in dnmt 3a-mutated leukemia cells and is implicated in apoptosis by the bromodomain inhibitor jq 1. Cancer medicine. 2013; 2(6):826-35.

238. Bates D, Eastman A. Microtubule destabilising agents: Far more than just antimitotic anticancer drugs. British journal of clinical pharmacology. 2017; 83(2):255-68.

239. Stander BA, Joubert F, Tu C, Sippel KH, McKenna R, Joubert AM. Signaling pathways of ese-16, an antimitotic and anticarbonic anhydrase estradiol analog, in breast cancer cells. PloS one. 2013; 8(1):e53853.

240. Banerjee S, Arnst KE, Wang Y, Kumar G, Deng S, Yang L, et al. Heterocyclic-fused pyrimidines as novel tubulin polymerization inhibitors targeting the colchicine binding site: Structural basis and antitumor efficacy. J Med Chem. 2018; 61(4):1704-18.

241. Stander BA, Marais S, Vorster CJJ, Joubert AM. In vitro effects of 2-methoxyestradiol on morphology, cell cycle progression, cell death and gene expression changes in the tumorigenic mcf-7 breast epithelial cell line. J Steroid Biochem Mol Biol. 2010; 119(3):149-60. doi:https://doi.org/10.1016/j.jsbmb.2010.02.019

242. Stander A, Joubert F, Joubert A. Docking, synthesis, and in vitro evaluation of antimitotic estrone analogs. Chem Biol Drug Des. 2011; 77(3):173-81. doi:10.1111/j.1747-0285.2010.01064.x

243. Leese MP, Jourdan FL, Gaukroger K, Mahon MF, Newman SP, Foster PA, et al. Structure-activity relationships of c-17 cyano-substituted estratrienes as anticancer agents. J Med Chem. 2008; 51(5):1295-308. doi:10.1021/jm701319c

244. Marais S, Mqoco T, Stander A, van Papendorp D, Joubert A. The in vitro effects of a sulphamoylated derivative of 2-methoxyestradiol on cell number, morphology and alpha-tubulin disruption in cervical adenocarcinoma (hela) cells. Biomed Res. 2012; 23(3):357-62.

245. Purohit A, Hejaz HAM, Walden L, MacCarthy-Morrogh L, Packham G, Potter BVL, et al. The effect of 2-methoxyoestrone-3-o-sulphamate on the growth of breast cancer cells and induced mammary tumours. Int J Cancer. 2000; 85(4):584-9. doi:10.1002/(sici)1097-0215(20000215)85:4<584::Aid-ijc22>3.0.Co;2-q

246. Foster PA, Stengel C, Ali T, Leese MP, Potter BV, Reed MJ, et al. A comparison of two orally bioavailable anti-cancer agents, irc-110160 and stx140. Anticancer Res. 2008; 28(3A):1483-91.

247. Ding L, Wang X, Zhang J, Mu Z, Zhou X, Liu P. Underlying mechanism of 2-methoxyestradiol-induced apoptosis and growth arrest in skov3 human ovarian cancer cells. Eur Rev Med Pharmacol Sci. 2015; 19(11):2084-90.

248. Viola G, Bortolozzi R, Hamel E, Moro S, Brun P, Castagliuolo I, et al. Mg-2477, a new tubulin inhibitor, induces autophagy through inhibition of the akt/mtor pathway and delayed apoptosis in a549 cells. Biochem Pharmacol. 2012; 83(1):16-26. doi:https://doi.org/10.1016/j.bcp.2011.09.017

249. Visagie MH, Joubert AM. 2-methoxyestradiol-bis-sulphamate refrains from inducing apoptosis and autophagy in a non-tumorigenic breast cell line. Cancer Cell Int. 2012; 12(1):37. doi:10.1186/1475-2867-12-37

250. Stander B, Marais S, Vorster C, Joubert A. In vitro effects of 2-methoxyestradiol on morphology, cell cycle progression, cell death and gene expression changes in the tumorigenic mcf-7 breast epithelial cell line. J Steroid Biochem Mol Biol. 2010; 119(3-5):149-60.

251. Azad MB, Chen Y, Gibson SB. Regulation of autophagy by reactive oxygen species (ros): Implications for cancer progression and treatment. Antioxid Redox Signal. 2009; 11(4):777-90.

252. Guan F, Ding R, Zhang Q, Chen W, Li F, Long L, et al. Wx-132-18b, a novel microtubule inhibitor, exhibits promising anti-tumor effects. Oncotarget. 2017; 8(42):71782-96. doi:10.18632/oncotarget.17710

253. Herrmann H, Blatt K, Shi J, Gleixner KV, Cerny-Reiterer S, Müllauer L, et al. Small-molecule inhibition of brd4 as a new potent approach to eliminate leukemic stem- and progenitor cells in acute myeloid leukemia (aml). Oncotarget. 2012; 3(12)

254. Mqoco T, Stander A, Engelbrecht A-M, Joubert AM. A combination of an antimitotic and a bromodomain 4 inhibitor synergistically inhibits the metastatic mda-mb-231 breast cancer cell line. BioMed Research International. 2019; 2019

255. Shu S, Lin CY, He HH, Witwicki RM, Tabassum DP, Roberts JM, et al. Response and resistance to bet bromodomain inhibitors in triple-negative breast cancer. Nature. 2016; 529(7586):413-7. doi:10.1038/nature16508

256. Trabucco SE, Gerstein RM, Evens AM, Bradner JE, Shultz LD, Greiner DL, et al. Inhibition of bromodomain proteins for the treatment of human diffuse large b-cell lymphoma. Clin Cancer Res. 2015; 21(1):113. doi:10.1158/1078-0432.CCR-13-3346

257. Vázquez R, Riveiro ME, Astorgues-Xerri L, Odore E, Rezai K, Erba E, et al. The bromodomain inhibitor otx015 (mk-8628) exerts anti-tumor activity in triple-negative breast cancer models as single agent and in combination with everolimus. Oncotarget. 2017; 8(5):7598-613. doi:10.18632/oncotarget.13814

258. Sakamaki J-i, Wilkinson S, Hahn M, Tasdemir N, O'Prey J, Clark W, et al. Bromodomain protein brd4 is a transcriptional repressor of autophagy and lysosomal function. Mol Cell. 2017; 66(4):517-32.

259. Lu J, Qian Y, Altieri M, Dong H, Wang J, Raina K, et al. Hijacking the e3 ubiquitin ligase cereblon to efficiently target brd4. Chem Biol. 2015; 22(6):755-63.

260. Sakamaki J-I, Ryan KM. Transcriptional regulation of autophagy and lysosomal function by bromodomain protein brd4. Autophagy. 2017; 13(11):2006-7. doi:10.1080/15548627.2017.1364822

261. Ishida CT, Bianchetti E, Shu C, Halatsch M-E, Westhoff MA, Karpel-Massler G, et al. Bh3-mimetics and bet-inhibitors elicit enhanced lethality in malignant glioma. Oncotarget. 2017; 8(18):29558-73. doi:10.18632/oncotarget.16365

262. Wang E, Sorolla A, Cunningham PT, Bogdawa HM, Beck S, Golden E, et al. Tumor penetrating peptides inhibiting myc as a potent targeted therapeutic strategy for triple-negative breast cancers. Oncogene. 2019; 38(1):140-50.

263. Wu X, Liu D, Gao X, Xie F, Tao D, Xiao X, et al. Inhibition of brd4 suppresses cell proliferation and induces apoptosis in renal cell carcinoma. Cell Physiol Biochem. 2017; 41(5):1947-56.

264. Tan Y, Wang L, Du Y, Liu X, Chen Z, Weng X, et al. Inhibition of brd4 suppresses tumor growth in prostate cancer via the enhancement of foxo1 expression. Int J Oncol. 2018; 53(6):2503-17.

265. Sahni JM, Gayle SS, Bonk KLW, Vite LC, Yori JL, Webb B, et al. Bromodomain and extraterminal protein inhibition blocks growth of triple-negative breast cancers through the suppression of aurora kinases. J Biol Chem. 2016; 291(45):23756-68.

266. Mqoco T, Stander A, Engelbrecht A-M, Joubert AM. A combination of an antimitotic and a bromodomain 4 inhibitor synergistically inhibits the metastatic mda-mb-231 breast cancer cell line. BioMed Res Int. 2019; doi:https://doi.org/10.1155/2019/1850462

267. Sahai V, Redig AJ, Collier KA, Eckerdt FD, Munshi HG. Targeting bet bromodomain proteins in solid tumors. Oncotarget. 2016; 7(33):53997-4009. doi:10.18632/oncotarget.9804

268. Wang J, Kim TH, Ahn MY, Lee J, Jung JH, Choi WS, et al. Sirtinol, a class iii hdac inhibitor, induces apoptotic and autophagic cell death in mcf-7 human breast cancer cells. Int J Oncol. 2012; 41(3):1101-9.

269. Bedalov A, Gatbonton T, Irvine WP, Gottschling DE, Simon JA. Identification of a small molecule inhibitor of sir2p. Proc Natl Acad Sci. 2001; 98(26):15113-8.

270. Ota H, Akishita M, Eto M, Iijima K, Kaneki M, Ouchi Y. Sirt1 modulates premature senescence-like phenotype in human endothelial cells. J Mol Cell Cardiol. 2007; 43(5):571-9.

271. Heltweg B, Gatbonton T, Schuler AD, Posakony J, Li H, Goehle S, et al. Antitumor activity of a small-molecule inhibitor of human silent information regulator 2 enzymes. Cancer Res. 2006; 66(8):4368-77.

272. Olaharski AJ, Rine J, Marshall BL, Babiarz J, Zhang L, Verdin E, et al. The flavoring agent dihydrocoumarin reverses epigenetic silencing and inhibits sirtuin deacetylases. PLoS Genet. 2005; 1(6):e77.

273. Napper AD, Hixon J, McDonagh T, Keavey K, Pons J-F, Barker J, et al. Discovery of indoles as potent and selective inhibitors of the deacetylase sirt1. J Med Chem. 2005; 48(25):8045-54.

274. Otto M. In vitro study of in silico designed sirtuin 1 and bromodomain 4 inhibitors on human neuroblastoma sh-sy5y and acute myeloid leukemia u937 cells: University of Pretoria; 2018.

275. Lara E, Mai A, Calvanese V, Altucci L, Lopez-Nieva P, Martinez-Chantar ML, et al. Salermide, a sirtuin inhibitor with a strong cancer-specific proapoptotic effect. Oncogene. 2009; 28(6):781-91. doi:10.1038/onc.2008.436

276. Kruse J-P, Gu W. Modes of p53 regulation. Cell. 2009; 137(4):609-22.

277. Yi J, Luo J. Sirt1 and p53, effect on cancer, senescence and beyond. Biochimica et Biophysica Acta (BBA)-Proteins and Proteomics. 2010; 1804(8):1684-9.

278. Carafa V, Rotili D, Forgione M, Cuomo F, Serretiello E, Hailu GS, et al. Sirtuin functions and modulation: From chemistry to the clinic. Clin Epigenetics. 2016; 8(1):61. doi:10.1186/s13148-016-0224-3

279. Yuan H, Marmorstein R. Structural basis for sirtuin activity and inhibition. J Biol Chem. 2012; 287(51):42428-35.

280. Parenti MD, Bruzzone S, Nencioni A, Del Rio A. Selectivity hot-spots of sirtuin catalytic cores. Mol Biosyst. 2015; 11(8):2263-72.

281. Deng C-X. Sirt1, is it a tumor promoter or tumor suppressor? Int J Biol Sci. 2009; 5(2):147-52. doi:10.7150/ijbs.5.147

282. Kokkola T, Suuronen T, Pesonen M, Filippakopoulos P, Salminen A, Jarho E, et al. Bet inhibition upregulates sirt1 and alleviates inflammatory responses. ChemBioChem. 2015; doi:10.1002/cbic.201500272

283. Marks PA. The clinical development of histone deacetylase inhibitors as targeted anticancer drugs. Expert Opin Investig Drugs. 2010; 19(9):1049-66. doi:10.1517/13543784.2010.510514

284. Liu PY, Sokolowski N, Guo ST, Siddiqi F, Atmadibrata B, Telfer TJ, et al. The bet bromodomain inhibitor exerts the most potent synergistic anticancer effects with quinone-containing compounds and anti-microtubule drugs. Oncotarget. 2016; 7(48):79217.

285. Berns K, Hijmans EM, Bernards R. Repression of c-myc responsive genes in cycling cells causes g 1 arrest through reduction of cyclin e/cdk2 kinase activity. Oncogene. 1997; 15(11):1347.

286. Mc Gee MM. Targeting the mitotic catastrophe signaling pathway in cancer. Mediators Inflamm. 2015; 2015:13. doi:10.1155/2015/146282

287. Nishiyama A, Dey A, Tamura T, Ko M, Ozato K. Activation of jnk triggers release of brd4 from mitotic chromosomes and mediates protection from drug-induced mitotic stress. PLoS One. 2012; 7(5):e34719.

288. da Motta LL, Ledaki I, Purshouse K, Haider S, De Bastiani MA, Baban D, et al. The bet inhibitor jq1 selectively impairs tumour response to hypoxia and downregulates ca9 and angiogenesis in triple negative breast cancer. Oncogene. 2017; 36(1):122-32. doi:10.1038/onc.2016.184

289. Lu Y, Chen J, Xiao M, Li W, Miller DD. An overview of tubulin inhibitors that interact with the colchicine binding site. Pharm Res. 2012; 29(11):2943-71.

290. Park C, Cha H-J, Lee H, Hwang-Bo H, Ji SY, Kim MY, et al. Induction of g2/m cell cycle arrest and apoptosis by genistein in human bladder cancer t24 cells through inhibition of the ros-dependent pi3k/akt signal transduction pathway. Antioxidants. 2019; 8(9):327.

291. Ghavami S, Eshragi M, Ande SR, Chazin WJ, Klonisch T, Halayko AJ, et al. S100a8/a9 induces autophagy and apoptosis via ros-mediated cross-talk between mitochondria and lysosomes that involves bnip3. Cell Res. 2010; 20(3):314-31. doi:10.1038/cr.2009.129

292. Osaki M, Oshimura Ma, Ito H. Pi3k-akt pathway: Its functions and alterations in human cancer. Apoptosis. 2004; 9(6):667-76.

293. Deng X, Gao F, Flagg T, May WS. Mono-and multisite phosphorylation enhances bcl2's antiapoptotic function and inhibition of cell cycle entry functions. Proc Natl Acad Sci. 2004; 101(1):153-8.

294. Deng X, Kornblau SM, Ruvolo PP, May WS, Jr. Regulation of bcl2 phosphorylation and potential significance for leukemic cell chemoresistance. JNCI Monographs. 2000; 2000(28):30-7. doi:10.1093/oxfordjournals.jncimonographs.a024254

295. Ruvolo PP, Deng X, Ito T, Carr BK, May WS. Ceramide induces bcl2 dephosphorylation via a mechanism involving mitochondrial pp2a. J Biol Chem. 1999; 274(29):20296-300.

296. Charles AG, Han T-Y, Liu YY, Hansen N, Giuliano AE, Cabot MC. Taxol-induced ceramide generation and apoptosis in human breast cancer cells. Cancer Chemother Pharmacol. 2001; 47(5):444-50.

297. Deng X, Gao F, May WS. Protein phosphatase 2a inactivates bcl2's antiapoptotic function by dephosphorylation and up-regulation of bcl2-p53 binding. Blood. 2009; 113(2):422-8.

298. Kurinna S, Konopleva M, Palla S, Chen W, Kornblau S, Contractor R, et al. Bcl2 phosphorylation and active pkc α are associated with poor survival in aml. Leukemia. 2006; 20(7):1316-9.

299. Li P-L, Zhang Y. Cross talk between ceramide and redox signaling: Implications for endothelial dysfunction and renal disease. Sphingolipids in disease: Springer; 2013. p. 171-97.

300. Annunziata I, van de Vlekkert D, Wolf E, Finkelstein D, Neale G, Machado E, et al. Myc competes with mit/tfe in regulating lysosomal biogenesis and autophagy through an epigenetic rheostat. Nat Commun. 2019; 10(1):3623. doi:10.1038/s41467-019-11568-0

301. Wadhwa E, Nicolaides T. Bromodomain inhibitor review: Bromodomain and extra-terminal family protein inhibitors as a potential new therapy in central nervous system tumors. Cureus. 2016; 8(5):e620. doi:10.7759/cureus.620

302. Tolani B, Gopalakrishnan R, Punj V, Matta H, Chaudhary PM. Targeting myc in kshv-associated primary effusion lymphoma with bet bromodomain inhibitors. Oncogene. 2014; 33(22):2928.

303. Gallagher SJ, Mijatov B, Gunatilake D, Tiffen JC, Gowrishankar K, Jin L, et al. The epigenetic regulator i-bet151 induces bim-dependent apoptosis and cell cycle arrest of human melanoma cells. J Invest Dermatol. 2014; 134(11):2795-805.

304. Jostes S, Nettersheim D, Fellermeyer M, Schneider S, Hafezi F, Honecker F, et al. The bromodomain inhibitor jq1 triggers growth arrest and apoptosis in testicular germ cell tumours in vitro and in vivo. J Cell Mol Med. 2017; 21(7):1300-14.

305. Sakamaki J-i, Wilkinson S, Hahn M, Tasdemir N, O'Prey J, Clark W, et al. Bromodomain protein brd4 is a transcriptional repressor of autophagy and lysosomal function. Mol Cell. 2017; 66(4):517-32.e9. doi:10.1016/j.molcel.2017.04.027

306. Ouyang L, Zhang L, Liu J, Fu L, Yao D, Zhao Y, et al. Discovery of a small-molecule bromodomain-containing protein 4 (brd4) inhibitor that induces amp-activated protein kinase-modulated autophagy-associated cell death in breast cancer. J Med Chem. 2017; 60(24):9990-10012. doi:10.1021/acs.jmedchem.7b00275